Combined Spectroscopic and Electrochemical Studies of Ion Transport and Corrosive de-Adhesion Processes at Polymer/Oxide/Metal Interfaces

Dissertation

zur Erlangung des Grades eines Doktors der Naturwissenschaften
der Fakultät für Naturwissenschaften der Universität Paderborn

vorgelegt im Juni 2009

von

Ralf Posner

aus Dormagen

Gedruckt mit Genehmigung der Fakultät für Naturwissenschaften
der Universität Paderborn

Erstgutachter: Prof. Dr.-Ing. Guido Grundmeier
Zweitgutachter: Prof. Dr. Wolfgang Bremser

Tag der mündlichen Prüfung: 14. Juli 2009

Danksagung/Acknowledgements

Die vorliegende Arbeit wurde während meiner Tätigkeit als wissenschaftlicher Angestellter der Max-Planck-Institut für Eisenforschung GmbH in Düsseldorf im Zeitraum von Juli 2006 bis Juni 2009 angefertigt.

Meinem Betreuer, Prof. Guido Grundmeier, gilt mein besonderer Dank für die Unterstützung, Förderung und Betreuung sowie die interessante Thematik der Dissertation, für seine stete Diskussionsbereitschaft und das Interesse am Fortgang der Arbeit. Prof. Martin Stratmann danke ich für die freundliche Aufnahme in sein Institut und für viele hilfreiche Diskussionen. Prof. Wolfgang Bremser gebührt mein Dank für die Übernahme des Koreferats.

Für die finanzielle Unterstützung der Arbeit möchte ich mich bei der Christian Doppler Forschungsgesellschaft, der Henkel AG & Co. KGaA, der voestalpine Stahl GmbH, der BASF SE und der Max-Planck-Institut für Eisenforschung GmbH bedanken. In einer Vielzahl von Projekttreffen mit den Industriepartnern konnte ich dabei von wertvollen Diskussionen mit Dr. J. Sander, A. De-Zeuuw, Dr. M. Wolpers, Dr. K.-H. Stellnberger und M. Fleischanderl vom Christian Doppler-Team profitieren, insbesondere aber auch von der Unterstützung durch Dr. S. Amthor und Dr. K. J. Roschmann von der BASF.

Allen Mitarbeitern der Arbeitsgruppe Adhäsion und Dünne Filme am MPIE und assoziierten Arbeitskreisen, insbesondere Dr. N. Fink, G. Giza, Dr. M. Giza, Dr. P. Keil, Dr. I. Klüppel, K. Pohl, M. Santa, M. Schmitt, P. Thissen, T. Titz, Dr. M. Valtiner und R. Vlasak danke ich für das angenehme Arbeitsklima, die Kollegialität, stete Hilfsbereitschaft und für viele heitere Stunden.

Ohne die hervorragende Arbeit der Abteilung Elektronik, besonders von B. Schönberger und der mechanischen Werkstatt, vertreten durch R. Selbach, wäre an ein Gelingen der vorliegenden Dissertation zudem nicht zu denken gewesen.

Mein spezieller Dank gilt Dr. K. Wapner, meinem Mentor für die ersten Monate als Doktorand am MPIE und M. Marazita, meinem „verlängerten Arm“ an der Universität Paderborn.

Special thanks also go to Dr. J. Wielant. Jan, you deeply impressed me during your stay at the MPIE with your exceptional scientific competences and skills. You functioned as the warrantor for an extremely fruitful cooperation between the Vrije Universiteit Brussel and the MPIE and are the kind of scientist everybody would like to work with. I am proud to have gained friendship with you.

Schließlich möchte ich mich auch besonders bei meiner Familie für ihre anhaltende Unterstützung während meiner Doktorandenzeit bedanken.

Abstract

The present study followed a comprehensive experimental approach to reveal the mechanisms of ion transport processes at polymer/oxide/metal interfaces, to evaluate determinant parameters for the progress of corrosive de-adhesion and to address them to the so called `electrolyte front position´. This could be achieved after probing of the interface stability by initiation of cathodic or combined cathodic/anodic delamination and monitoring its progress in particular with the height-regulated Scanning Kelvin Probe. The polymer/substrate interface design could be specifically adjusted by variation of the substrate material, in particular zinc and iron samples or steel substrates with distinct passive films. It was also focussed on the influence of the interfacial contact between adhesive layer and nano-rough oxide surface as well as the barrier properties of latex copolymer films of different monomer composition, glass transition temperature and polymer network density. Polymer/substrate interface potentials were compared to resulting ion distributions after interfacial ion transport processes applying X-ray Photoelectron Spectroscopy and Time-of-Flight Secondary Ion Mass Spectrometry. It could be shown that ions do not diffuse along the interfaces. In fact, ion migration in an electrostatic field is dominant even in extremely oxygen deficient humid atmosphere. Reactive electrolyte spreading along uncoated oxide surfaces can be applied to simulate corrosive delamination processes without the complex polymer/ substrate interface structure. It was proven that electrochemical interface degradation precedes a macroscopic polymer de-adhesion. The progress of delamination strongly responded to the available interfacial water activity. Increased hydrostatic pressure of the defect electrolyte accelerated the interfacial ion transport, but electrochemical stimulation turned out to be an even more effective tool to address corrosive de-adhesion kinetics. Nevertheless they were also found to end up with self-inhibition at reduced atmospheric moisture; the relevant lateral dimensions of the electrolyte front thereby could be confined to cover less than 250 μm. The polar surface energy component turned out to be a suitable parameter to estimate resulting polymer/ iron oxide adhesion forces and can be applied to predict rates of subsequently initiated delamination processes. Reactive electrolyte spreading along uncoated iron surfaces in contrast is not determined by the respective water contact angles and surface energies. Flexible and elastic polymers with a glass transition temperature below ambient temperature resulted in reduced pore densities, which could be evaluated by Electrochemical Impedance Spectroscopy. Such films obviously also sealed interfacial free volumes and inhibited corrosive delamination. An advantageous effect of reduced averaged polymer chain lengths could be explained with an increased macromolecular mobility to support latex particle interdiffusion and coalescence. It can be concluded that important results towards a distinctly increased knowledge of corrosion processes at polymer/oxide/metal interfaces and promising strategies for interface protection were received.

Zusammenfassung

Die vorliegende Studie verfolgte einen umfassenden experimentellen Ansatz zur mechanistischen Untersuchung von Ionentransportprozessen entlang Polymer/Oxid/Metall-Grenzflächen, zur Ermittlung bestimmender Parameter für den Fortschritt korrosiver Enthaftung und Nutzung dieser zur gezielten Adressierung der sogenannten `Elektrolytfront´. Für die Sondierung der Grenzflächenstabilität wurden kathodische oder kombiniert kathodisch/anodische Unterwanderungsprozesse induziert und deren zeitlicher Verlauf insbesondere mit einer höhengeregelten Raster-Kelvinsonde verfolgt. Das Polymer/Substrat-Grenzflächendesign konnte der wissenschaftlichen Fragestellung entsprechend gezielt angepasst werden. Hierzu wurden verschiedene Substratmaterialien, insbesondere Zink- und Eisenproben, sowie Stahlbleche mit spezifischen Eisenpassivschichten eingesetzt. Ein weiterer Fokus lag auf einer gezielten Variation des Grenzflächenkontakts zwischen Klebstoffschicht und nano-rauer Oxidoberfläche. Eingeschlossen war dabei die Untersuchung der Barriereeigenschaften von Latex-Copolymerschichten gegenüber einer Wasseraufnahme mittels Elektrochemischer Impedanzspektroskopie. Die Evaluation resultierender Effekte aus verschiedenen Glasübergangstemperaturen und Polymernetzwerkdichten vervollständigte das erhaltene Bild. Polymer/Substrat-Grenzflächenpotentiale wurden mit Ionenverteilungen an der Grenzfläche verglichen, die sich aus entsprechend initiierten Ionentransportprozessen ergaben. Methodisch bewährten sich hierbei die Röntgenphotoelektronenspektroskopie und Sekundärionen-Flugzeitmassenspektrometrie. Es konnte nachgewiesen werden, dass keine makroskopisch relevante Ionendiffusion entlang verdeckter Grenzflächen stattfindet, sondern Ionentransportprozesse sogar in extrem sauerstoffarmer, feuchter Atmosphäre elektrostatisch determiniert sind. Reaktives Elektrolytspreiten entlang unbeschichteter Metallsubstrate kann zur Simulation korrosiver Unterwanderungsprozesse genutzt werden, sodass komplexe Polymer/Substrat-Grenzflächenstrukturen für grundlegende Untersuchungen nicht zwingend erforderlich sind. Es gelang der Nachweis, dass eine elektrochemisch induzierte Grenzflächenschädigung einer makroskopischen Polymerenthaftung vorauseilt. Der Unterwanderungsfortschritt, so zeigte sich, ist in hohem Maße von der effektiven Wasseraktivität an der Grenzfläche abhängig. Ein erhöhter hydrostatischer Elektrolytdruck beschleunigte den Ionentransport, jedoch stellte insbesondere die elektrochemische Stimulation einen besonders effektiven Steuerungsparameter für korrosive Enthaftungskinetiken dar. Eine Reduzierung der Luftfeuchte in der umgebenden Atmosphäre kann in diesem Sinne bis zur Selbstinhibierung der entsprechenden Prozesse führen, wobei die relevante laterale Ausdehnung der Elektrolytfront unter diesen Umständen weniger als 250 μm beträgt. Die polare Komponente der Oberflächenenergie stellte sich als geeigneter Parameter zur Einschätzung möglicher Polymer/Eisenoxid-Adhäsionskräfte heraus. Im Gegensatz dazu werden die Kinetiken des reaktiven Elektrolytspreitens entlang unbeschichteter Eisenpassivschichten nicht durch entsprechend bestimmte Wasserkontaktwinkel oder Oberflächenenergien wiedergegeben. Viskoelastische Polymere mit einer Glastemperatur unterhalb der Raumtemperatur besitzen nicht nur eine verringerte Porendichte, sondern sind offensichtlich auch in der Lage, freie Volumina nahe der Grenzfläche zum Substrat zu verschließen und damit korrosive Enthaftungsprozesse wirkungsvoll zu inhibieren. Der vorteilhafte Effekt reduzierter mittlerer Polymerkettenlängen konnte dabei mit einer gesteigerten Mobilität der Makromoleküle erklärt werden, die eine optimierte Interdiffusion von Latexpartikeln ermöglichen und dabei zu ihrer vollständigeren Koaleszenz beitragen. Mit der vorliegenden Arbeit konnte ein vertieftes Verständnis von elektrochemischen Prozessen an Polymer/Oxid/Metall-Grenzflächen erzielt werden, welches für zukünftige Strategien zur Steigerung der Grenzflächenstabilität gegenüber korrosiven Einflüssen Verwendung finden wird.

Contents

Chapter 1 –

General Introduction

1.1 Scientific question and motivation

Polymer/substrate interfaces and in particular organic adhesives applied on metal surfaces play a dominant role in daily life. The major amount of fabricated steel sheets is protected against corrosion by a multi layer coating system: Zinc cathodically protects steel and iron and prevents its corrosive dissolution because it will function as sacrificial anode. Non-conductive conversion or phosphate layers inhibit electrochemical processes at the substrate surface. Adhesion promoting primers optimise the cohesion between topcoats and substrates. Nevertheless corrosion of metal sheets still is responsible for enormous economical damage. It is reported that already the replacement of deteriorated low alloyed steel components results in expenses of several hundreds of billion euros each year [1-2]. Significant scientific resources are applied and required to cover this challenging field of science. The avoidance of corrosion induced failure of adhesive joints and polymer coated metal surfaces has to result in a distinct increase of the economic performance and will promote a sustainable use of limited global reserves of raw materials.

Due to the complexity of processes the mentioned research area is advantageously inspired by a close cooperation of steel manufacturers, the chemical industry providing (in)organic and polymer based corrosion protective coating systems and consumers such as the automobile industry. Polymer coated and thereby protected surfaces dominate the first optical impression of a car. The long-term stability of an auto body usually is implicitly expected, but nevertheless decisively connected to the economical success of such product. An increase of the polymer/substrate interface stability in fact requires a detailed knowledge about de-adhesion mechanisms and interfacial structures.

Although strong efforts are currently made to develop improved corrosion protective systems, their performance nevertheless often cannot be adequately predicted up to now. Cost-intensive and time-consuming exposure tests are applied to simulate resulting failure modes. They in fact represent the result of a complex interaction of different corrosive mechanisms occurring in parallel. Advantageous coating compositions are found, but the single contributions of applied molecular structures cannot be entirely understood following solely this approach. If the composition recipe or the conditions of coating application have to be adjusted, e.g. due to ecological requirements, the exchange of already a single ingredient may result with an unacceptable loss of protective properties. A systematic and comprehensive understanding of polymer/substrate adhesion and interfacial corrosion processes represents an important prerequisite to further increase the efficiency for the development of promising strategies for interface protection.

In this context the present study offers a detailed insight into corrosive delamination at polymer/oxide/metal composites. It is focussed on the investigation of electrochemically induced failure events relevant for adhesive joints and polymer coated metal surfaces also applied in daily life. Interfacial ion transport processes are initiated to probe the interface stability. They can be monitored with a Scanning Kelvin Probe (SKP), which has been established as method for the non-destructive measurement of electrode potentials at buried interfaces.

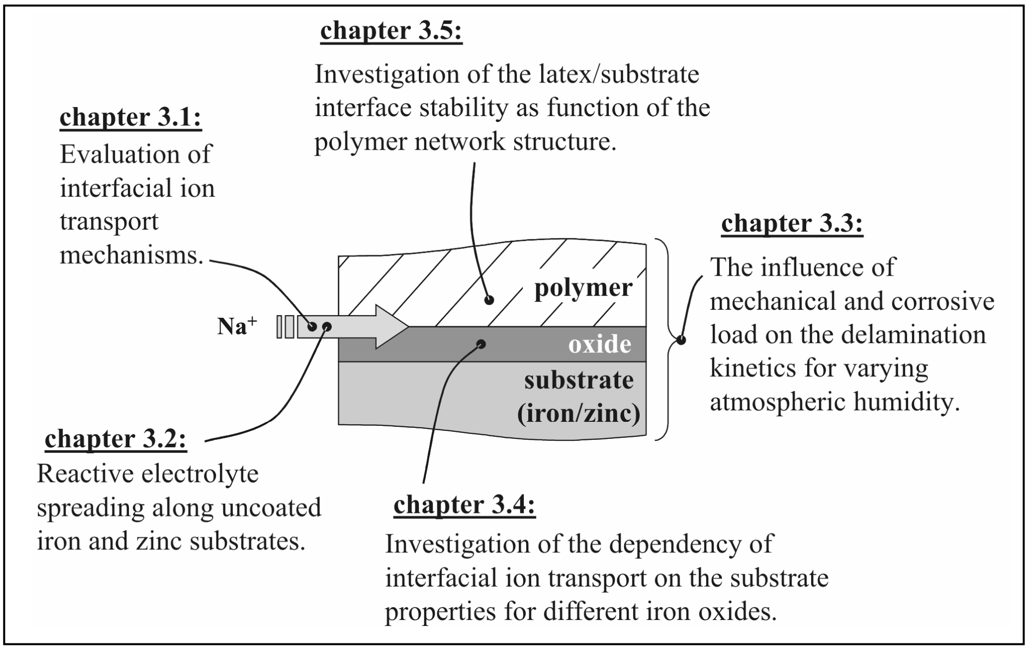

Fig. 1.1: Schematic overview of the scientific approach followed in the present study.

Section 2 will give a detailed methodical introduction to the SKP and provides the reader with necessary information about Electrochemical Impedance Spectroscopy (EIS), determination of surface energies, Infrared Spectroscopy, X-ray Photoelectron Spectroscopy (XPS), Time-of-Flight Secondary Ion Mass Spectrometry (ToF-SIMS) and Atomic Force Microscopy (AFM). The discussions and presentation of results within chapter 3 thereby can be easily followed and understood.

Important conclusions concerning the mechanisms of ion transport along zinc and iron substrates are presented within sections 3.1 and 3.2. It will be shown that the established model for cathodic delamination has to be extended and corrected. A fundamental approach can be already based upon reactive electrolyte spreading processes along uncoated substrates. Conclusions thereby drawn can be correlated to the conditions at the complex and buried interface structure of polymer coated samples. Within chapter 3.3 the application of mechanical and corrosive loads to polymer/zinc oxide/zinc interfaces is studied with a Scanning Kelvin Probe Blister-Test (SKP-BT). A variation of the relative atmospheric humidity will lead to distinct knowledge concerning the interaction of electrochemical interface pre-damaging and subsequent mechanic de-adhesion, the lateral dimensions of the `electrolyte front´ and the dependency of the delamination progress on this small interface section. Within chapter 3.4 the influence of different oxide structures on the resulting polyurethane/iron oxide/iron interface stability is investigated. It will be shown that surface energies seem to be suited to generally predict different delamination progress rates detected on the oxides, but cannot be applied to describe the rate-determining parameters for reactive electrolyte spreading along the uncoated substrates. Section 3.5 completes the presented approach with a detailed evaluation of advantageous latex coating properties and their correlation to the resulting interface stability applying zinc, iron and SiO_2 modified substrates, partly in simulated cut-edge geometry. Fig. 1.1 provides a schematic overview over the followed strategy of research.

1.2 Adhesion and de-adhesion at polymer/substrate interfaces

The practical use of polymer/substrate adhesive joints and coated metal sheets for daily life is strongly dependent on the interface stability. Adhesion forces can be thermodynamically quantified and different approaches were developed to specify the chemical and physical aspects of adhesion [3-6]:

→ An exchange of charge between two phases results in an electrostatic attraction.
→ The interdiffusion of two phases is observed.
→ Two phases mechanically interlock.
→ The adsorption theory: Adhesion occurs based on covalent, polar, dispersive and acid-base interactions between two phases.

The interdiffusion mechanism is hardly of relevance for polymer/oxide interfaces and adequately describes the adhesion between two polymer phases [3]. Within the present study it will be in fact distinguished between polymer chain interdiffusion during coalescence of latex particles for adequate film formation and an improved latex/oxide contact. It is indeed relieved by macromolecular diffusion towards the nano-rough oxide surface (see chapter 3.5), but rather depends on secondary forces between both phases.

The interlock mechanism is applied for a high number of pores and inhomogeneities at an oxide surface, so that the adhesive can penetrate these additional cavities and increase the effective polymer/substrate interface area [2-4,7-8]. A porous layer, e.g. SiO_2 generated by plasma polymerisation, should generally support the polymer/ substrate interlock strength.

Due to their different band structure, dipole layer will be formed between polymers in contact with an oxide phase (see also section 2.1). The resulting electrostatic interactions can be roughly quantified and are often also suited to describe macroscopically detectable peel-forces. Furthermore it is correctly predicted that water ingress at the polymer/substrate interface will reversibly weaken the adhesion strength (`wet de-adhesion´), but does not lead to a total loss of attractive interactions [3-4,9].

The adsorption theory can be regarded as the most common approach for an estimation of nature and quality of adhesion forces [3]. Primary interactions arise from ionic, covalent or metallic bonds with an energy between around 60 kJ/mol and up to several hundred kJ/mol [2,10-11]. Most adhesives do not interfere with the substrate surface via primary forces. Such interactions are nevertheless important for the adhesion promoting effect of additive molecules, e.g. organic silanol species or molecules covalently bonding to specific substrates, for example organic thiols on gold or copper. It is interesting to note that adhesion promotion via covalent bonds often does not lead to increased adhesion strength compared to pure secondary force mediated adhesion. Its advantageous contribution to improved interface stability rather has to be attributed to a reduced sensitivity of covalent bonds to hydrolysis and thereby to impassivity towards the interfacial ingress of water [3]. Intermolecular secondary forces cover van-der-Waals forces, which can be separated into the contributions of London dispersive interactions, attractions of the Debye type after induction of dipole moments between neighbouring molecules and interactions resulting with Keesom orientation [2]. They are of limited range and with only weak binding energy of between 0.1 and 10 kJ/mol, but are effective between all molecules. Acid-base interactions range between 10-25 kJ/mol, but can also reach 40 kJ/mol if H-bonds are taken into account [2,10-11]. They are quantitatively analysed applying the HSAB (`hard/soft acid base´) approach [11-13]. It postulates that attractive forces between molecules arise from an exchange of electron pairs. One molecule acts as Lewis base and is expected to transfer electrons from its highest occupied molecular orbital (HOMO) to the lowest unoccupied molecular orbital (LUMO) of a Lewis acid. The interaction strength can be roughly predicted by a common rule that soft bases (in particular most metal oxides) preferably interact with soft acids, which are adequately represented by voluminous and easy polarisable organic functional groups like COO^-. In contrast hard bases are highly charged, typically occupy a small volume, are hardly polarisable and preferably interact with hard acids.

For the interpretation of adhesion forces at polymer/oxide interfaces surface pH and oxidation state of the substrate are of special importance [3]. An inversion of charge has to be expected at the isoelectric point (IEP), at which the amount of positively and negatively charged ions at the surface is equalised. The point of zero charge (PZC) represents a pH value at which the surface is not affected by the presence of ions [3,14-15]. The difference between surface pH and IEP can result with electrokinetic effects and may be also applied to further specify electrolyte spreading processes along oxide substrates.

The present studies focus on corrosive de-adhesion, which is determined by electrochemical processes occurring at the substrate surface. Electrode kinetics in fact depend upon a formation or discharge of ions at the solid. A minimum interfacial water activity or a liquid phase covering the substrate is required. H_2O molecules will be always adsorbed to solids in ambient atmosphere. Matrices of common adhesives may retard or reduce, but cannot entirely prevent a diffusion of small and neutral molecules like O_2 or H_2O (kinetic diameter ≈ 3 Å [3,16]) to the interface. Nevertheless they usually act as an effective barrier for ion transport due to their low dielectric constant and relatively small free volumes of the polymeric network (epoxy resins e.g. exhibit nanopores of around 5-6 Å) [3,16-17]. Such a water uptake leads to a change of the viscoelastic polymer properties and results in a substitution of secondary forces between adhesive and oxide surface after an interfacial adsorption of water molecules. In dry state, forces typically range in the order of 25 kJ/mol, while metal/water interactions exhibit binding energies of up to 60 kJ/mol and therefore can replace the adhesive [17]. Peeling in most cases then occurs at the polymer/substrate interface, whereas cohesive disbonding through the polymer bulk or within the interphase near the substrate surface rather results from dry environment [3,18-21]. In fact this underlines that the adhesion of polymers to an oxide substrate should not be regarded as a simple assembly of two solids with distinct interface. It has to be expected that the complex interaction of both phases leads to the generation of an interphasial transition with different physical and chemical properties compared to the bulk volume of oxide and polymer [3,18-21]. It is discussed that water transport may proceed accelerated within such interphases [17]. A less dense polymer structure with increased free volumes should support H_2O diffusion. In fact also an acceleration of water transport due to the effect of capillary forces is to be supposed. Spontaneous wetting of a porous structure [3-4,9,22] (`wicking´) is known for sponges and will be supported by adsorption of water molecules along the capillary walls and/or diffusion of H_2O into the solid matrix itself.

If a polymer is applied on salt contaminated surfaces with high ionic density, their crystals will be dissolved. This may result with high osmotic pressures and osmotic blistering [3,9]. Nevertheless also intact polymer/oxide/metal interfaces undergo mechanic deformation during usage. This affects electrochemical kinetics at the substrate surface and thereby should influence interfacial corrosive de-adhesion processes as well. A realistic simulation can be regarded as extremely challenging due to the complexity of contributing parameters. Blister-Test geometries apply hydrostatic pressures from a fluid-filled hole through the sample sheet. Shape and growth of resulting polymer blisters are interpreted [23-32]. Wapner et al. first combined such experiments with a simultaneous detection of cathodic delamination rates at polymer/oxide/metal interfaces [33]. The mentioned approach will be also followed and extended within the present study to gain further insight into the determining parameters for oxidative interface degradation.

1.3 Transport of hydrated ions

Corrosion processes are usually dependent on the formation of a galvanic cell with separated local anode and cathode in contact with a conductive electrolyte. Electrons are exchanged via a metallic connection, but the circuit has to be nevertheless completed by a transport of ions to compensate the generated charge surplus near the electrodes. The ion transport is enforced by an electric field with field strength E

$$E = \frac{U}{l} \tag{1-1}$$

(U: potential drop within the electrolyte, l: distance between the electrodes) [34]. This electric field affects ions of species i with (unsigned) charge z·e (e: elementary charge) by a force $\left|\vec{F}_E\right|$,

$$\left|\vec{F}_E\right| = z_i \cdot e \cdot \left|\vec{E}\right| \tag{1-2}$$

by which anions are accelerated towards the anode and cations move towards the cathode. The ions are transported through an aqueous solution and become decelerated by a rising friction force $\left|\vec{F}_R\right|$ with increasing transport velocity

$$\left|\vec{F}_R\right| = 6\pi \cdot r_i \cdot \eta \cdot \left|\vec{v}_i\right| \tag{1-3}$$

(r_i: ion radius, η: solvent viscosity, $\left|\vec{v}_i\right|$: ion velocity) [34]. A constant transport rate will be reached for

$$\left|\vec{v}_i\right| = \frac{\left|\vec{F}_E\right|}{\left|\vec{F}_R\right|} \tag{1-4}$$

The electric conductivity κ of an electrolyte can be calculated from its specific resistance ζ

$$\kappa = \frac{1}{\xi} = \frac{l}{R \cdot A} \tag{1-5}$$

(R: measured electric resistance between the electrodes, A: electrode area) [34]. It is a function of ion charge, concentration and ion mobility u_i, which can be quantified as:

$$u_i = \frac{|\vec{v}_i|}{|\vec{E}|} \tag{1-6}$$

Specific electrolytic conductivities in fact usually decrease with increasing ion concentration due to interionic interactions. For aqueous electrolytes especially the dipole properties of water molecules are of importance. Dependent on the electrostatic field of the ion charge and the ion radii, H_2O species form solvation shells of different structure and spatial dimensions. Na^+ for example exhibits an ion radius of around 0.097 nm and thereby generates a stronger electric field than K^+ with a radius of around 0.133 nm. Consequently the number of water molecules forming the hydration shell of Na^+ with 7-8 is also increased compared to 4-5 for K^+ [34]. For alkali cations this results in increasing hydrodynamic radii in the order Cs < Rb < K < Na < Li. Exceptional effective charge compensation between the electrodes of a galvanic cell can be achieved with acid and alkaline solutions due to a fast structure diffusion of protons between H_2O molecules. In particular at high ionic concentrations, which can be expected in the delaminated area of polymer/oxide/metal interfaces, ion-ion interactions further affect the mobility of charged species. Coulomb attractions promote the generation of short range orders between a central ion and hydrated ions of opposite charge. Brownian motion counteracts such formation of ordered structures within the bulk electrolyte, but they cannot be neglected when ions are moving in an electrostatic field between two electrodes of a galvanic cell. Cations and anions will be accelerated in opposite directions. The short range order is distorted and has to be continuously re-arranged, which takes some time. The central ion therefore moves ahead its \`cloud´ of counter ions and is retained. As these species are also accelerated in opposite direction by the outer electric field, the central ion moves additionally decelerated due to electrophoretic effects [34-37].

Not solely electrostatic forces affect ion transport processes. Inhomogeneous ion distributions are also released by diffusion. They can be quantified applying Fick´s approach. The proportionality of particle flow J and concentration gradient $\delta c/\delta x$ is represented by Fick´s first law

$$J = -D\frac{\delta c}{\delta x} \tag{1-7}$$

(D: diffusion coefficient). The particle flow is dependent on the particle (drift) velocity $|\vec{v}|$ and the concentration c [35]:

$$J = \vec{v} \cdot c = -D\frac{\delta c}{\delta x} \tag{1-8}$$

The thermodynamic force $\left|\vec{F}\right|$ for particle movement arises from an inhomogeneous distribution of species i, which results in a locally different chemical potential μ_i [35]:

$$\left|\vec{F}\right| = -\left(\frac{\delta \mu_i}{\delta x}\right)_{p,T\,const} \tag{1-9}$$

(x: respective location in the first dimension). The chemical potential is defined as:

$$\mu_i = \mu_{i0} + RT\ln(a_i) \tag{1-10}$$

(μ_{i0}: chemical potential of species i for standard conditions, R: universal gas constant, T: temperature, a_i: activity of species i). Combination of equations (1-9) and (1-10) leads to:

$$\left|\vec{F}\right| = RT\left(\frac{\delta \ln(a_i)}{\delta x}\right)_{p,T\,const} \tag{1-11}$$

For ambient conditions the atmospheric pressure p and temperature can be expected to remain constant, and for ideal solutions the activity can be replaced by the concentration of species i:

$$\left|\vec{F}\right| = -\frac{RT}{c_i}\left(\frac{\delta c_i}{\delta x}\right) \tag{1-12}$$

With application of equation (1-8) the resulting drift velocity can be generally attributed to the contributions of concentration gradients and external forces [35]:

$$\left|\vec{v}_i\right| = -\frac{D}{c_i}\frac{\delta c}{\delta x} = \frac{D}{RT}\cdot\left|\vec{F}\right| \tag{1-13}$$

If species i move in an external electrostatic field, its force $\left|\vec{F}\right|$ can be specified by the electrostatic force $\left|\vec{F}_E\right|$ of equation (1-2) and the drift velocity can be expressed by the ion mobility u_i (see equation (1-6)). The resulting effective ion mobility then is [35]:

$$u_i = \frac{z_i \cdot F \cdot D}{RT} \tag{1-14}$$

Even if no outer electric field supports ion transport, another electrostatic effect has to be mentioned when cations and anions move along a concentration gradient. If the diffusion coefficients of the two ion types differ from each other, diffusion potentials become effective in this case. The smaller ion exhibits a larger mobility and moves ahead. This results in a separation of positive and negative ion charge and thereby in a potential drop along an emerging phase boundary. Due to the resulting electrostatic field ions with higher mobility are retained, whereas the counter ion transport proceeds accelerated. At steady state conditions both ion types move with same velocity and a diffusion potential $\Delta\varphi_{Diff}$ is adjusted [35]. In most cases such diffusion potentials are distinctly smaller than e.g. Galvani potential differences (see section 2.1), but should not be generally neglected. In such cases an adequate compensation is a common strategy. The thermodynamic driving force to overcome the diffusion potential drop can be calculated by

$$\Delta G_{Diff} = -z \cdot F \cdot \Delta\varphi_{Diff} \qquad (1\text{-}15)$$

(ΔG: free enthalpy; z: charge number of the ions, F: Faraday constant) [35]. ΔG_{Diff} can be described as the sum of the chemical potential changes $\delta\mu$ of all involved ion species i. The contribution of the different ions with charge z_i to the overall current density is reflected by their transference number t_i:

$$\Delta G_{Diff} = \sum_i \int_{\mu_i(I)}^{\mu_i(II)} z \frac{t_i}{z_i} \delta\mu_i \qquad (1\text{-}16)$$

($\mu_i(I)$, $\mu_i(II)$: chemical potential of ion i between inner (I) and outer (II) boundary of the diffusion layer) [35]. Applying equation (1-10) the diffusion potential can be connected with the ion activity [35]:

$$\Delta G_{Diff} = -\frac{RT}{F} \sum_i \int_{a_i(I)}^{a_i(II)} \frac{t_i}{z_i} \delta \ln(a_i) \qquad (1\text{-}17)$$

In particular electrode kinetics often depend on the velocity of particle diffusion. Redox processes with low activation energy barrier can proceed that fast that every molecule or ion accessing the electrode surface will be immediately oxidised or reduced. The maximum current density level then is determined by the rate particles diffuse to the electrode [34-37]. In this context the maximum progress rate e.g. for the cathodic delamination mechanism should be limited to the velocity oxygen molecules find access to the respective polymer/oxide/metal interface by diffusion.

1.4 Corrosive delamination at polymer/oxide/metal interfaces

Polymer coatings are applied on metal substrates to inhibit electrochemical processes at the solid surfaces. Adhesives with adequate corrosion protective properties prevent the access of hydrated ions to the polymer/substrate interface, occupy metal or oxide adsorption sites and reduce the reachable interfacial water activity usually as function of the polymer hydrophobicity. The lower the interfacial ion concentration, the less compact the electric double layer at the oxide surface will be.

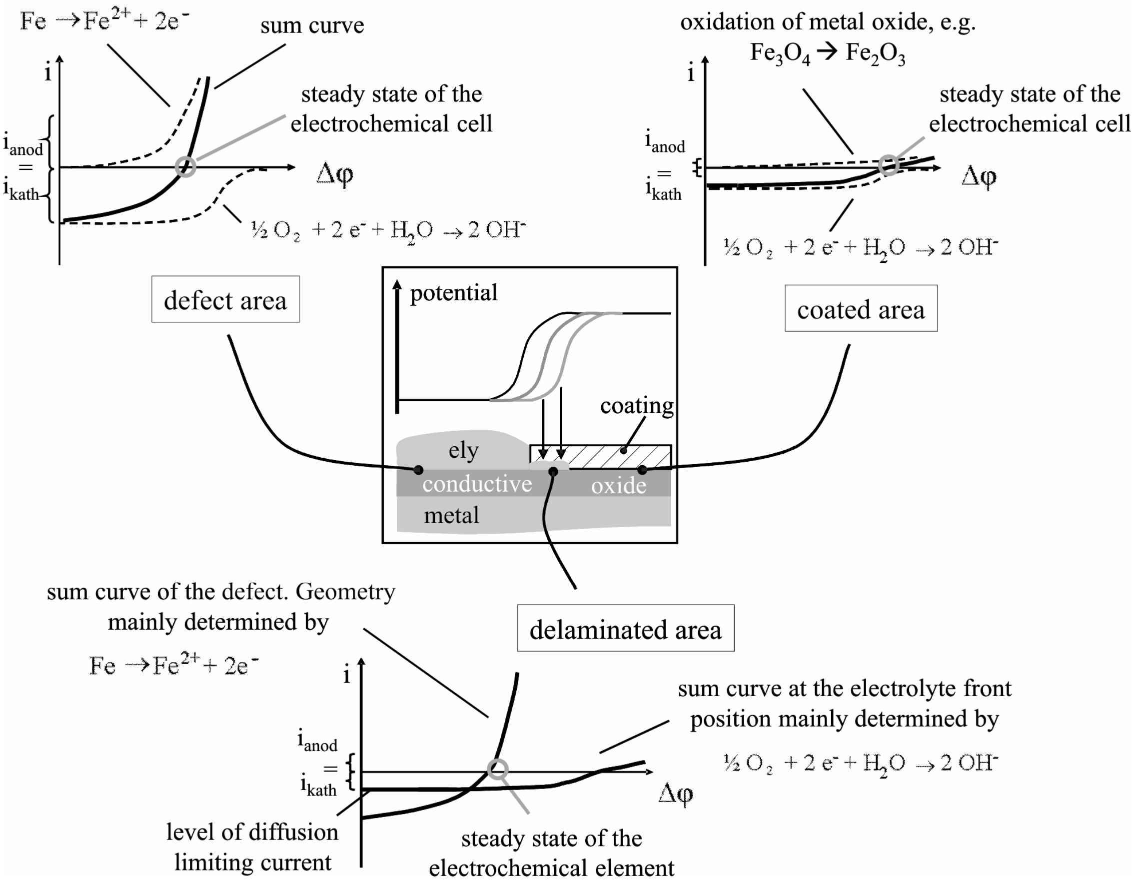

Fig. 1.2: Illustration of current (i) vs. Galvani potential difference (Δφ) curves for the description of substrate/electrolyte, substrate/polymer and substrate/electrolyte/polymer interface potentials [3,44].

A diffuse double layer can be regarded as kinetic barrier for electrochemical processes and therefore has to result in decelerated interface corrosion [38]. Unfortunately it was observed that also adjacent coated surface areas tend to continuously de-adhere in humid atmosphere when coating defects come into contact with an aerated electrolyte. Although already the interfacial ingress of water often weakens the polymer/substrate adhesion forces, such corrosive de-adhesion is strongly accelerated and supported by electrochemical corrosion processes. It is dominant for high atmospheric humidity and occurs on metals like iron or zinc, which are covered by conductive oxide structures. For cathodic delamination the electrochemical and pH-stability of the metal oxide, the oxygen permeability and adhesion of the organic layer, the type and form of an electrolyte filled coating defect as well as the relative humidity of the surrounding atmosphere were highlighted as determinant factors [39-45]. The resulting processes can be interpreted in terms of current-potential-curves (see Fig. 1.2). Applying iron substrates [44-46] oxygen will be reduced in the defect area until the diffusion limiting current density level is reached or nearly reached:

$$\frac{1}{2}\, O_2 + H_2O + 2e^- \rightleftarrows 2\, OH^- \tag{1-18}$$

Iron dissolves as anodic counter reaction:

$$Fe \rightleftarrows Fe^{2+} + 2e^- \tag{1-19}$$

Steady state conditions are reached if the cathodic current density i_{cath} is equal to the anodic current density i_{anod} (see Fig. 1.2). Iron irons are precipitated within the defect area as ferric or ferrous (oxidic) hydroxides:

$$Fe^{2+} + 2\, OH^- \rightleftarrows Fe(OH)_2\downarrow \tag{1-20}$$

$$Fe^{2+} + 3\, OH^- \rightleftarrows FeO(OH)\downarrow + 1\, H_2O + e^- \tag{1-21}$$

Initial oxygen reduction according to equation (1-18) can also occur at the intact polymer/oxide/metal interface. But due to the diffuse electric double layer it is kinetically strongly inhibited. Iron oxide oxidation as anodic counter reaction quickly results in a depletion of donor states within the oxide. This further reduces the reachable anodic maximum current density and from the electrochemical point of view has to result in a high anodic overpotential at steady state conditions (see Fig. 1.2). The increased Fe^{3+} concentration within the oxide also leads to an anodic shift of the detectable Volta potential difference between an inert reference metal and the oxide covered iron sample (see chapter 2.1). Consequently a distinct potential step between defect area and intact interface will be monitored when scanning along these sections with a Kelvin Probe [44-46]. The defect electrolyte now can penetrate adjacent polymer covered interface areas. Thereby the kinetic barrier for oxygen reduction at the polymer/oxide/metal interface will be bypassed by an increased anodic metal dissolution within the defect. A direct connection of the two formerly isolated electrochemical cells at defect and intact interface is resulting. The two current-potential-sum curves then determine the interface potential in the delaminated area (see Fig. 1.2). Steady state conditions will be reached at or near the oxygen diffusion limited maximum cathodic current density level. Due to the barrier properties of the polymer towards oxygen diffusion, i_{cath} will be relatively small compared to that one at the defect. This means that only a slightly increased anodic current density for iron dissolution will be necessary to compensate the interfacial cathodic process within the section of interfacial electrolyte ingress. The corrosion potential will be hardly anodic shifted, and because no anodic overpotential is effective within the delaminated area any longer, a Scanning Kelvin Probe (SKP) will detect a potential similar to that one of the defect. This allows a continuous tracing of the delamination process. Usually the lateral displacement of the turning point within the recorded potential profile (see Fig. 1.2) is applied as indicator for the front position of corrosive de-adhesion [44-46].

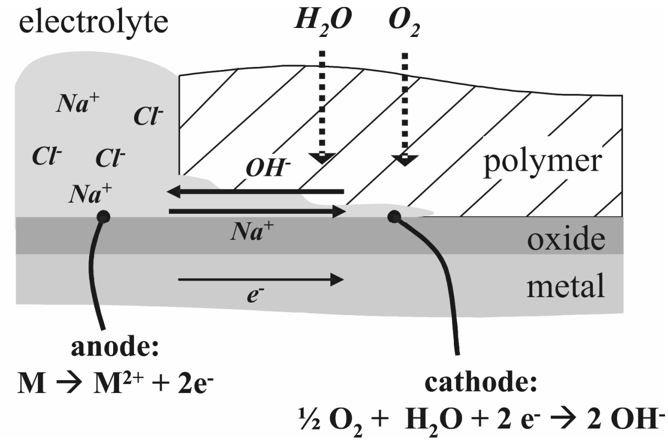

Fig. 1.3: Schematic illustration of the cathodic delamination mechanism.

The separation of local anode (iron dissolution within the defect) and local cathode (oxygen reduction within the delaminated area) requires a transfer of electrons to the electrolyte front position. The conductivity of the oxide determines the resulting resistance for this process step. In fact, also an interfacial transport of (hydrated) ions is required to complete the circuit. Therefore cations of the defect electrolyte are transported to the delamination front position, electrostatically attracted by the negative charge of hydroxide ions formed during interfacial oxygen reduction. Because interfacial iron dissolution is still inhibited, the Fe surface becomes passivated at increasing interfacial pH value due to the increasing OH^- concentration [44-46]. No Fe-hydroxide precipitation is observed and OH^- ions are transported in direction to the defect to support charge compensation between the local electrodes. It was experienced that the required interfacial ion transport usually represents the slowest process step and therefore is rate-determining. It is expected that oxidative degradation of the polymer is mainly caused by highly reactive oxygen species, in particular radicals and intermediates evolving during the O_2 reduction process [46]:

$$O_2 + e^- \rightleftharpoons O_2^{-\cdot} \tag{1-22}$$

$$O_2^{-\cdot} + H^+ \rightleftharpoons O_2H^{\cdot} \tag{1-23}$$

$$O_2H^{-\cdot} + e^- \rightleftharpoons O_2H^- \tag{1-24}$$

$$O_2H^- + H^+ \rightleftharpoons H_2O_2 \tag{1-25}$$

$$H_2O_2 + e^- \rightleftharpoons OH^{\cdot} + OH^- \tag{1-26}$$

$$OH^{\cdot} + e^- \rightleftharpoons OH^- \tag{1-27}$$

A destruction of chemical bonds thereby may be induced via a radical chain reaction [3].

Initiation:

$$O_2^{-\cdot} + R\text{-}H \rightleftharpoons R^{\cdot} + O_2H^- \tag{1-28}$$

Propagation:

$$R^{\cdot} + O_2 \rightleftharpoons ROO^{\cdot} \tag{1-29}$$

$$ROO^{\cdot} + R\text{-}H \rightleftharpoons ROOH + R^{\cdot} \tag{1-30}$$

De-adhesion of the polymer is resulting, its corrosion protective properties are distinctly reduced and in many cases respectively coated components or adhesive joints have to be renewed or entirely replaced. Fürbeth et al. compared the mechanisms cathodic delamination at iron substrates with corrosive de-adhesion occurring at polymer coated zinc samples [47-49]. Although the basic mechanisms occurred to be similar, an anodic process component was pointed out, especially when applying iron as substrate material within the defect area. It was attributed to amphoteric properties of zinc oxide. In contrast to iron zinc also gets passivated in alkaline environment, but exhibits amphoteric properties when the pH is further increasing. $Zn(OH)_2$ tends to dissolve as zincate species, e.g. $Zn(OH)_4^{2-}$. In the defect area, this is hardly of relevance for the delamination process, because anionic species will be more or less repulsed from negative hydroxide charge generated at the delaminated interface. But within the section of interfacial ion transport zinc hydroxide is partly dissolved in a dissolution/ precipitation mechanism [47]:

$$Zn + OH^- \rightleftarrows ZnOH + e^- \quad (1\text{-}31)$$

$$ZnOH + 2\,OH^- \rightleftarrows Zn(OH)_3^- + 2e^- \quad (1\text{-}32)$$

$$Zn(OH)_3^- + OH^- \rightleftarrows Zn(OH)_4^{2-} \quad (1\text{-}33)$$

$$Zn(OH)_4^{2-} \rightleftarrows Zn(OH)_2 + 2\,OH^- \quad (1\text{-}34)$$

$$Zn + 2\,OH^- \rightleftarrows Zn(OH)_2 + 2e^- \quad (1\text{-}35)$$

$$Zn + 2\,OH^- \rightleftarrows ZnO + H_2O + 2e^- \quad (1\text{-}36)$$

Distinct oxide growth is reported for ongoing delamination at polymer/zinc interfaces. In contrast the iron oxide/hydroxide growth is determined by solid state diffusion of cations through the already formed oxide scale and therefore less pronounced. A difference between cathodic delamination on iron substrates and corrosive de-adhesion at zinc surfaces can be already visually observed: Iron or low alloyed steel remains shiny within the delaminated area, whereas oxidic zinc species are precipitated and form white coloured gel-like deposits on the surface when zinc is applied as substrate material.

1.5 References

[1] N. Ahmad, A. MacDiarmid, Synthetic Metals 78 (1996), 103.

[2] J. Wielant, Thesis, Vrije Universiteit Brussel (April 2009), ISBN 978-90-5487-563-5.

[3] K. Wapner, Thesis, Ruhr-University Bochum/Germany, 2006.

[4] A.J. Kinloch, *Durability of structural adhesives*, Applied Science Publishers, London and New York (1983).

[5] A.J. Kinloch, *Adhesion and Adhesives – Science and Technology*, Chapman and Hall, London, New York (1987).

[6] F.M. Fowkes, C.-Y. Sun, S.T. Joslin, *Corrosion Control by Organic Coatings*, 1, NACE International, Houston (1981).

[7] J.v.d. Brand, S.v. Gils, P.C.J. Beentjes, H. Terryn, V. Sivel, J.H.W.d. Wit, Prog. Org. Coat. 51 (2004), 339.

[8] K. Allen, *Theories of Adhesion*, in *Handbook of Adhesion*; Wiley, Chichester (2005).

[9] M.R. Bowditch, Int. J. Adhes. Adhes. 16 (1996), 73.

[10] J. Berg, *Semi-empirical strategies for predicting adhesion*, in: *Adhesion Science and Engineering-2: Surfaces, Chemistry and Applications*, Elsevier, Amsterdam (2002).

[11] D.A. Hayes, L.-H. Lee (editor), in *Fundamentals of Adhesion*, Plenum Press, New York (1991).

[12] K.L. Mittal, *Acid-Base Interactions: Relevance to Adhesion Science and Technology*, VSP, Zeist, The Netherlands (2000).

[13] L. Lee, J. Adhesion 46 (1994), 15.

[14] M.G. Barthes-Labrousse, Vacuum 67 (2002), 385.

[15] I.G. Gorichev, V.V. Batrakov, I.S. Shaplygin, N.M. Dyatlova, I.S Mikhalchenko, Inorganic Materials 30 (1994), 1119.
[16] C.L. Soles, F.T. Chang, D.W. Gidley, A.F. Yee, J. Polym. Sci. Pt. B-Polym. Phys. 38 (2000), 776.
[17] K. Wapner, M. Stratmann, G. Grundmeier, Electrochim. Acta 51 (2006) 3303.
[18] P. Frantzis, JSME International Journal A 41 (1998), 405.
[19] J. Erichsen, J. Kanzow, U. Schürmann, K. Dolgner, K. Günther-Schade, T. Strunskus, V. Zaporojtchenko, F. Faupel, Macromolecules 37 (2004) 1831.
[20] J.J. Bikerman, *The Science of Adhesive Joints*, Academic Press, New York (1961).
[21] J.J. Bikerman, Ind. Eng. Chem. 59 (1967), 40.
[22] V. Barron, M. Buggy; Plastics, Rubber and Composites 29 (2000), 243.
[23] H. Dannenberg, J. Polym. Sci. V (1961) 125.
[24] M.G. Allen, S.D. Senturia, J. Adhes. 25 (1988) 303.
[25] D.A. Dillard, Y. Bao, J. Adhes. 33 (1991) 253.
[26] H.M. Jensen, B. Cochelin, J. Adhes. 47 (1994) 231.
[27] K.R. Jiang, L.S. Penn, J. Adhes. 32 (1990) 203.
[28] K.T. Wam, Y.W. Mai, Acta Metall. Mater. 43 (1995) 4109.
[29] J.G. Williams, Int. J. Fract. 87 (1997) 265.
[30] T.J. Chuang, T. Nguyen, S. Lee, J. Coat. Technol. 71 (1999) 75.
[31] N. Taheri, N. Mohammadi, N. Shahidi, Polym. Test. 19 (2000) 959.
[32] A. Shirani, K.M. Liechti, Int. J. Fract. 93 (1998) 281.
[33] K. Wapner, B. Schönberger, M. Stratmann, G. Grundmeier, J. Electrochem. Soc. 152 (2005) E 114.
[34] G. Wedler, *Lehrbuch der physikalischen Chemie*, 5. Aufl. Wiley VCH, Weinheim (2004).
[35] P.W. Atkins, *Physikalische Chemie*, 3. Aufl., Wiley VCH, Weinheim (2001).
[36] C.H. Hamann, W. Vielstich, *Elektrochemie*, 3. Aufl., Wiley VCH, Weinheim (1998)
[37] W. Schmickler, *Grundlagen der Elektrochemie*, Vieweg, Braunschweig (1996).
[38] G. Grundmeier, M. Stratmann, Annu. Rev. Mater. Res. 35 (2005), 571.
[39] H. Leidheiser, *Corrosion Control by Organic Coatings*, H. Leidheiser (Ed.), Science Press, Princeton, NJ (USA), 1979.
[40] H. Leidheiser, W. Wang, L. Igetoft., Prog. Org. Coat. 11 (1983) 19.
[41] K. Wapner, Thesis, Ruhr-University Bochum/Germany, 2006.
[42] M. Stratmann, A. Leng, W. Fürbeth, H. Streckel, H. Gehmecker, K.H. Große-Brinkhaus, Prog. Org. Coat. 27 (1996) 261.
[43] W. Fürbeth, M. Stratmann, Prog. Org. Coat. 39 (2000) 23.
[44] A. Leng, H. Streckel, M. Stratmann, Corr. Sci. 41 (1999) 547.
[45] A. Leng, H. Streckel, M. Stratmann, Corr. Sci. 41 (1999) 579.
[46] A. Leng, H. Streckel, K. Hofmann, M. Stratmann, Corr. Sci. 41 (1999) 599.
[47] W. Fürbeth, M. Stratmann, Corr. Sci. 43 (2001) 207.
[48] W. Fürbeth, M. Stratmann, Corr. Sci. 43 (2001) 229.
[49] W. Fürbeth, M. Stratmann, Corr. Sci. 43 (2001) 243.

Chapter 2 –

Fundamentals of Applied Techniques

The following chapter presents a general overview of analytical tools applied for the studies described in the `Results and Discussions´ section.

2.1 Interface potential measurements with a Scanning Kelvin Probe

Depending on the type of metal electrons in valence bands exhibit different energies. When two metals are conductively connected, electrons are transported to the metal of lower electron energy until the Fermi levels of both solids (with respect to the vacuum levels) are equalised for thermodynamic reasons. Thereby one metal carries a positive surplus of charge, the other a negative surplus. Such additional charge carriers within a solid phase generate an electrostatic field in the phase environment. Near the surface asymmetric electrostatic forces affect the atomic, ionic or molecule components of which a phase is composed of. Thereby a formation of oriented dipoles is caused which results in a dipole layer surrounding the solid even in case of ideal vacuum conditions. To transfer a unit charge e from the interaction free vacuum into a metal (a solid phase) it first has to be transported through the electrostatic field generated by the charge surplus within the phase. In other words, the outer electric potential, the Volta potential ψ, has to be overcome. The same applies to the Surface potential χ, which is determined by the electrostatic forces the superficial dipole layer generates. Both ψ and χ can be summed up to the Galvani potential φ, the inner electric potential within the phase:

$$\varphi = \psi + \chi \tag{2-1}$$

Solely the Volta potential is accessible to measurements, as it represents a potential difference between two locations of the same medium. Positive and negative charging of two metals in conductive connection therefore has to result in a Volta potential difference $\Delta\psi$. In fact charge is always connected to matter, e.g. to electrons or ions. A transport of charge through phase interfaces therefore also requires a transport of matter. Thereby its chemical environment changes and chemical work (a synonym for the chemical potential μ) has to be invested additionally to the electric work $F\varphi$. The transport of 1 mol of species i with charge z from infinity into a phase requires the electrochemical potential $\tilde{\mu}$:

$$\tilde{\mu}_i = \mu_i + z_i F \varphi \tag{2-2}$$

(with F as the Faraday constant). If one of the two metals in conductive connection is nearly inert in ambient atmosphere and no charge or matter is exchanged with the environment, it can act as reference (`ref´). The other metal, from now on subscripted with `sample´, in contrast may be surrounded by an electrolyte and take part in electrochemical reactions occurring at its surface. The electrochemical work necessary to transfer charged matter from the electrolyte into the sample phase then can be thermodynamically described as a Galvani potential difference. It reflects the equilibrium of species i between solid and electrolyte:

$$\Delta\varphi^{sample}_{electrolyte} = \frac{\mu_i^{0(electrolyte)} - \mu_i^{0(sample)}}{z_i F} + \frac{RT}{z_i F} \cdot \ln\left(\frac{a_i^{(electrolyte)}}{a_i^{(sample)}} \right) \tag{2-3}$$

(with μ^0 as chemical potential of i in the respective phase for standard conditions, T as temperature, R as the universal gas constant and a as the activity of i in the respective phase) [1-4]. It is clear that electrochemical processes at the sample surface then determine the Volta potential difference $\Delta\psi^{ref}_{sample}$ between sample and reference, as long as ψ_{ref} is constant after a first initial equalisation of Fermi levels between sample and reference. The following quantitative correlation could be drawn between corrosion potential E_{corr} of the sample/electrolyte//reference/environment cell and the Volta potential difference [5-7]:

$$E_{Corr} = \Delta\varphi^{ref}_{electrolyte} - \Delta\varphi^{ref}_{environment} = \tag{2-4}$$

$$\left(-\frac{\tilde{\mu}_e^{ref}}{z_e F} - \chi_{electrolyte} - \Delta\varphi^{ref}_{environment} \right) + \Delta\psi^{ref}_{electrolyte}$$

(with electron charge $z_e = 1$, $\tilde{\mu}_e$ as the electrochemical potential of electrons within the respective phase, $\chi_{electrolyte}$ as surface potential of the liquid [equation (2-1) is not limited to solid phases], $\Delta\varphi^{ref}_{electrolyte}$ as Galvani potential difference between reference and electrolyte and $\Delta\varphi^{sample}_{electrolyte}$ as Galvani potential difference between sample and electrolyte). In fact the term in brackets can be regarded as nearly constant as long as the reference phase stays inert towards electrochemical processes [5,8]. As summary it can be stated that a measurement of Volta potential differences between an inert metal (reference) in conductive connection to another metal (sample) can be adequately correlated to electrochemical potentials occurring at a sample/electrolyte interface.

The measured Volta potential difference can be referenced to a half cell with known sample/electrolyte corrosion potential. For the experiments presented in this study it was compared to E_{corr} of saturated $CuSO_4$ solution in contact with pure copper metal, which was calculated to be + 320 mV versus standard hydrogen electrode (SHE) [7]. If the sample metal is covered with a polymer in humid atmosphere, the polymer is non-orientated and therefore only a small dipole moment may result. Then a connection similar to equation (2-4) can be drawn:

$$E_{Corr} = \left(-\frac{\tilde{\mu}_e^{ref}}{F} - \chi_{pol} - \Delta\varphi^{ref}_{environment} \right) + \Delta\psi^{ref}_{pol} \tag{2-5}$$

($\Delta\psi^{ref}_{pol}$: Volta potential difference between reference and outer surface of the polymer, χ_{pol}: polymer surface potential or polymer surface dipole moment, respectively. χ_{pol} can be expected to be constant for the selected experimental conditions). If the sample metal is covered by an oxide layer in contact with the electrolyte the Volta potential difference results from the sum of potentials of all involved interfaces [9]:

$$\Delta\psi^{ref}_{pol} = \Delta\varphi^{sample}_{electrolyte} - \frac{\mu_e^{sample}}{F} + \frac{\tilde{\mu}_e^{ref}}{F} + \chi_{pol} \tag{2-6}$$

(μ_e^{sample}: chemical potential of electrons in the sample). The Galvani potential difference between sample and electrolyte in this case can be regarded as sum of the Galvani potential differences between metal (sample) and oxide layer $\Delta\varphi^{sample}_{ox}$, the potential drop within the oxide $\Delta\varphi_{ox}$ and the potential difference between oxide and polymer $\Delta\varphi^{ox}_{pol}$:

$$\Delta\varphi^{sample}_{electrolyte} = \Delta\varphi^{sample}_{ox} + \Delta\varphi_{ox} + \Delta\varphi^{ox}_{pol} \tag{2-7}$$

Under the conditions of corrosive delamination electrolyte enters the polymer/oxide/metal interface. Also in this case the Volta potential difference can be correlated to the corrosion potential at the interface. An additional potential drop, the membrane or Donnan potential $\Delta\varphi_D$ has to be taken into account, which is defined as Galvani potential difference of the electrolyte/polymer interface. It arises from the ingress of ions into the polymer membrane [10-12].

$$E_{Corr} = \left(-\frac{\tilde{\mu}_e^{ref}}{F} - \chi_{pol} - \Delta\varphi_{environment}^{ref} + \Delta\varphi_D \right) + \Delta\psi_{ref}^{pol} \qquad (2\text{-}8)$$

It is obvious that the Donnan potential has to be small or known for a quantitative evaluation of the corrosion potential at a buried metal/electrolyte interface. In fact it can be neglected in most cases because it is only of relevant size for polymers with a high density of fixed charges (ion exchange membranes), as polymers with fixed cationic functional groups will exclusively exchange anions and vice versa [13]. Corrosion protective coatings or adhesives can also contain fixed charges, but their concentration is usually that small that their Donnan potential is not relevant. Based on equation (2-3) it can be also postulated that for steady state conditions of electrode processes at the sample surface the measured Volta potential difference has to reflect the ratio of different metallic oxidation states within the oxide layer. For iron oxide the resulting correlation can be described as:

$$\Delta\psi_{ref}^{pol} = -\frac{\Delta\mu^0_{Fe^{2+}/Fe^{3+}}}{F} + \Delta\varphi_{pol}^{ox} + \frac{\tilde{\mu}_e^{ref}}{F} + \chi_{pol} + \frac{RT}{F}\ln\left(\frac{a(Fe^{3+})}{a(Fe^{2+})}\right) \qquad (2\text{-}9)$$

($\Delta\mu^0_{Fe2+/Fe3+}$: chemical potential of the redox couple Fe^{2+}/Fe^{3+} for standard conditions). Volta potential differences can be monitored with a Kelvin Probe [7,14-21]. For the experimental approach the reference is located above the sample surface without touching it. In this geometry sample and reference surface can be regarded as the two plates of a conventional plate condenser (see Fig. 2.1). Any process that affects the potential differences at the sample/electrolyte, sample/oxide/electrolyte or sample/oxide/(electrolyte)/polymer interface will result in a change of $\Delta\psi$ and thereby also in a change of the sample \`plate´ charge. If a polymer is present and itself exhibits a minimum conductivity (this requirement is usually fulfilled after an initial water uptake in humid air), a correlated counter-charging of the reference \`plate´ is induced.

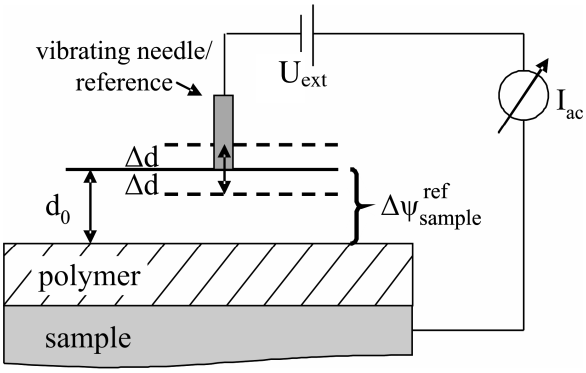

Fig. 2.1: Principles of a Kelvin Probe set-up [7].

A change Δ of the condenser charge Q results in a change of the capacitance C:

$$\Delta Q = \left(\Delta\psi + U_{ext}\right) \cdot \Delta C \tag{2-10}$$

To suppress a thereby induced current an external counter voltage U_{ext} can be applied. At full compensation U_{ext} is equal to $-\Delta\psi$ and the Volta potential difference can be detected without a distortion of the electrode kinetics by the measurement itself. To minimise the influence of interfering signals and to meet metrological requirements of the electronics, the reference is brought into sinusoidal oscillation [22]. Thereby the distance d between the condenser plates is oscillating as well:

$$d(t) = d_0 + \Delta d \cdot \cos(\omega t) \tag{2-11}$$

(t: time, ω: angular frequency, d_0: mean plate distance). Because the condenser capacity C is dependent on the plate distance

$$\frac{C = \varepsilon_0 \varepsilon_r \cdot A}{d} \tag{2-12}$$

(A: plate area, ε_0: dielectric constant in vacuum, ε_r: material dependent dielectric constant) a periodic change of C results:

$$C(t) = \frac{\varepsilon_0 \varepsilon_r \cdot A}{\delta t} = \frac{\varepsilon_0 \varepsilon_r \cdot A}{d_0 + \Delta d \cdot \cos(\omega t)} \tag{2-13}$$

Applying equation (2-10) a periodic current I can be quantified:

$$I(t) = \frac{\delta Q(t)}{\delta t} = (\Delta\psi + U_{ext}) \frac{\delta C(t)}{\delta t} \tag{2-14}$$

It can be again fully compensated with the counter voltage $U_{ext} = -\Delta\psi$. Required electronic devices for a Kelvin Probe therefore is a lock-in amplifier applying a sinusoidal voltage with a frequency of around 1 kHz to an electromagnet which periodically attracts and repulses a metallic membrane. The reference, usually a Cr-Ni needle with smoothed top of 100-200 μm in diameter, is mechanically connected to it and thereby induced to oscillate. The resulting alternating current between the condenser plates is compensated by an integrator, the necessary counter voltage amplified and its amplitude is displayed as the requested Volta potential difference versus standard hydrogen electrode (SHE) after calibration to the Cu/Cu^{2+} redox equilibrium.

The dependency of the capacitance C(t) on the plate distance (see equation (2-13)) additionally allows the implementation of a distance control mode [7,23]. This is done by modulation of the compensation voltage with an alternating current U_m of different angular rate ω_m (frequency usually 10 Hz):

$$U(t) = U_{ext} + U_m \sin(\omega_m t) \tag{2-15}$$

Equation (2-14) then can be extended to:

$$I(t) = \frac{\delta Q(t)}{\delta t} = \frac{\delta}{\delta t}\left\{\left(\Delta\psi + U(t)\right) \cdot C(t)\right\} \tag{2-16}$$

C(t) can be replaced by equation (2-13). Assuming that the mean plate distance is much larger than the oscillation amplitude ($d_0 >> d$), which is usually true for standard SKP measurement conditions, Wapner et al. [7,23] could show that the current amplitude can be demodulated. The contributions of reference (= SKP needle) vibration at 1 kHz (resulting with angular rate ω) and 10 Hz (resulting with angular rate ω_m) can be distinguished and detected independent from each other:

$$I_\omega = (\Delta\psi + U_{ext}) \cdot \varepsilon_0 \varepsilon_r A \cdot \omega \frac{\Delta d}{{d_0}^2} \tag{2-17}$$

$$I_{\omega m} = U_m \cdot \varepsilon_0 \varepsilon_r A \cdot \omega_m \frac{1}{d_0} \tag{2-18}$$

(angular rate $\omega = 2\pi f$; f as frequency). I_ω is compensated by the regular circuit for the Volta potential detection. $I_{\omega m}$ is measured for a favoured plate distance. If this distance is changing during movement of the SKP needle above the sample surface and the difference $\Delta I_{\omega m}$ between initial and current $I_{\omega m}$ value exceeds a threshold value, a piezo positioning stage readjusts the sample height position and thereby keeps the distance d_0 constant [7,23]. Standard SKP experiments analysed within the present study were usually performed under height distance control.

2.2 Electrochemical Impedance Spectroscopy

Corrosion processes at liquid/oxide/metal interfaces are connected to an exchange of charged species. Ions and molecules are transported to the solid bulk and may be oxidised or reduced; on the other hand metal atoms of the bulk structure can enter the liquid phase and become hydrated cations after a transfer of electrons. Even if such processes are thermodynamically allowed, the electrode kinetics nevertheless strongly depend on the activation energy barrier for the transition of ions through the liquid/bulk interface. Because charged species are transported, equivalent circuits can be applied to describe such kinetic resistances of electrode processes. Usually a parallel connection of an ohmic charge transfer resistor R_{CT} with a double layer capacitance C_{DL} in series to another ohmic electrolyte resistor R_{el} is regarded as simple basic circuit to characterise an electrode system. An electric double layer in fact will be always present as the negatively charged \`electron gas´ of a metallic bulk structure outreaches the lattice of positively charged atomic cores. And even if an oxide of the ionic type covers the conductive solid, its surface will potentially express either a negatively charged oxygen layer or a positively charged layer of metal atoms (see also section 2.1). This leads to a specific adsorption of counter ions from the liquid and thereby to a formation of two contrary charged \`plates´, which also exhibit the typical macroscopic properties of a plate condenser [1-4].

For investigation of the resulting electrode resistance (commonly: impedance) the contributions of capacitors and ohmic resistors have to be distinguished and quantified. This can be achieved by application of an alternating voltage U(t) with low amplitude and thereby avoidance of distortion of the electrode kinetics. The measurements are carried out in three electrode arrangement with a potentiostat and applying a highly conductive, usually chemically inert electrolyte solution. The sample is connected as working electrode, whereas an inert counter electrode (pure gold or platin) is used to apply the voltage to the investigated interface system. A reference electrode detects the resulting potential difference to the sample. Usually an electrode with constant potential is applied. This can be achieved by correlation of the potential determining redox couple to the precipitation equilibrium of ionic species, e.g. using the system Ag/AgCl/Cl$^-$. The applied alternating voltage U(t) can be described as:

$$U(t) = U_0 \cdot \sin(\omega t) \tag{2-19}$$

(with U_0 as voltage amplitude, ω as angular rate and t as time). A current I results, phase shifted by φ towards the voltage due to the capacitor properties:

$$I(t) = |I_0| \cdot \sin(\omega t + \varphi) \tag{2-20}$$

(with I_0 as current amplitude). The angular rate is directly connected to the applied frequency f:

$$\omega = 2\pi f \tag{2-21}$$

The impedance Z results applying Ohm´s law:

$$Z(\omega) = \frac{U(t)}{I(t)} = |Z| \frac{\sin(\omega t)}{\sin(\omega t + \Delta\varphi)} \tag{2-22}$$

Thereby the capacitance C is accessible:

$$C = \frac{1}{\omega |Z|} \tag{2-23}$$

For impedance spectroscopy a frequency range of 10^{-2} Hz to 10^6 Hz is generally applied. The measured impedance can be analysed with respect to its absolute value and phase, which are often displayed in Bode plots.

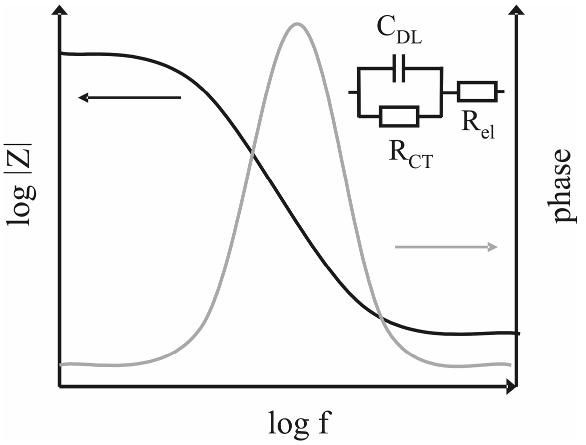

Fig. 2.2: Bode plot and equivalent circuit for a simple electrochemical electrode system.

Fig. 2.2 schematically illustrates the resulting graphs for the simple and idealised electrode system explained above [24-27]. For high frequencies the current results with nearly zero phase, indicating that the impedance of the capacitor C_{DL} is negligible. At very low frequencies the capacitive impedance reaches a maximum and the overall electrode resistance is determined by R_{el} and R_{CT}. Between these extremes the phase constantly increases and finally reaches 90°. At this frequency the overall impedance is nearly entirely dominated by the capacitor, which allows the calculation of C_{DL} by application of equation (2-23). When the substrate surface is covered with a polymer, at least one additional coating capacitance C_C in parallel connection to an ohmic coating resistance R_C is effective. As long as the barrier properties of the adhesive layer can be regarded as sufficient and no coating pores are short-circuiting, C_C usually dominates all other circuit elements. For Bode plots this is reflected by high phase values over a wide frequency range [28-29].

During water ingress, the polymer adjusts its capacitive properties. Monitoring of such changes allows important hints concerning the velocity of H_2O diffusion through the polymer bulk. Brasher and Kingsbury [30-31] developed an equation to quantify the water uptake ϕ (in %):

$$\phi = \frac{\log(C_{p_{sat}} / C_{p0})}{\log \varepsilon_w} \tag{2-24}$$

(with C_{p0} as coating capacitance extrapolated to $t = 0$, C_{psat} as adhesive capacitance at saturation prior to any polymer swelling and $\varepsilon_w = 78.3$ as dielectric constant of water). Zhang et al. [31-32] correlated the time resolved initial coating capacity increase with the coefficient D for water diffusion. Constant coating thickness L was assumed. An equation to evaluate D was developed based on Fick´s second law for one dimension:

$$\frac{\log C_{pt} - \log C_{p0}}{\log C_{psat} - \log C_{p0}} = \frac{2\sqrt{t}}{L\sqrt{\pi}}\sqrt{D} \tag{2-25}$$

(with C_{pt} as adhesive capacitance at time t). The diffusion coefficient in this case can be calculated by linear fitting of the log C_{pt} vs. $\sqrt{t}$ graph during the initial time the adhesive film is in contact with the applied electrolyte prior to polymer swelling.

2.3 Determination of surface energies

The surface tension is equivalent to the energy that has to be invested to generate a new (area normalised) surface during an isothermally and isobaric process. The surface energy of a solid can be calculated based on measurements of the contact angle θ [1-2,33-34]. It is defined as angle between the vectors of liquid/gas interface tension σ_{lg} and solid/liquid interface tension σ_{sl}. Young´s equation allows a correlation between θ and the solid/gas interface tension σ_{sg} (see also Fig. 2.3):

$$\sigma_{sg} = \sigma_{sl} + \sigma_{\mathrm{lg}} \cdot \cos\theta \qquad \text{(2-26)}$$

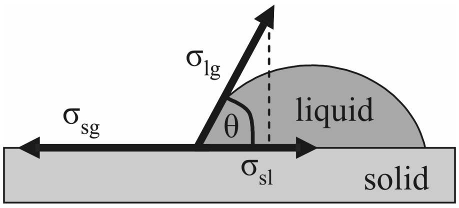

Fig. 2.3: Illustration of contact angle and interface tensions.

A connection to the work of adhesion W_{ad} is given by the Young-Dupré equation:

$$W_{ad} = \sigma_{sg} + \sigma_{\mathrm{lg}} - \sigma_{sl} = \sigma_{\mathrm{lg}}(1 + \cos\theta) \qquad \text{(2-27)}$$

W_{ad} is a common parameter to thermodynamically quantify adhesion and to estimate the quality of bonded joints and adhesive sealings. It is the area normalised reversible work which is necessary to separate the solid/liquid interface. Thereby new solid/gas and liquid/gas interfaces of the same size are generated. The liquid/gas interface tension is relatively easy accessible by laboratory experiments, but usually σ_{sl} and σ_{sg} are of interest. In this case the work of adhesion has to be further specified by another dependency. For determination by contact angle measurements Owens and Wendt partly adopted and partly extended existing approaches. Their model postulates that W_{ad} can be described as geometric mean of the work of cohesion. For separation of two solids, the double amount of σ_{sg} has to be invested, because two new surfaces of identical size have to be generated (at solid 1 as well as at solid 2), whereas the solid/solid interface vanishes. The same applies to the separation of two immiscible liquids. The resulting work of cohesion then can be described as:

$$W_{cohesion} = 2\sigma_{sg} \cdot 2\sigma_{\mathrm{lg}} \qquad \text{(2-28)}$$

The geometric mean is W_{ad}:

$$W_{ad} = \sqrt{W_{cohesion}} = 2\sqrt{\sigma_{sg}\sigma_{\lg}} \qquad (2\text{-}29)$$

It was considered that adhesion forces can be based upon atomic and molecular interactions of different types, depending on the liquid and solid structure under investigation. Owens and Wendt therefore tried to distinguish between polar and dispersive interactions and defined interface tensions as sum of dispersive (D) and polar (P) contributions:

$$\sigma = \sigma^{D} + \sigma^{P} \qquad (2\text{-}30)$$

The resulting equation for the work of adhesion is then:

$$W_{ad} = 2\sqrt{\sigma_{sg}^{D} \cdot \sigma_{\lg}^{D}} + 2\sqrt{\sigma_{sg}^{P}\sigma_{\lg}^{P}} \qquad (2\text{-}31)$$

Expressed by the Young-Dupré relation of equation (2-27):

$$\sigma_{\lg}(1+\cos\theta) = 2\sqrt{\sigma_{sg}^{D} \cdot \sigma_{\lg}^{D}} + 2\sqrt{\sigma_{sg}^{P}\sigma_{\lg}^{P}} \qquad (2\text{-}32)$$

The solid/gas interface tension (which is applied as synonym for solid surface tension or total solid surface tension) then can be determined by measurement of the contact angle θ_i for several liquids i with different polarity and thereby different liquid/gas interface tensions (= liquid surface tensions). Equation (2-32) than can be divided by $2\sqrt{\sigma_{\lg,i}^{D}}$ and after re-arrangement of terms it can be written as [35-37]:

$$\frac{(1+\cos\theta_i)\cdot\sigma_{\lg,i}}{2\sqrt{\sigma_{\lg,i}^{D}}} = \sqrt{\sigma_{sg}^{P}} \cdot \sqrt{\frac{\sigma_{\lg,i}^{P}}{\sigma_{\lg,i}^{D}}} + \sqrt{\sigma_{sg}^{D}} \qquad (2\text{-}33)$$

σ^{P}_{sg} then can be calculated from the slope of the linear graph and σ^{D}_{sg} from the intercept. For the experiments applied within the present study purified water with $pH = 6.9$ ($\sigma_{\lg} = 72.8, \sigma^{D}_{\lg} = 21.8, \sigma^{P}_{\lg} = 51.0$), diiodemethane ($\sigma_{\lg} = 50.8, \sigma^{D}_{\lg} = 50.4$, $\sigma^{P}_{\lg} = 0.4$) and ethylene glycol ($\sigma_{\lg} = 48.0$, $\sigma^{D}_{\lg} = 29.0$, $\sigma^{P}_{\lg} = 9.0$) were used as liquids (liquid surface tension values given in mJ/mm^2). All common approaches for the calculation of solid/gas interface tensions use the geometric mean of σ_{sg} and $\sigma_{\lg}$ to further specify the work of adhesion. For a wide range of surface energies this leads to acceptable results. Nevertheless it has to be mentioned that dispersive van der Waals forces indeed can be adequately reflected, whereas non-dispersive contributions mainly depend upon electron donor-acceptor interactions of atoms and molecules. They are not generally symmetric in nature so that application of the geometric mean is an approximation with limited accuracy.

2.4 Time-of-Flight Secondary Ion Mass Spectrometry

Time-of-Flight Secondary Ion Mass Spectrometry (ToF-SIMS) is an extremely sensitive tool to investigate elemental distributions at conductive solid surfaces. In ultra-high vacuum conditions a pulsed primary ion beam (for the present study Ga^+ ions were applied) is focussed on the substrate sample, desorbs and partly ionises species in dependency of the surrounding matrix and ionisation probability. Such charged secondary ions then are accelerated in an external electrostatic field of contrary charge. The time the ions need until they impact on a detector is a function of their mass to charge ratio. This allows conclusions concerning structure of ionic fragments and presence of elements at the sample surface. Due to the relatively small number of ions generated and desorbed from the substrate, ToF-SIMS is a nearly non-destructive technique. The penetration depth is only about 1-2 nm and consequently also e.g. organic monolayer adsorbed on solid structures are generally accessible to analysis. A disadvantage is that the correlation of detected ion signal intensities to a realistic quantitative elemental concentration at the substrate surface is difficult and depends on the availability of adequate references [38-39].

2.5 X-ray Photoelectron Spectroscopy

For the quantitative analysis of the elemental distribution as well as for the investigation of presence and ratio of atomic oxidation states on conductive solids X-ray Photoelectron Spectroscopy (XPS) has been established as versatile and essential tool. It offers conclusions towards chemical bonding states and compositions of chemical compounds near the sample surface. Measurements are performed in ultra-high vacuum. X-ray radiation is generated by acceleration of high energetic electrons to a metal plate. Inner electrons of metal atoms are thereby liberated and electrons of higher energetic levels reoccupy free inner core shells. The resulting energy difference is emitted as x-ray radiation of characteristic wavelength, which is focussed to the sample. Usually the most intensive K_α line of Mg (at 1254 eV) or Al (with 1487 eV) is applied. By absorption of discrete x-ray radiation energy hν (h: Planck constant, ν: frequency) electrons of sample atoms leave the solid bulk. Their kinetic energy E_{kin} is characteristic for the element atom and its current binding condition. E_{kin} can be quantified as:

$$E_{kin} = h\nu - E_{binding\,(sample)} - \Phi_{sample} \tag{2-34}$$

(with $E_{binding}$ as binding energy of the electron, Φ_{sample} as electron work function of the sample). Detection of the kinetic energy of the electrons is accessible with a detector which is conductively connected to the sample. As the Fermi-levels of sample and spectrometer thereby equalise, the detected kinetic energy has to be dependent on the electron work function of the analyser ($\Phi_{analyser}$):

$$E_{binding} = h\nu - E_{kin\,(analyser)} - \Phi_{analyser} \tag{2-35}$$

For correct correlation of these parameters with respect to thermodynamic data of the vacuum level, measured spectra have to be internally referenced to known peak positions of reference substances. Within the present study the C_{1s} peak of surface carbon contaminations was shifted to 285 eV of the C_{1s} reference signal. Quantative comparison of elements was possible after correction of received peak signal areas with sensitivity factors for ionisation probabilities of the respective atom types. XPS in general is less surface sensitive than e.g. ToF-SIMS. The depth resolution can be estimated to vary around the triple mean free path of the liberated photoelectrons, which is approximately 3-7 nm. XP spectroscopy is often used in combination with sputter depth profiling. Thereby the solid bulk surface is stepwise ablated in layers with focussed ion beams. After each sputter step XPS analysis of the laid open bulk structure is performed.

During XPS measurements usually also so called Auger signals will be detected. They originate after electrons of outer core shells reoccupy free inner electronic states after liberation of primary photoelectrons. If the emitted energy difference between these electronic states is absorbed by a third electron (the Auger electron), it will leave the atom and its E_{kin} can be analysed as well. This approach is called Auger Electron Spectroscopy (AES). The surface intensity of AES can be increased when Auger transitions are not induced by x-ray radiation, but by high energetic electrons. Their interaction with atoms of the sample surface is limited to the very first atomic layers. The depth resolution of AES therefore can be roughly compared to ToF-SIMS [38,40-44].

2.6 Infrared Spectroscopy

As long as molecules carry a permanent dipole moment or their dipole moment changes during an exposure to infrared (IR) radiation, vibration and rotations can be excited. The absorption of light with characteristic wavenumber is correlated to a transition between discrete vibration states of quantized molecular energy levels. Usually a wavenumber range between 400 cm^{-1} and 4000 cm^{-1} is under investigation. The number of excitable vibrations can be calculated from the number of degrees of freedom, which is dependent on the geometry of a molecule and the number of atoms it is composed of. Vibrations are of symmetric or asymmetric valence type ν if they lead to deformations along bonding axes of atoms. For constant irradiation conditions the absorbed energy is proportional to the detected intensity loss -dI for characteristic wavelengths. A one-dimensional quantitative connection between concentration c of the excited species at length dx, the absorption factor k and the original incident beam intensity I was found [1-2,29,45]:

$$-dI = k \cdot I \cdot c \cdot dx \qquad (2\text{-}36)$$

Consequently a change within the absorption intensity of e.g. water valence vibrations can be linearly attributed to changes of the water concentration. Attenuated Total Reflection Infrared (ATR-IR) Spectroscopy in this context has the advantage that the IR light entering a single crystal of usually Si, ZnSe or Ge under certain angles of incidence is entirely reflected if the medium in contact with the crystal exhibits a lower refractive index. Nevertheless vibrations of molecules near the crystal surface are excited by a thereby generated evanescent field of the IR radiation. To amplify the detected IR beam intensity loss, it is aimed for manifold reflections within the ATR crystal due to adjustment of its lateral dimensions. The penetration depth d of the evanescent field can be calculated by:

$$d = \frac{\lambda}{2\pi\sqrt{n_1^{2} \cdot \sin^{2}(\gamma) - n_2^{2}}} \qquad (2\text{-}37)$$

(λ: wavelength of the IR radiation, n_1: refractive index of the ATR crystal, n_2: refractive index of the material under investigation, γ: angle of incidence) [29,31,46-48].

2.7 Atomic Force Microscopy

Among other modes of application the Atomic Force Microscope (AFM) has been established as essential technique for the investigation of nanoscopic surface topographies in many fields of research. Surface analysis is performed by scanning with a cantilever spring as mechanical probe along a solid structure. Topographical inhomogeneities will result with changing electrostatic forces between surface and tip, which leads to attraction or repulsion of the cantilever and therefore to bending. Bending angle and deflection are detected by a laser focussing on the back side of the probe. Editing of the recorded data allows a visual illustration of the investigated surface structure. Alternatively a constant force between tip and surface is preset and kept constant during scanning by adjustment of the vertical cantilever position with a piezo. Again a topographic feature results after readout of the surface position dependent piezo deflection. The reachable height resolution of an AFM in ambient conditions is connected to the investigated substrate material, but in general is in the range of at minimum 1-2 Å [38,49-50].

2.8 References

[1] G. Wedler, *Lehrbuch der physikalischen Chemie*, 5. Aufl. Wiley VCH, Weinheim (2004).
[2] P.W. Atkins, *Physikalische Chemie*, 3. Aufl., Wiley VCH, Weinheim (2001).
[3] C.H. Hamann, W. Vielstich, *Elektrochemie*, 3. Aufl., Wiley VCH, Weinheim (1998)
[4] W. Schmickler, *Grundlagen der Elektrochemie*, Vieweg, Braunschweig (1996).
[5] M. Stratmann, H. Streckel, Corr. Sci. 30 (1990), 681.
[6] M. Stratmann, *Die Korrosion von Metalloberflächen unter dünnen Elektrolytfilmen*, VDI-Verlag GmbH, Düsseldorf (1994).
[7] K. Wapner, Thesis, Ruhr-Universität Bochum (2006).
[8] S. Yee, M. Stratmann, R.A. Oriani, J. Electrochem. Soc. 138 (1991), 55.
[9] G. Grundmeier, K.M. Jüttner, M. Stratmann in *Materials Science and Technologie*, R.W. Cahn, P. Haasen and E.J. Kramer, Editors, Wiley-VCH, Weinheim (2000), p. 285.

[10] M. Cappadonia, K. Doblhofer, M. Jauch, Ber. Bundesges. Phys. Chem., 92 (1988), 903.

[11] K. Doblhofer, Bull. Electrochem. 8 (1992), 96.

[12] K. Doblhofer and R.D. Armstrong, Electrochim. Acta 33 (1988), 453.

[13] G. Grundmeier, A. Simoes, in *Encyclopedia of Electrochemistry*, A.J. Bard, M. Stratmann and G.S. Frankel, Editors, Wiley-VCH, Weinheim (2003), p. 500.

[14] W. Fürbeth, M. Stratmann, Prog. Org. Coat. 39 (2000), 23.

[15] G. Williams, H.N. McMurray, J. Electrochem. Soc. 148 (2001) B377.

[16] A. Leng, H. Streckel, M. Stratmann, Corr. Sci. 41 (1999), 547.

[17] W. Fürbeth, M. Stratmann, Corr. Sci. 43 (2001), 207.

[18] W. Schmidt, M. Stratmann, Corr. Sci. 40 (1998), 1141.

[19] G. Williams, H.N. McMurray, D. Hayman, P.C. Morgan, Phys. Chem. Comm. 6 (2001), 1.

[20] R. Hausbrand, Thesis, Ruhr-Universität Bochum (2003).

[21] L. Kelvin, Phil. Mag. and J. Sci 46 (1898), 82.

[22] W. Zisman, Rev. Sci. Instrum. 3 (1932), 367.

[23] K. Wapner, B. Schönberger, M. Stratmann, G. Grundmeier, J. Electrochem. Soc. 152 (2005) E 114.

[24] H. Vogel, *Gerthsen Physik*, Springer Verlag, Berlin (1997)

[25] A.J. Bard, L.R. Faulkner, *Electrochemical Methods Fundamentals and Application*, John Wiley & Sons, Hoboken (2001).

[26] J.R. Macdonald, *Impedance Spectroscopy; Emphasizing solid Materials and Systems*, John Wiley & Sons, New York (1987).

[27] Gamry, *Basics of Electrochemical Impedance Spectroscopy*, (2008).

[28] F. Mansfeld, J. Appl. Electrochem. 25 (1995), 1145.

[29] I. Klüppel, Thesis, University of Paderborn (2008).

[30] D.M. Brasher, A.H. Kingsbury, J. Appl. Chem. 4 (1954) 62.

[31] R. Vlasak, I. Klüppel, G. Grundmeier, Electrochim. Acta 52 (2007) 8075.

[32] J.T. Zhang, J.M. Hu, J.Q. Zhang, C.N. Cao, Prog. Org. Coat. 49 (2004), 293.

[33] J. Berg, *Semi-empirical strategies for predicting adhesion*, in: *Adhesion Science and Engineering-2: Surfaces, Chemistry and Applications*, Elsevier, Amsterdam (2002).

[34] K. Allen, *Theories of Adhesion*, in: *Handbook of Adhesion*, Wiley, Chichester (2005).

[35] D. Owens, R. Wendt, J. Appl. Pol. Sci. 13 (1969) 1741.

[36] N. Correia, J. Moura Ramos, B. Saramago, J. Calado, J. Coll. Int. Sci. 189 (1997), 361.

[37] J. Wielant, Thesis, Vrije Universiteit Brussel (April 2009), ISBN 978-90-5487-563-5.

[38] M. Valtiner, Thesis, Technical University Vienna (November 2008).

[39] K. Butt, H.J. Graf, M. Kappl, *Physics and chemistry of interfaces*, Wiley-VCH, Weinheim (2006).

[40] R. Posner, Diploma-Thesis, Heinrich-Heine Universität Düsseldorf (2006).

[41] P. Keller, Thesis, Heinrich-Heine Universität Düsseldorf (2006).

[42] M.P. Seah, W.A. Dench, Surf. and Interf. Anal. 1 (1979), 2.

[43] J.H. Scofield, J. Electron Spectrosc. 8 (1976), 129.

[44] G. Ertl, J. Küppers, *Low energy electrons and surface chemistry*, Wiley VCH, Weinheim (1986).

[45] M. Hesse, H. Meier, B. Zeeh, *Spektroskopische Methoden in der organischen Chemie*, Thieme Verlag, Stuttgart (1991).

[46] E. Almeida, M. Balmayore, T. Santos, Prog. Org. Coat. 44 (2002), 233.

[47] M. Milosevic, Appl. Spectrosc. Rev. 39 (2004), 365.
[48] K. Wapner, M. Stratmann, G. Grundmeier, Electrochim. Acta 51 (2006) 3303.
[49] G. Binnig, K.H. Frank, H. Fuchs, N. Garcia, B. Reihl, H. Rohrer, F. Salvan, A.R. Williams, Phys. Rev. Lett. 55 (1985), 991.
[50] G. Binnig, H. Rohrer, C. Gerber, E. Weibel, Phys. Rev. Lett. 49 (1982), 57.

Chapter 3 –

Results and Discussions

3.1 Hydrated ion transport at interfaces of polymer coated oxide covered iron and zinc substrates

3.1.1 Fundamentals

In this chapter recent results are presented which were received during the investigation of general driving forces for interfacial ion transport at polymer/oxide/metal interfaces. It is focussed on acrylic copolymer films and epoxy amine layer applied on zinc coated iron substrates in cut-edge geometry. Although complex interface structures have to be expected, it will be shown that general conclusions can be drawn to further develop and improve the established model for interfacial ion transport. This is necessary to better distinguish the contributions of interfacial water activity and electrochemical processes at the interface to the resulting de-adhesion of polymer/oxide/metal composites.

Previous studies focussed on the mechanism of cathodic or combined cathodic/anodic delamination and proved that the progress of interfacial ion transport in humid air is electrochemically determined [1-7]. Especially the Scanning Kelvin Probe (SKP) was applied as method for the necessary non-destructive measurements of electrode potentials at buried polymer/oxide/metal interfaces [8-15].

The common delamination model postulates that first ions have to diffuse along the polymer/substrate interface before a galvanic cell will be established that further promotes corrosive degradation in humid air [2]. Nevertheless up to now ion transport was not comprehensively investigated for humid inert atmospheres in which interfacial corrosive delamination was expected to be inhibited. Leng et al. discussed ion transport processes on polymer coated iron [1-3] in humid air and argon atmospheres of reduced oxygen partial pressure and calculated formal diffusion coefficients. The authors based their interpretation on diffusion as limiting factor for the de-adhesion rate. Pommersheim et al. also mentioned diffusion when investigating a cation transport along a polymer/oxide/metal interface [16]. Fürbeth et al. studied the delamination processes and corresponding ion distributions for polymer coated zinc substrates [4-6]. Wapner et al. [17] concluded that hydrated ions are transported along polymer/ oxide/metal interfaces in inert atmosphere by applying different alkali chloride solutions as electrolytes.

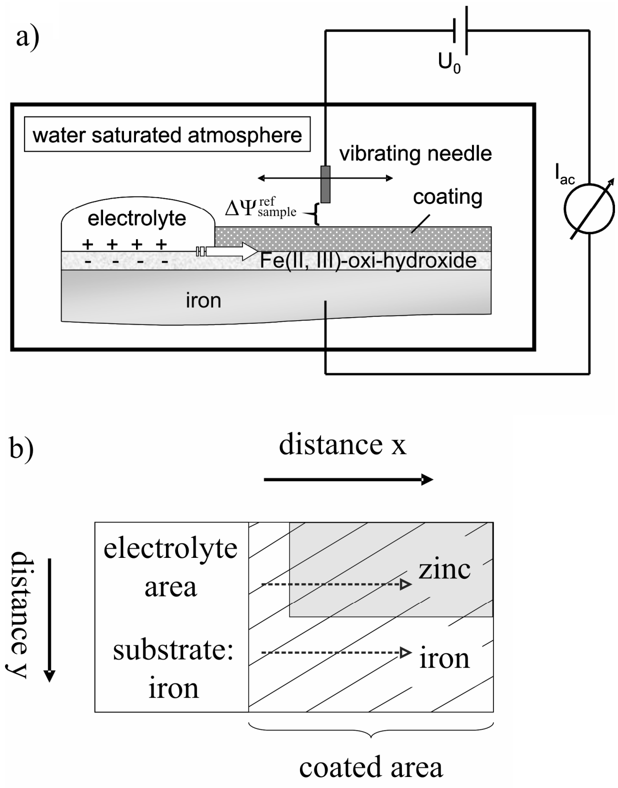

Fig. 3.1: Investigation of ion transport processes along polymer/metal interfaces. a) SKP measurement set-up. b) Sample configuration with iron-, zinc- and electrolyte area. A short iron band between defect and zinc domain avoids a direct electrolytic coupling. The axes x and y serve as orientation for the interpretation of the potential maps and profiles presented in the following figures. SKP line scans have been recorded in direction of the dashed arrows.

The cited authors assumed non-corrosive conditions for the interfacial ion transport in inert atmosphere and attributed the detected ion transport mainly to diffusion.

In this section an experimental approach is followed that illustrates the importance of a general understanding of electrostatic fields for ion transport along polymer/oxide/metal interfaces. In-situ Scanning Kelvin Probe studies of the local interfacial potentials of polymer coated zinc and iron substrates were performed in humid nitrogen atmospheres of strongly reduced oxygen partial pressure. They were supported by ex-situ small spot X-ray Photoelectron Spectroscopy (XPS) and Time-of-Flight Secondary Ion Mass Spectroscopy (ToF-SIMS) analysis of the interfacial ion distribution after removal of the polymer film. Spatial resolved studies of ion transport were complemented by Electrochemical Impedance Spectroscopy of the water uptake of the applied polymer films and the analysis of the interfacial morphology by means of Atomic Force Microscopy (AFM).

A general survey of the applied SKP set-up is given in Fig. 3.1. Scheme 3.1a permits a lateral view of the experimental configuration. The main ingress pathway of the electrolyte along the adhesive/metal interphase is marked.

3.1.2 Experimental procedures

3.1.2.1 Application of polymeric films

Two organic films were used for the investigated polymer/oxide/substrate model composites. As model adhesive, hot-curing two component epoxy-amine resin provided by Henkel AG & Co. KGaA (Düsseldorf, Germany) was employed. The adhesive was carefully mixed and degassed, then applied on the substrate in dry nitrogen atmosphere. The polymer was hardened for one hour at 120 °C applying a pressure of 50 g/cm^2. For the preparation of an epoxy-amine layer with a defect rich interface the application was done in humid nitrogen atmosphere (> 95 % r. h.) and without any mechanical pressure during the curing process. Keeping these preparation conditions a Surfix layer thickness analyser (Phynix Company, Cologne / Germany) confirmed film thicknesses of 80-100 μm. Prior to the SKP-experiments these samples were exposed to humid air (> 95 % r. h.) to remove any electrostatic charging of the polymer. A more detailed description of the coating preparation and analysis can be found in publications of Wapner and Grundmeier [15, 17, 18].

Most measurements were carried out using latex films made from water-borne acrylic model emulsions based on n-butyl acrylate and styrene (averaged particle size approx. 150 nm, solid content 40 %). These dispersions were provided by BASF SE, Ludwigshafen / Germany and usually applied on the respective substrates by spin coating using a P 6700 (Specialty Coating Systems Inc., Indianapolis, USA). Subsequently the layers were annealed in a furnace for one hour at 60 °C (low film formation temperature) or 100 °C (high film formation temperature) without addition of solvent as film forming agent. Complying with these conditions layers with a thickness of 3-6 μm were received. The thickness values were analysed by cross section images in a Scanning Electron Microscope (SEM), model LEO 1550 VP.

3.1.2.2 Substrates

Iron and zinc samples of 99.99 % purity were ground and polished with 3 μm or 1 μm diamond paste. Residues were removed with pure ethanol (99.9 %) during 10 minutes in an ultrasonic bath and rinsed with pure ethanol before being dried in a stream of nitrogen. Smooth stainless steel substrates were cleaned in the same way. All used chemicals and solvents were of p.a. quality. Iron sheets, covered with an approx. 7.5 μm thick electrogalvanised zinc layer were obtained from voestalpine Stahl GmbH, Linz / Austria. These plates were ultrasonically cleaned with tetrahydrofurane, 2-propanol and ethanol, then alkaline cleaned with a 3 % Ridoline 1570™ and 0.3 % Ridosol 1237™ solution for 30 seconds at 55 °C (Ridoline 1570™ and Ridosol 1237™ were provided by Henkel AG & Co. KGaA Düsseldorf / Germany) [19]. Subsequently the substrates were rinsed with ultra-pure water and dried in a nitrogen stream. To prepare iron surfaces next to zinc surfaces on one galvanised steel sample zinc coatings were partly chemically etched. After masking with adhesive tapes zinc was removed by dipping the plates into a hydrochloric acid solution of 15 % concentration. After rinsing and drying with nitrogen the sample surfaces were cleaned in microwave argon plasma for 300 s at 0.2 mbar with 400 W (microwave source by Roth and Rau, Wüstenbrand / Germany).

Zinc layers with a thickness of approximately 5 nm were synthesised by direct current magnetron sputtering using an ION´X ion sputter source (Thin Film Consulting, Grafenberg / Germany) applying targets of pure zinc (99.95 %). Subsequently these thin films were oxidised in microwave oxygen plasma (400 W at 0.2 mbar and for 300 s) and thereby converted to zinc oxide layers.

3.1.2.3 Analytical methods

SKP measurements were carried out with a custom made Scanning Kelvin Probe [15] in an atmosphere of high humidity (> 95 % r. h.). A Clark Electrode (Rank Brothers, Ltd., UK) was used to confirm a residual oxygen partial pressure of less than 1 mbar when purging the SKP chamber with humid nitrogen.

X-ray Photoelectron Spectroscopy (XPS) analysis was performed with a Quantum 2000, Physical Electronics, USA. Spectra were measured with 100 x 100 μm spot size at 45° using a monochromated Al K_α at 23.9 eV pass energy and a step size of 0.2 eV for high resolution spectra. Sputter depth profiles were recorded with an argon ion sputter gun on an area of 2 x 2 mm with an acceleration voltage of 2 kV.

Time-of-Flight Secondary Ion Mass Spectroscopy (ToF-SIMS) measurements have been executed by means of a PHI TRIFT CE, Physical Electronics, USA, applying a gallium ion gun at an acceleration voltage of 15 kV and a spot size of 100 x 100 μm.

Atomic Force Microscopy (AFM) experiments were performed using a Digital Instruments Dimension 3100 AFM. Topography images were recorded in tapping mode with a line rate of 1 Hz.

Electrochemical Impedance Spectroscopy (EIS) measurements were carried out using a Gamry FAS2 Femtostat. A potential amplitude of 10 mV was applied at the open circuit potential of the investigated sample system covering a frequency range of 1 Hz to 10^5 Hz. As electrolyte chloride free borate buffer solution (with pH 8.4) was chosen. The water uptake of the polymeric film was calculated according to the approach of Brasher and Kingsbury [20-21].

3.1.3 Experimental results

3.1.3.1 Interfacial electrode potentials of coated iron and zinc substrates

Fig. 3.2 and Fig. 3.3 present an SKP measurement of a steel sample half covered with zinc (for sample design see Fig. 3.1b). As electrolyte 0.5 molar NaCl solution was filled into the defect. The analysis of interfacial potentials was started in humid nitrogen atmosphere (Fig. 3.2a and 3.3a). In the coated iron area a transport of hydrated ions along the polymer/metal/oxide interface was observed as a proceeding front that causes a potential decrease to the level of actively corroding iron in the defect (interface potential: about -500 mV_{SHE}). The polymer coated zinc area did not show any potential changes. Based on the assumption that ion incorporation leads to a change of the interfacial potential, no ion transport was observed beyond the iron oxide-zinc oxide transition.

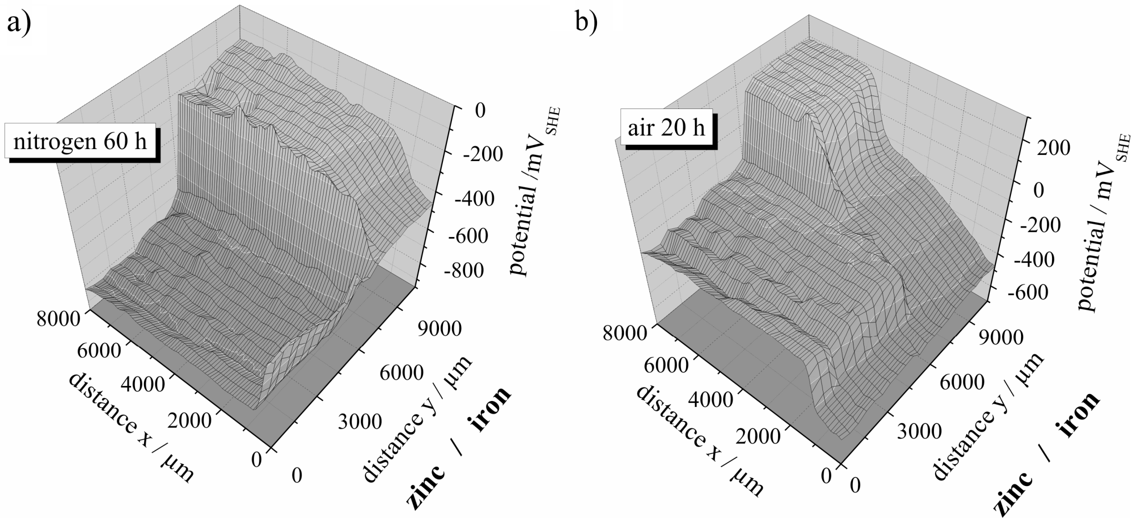

Fig. 3.2: SKP measurement of a zinc / iron sample (for sample design see Fig. 3.1b), coated with an intact latex layer. Defect filled with 0.5 molar NaCl solution. a) Potential map after 60 h in nitrogen atmosphere. b) Potential map 20 h after switching to air.

After flushing the recipient with humid air atmosphere the potential levels between defect and zinc showed an inversion (Fig. 3.2b and 3.3b). In comparison to the defect the potential of oxide covered zinc underneath the polymer film shifted anodically and cathodic delamination started. The corresponding potential step between the actively corroding defect and the polymer coated area was smaller than in case of iron and the front proceeded more slowly. It is interesting to note that in Fig. 3.3b delamination on iron did not start at the front of ion ingress before changing to normal air but close to the defect border. This shows that ingress of hydrated ions does not directly lead to a de-adhered polymer film.

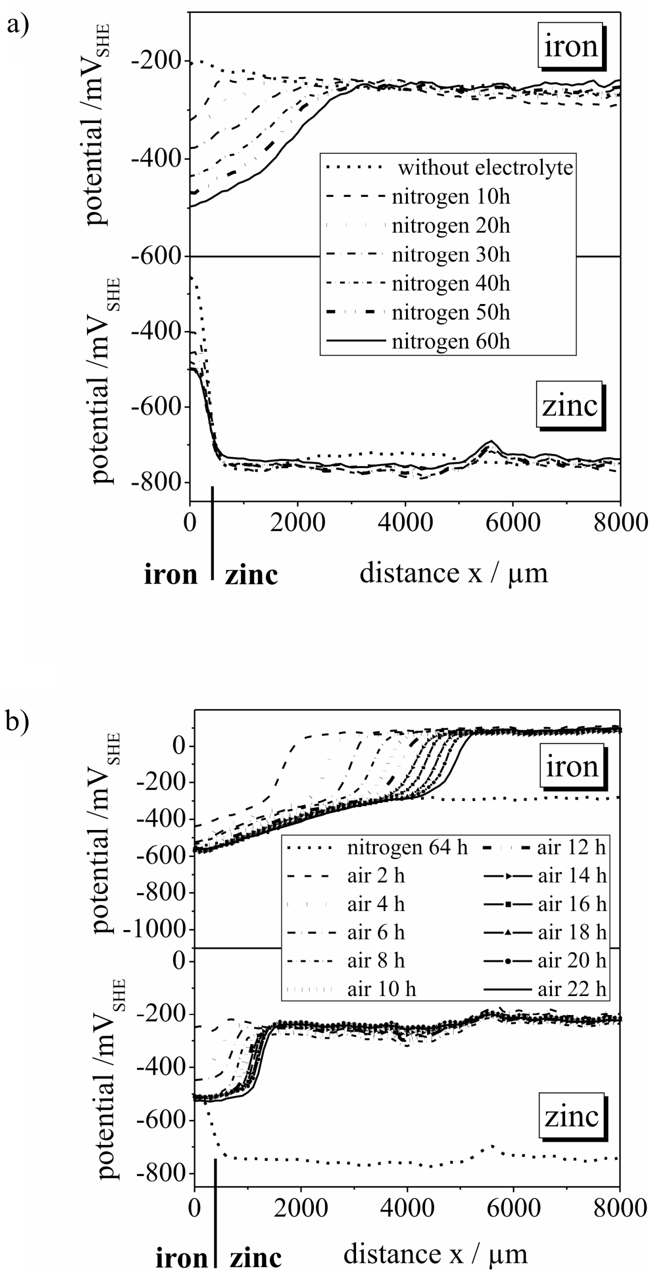

Fig. 3.3: SKP potential profiles for the ion ingress processes presented in Fig. 3.2. a) Potential profiles recorded in inert atmosphere. b) Cathodic delamination process after switching to air.

3.1.3.2 The influence of coating properties on ion transport processes

The result that obviously no ions are transported along the polymer/oxide/zinc interfacial region could be explained by the chemical composition of the surface oxides in comparison to iron oxides, the chemical composition and morphology of the adhering polymeric interphase and the localised interfacial electrode potential.

To reveal a possible influence of the latex film, its barrier properties were varied. Different film formation temperatures lead to significant changes in the latex film quality. Electrochemical impedance measurements point at extremely reduced barrier properties of the layer when curing at 60 °C (low film formation temperature) instead of 100 °C (high film formation temperature). Fig. 3.4a shows the Bode plot recorded on a bare steel substrate. No significant change with time can be observed. For a steel substrate covered with a latex layer annealed at low film formation temperature, only slightly higher pore resistance and impedance values at higher frequencies were observed. This indicates that the film is defect rich and does not effectively act as a barrier for water and ions.

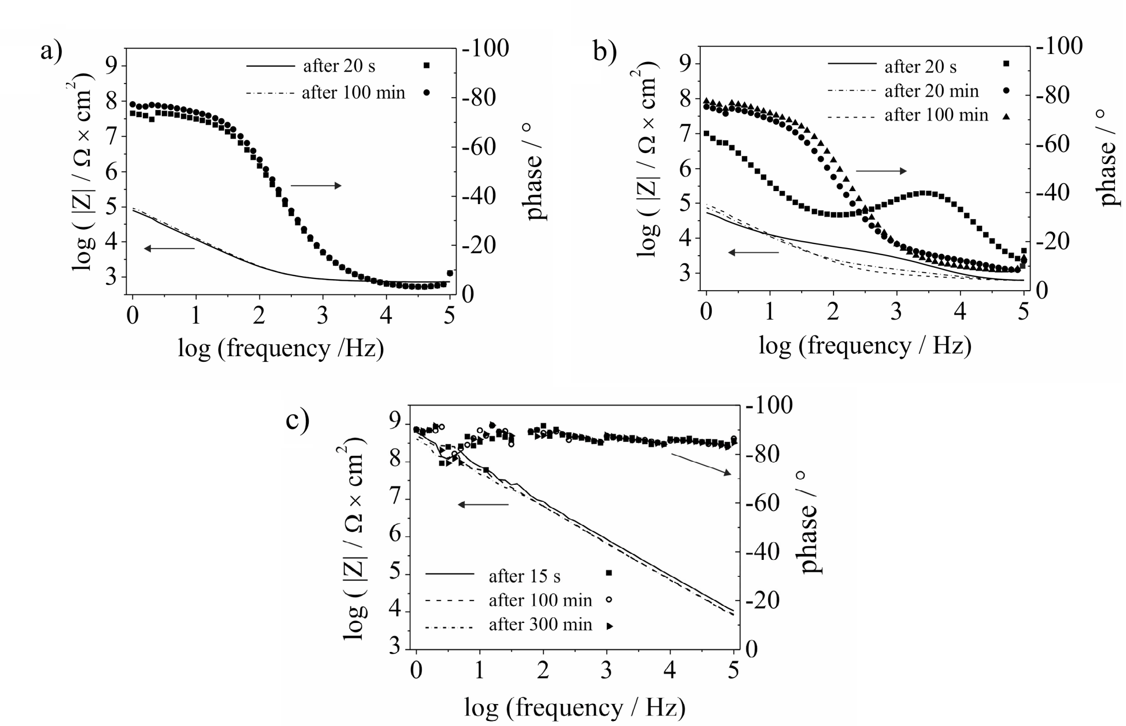

Fig. 3.4: EIS characterisation of the latex film quality. Substrate material: Stainless steel. a) Bode plots recorded on a bare metal sheet. b) Bode plots recorded on a latex layer annealed at low film formation temperature. c) Bode plots recorded on a latex layer annealed at high film formation temperature.

The latex layer annealed at high film formation temperature (Fig. 3.4c) exhibited an almost perfect capacitive behaviour down to very low frequencies which indicates that the film acted as an effective barrier for vertical water diffusion during the measurement. The development of the film capacitance with time, shown in Fig. 3.5, was analysed based on the approach of Brasher and Kingsbury (see Chapter 2 and [21]). The resulting maximum water uptake was calculated to be 4.5 %. This value is higher compared to that one of the epoxy-amine coating system with 2.5 - 3 %, which is discussed later. Generally it should be expected that higher water content in the coating should also lead to an increased water concentration at the polymer/oxide/metal interface. Consequently, diffusion of hydrated ions should be promoted for the defect rich latex film cured at low temperatures.

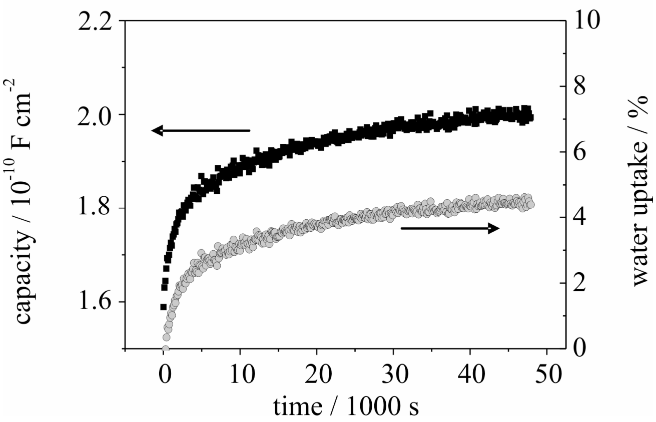

Fig. 3.5: Capacitance change (measured at 10 kHz) and water uptake for a latex layer annealed at high film formation temperature.

Fig. 3.6 shows the results of the SKP investigation of interfacial ion transport processes for a latex layer annealed at low film formation temperature. The ion transport on iron indeed is accelerated (progress ≈ 3200 μm after 20 hours) compared to that one presented in Fig. 3.3a for a latex layer annealed at high film formation temperature (progress ≈ 2500 μm after 60 hours). However, no potential shift could be observed beyond the borderline between the iron and zinc area (Fig. 3.6).

To draw explicit conclusions suggesting that the observed effect is independent from the organic layer, a totally different polymer film was applied. An epoxy/amine adhesive was chosen, which should lead to a cross linked polymer at the film/oxide interface [18]. By varying the basic conditions for application described in the experimental part (application in dry atmosphere and hardening with 50 g/cm^2 pressure or application in humid atmosphere and hardening without any pressure) it could be shown that the polymer/oxide interphase morphology changes accordingly.

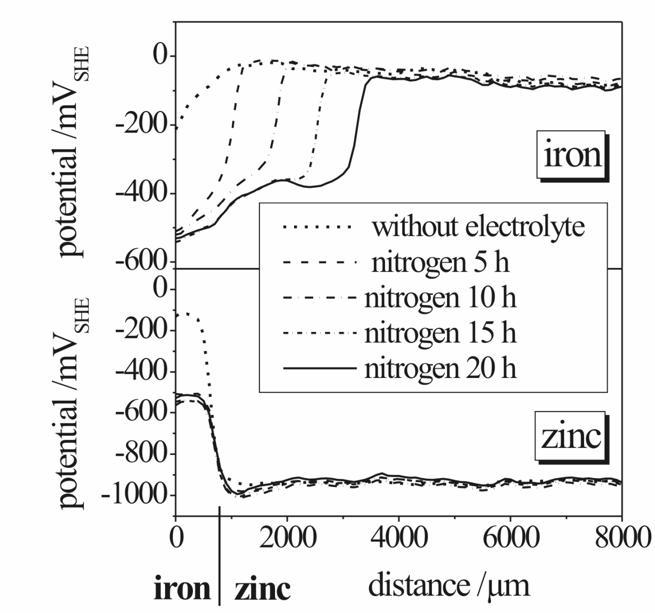

Fig. 3.6: Ion transport process on a zinc / iron sample (see Fig. 3.1b) in inert atmosphere illustrated by SKP potential profiles. A latex layer was applied and annealed at low film formation temperature. Defect electrolyte: 0.5 molar NaCl solution.

Fig. 3.7 presents AFM morphology images of uncovered epoxy amine/zinc interfaces. Pure zinc sheets were ground and polished with 1 μm diamond paste. The resulting surface topography is illustrated in Fig. 3.7a. After the preparation of zinc/adhesive/glass compounds the epoxy amine layer was hardened. Subsequently the zinc substrate was etched away with 10 % hydrochloric acid and the laid open adhesive/zinc interface was investigated by means of AFM. Fig. 3.7b presents a topographic image of the epoxy amine/zinc interface with the polymer cured at 50 g/cm^2 pressure. The picture confirms a perfect wetting of the zinc surface. Nearly an identical imprint of the substrate surface structure was observed and even small grinding grooves have been detected as elevations on the polymer. In contrast application at high humidity and curing without pressure leads to a distinct increase of the interfacial polymer roughness (see Fig. 3.7c). The zinc surface structure is not observable any more. This leads to the conclusion that the epoxy amine layer will be partial de-wetted under these conditions, which leads to distinctly increased free volumes at the polymer/oxide/metal interface [18]. Thus, higher amounts of interfacial water molecules will occupy a larger amount of adsorption sites on the oxide surface.

This should also promote the interfacial transport of hydrated ions due to formation of locally extended water adsorption layers.

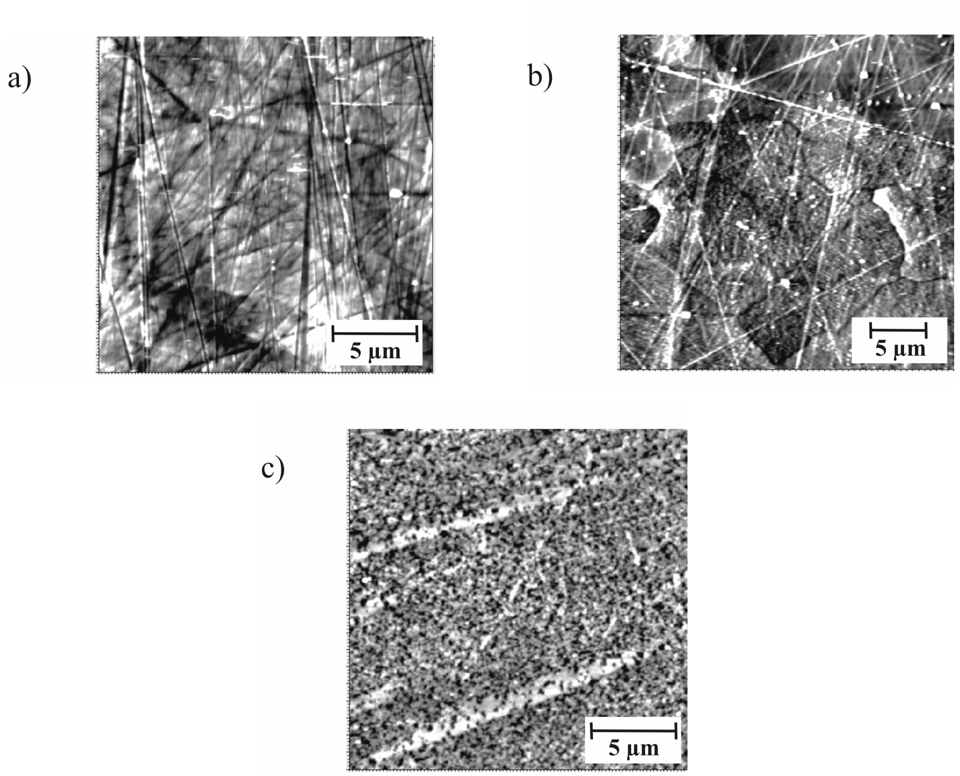

Fig 3.7: AFM topography images of uncovered epoxy amine/zinc interfaces (see also [18]). a) Polished zinc surface (z-scale 30 nm). b) Epoxy-amine layer after etching away the zinc substrate (z-scale 55 nm). The adhesive was cured under pressure before. c) Epoxy-amine layer after curing without pressure and etching away the zinc substrate (z-scale 115 nm).

The investigation of the ion transport process by SKP was performed for the partially de-wetted epoxy amine film on a zinc / iron sample (see Figure 3.8).

Qualitatively, the experimental results did not differ from those presented in Fig. 3.6 for the latex layer regarding the progress of the potential curves on iron and zinc. The potential of the polymer/oxide/metal interface at the coated zinc domain stays stable as for the measurements with the applied latex film (compare to Fig. 3.6 and Fig. 3.3). So it can be concluded that the selected film properties did not contribute to the observed behaviour of the polymer/zinc oxide/zinc interface. In general the basic mechanistic conditions for ion transport phenomena on zinc and iron surfaces in inert atmosphere seem to be similar for substrates coated with intact polymer and defect rich polymer layer. These facts already point to the surface charge of the iron/iron oxide and zinc/zinc oxide layer as reason for the observed differences in interfacial hydrated ion transport. Due to Leng et al. [1-3] an initial reduction of oxygen is responsible for the highly anodic shifted potential of the intact polymer/iron oxide/iron interface. The atmospheric oxygen partial pressure will not decrease down to zero when purging the SKP chamber with humid purified nitrogen.

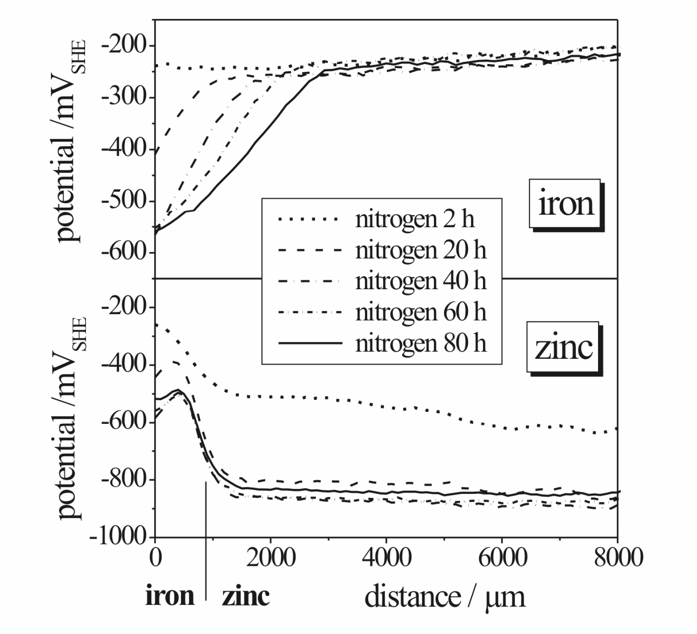

Fig. 3.8: Ion transport process on a zinc / iron sample (see Fig. 3.1b) in inert atmosphere illustrated by SKP potential profiles. The sample was coated with a two-component epoxy resin partially dewetted according to the preparation conditions. Defect electrolyte: 0.5 molar NaCl solution.

A reduction of residual O_2 at the iron oxide surface then also should lead to an accumulation of negative charge within the layer of adsorbed water molecules due to hydroxide formation. An electrostatic attraction of cations from the defect should be plausible to assume. Anyhow, the presence of charge on the iron oxide surfaces may also cause contributing electrokinetic effects. The connection between surface pH and electrolyte/substrate interface tension reduction as supporting parameter for ion transport will be discussed within section 3.2.

In contrast, on zinc oxide no comparable excess charge seems to be existent in inert atmosphere. This assumption can be confirmed regarding the polymer/zinc oxide/zinc interface potential, which is distinctly lower compared to that one for iron substrates. Consequently also the initial oxygen reduction rate and zinc oxide surface charge density should be decreased.

3.1.3.3 Analysis of the interfacial ion distribution on zinc and iron by XPS and ToF-SIMS

The presented results cannot be adequately explained on the basis of diffusion as transport mechanism, as diffusive transport along both polymer/iron oxide and polymer/zinc oxide interfaces should be comparable as a first approximation.

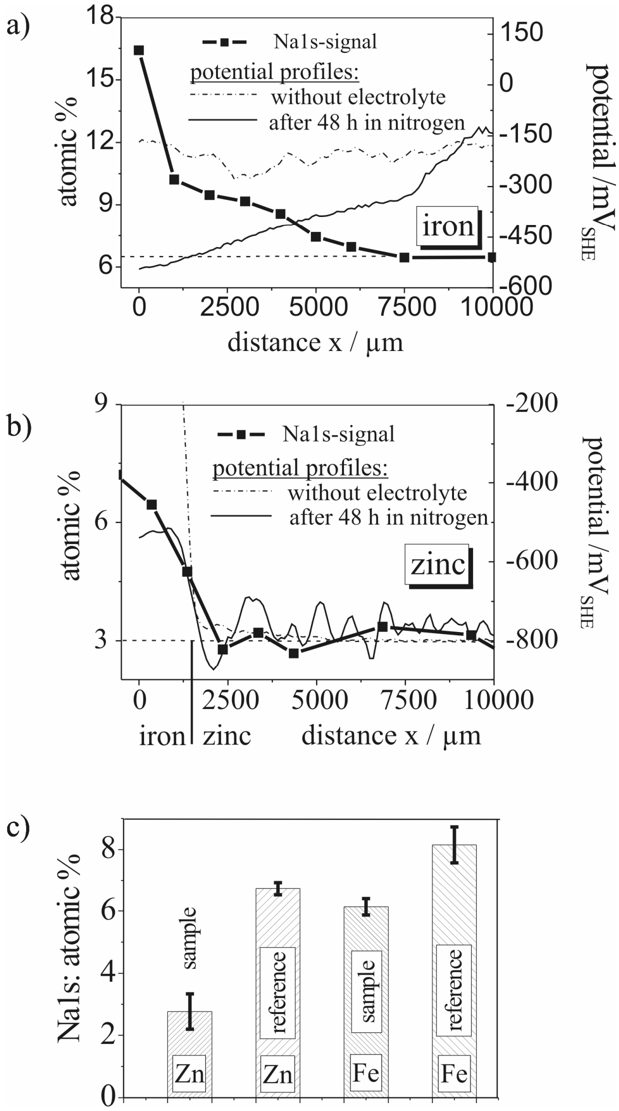

Fig. 3.9: Investigation of the interfacial ion transport process on a zinc / iron sample (see Fig. 3.1b) in inert atmosphere, coated with a latex layer annealed at low film formation temperature and applying 0.5 molar NaCl solution as defect electrolyte. a) Comparison between SKP potential profiles in the iron area (right scale) and corresponding XPS line scan of the Na^+ content (left scale) after removal of the coating. b) Comparison between SKP potential profiles in the zinc area (right scale) and corresponding XPS line scan of the Na^+ content (left scale). c) Evaluation of the basic Na^+ level of the zinc and iron sample area by XPS, compared to those of an identical prepared reference surface (without applying a defect electrolyte).

To investigate whether such an ion transport process occurred and the Kelvin Probe was just not able to detect it, complementary surface analytical measurements were carried out. A sample equivalent to that one used for the experiments presented in Fig. 3.6 was studied by means of the SKP in inert atmosphere and then dried, so that a subsequent cathodic delamination or corrosion process was avoided. To uncover the interface the organic film was oxygen plasma treated afterwards (at 0.2 mbar and 400 W for 60 minutes). Thereby the organic latex film was etched, whereas non-volatile ions remained on the sample surface. Afterwards, small spot XPS analysis was performed to reveal the ion distribution on the relevant surface area. Using a positioning stage, line scans on both iron and zinc area were recorded in steps between 500 μm and 2500 μm in distance with a measuring spot size of 100 μm x 100 μm. Fig. 3.9 presents a comparison of SKP and XPS results when applying 0.5 molar NaCl solution as defect electrolyte.

During the ion transport processes it could be ensured by means of SKP that the transport kinetics were similar to the experiments presented before. In Fig. 3.9a the SKP potential profile of the coated iron area after 48 h and the corresponding Na^+ concentration detected by XPS are plotted versus the distance to the defect area. The sodium ion surface concentration decreases from approx. 16.5 % (0 μm) to 6 % (7500 μm). This trend can roughly be correlated to an increase in potential, starting from -500 mV_{SHE} at 0 μm and increasing almost linearly up to -150 mV_{SHE} at 7500 μm. In any case a ground level of approx. 6 % of Na^+ was observed. This basic concentration also appears in Fig. 3.9b in which the corresponding line scans for the zinc area are visualised. However, the XPS graph geometry almost exactly reflects the SKP line scan characteristics. Fig. 3.9c offers a comparison between the basic XPS Na^+ content of the zinc and iron sample area with those of an identically prepared reference surface (but without an electrolyte filled defect). It is shown that in contrast to the sample used for the ion mobility measurement the Na^+ level on the reference sheet appears to be even higher on both iron and zinc. A supplementary XPS investigation of a bare zinc-iron sheet on which no latex layer has been applied before did not show a detectable sodium or chloride amount. Therefore it can be concluded that the detected 6 % and 3 % of sodium ions in Fig. 3.9a and Fig. 3.9b can be attributed to sodium-containing ingredients employed in the synthesis of the acrylic emulsions. Chloride ions were not detectable on the investigated surfaces.

The XPS results of ion distribution clearly support the SKP data. To avoid the influence of a general contamination level of sodium ions, the experiment was repeated using a 0.5 molar KCl solution as electrolyte. This also allowed checking whether a change of the electrolyte cation has an influence on the shape of the detected potassium ion gradients on zinc and iron. The results of the measurement are shown in Fig 3.10.

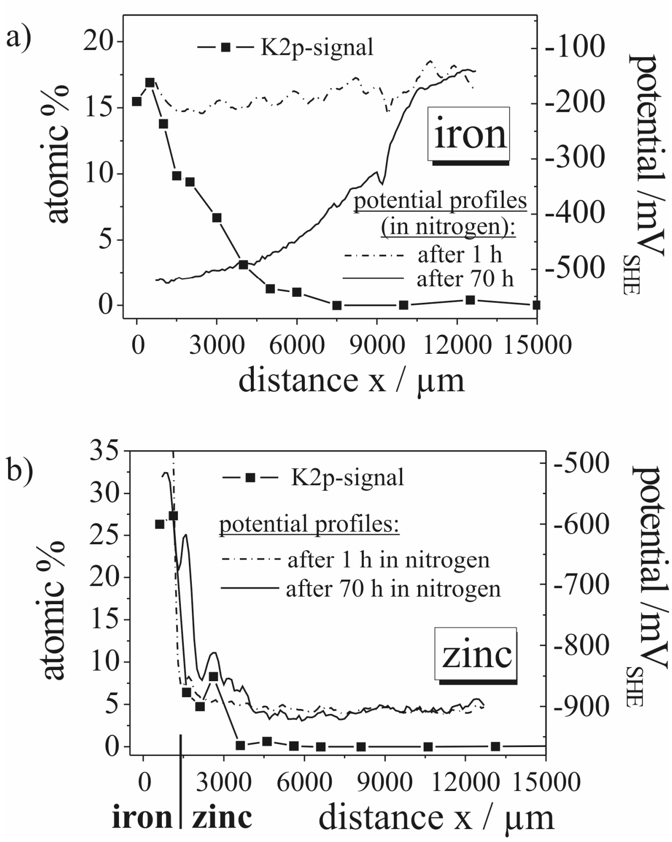

Fig. 3.10: Investigation of the interfacial ion ingress process on a zinc / iron sample (see Fig. 3.1b) in inert atmosphere, coated with a latex layer annealed at low film formation temperature and applying 0.5 molar KCl solution as defect electrolyte. a) Comparison between SKP potential profiles in the iron area (right scale) and corresponding XPS line scan of the K^+ content (left scale) after removal of the coating. b) Comparison between SKP potential profiles in the zinc area (right scale) and corresponding XPS line scan of the K^+ content (left scale).

The SKP potential profiles for KCl electrolytes show the same trend as for the NaCl electrolytes. A potassium ion gradient can be clearly observed in the iron area (see Fig. 3.10a). At the iron-zinc transition in Fig. 10b a strong decrease of the potassium signal intensity is observed. Comparison of the SKP and XPS data reveals that the line scans of the potassium ion concentrations exactly agree with the potential profiles. The Na^+ amount in the iron region (Fig. 3.10a) and zinc domain (Fig. 3.10b) do not show any basic level beyond the expected electrolyte front. Interfacial potassium ion ingress on zinc could not be observed. Consequently the SKP results could be clearly supported by the XPS results. Complementary to the XPS analysis ToF-SIMS mapping was done to reveal even smaller surface concentrations of ions. Fig. 3.11 presents the obtained ToF-SIMS data of the sample already studied by XPS (see Fig. 3.10).

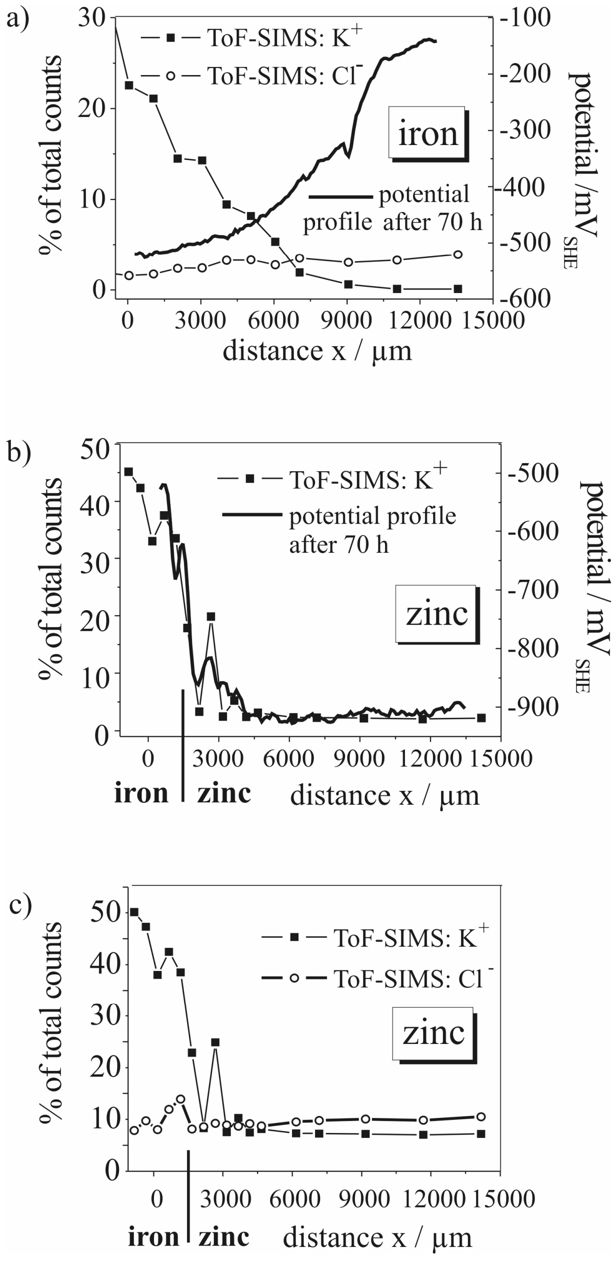

Fig. 3.11: Investigation of the surface ion distribution for the samples presented in Fig. 3.10 by means of ToF-SIMS. a) SKP potential profile of the coated iron area 70 h after initiating the ion transport process in inert atmosphere (right scale). Corresponding ToF-SIMS line scan of the K^+ and Cl^- content in the iron area after removal of the coating (left scale). b) Comparison between SKP 70 h - potential profile of the coated zinc area (right scale) and corresponding ToF-SIMS line scan of the K^+ content after removal of the coating (left scale). c) Comparison between ToF-SIMS K^+ and Cl^- line scans of the zinc area.

For interpretation of the line scans it should be noted that the presented ToF-SIMS data are non-quantitative. Therefore, a direct correlation of the concentration of cations and anions is not possible. Fig. 3.11a shows a comparison between the SKP potential profile and transient of the potassium and chloride ion surface concentration in the iron area. The K^+ signal again reflects the shape of the SKP potential profile. Using ToF-SIMS, also chloride ions were detectable. However, the Cl^- distribution cannot be correlated with that of the potassium ions. This is in contradiction to an interfacial diffusion process of ions in inert atmosphere. It is consequently assumed that the chloride ions originated from contaminations and cannot be attributed to the defect electrolyte.

Fig. 3.11b shows that the potassium line scan also reflects the SKP potential profile in the Fe transition area between defect and zinc. Fig. 3.11c illustrates that the chloride concentration profile again does not show a comparable gradient. In the iron area between defect and borderline to the zinc region the signal is fluctuant but does not really fit to a diffusive transport of K^+ and Cl^- ions. To evaluate whether the basic amounts of chloride and potassium beyond the expected front positions point at low level ingress rates along the whole interface, they were compared to the detected counts on a reference sample.

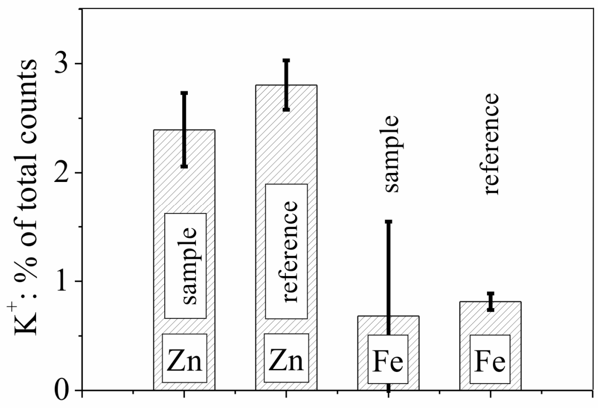

Fig. 3.12: Evaluation of the basic K^+ levels of the zinc and iron sample area by ToF-SIMS, compared to those of an identical prepared reference surface (without applying a defect electrolyte).

After coating with a latex layer the adhesive was removed again without bringing it into contact with a defect electrolyte. It was found that the percentage of the total counts of potassium on the reference for both iron and zinc area was comparable (see Fig. 3.12). Furthermore the K^+ signal in the iron area of the sample appeared to be relatively fluctuant. But this fluctuation did not follow any tendency or concentration gradient for the chosen sample positions. Based on these facts, a low level potassium ingress rate beyond the expected electrolyte front positions on the sample can be excluded. The same conclusion can be drawn for the analysis of the chloride data. The basic Cl^- amount observed on the sample for both iron and zinc area was comparable with that one of the reference. Regarding the fact that chloride does not show a concentration gradient in the area of cation ingress (see Fig. 3.11a and 3.11c) it seems justifiable to attribute these amounts to contaminations of the surface and not to transport processes.

3.1.3.4 Influence of the oxide properties on ion transport processes on zinc

It has been proven that in contrast to iron substrates no interface ion transport occurs on zinc in inert atmosphere. The question arises whether this observation is a result of special chemical properties of the oxide surface or explicitly connected to the electrode potential of the oxide covered zinc substrate. The aim was to evaluate whether interfacial ion ingress is detectable when zinc oxide is not conductively connected to metallic zinc. Therefore a 5 nm zinc oxide layer was deposited on iron by means of magnetron sputtering of Zn and subsequent plasma oxidation. The ZnO layer was investigated by means of XPS to evaluate the film quality. Fig. 3.13 presents a sputter depth profile recorded on such a sample. Metallic zinc could not be detected.

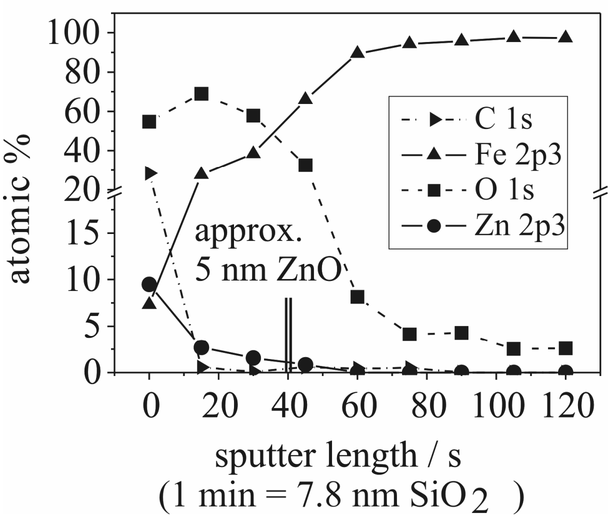

Fig. 3.13: XPS-sputter depth profile of a 5 nm zinc oxide layer on iron (correlation by SiO_2 sputter time reference of 7.8 nm / min). Zinc was deposited by magnetron sputtering and subsequently oxidised applying an oxygen plasma. For details of preparation see section 3.1.2.2.

To check the influence of the layer on the SKP potential, an iron sample covered with 5 nm zinc oxide on one half of the surface area was studied after application of a latex polymer film of 3-6 μm thickness (see Fig. 3.14a). The resulting three dimensional plot recorded in nitrogen atmosphere is shown in Fig. 3.14b. The potential in the ZnO covered left part is shifted negatively by approximately 100 mV.

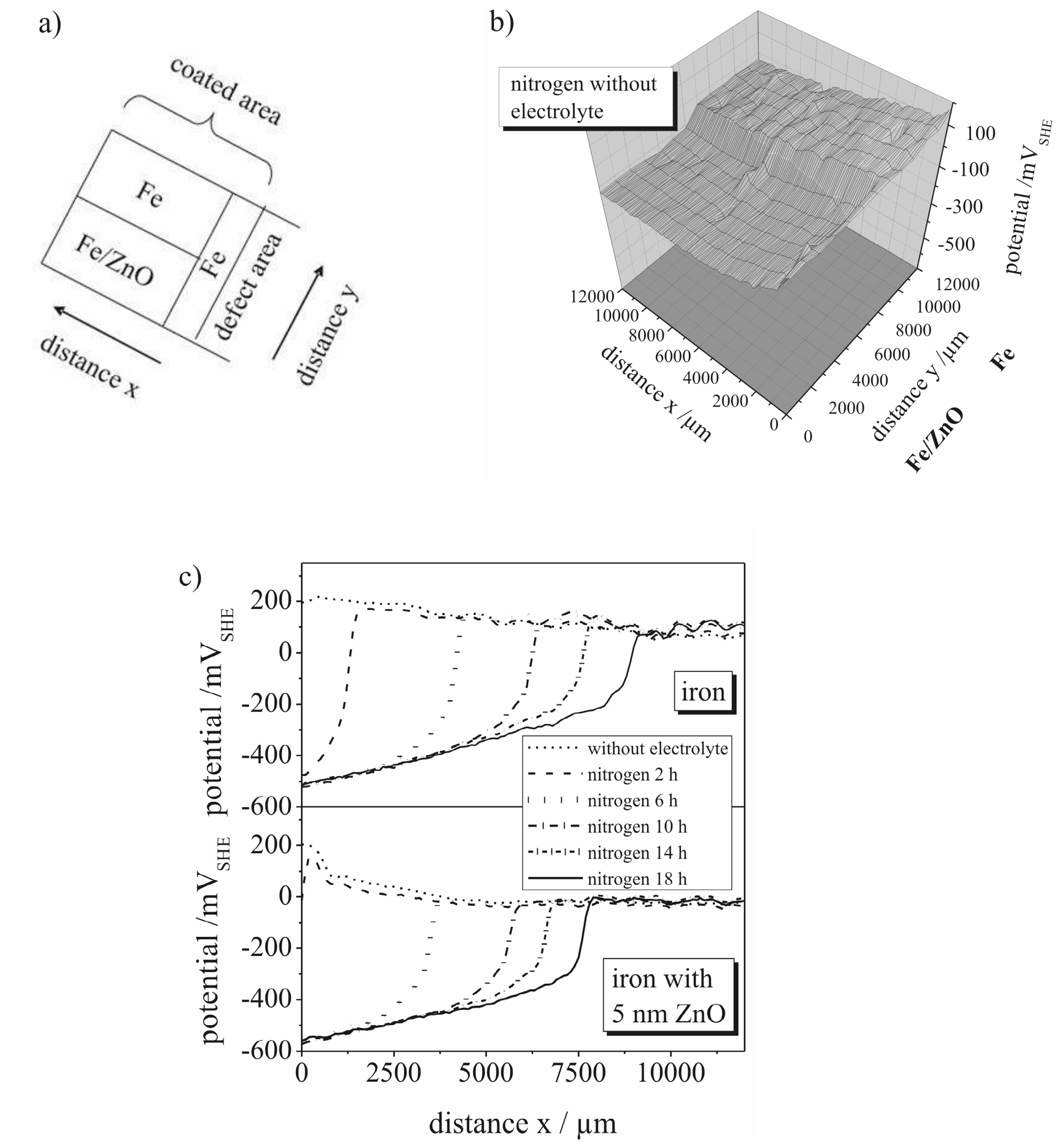

Fig. 3.14: Investigation of the interfacial ion transport processes on an iron sample semi covered with a 5 nm ZnO layer and coated with a latex polymer film at high film formation temperature. Defect electrolyte: 0.5 molar NaCl solution. Defect substrate: Iron/iron oxide a) Sample geometry. b) SKP potential map in nitrogen atmosphere before filling the defect with electrolyte. c) Chronological development of the SKP potential profiles during the ion ingress process.

Fig. 3.14c gives an impression of the ion transport processes occurring at the polymer/oxide/metal interfaces in nitrogen atmosphere applying a 0.5 molar NaCl solution as defect electrolyte. An ion transport obviously proceeds along both polymer/iron oxide and polymer/zinc oxide interfaces with a comparable velocity. It can be assumed that the electronic properties of the sputtered zinc oxide layer will differ from that ones of native zinc oxide [22]. Moreover, a 5 nm layer will not be free of small pores down to the oxide covered iron substrate. However, it can be shown that the chemical structure of the zinc oxide is not necessarily responsible for the missing interfacial ion ingress. To make sure that the sputtered thin ZnO layer does not permit an access of hydrated ions to the interfacial region independent from the underlying substrate, a complementary proof is given with the experimental data visualised in Fig. 3.15. A zinc/iron sample similar to that one presented in Fig. 3.1b was entirely covered with a sputtered 5 nm ZnO layer. Only the defect area and a small band of iron between defect and zinc domain was omitted. Afterwards the sample was coated with latex and subsequently investigated by means of SKP. Fig. 3.15 offers an overview over the development of the SKP potential line scans.

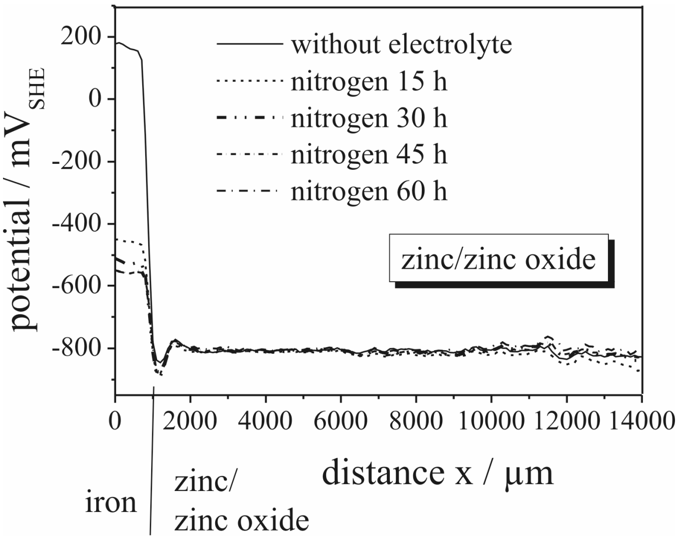

Fig. 3.15: SKP measurement of a zinc/iron sample covered with a 5 nm sputtered ZnO layer (except the defect region and a short band of iron between defect and zinc area to avoid a direct electrolytic coupling). As coating a latex layer was applied at low film formation temperature. Defect electrolyte: 0.5 molar NaCl solution. Defect substrate: iron/iron oxide. The chronological development of the potential profiles during the experiment at the zinc / zinc oxide area is shown.

Again no ion ingress beyond the iron-zinc transition could be observed. As a result it is ensured that an ion transport is not inhibited by the chemical characteristics of the zinc oxide layer but has to be discussed in connection with the electrochemical properties of the zinc/zinc oxide layer.

3.1.4 Conclusions

The complementary electrochemical and spectroscopic polymer/oxide/metal interface analysis of zinc and iron substrates proofs that in non-corrosive humid atmosphere of strongly reduced oxygen partial pressure electrostatic fields determine the ion transport processes. No ingress of ions was observed even for defect rich interfaces on oxide covered zinc substrates while selectively cations were transported along the polymer/iron oxide/iron interface.

The selective cation transport is assigned to the electrostatic field based on an interfacial accumulation of negative charge. It is assumed that for oxide covered iron substrates this electrostatic field arises from an oxygen reduction induced interfacial hydroxide ion formation. In humid air the induced interfacial charge densities are high enough to promote a corrosive de-adhesion process. The oxygen partial pressure will not decrease down to zero when purging the SKP chamber with humid purified nitrogen. A residual O_2 amount probably still supports a low-level, but continuous oxygen reduction reaction at the polymer/iron oxide interface. Consequently the interfacial negative excess charges are not completely removed from oxide covered iron substrates in humid nitrogen atmospheres and therefore also electrokinetic effects may support an interfacial electrolyte transport.

However, on zinc oxide either no comparable excess charge seems to be existent in inert atmosphere, or a continuous reduction of residual O_2 is hindered at low oxygen partial pressures. This hypothesis explains the observation that in the frame of the presented studies no ions were transported along the polymer/zinc oxide/zinc interface.

Nevertheless diffusion seems to be negligible for interfacial ion transport at such interfaces, anyhow. This consequently also applies to the initial stage of the cathodic delamination process in air.

3.1.5 References

[1] A. Leng, H. Streckel, M. Stratmann, Corr. Sci. 41 (1999) 547.
[2] A. Leng, H. Streckel, M. Stratmann, Corr. Sci. 41 (1999) 579.
[3] A. Leng, H. Streckel, K. Hofmann, M. Stratmann, Corr. Sci. 41 (1999) 599.
[4] W. Fürbeth, M. Stratmann, Corr. Sci. 43 (2001) 207.
[5] W. Fürbeth, M. Stratmann, Corr. Sci. 43 (2001) 229.
[6] W. Fürbeth, M. Stratmann, Corr. Sci. 43 (2001) 243.
[7] M. Rohwerder, P. Leblanc, G.S. Frankel, M. Stratmann in P. Marcus, F. Mansfeld (Eds.), Analytical Methods for Corrosion Science and Engineering, Marcel Dekker Ltd. (2005) 605.
[8] H.N. McMurray, G. Williams, J. Appl. Phys. 91 (2002) 1673.
[9] H. Baumgärtner, H.D. Liess, Rev. Sci. Instrum. 59 (1988) 802.
[10] F. Kohlrausch, Praktische Physik 22 (1968).
[11] M. Stratmann, H. Streckel, Corros. Sci. 30 (1990) 681.
[12] G. Grundmeier, K.M. Jüttner, M. Stratmann, in: R.W. Cahn, P. Haasen, E.J. Kramer (Eds.), Materials Science and Technologies, Wiley-VCH, Weinheim, 2000.
[13] K.B. Johnson, W.N. Hansen, Rev. Sci. Instrum. 66 (1995) 2967.
[14] K. Wapner, G. Grundmeier, Adv. Eng. Mater. 6 (2004) 163.
[15] K. Wapner, B. Schönberger, M. Stratmann, G. Grundmeier, J. Electrochem. Soc. 152 (2005) E 114.
[16] J. Pommersheim, T. Nguyen, Z. Zhang, C. Lin, J. Adhesion Sci. Technol. 9 (1995) 935.
[17] K. Wapner, M. Stratmann, G. Grundmeier, Electrochim. Acta 51 (2006) 3303.
[18] K. Wapner, Thesis, Ruhr-University Bochum/Germany, 2006.
[19] N. Fink, B. Wilson, G. Grundmeier, Electrochim. Acta 51 (2006) 2956.
[20] R. Vlasak, I. Klüppel, G. Grundmeier, Electrochim. Acta 52 (2007) 8075.
[21] D.M. Brasher, A.H. Kingsbury, J. Appl. Chem. 4 (1954) 62.
[22] X.G. Zhang, Corrosion and Electrochemistry of Zinc, Plenum Press, New York, 1996.

3.2 Hydrated ion transport along oxide covered iron and zinc surfaces

3.2.1 Fundamentals

In section 3.1 it was shown that also in non-corrosive humid atmosphere electrostatic fields determine the transport of hydrated ions along polymer/oxide/metal interfaces for iron and zinc substrates. This was surprising and rebutted the established mechanistic model that seemed to allow the calculation of ion transport velocities on the basis of diffusion [1-7]. The investigation of polymer/oxide/metal composite properties usually has the disadvantage that buried interfaces are hardly accessible by many common analytical techniques. On the other hand it can be argued that electrochemical processes at the substrate surfaces cannot be correlated to those occurring when the substrate bulk is covered by a polymer layer. Nevertheless it will be shown within this chapter that ion transport can be initiated also on uncovered iron and zinc surfaces and that the basic mechanisms of reactive electrolyte spreading and corrosive delamination seem to be well comparable. This enables the assignment of the results purely to the properties of the oxide without the influence of any polymer and will open the gate for easier access to a detailed analysis of the interface structure determinant for corrosive delamination in future. The experimental approach and tools introduced in section 3.1 are further developed in this chapter. Again Scanning Kelvin Probe (SKP) studies were performed to monitor electrolyte spreading on non polymer covered zinc coated iron substrates in cut-edge geometry. Subsequently the detected potential profiles are compared to the resulting ion distribution at the surface, investigated by Time-of-Flight Secondary Ion Mass Spectrometry (ToF-SIMS). It will be critically discussed in how far the established model of interfacial ion transport has to be modified and why this model came to incorrect conclusions concerning the driving forces for interfacial ion transport.

3.2.2 Experimental procedures

For additional details concerning sample preparation, sample configuration and experimental techniques it is referred to section 3.1.2.

Contact angles have been investigated in inert atmosphere with 15 μl droplets of ultra purified water (pH = 6.9), measured 15 s after deposition on the surfaces and applying a dataphysics Contact Angle System OCA 20.

3.2.3 Experimental results

3.2.3.1 Ion transport along uncovered oxide/metal surfaces in inert atmosphere

In section 3.1 it could be shown that no cation transport could be recorded at polymer/zinc oxide/zinc interfaces in non-corrosive atmosphere of high humidity (> 95 % r. h.). Applying strongly defected coatings led to the same result. The question arises whether a polymer layer is generally necessary for studying the basic ion transport process.

A key experiment is illustrated in Fig. 3.16. It reflects a Scanning Kelvin Probe (SKP) measurement recorded on a zinc/iron sample (the sample geometry is given in Fig. 3.16a) without any organic film. To remove all organic contaminations, the surface was treated with 400 W oxygen plasma for 10 minutes (except the defect region) according to the normal cleaning procedure described in section 3.1.2. As electrolyte 0.5 M KBr solution was chosen. To prevent it from spontaneous spreading along the surface, it was stabilised with 3 % agar. The experiment was executed in a nitrogen atmosphere of 95-96 % relative humidity. The potential map in Fig. 3.16b and potential profiles of Fig. 3.16c indicate a process that was also observed visually: An electrolyte front was spreading along the iron surface starting from the defect and forming a pattern of isolated, small droplets. No continuous water layer could be observed. With increasing distance (about 5000 µm) to the electrolyte front the droplets started to aggregate. At the transition to the zinc area the front stopped according to visual inspection and potential profiles. In comparison to the 7-9 μm vertical iron-zinc step the average droplet height appeared to be much larger; so the step itself could not serve as simple physical barrier for electrolyte ingress.

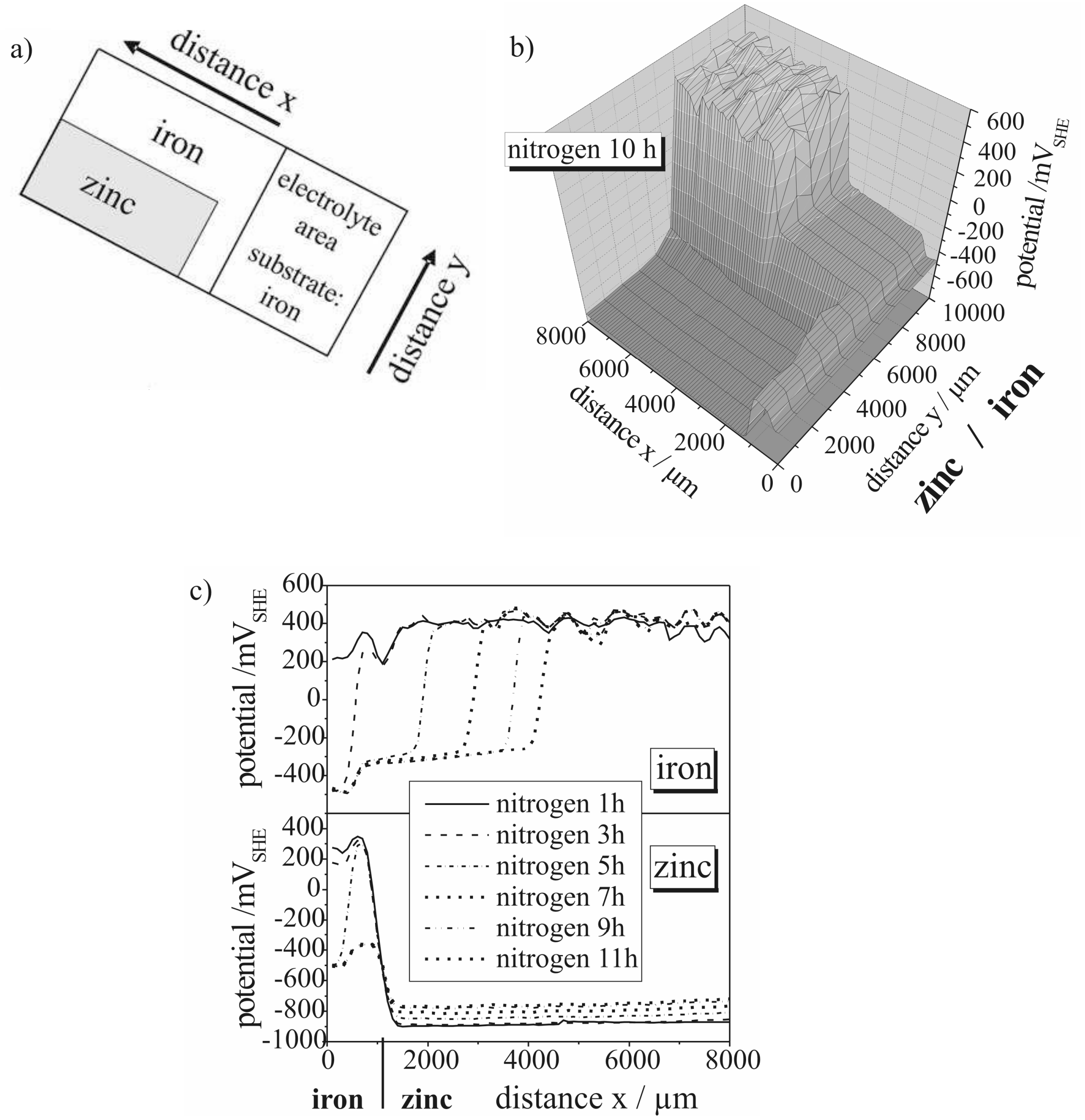

Fig. 3.16: SKP measurement of an uncovered zinc/iron sample after 10 min of 400 W oxygen plasma treatment to remove possible organic contamination. Defect electrolyte: 0.5 molar KBr solution, stabilised with 3 % agar. a) Sample configuration. b) Potential map after 10 h in nitrogen atmosphere (> 95 % r. h.). c) Chronological development of the potential profiles during the ion transport process.

With increasing time the electrolyte seemed to be more and more retained at the borderline to the zinc area without wetting it. Contact angle measurements with water droplets deposited on the two substrate types did not prove observable differences in the hydrophobic properties. The static water contact angles on oxide covered iron (71.8° ± 1.4°) and zinc (69.7° ± 1.8°) were very similar. Regarding the short timescale relevant for the experiments it can be assumed that these contact angles should be unaffected from corrosion processes at the droplet/substrate interface in inert atmosphere. Therefore, distinct differences in surface wettability cannot act as an explanation for the different transport kinetics on zinc and iron oxide.

The experiment presented in Fig. 3.16 was also reproduced for longer timescales, but no detectable ion transport process on zinc oxide with the SKP could be observed. However, the transport rate on iron showed large variations. This can be assigned to slightly different gas flow rates and relative humidities in the SKP chamber, which strongly affect the formation of the adsorbed electrolyte layer. As no covering polymer film stabilised a relatively constant water concentration at the interface, the process kinetic sensitively responded to the environmental changes.

It can be concluded that the basic mechanistic conditions for ion transport phenomena on oxide covered zinc and iron surfaces in inert atmosphere seem to be similar for substrates coated with intact polymer layers, defected polymer layers and even without any polymer film. The missing polymer films allow kinetic investigations without regarding the complex polymer/oxide interphase structure.

Section 3.1 displayed that cations of the defect electrolyte were transported selectively. Furthermore, the distribution of these cations on the substrate surface nearly exactly reflected the received SKP potential profile geometry. To check whether this also applies to transport processes along free oxide surfaces and to investigate if anions really are not transported, Time-of-Flight Secondary Ion Mass Spectroscopy (ToF-SIMS) measurements have been performed.

Therefore, the experiment presented in Fig. 3.16 was repeated investigating the interfacial transport process on an iron-zinc sample. A solution of 0.5 molar KBr stabilised with 3 % agar was chosen as defect electrolyte. The sample surface was prepared similar to the measurement presented in Fig. 3.16, but was exposed to a 400 W argon plasma for 300 s to remove organic contaminations. No polymer layer was applied on the sample. During the ion ingress process in non-corrosive atmosphere the surface was mapped by SKP. Afterwards it was carefully dried in nitrogen and investigated by means of ToF-SIMS focussing on the transition between defect area and region of the ion transport processes (see Fig. 3.17). The elemental distribution of K^+ and Br^- is visualised in Fig. 3.17a and 3.17b. In both diagrams three zones can be distinguished. In the area of the electrolyte in the defect between position 0 mm and 5.5 mm of the iron line scan (Fig. 3.17a) as well as between 2.5 mm and 5 mm of the iron-zinc line scan (Fig. 3.17b) the ToF-SIMS signals appear to be fluctuant. This is explained with an inhomogeneous distribution of small KBr crystals and residuals of agar. In fact both bromide and potassium signals change their characteristics nearly exactly at the borderline to the free surface. The Br^- content decreases to a base level and stays stable.

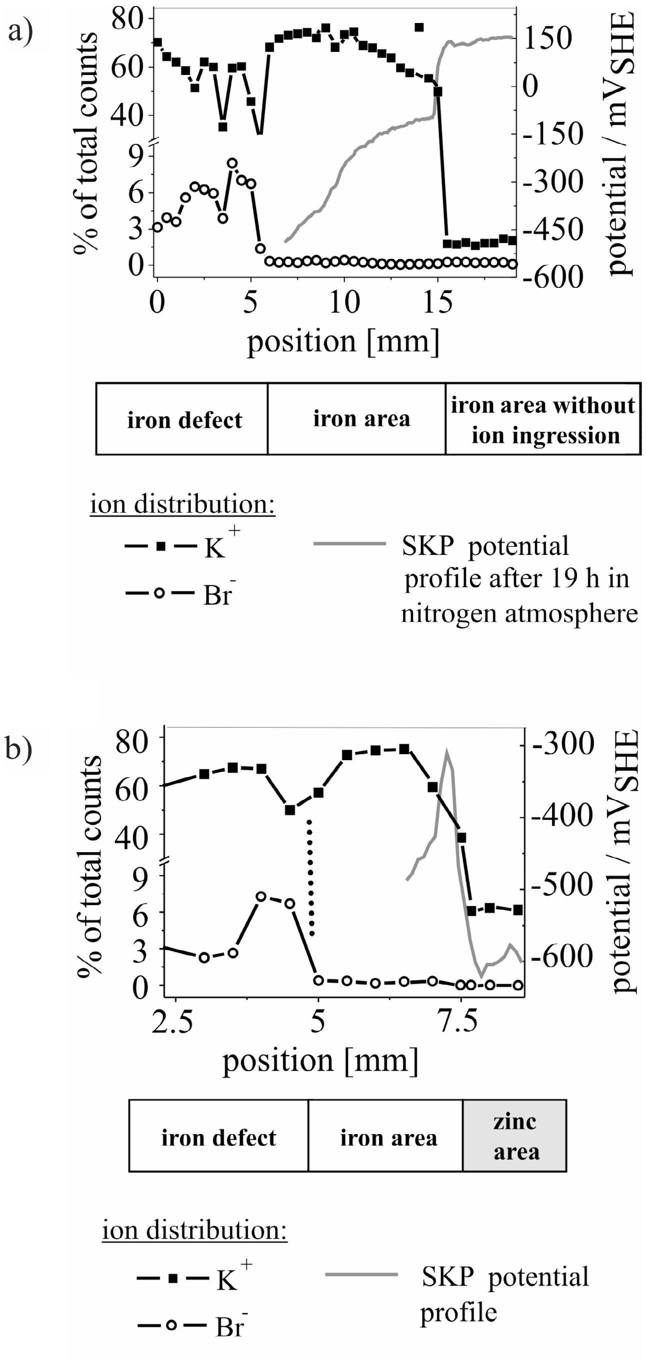

Fig. 3.17: Investigation of ion transport processes along the uncovered surface of a zinc/iron sample in inert atmosphere (for sample geometry see Fig. 3.16a) after 5 min 400 W argon plasma treatment. Defect electrolyte: 0.5 molar KBr solution, stabilised with 3 % agar. After SKP mapping the elemental distribution on the surface was detected by Tof-SIMS. a) Concentration profiles of K^+ and Br^- in the iron area (left scale) and corresponding SKP potential profile after 17 h in inert atmosphere (> 95 % r. h.) (right scale). b) Concentration profiles of K^+ and Br^- between defect area and iron-zinc transition (left scale), correlated with a typical SKP potential profile (right scale).

In contrast the K^+ graph shows a decreasing concentration gradient of potassium between 5.5 mm and 15.5 mm of the iron line scan (Fig. 3.17a) as well as between 5 mm and 7.5 mm of the iron-zinc line scan (Fig. 3.17b). The transition to the surface not affected from ion transport processes (zone 3) is indicated by an abrupt drop to a static basic potassium level. Before drying the sample, the electrolyte front position was also observed visually. The front of transported ions analysed via ToF-SIMS agreed well with the SKP line scans (see Fig. 3.17a and 3.17b). In case of the iron-zinc line scan, the step in the K^+ distribution reflected the transition from the iron to the zinc area and showed that no cations were transported beyond this line. Fig. 3.17 again proves the selective transport of cations along the substrate surface supporting the conclusion that electrostatic fields determine the ion transport. Br^- stays in the area of bulk electrolyte and no concentration gradient hints at an anion movement. Furthermore, this result also supports the concept of investigating the basic kinetic conditions for interfacial ion transport along uncovered substrates.

3.2.3.2 Ion transport along uncovered oxide/metal surfaces in humid air

Ion transport processes on uncovered iron and zinc oxide surfaces were also studied in humid air. Fig. 3.18 presents the investigation of the ion transport processes monitored by SKP using an uncoated zinc/iron sample. Again the sample was argon plasma cleaned and 0.5 molar KBr solution was used as defect electrolyte. The experiment was started in inert atmosphere of high humidity (> 95 % r. h.). Fig. 3.18a illustrates the resulting potential map after 60 hours. Although the progress appears to be relatively slow even on iron, it can be clearly observed that the electrolyte front stopped at the iron-zinc transition. Subsequently, the atmosphere was changed to humid air. Fig. 3.18b now proves an anodic shift of the zinc area potential from around -750 mV_{SHE} to -500 mV_{SHE} for the whole zinc surface. Nearly an equipotential level for both substrate types was established so that no further ion transport could be detected based on potential measurements. On iron, the ion transport appeared to be accelerated, as it should be expected for an oxygen reduction induced ion transport process on iron oxide in air. To get a visual impression of such a process Fig. 3.19 presents two photos taken at 20 and 50 hours after initiation in humid air (> 95 % r. h.). An iron sheet was used as substrate material. Electrolyte droplets indicate the borderline between the area of ion transport and the unaffected iron area. The oxygen reduction leads to an increased amount of hydroxide ions passivating the surface [1].

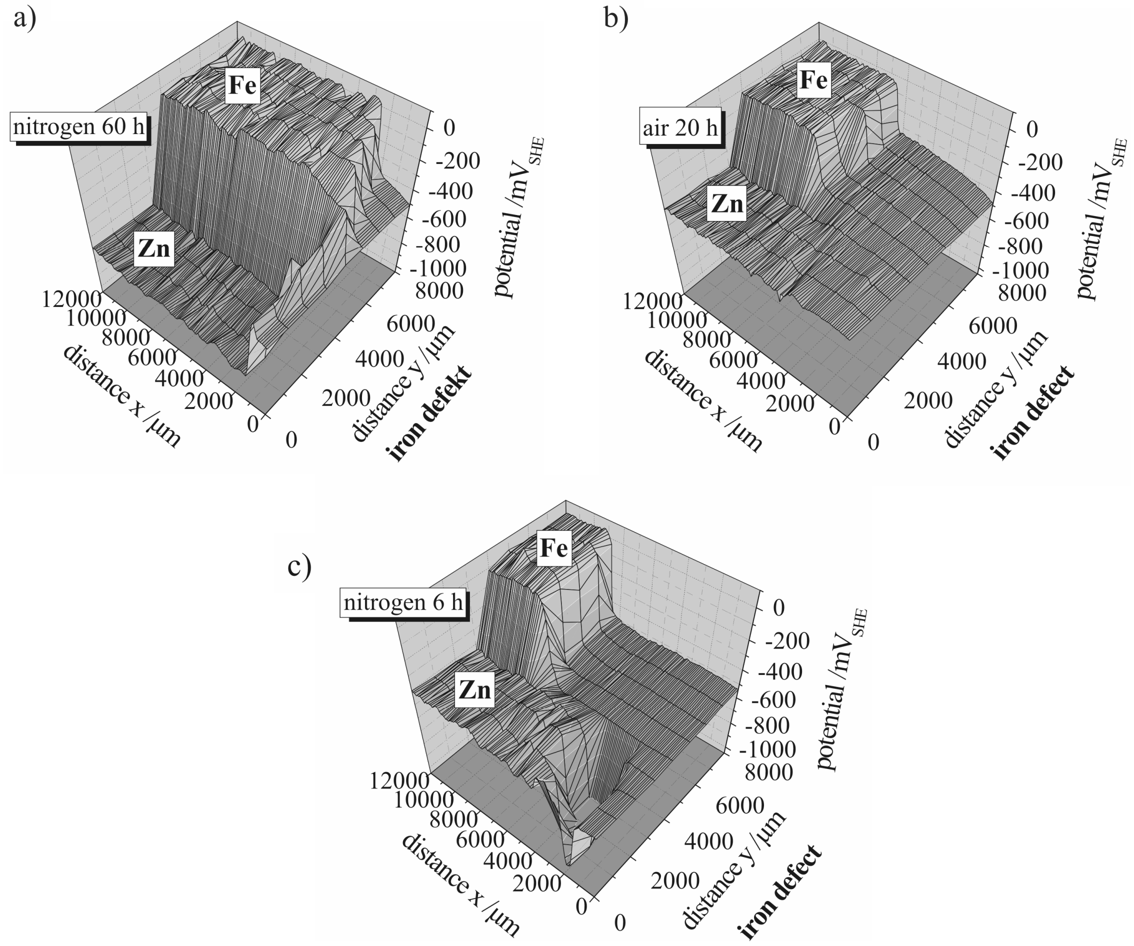

Fig. 3.18: SKP measurement of an uncovered zinc/iron sample (see Fig. 3.16a) after 5 min of 400 W argon plasma treatment. Defect electrolyte: 0.5 molar KBr solution, stabilised with 3 % agar. a) Potential map after 60 hours in nitrogen atmosphere (> 95 % r. h.). b) Potential map after 20 hours after switching to air (> 95 % r. h.). c) Potential map 6 hours after switching back to inert atmosphere (of high humidity).

The potential profiles recorded in the iron area of the sample investigated in Fig. 3.18 reveal only a small slope (25 mV/mm) of the graph between defect area and electrolyte front position during the oxygen reduction induced ion transport process in air (see Fig. 3.20). The respective potential profile slope for the ion transport process on iron oxide in inert atmosphere is larger with around 30 mV/mm (see Fig. 3.16c). In contrast Leng et al. assumed no such increase for ion transport along polymer/iron oxide/iron interfaces in inert atmosphere and reported a distinctly larger linear potential increase for profiles reflecting cathodic delamination. This was assigned to an ohmic potential drop between the local electrodes, whereas no galvanic cell should be effective in inert atmosphere [1-3]. As shown within this report such a criterion cannot be adopted to uncovered iron oxide substrates to distinguish between ion transport in air and inert atmosphere.

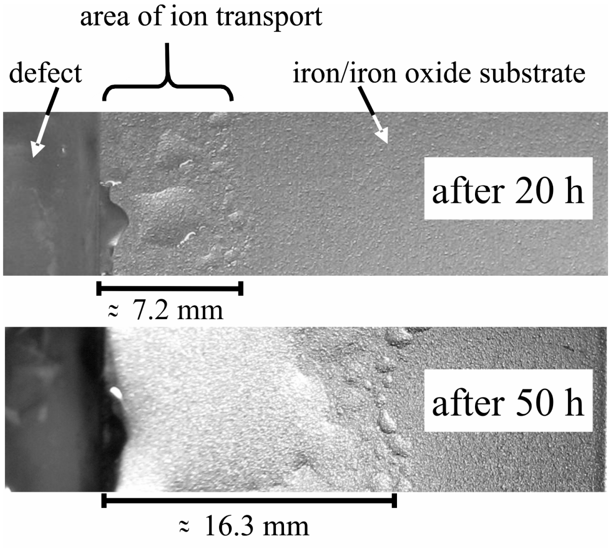

Fig. 3.19: Oxygen reduction induced ion transport process on an uncovered iron/iron oxide sample in air (> 95 % r. h.) after 5 min 400 W argon plasma cleaning. Defect electrolyte: 0.5 molar KBr solution, stabilised with 3 % agar. Upper photo taken after 20 hours, bottom photo recorded after 50 hours.

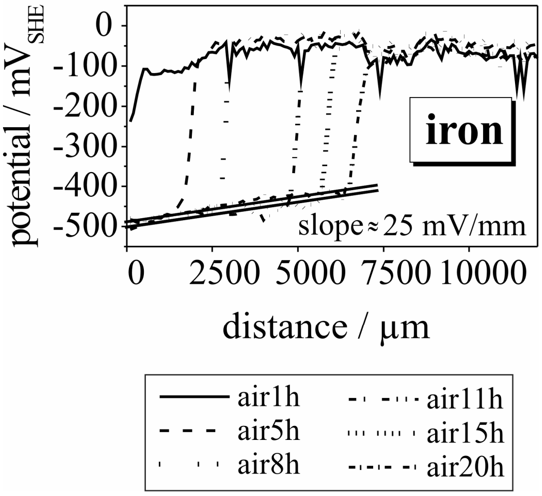

Fig. 3.20: SKP potential profiles recorded in the iron area of the sample presented in Fig. 3.18 (no coating, iron defect, 0.5 molar KBr with 3 % agar as defect electrolyte, atmosphere of > 95 % r. h.). The ion transport process has been detected after switching from inert to normal air atmosphere. The graph "air 20h" can be correlated with Fig. 3.18b and Fig. 3.21b.

Figure 3.21 presents the SKP potential profiles of the ion transport processes on the zinc/zinc oxide surface (same experiment as shown in Figure 3.18). In Fig. 3.21a the ion ingress along the short iron area between defect and zinc covered part is visualised. Fig. 3.21b illustrates a continuous equalisation of the potential levels of defect and zinc area. The SKP could not detect a further ion transport. However, oxygen reduction induced ion transport could still occur on the substrate surface at the measured potential. The shape of the potential profiles recorded after re-establishment of an inert atmosphere supports this assumption as explained in the following. A mechanism similar to cathodic delamination is plausibly assumed as it is obviously effective on iron oxide, too. In this case a distinct potential step between defect and uncovered zinc oxide surface does not seem to be a prerequisite for the process. However, this was reported as necessity for ion transport at polymer/zinc oxide/zinc interfaces in air; the defect potential has to be more cathodic than that of the coated area [4-6].

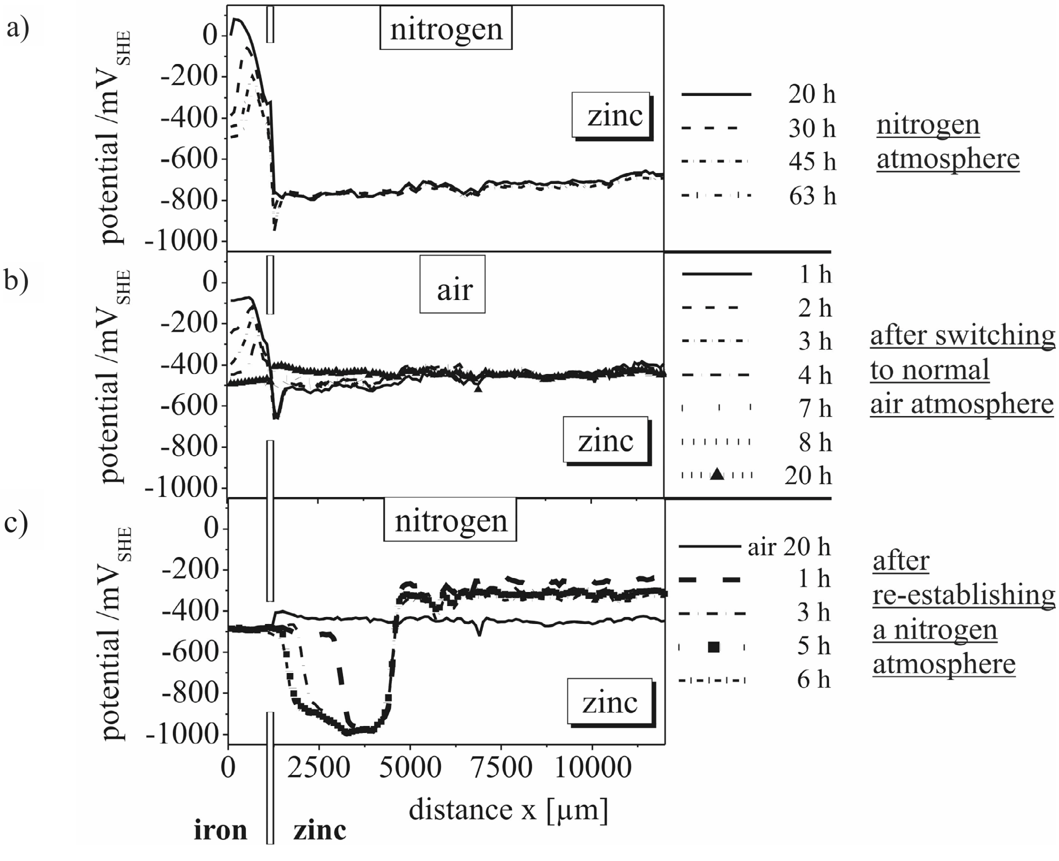

Fig. 3.21: Investigation of the surface ion transport processes at the zinc area of the zinc/iron sample presented in Fig. 3.18 (no coating, iron defect, 0.5 molar KBr with 3 % agar as defect electrolyte, atmosphere > 95 % r. h.). a) Chronological development of the SKP potential profiles in inert atmosphere. b) Chronological development of the SKP potential profiles after switching to normal air atmosphere. c) Chronological development of the SKP potential profiles after re-establishing an inert atmosphere.

Fig. 3.18c and Fig. 3.21c show that after re-establishing a humid nitrogen atmosphere the zinc area is now more anodic (-300 mV_{SHE}) than the defect. At a distance of 2500 μm within the zinc area a cathodic potential valley with a minimum of -1000 mV_{SHE} developed. Moreover, this valley broadened in direction to the defect with time.

Fürbeth et al. try to give possible explanations for the observed potential changes [4-5]. The high amount of hydroxide ions generated due to oxygen reduction in air before is still existent after changing to inert atmosphere. A break down of the galvanic element is assumed, but an electrolytic connection to the defect should be still effective [4]. To balance the surplus of hydroxide, a transport back to the defect is discussed. Due to an extremely reduced faradaic current the SKP now detects the cathodic local equilibrium potential of a zinc oxide/hydroxide surface in contact with an electrolyte of pH 11. Also a fast relaxation of the potential within the timescale hydroxide needs to diffuse back to the defect is reported [4]. Such a process could not be observed in Fig. 3.21.

To receive more detailed results concerning the elemental and ion distribution on the surfaces mapped by SKP the sample was subsequently investigated by means of ToF-SIMS. Fig. 3.22 presents the received data of a ToF-SIMS line scan. It can be correlated with the SKP potential profiles of Fig. 3.21c. Starting in the iron defect area the short iron band between defect and zinc was mapped. Fig. 3.22a offers qualititative information about the local potassium distribution. Fig. 3.22b provides the corresponding information about the signal development of important anions. Between -6000 μm and approximately -3500 μm distance, the ion signals were extremely fluctuant and unstable. It could be visually checked that this refers to the surface properties of the defect. Between defect border and transition between iron band and zinc area the cation amount seems to be stabilised on a high level. In contrast the bromide quantity seems to be more comparable to the basic amount detected in the zinc area beyond 4500 μm. In the zinc zone that showed a very negative electrode potential, the ratio of both ion types is shifted in favour of the anions. Potassium ions were not detected in this area when neglecting the basic contamination also detectable in the zinc area beyond 4500 μm. The hydroxide amount seemed to be slightly increased, but quantification with regard to the unaffected zinc area (> 4500 μm) is not possible. The ion distribution supports the hypothesis that the hydroxide ions generated in air may be transported back to the defect after re-establishing an inert atmosphere.

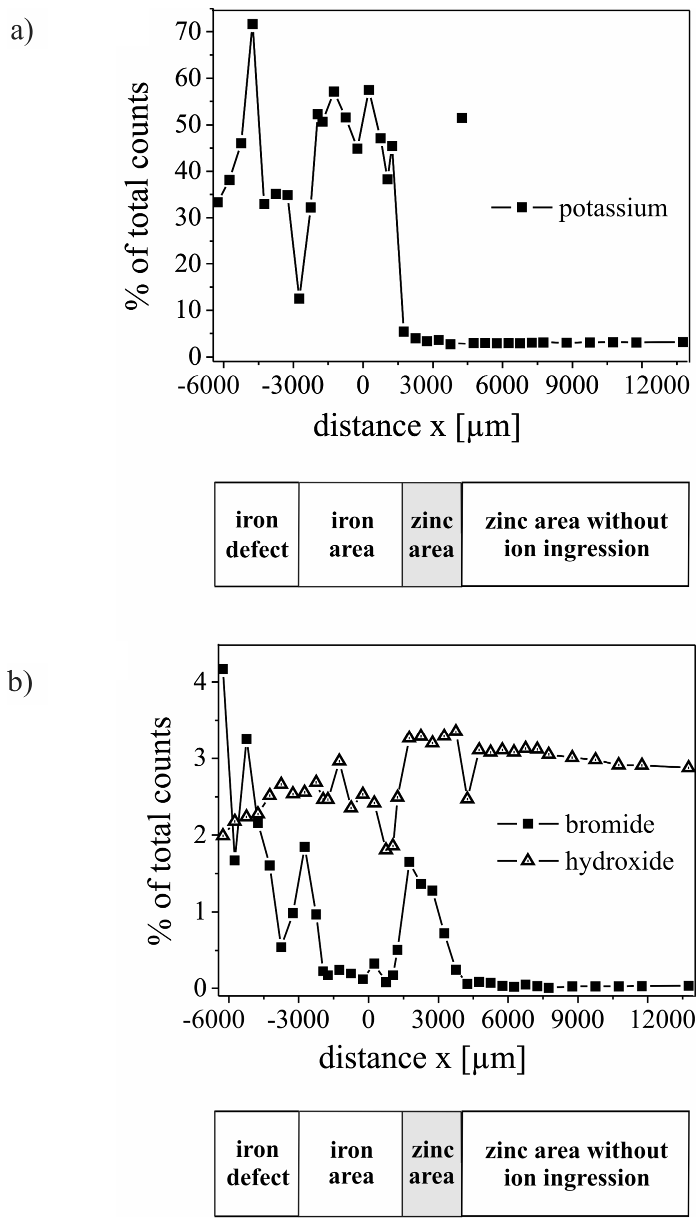

Fig. 3.22: Study of the interfacial ion distribution on the sample presented in Fig. 3.21. A ToF-SIMS line scan is shown that corresponds to the SKP potential profile of Fig. 3.21c (6 hours after switching back from air to inert atmosphere). Defect region, iron band between defect and zinc area, iron-zinc transition and zinc area have been investigated. a) Cation distribution. b) Anion distribution.

3.2.3.3 Non-corrosive ion transport along uncovered zinc oxide surfaces with a zinc defect

It has been concluded that cation transport on iron in inert atmosphere has to be attributed to the attraction of negative excess charges at the surface. For zinc no such surplus of negative charge carrier seems to be effective.

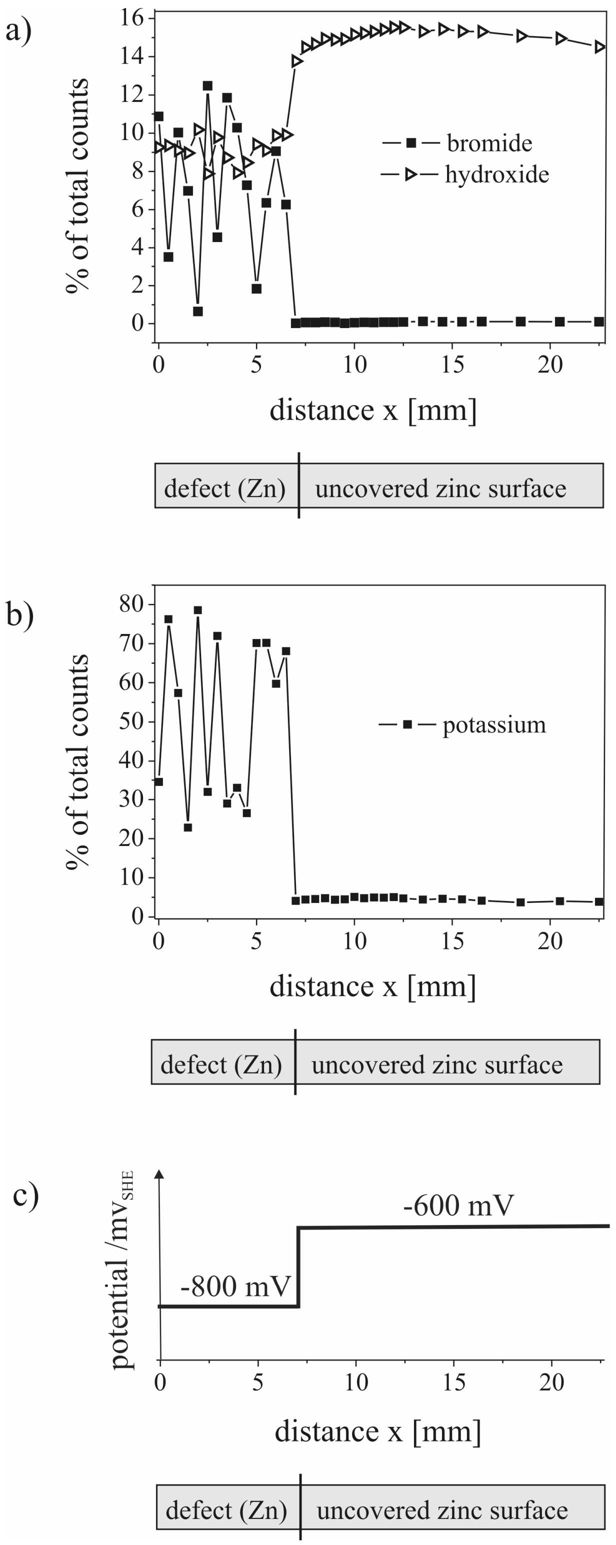

Fig. 3.23: ToF-SIMS study of the surface ion distribution on an uncovered zinc sample. The surface has been cleaned in 400 W argon plasma for 5 minutes before. After filling the zinc defect with 0.5 molar KBr solution (stabilised with 3 % agar), the sample has been stored for 137 h in inert atmosphere of high humidity. Defect area and free zinc area have been investigated afterwards with a ToF-SIMS line scan. a) Anion distribution. b) Cation distribution.

In the following the interfacial ion transport processes on an uncovered zinc sample were studied for an electrolyte/zinc interface in the defect. The development of the interfacial potential distribution was mapped by means of the SKP in inert atmosphere. During 137 hours no proceeding ion front could be observed. The interfacial potential distribution did not change at all. At the end of the measurement the potential of the free zinc/zinc oxide surface appeared to be around 200 mV more anodic than that one of the defect region (see schematic illustration in Fig. 3.23c). Compared to the case when iron/iron oxide was applied as substrate material in the defect (see Fig. 3.16) this means an inversion of potential levels. To determine whether this also should be correlated to a reversal of the surface charge, the sample was dried after terminating the ion transport experiment. Subsequently it was investigated by ToF-SIMS.

The line scan started in the defect region and followed the direction of surface ion transport processes along the uncoated zinc substrate. Fig. 3.23a presents the development of selected anion signals. Two areas can be easily distinguished. In the defect region the ToF-SIMS signals again are fluctuant, whereas at the border to the free zinc/zinc oxide surface the bromide and hydroxide signals immediately drop to a basic level and remain stable. The same applies to potassium in Fig. 3.23b. No ion ingress is detectable for the uncovered substrate area. If a highly positive charge density at the surface would have been established, at least a preferential transport of anions should have been recorded. As this is not the case it can be concluded that on zinc no charged layer of immobilised adsorbed ions is effectively promoting the interface and surface ion transport processes in inert atmosphere.

3.2.3.4 Discussion of contradictive conclusions drawn in literature

In contrast to the results received with this study, the publications of Leng et al. [1-3] and Fürbeth et al. [4-6] claim to prove diffusive ion transport at polymer/oxide/metal interfaces, in particular when applying iron substrates. Wapner et al. adopted this point of view when calculating formal diffusion coefficients for interfacial ion transport in inert atmosphere [7]. Several arguments were presented [1-3]:

- *Addition of 1,10-phenantroline to the defect electrolyte resulted with red colouration of the liquid due to formation of* Fe^{2+}*-phenantroline complexes during sample exposure in humid air. In contrast, no colouration was found* *during exposure in humid nitrogen atmosphere. Obviously no remarkable iron dissolution occurs in inert atmosphere, which is expected to be necessary for electrochemically determined ion transport.*

- *Addition of phenolphthalein to the delaminated area indicated a strong alkaline pH shift of the interface during sample exposure in humid air, but did not lead to colouration in humid nitrogen atmosphere. Obviously a galvanic cell is absent in inert atmosphere which would be necessary for hydroxide formation. Consequently any detected ion transport has to be mainly attributed to diffusion.*
- *SKP potential profiles should exhibit a linear ohmic potential drop between the local electrodes during interface delamination in air. For exposure in humid nitrogen atmosphere, such linear potential increase should vanish as the galvanic cell is absent.*
- *Auger Electron spectra recorded after sample exposure in inert atmosphere proved that chlorine was present in the area of ion transport and that the amount of chlorine and sodium was comparable. Such equal distribution of cations and anions supports the assumption that diffusion was effective as driving force.*

In fact these arguments can be rebutted based on the results presented in this study as well as by a detailed analysis of the experiments illustrated in [1-3]. The absence of any colouration during sample exposure in inert atmosphere (argument 1 and 2) is not suited to prove the absence of a galvanic cell. It just indicates that the oxygen current density is strongly reduced and that corrosive processes occur at decelerated rate, so that the necessary amount of hydroxide and Fe^{2+} may be too small to be detected with a pH-indicator or a complexing agent. Argument 3, the applicability of the ohmic potential drop as differentiating factor between diffusive and electrochemically determined ion transport was already disproven in section 3.2.3.2. Argument 4 is also not valid. The Auger Electron spectrum displayed in Fig. 3.24 was published in [3] and indeed indicates a presence of chlorine within the area of interfacial ion transport. The Cl : Na intensity ratio can be roughly estimated to vary around 1 : 1.5, but has to be corrected by sensitivity factors for quantification. According to [8], the sensitivity factor for sodium is about 0.3, for chlorine between 6.5 and 12, depending on the acceleration voltage during measurement. The number of species can be simply calculated by dividing the Auger intensity through the respective sensitivity factors [8]. The resulting quantitative ratio of Cl : Na in this case is around 1 : 50.

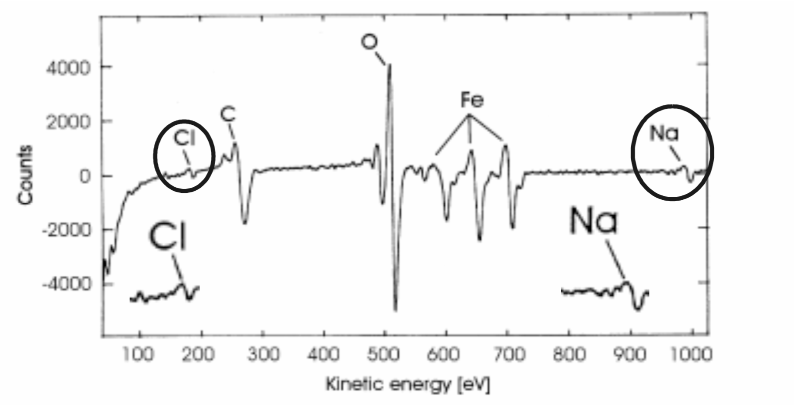

Fig. 3.24: Auger spectrum of the interfacial elementary distribution after ion transport in inert atmosphere. A polymer coated iron sample was applied with NaCl solution as defect electrolyte. The selected diagram represents Fig. 5 of publication [3]. Chlorine and sodium signals are marked and enlarged.

So obviously the spectrum of Fig. 3.24 rather supports the assumption of a preferential cation transport at the polymer/iron oxide/iron interface in humid nitrogen atmosphere than the expectance of a dominating ion diffusion process. As Auger Electron Spectroscopy (AES) is an extremely surface sensitive method, it cannot be excluded that the chloride signal of the spectrum in Fig. 3.24 has to be attributed to a basic contamination level, as it was also detectable by ToF-SIMS (see section 3.1.3.3).

3.2.3.5 Discussion of electrostatic and electrokinetic contributions to ion transport processes

It could be shown that results gained from studies of ion transport mechanisms on uncovered zinc/zinc oxide and iron/iron oxide substrates can be directly compared to those of the corresponding polymer/oxide/metal interfaces. The absence of any ion transport on oxide covered zinc in inert atmosphere does not seem to be dependent on the choice of the substrate material and thus the electrode potential in the defect (compare Fig. 3.17 and Fig. 3.23). A change of the potential levels to a defect potential more cathodic than that one of the uncovered zinc oxide surface does not effectively influence ion transport processes, either. Selective cation movement along iron oxide requires an accumulation of negative charge near or at the oxide surface within the adsorbed water layer. For zinc oxide no such positive or negative charge accumulation seems to be effective in inert atmosphere. According to Leng et al. [1-3] the Volta-potential of polymer coated iron/iron oxide interfaces is anodically shifted due to initial oxygen reduction in air. Fig. 3.18b proves a comparable potential level for uncovered iron substrates. Oxygen reduction leads to the formation of hydroxide ions at the surface, whereas the corresponding oxide oxidation is self-inhibiting due to a depletion of donor states [1]. This results in a high anodic overpotential with an initial base amount of OH^- at steady state condition. It may be regarded as origin of the electric field affecting cations from the defect to move along the interface.

In inert atmosphere this steady state amount of OH^- on oxide covered iron surfaces either will not be removed or continuously re-generated. It is assumed that during purging the SKP chamber with humid nitrogen the atmospheric oxygen partial pressure will not decrease down to zero. At oxide covered iron electrodes this residual O_2 amount may still promote a low-level, but continuous reduction reaction to keep up the ion exchange between defect and local cathode. In this respect, the situations with and without applied polymer film are similar.

For iron surface areas not electrolytically connected to the defect, removal of negative hydroxide excess charge in inert atmosphere requires a local reduction of Fe^{3+} states within the interfacial iron oxide. However, this process is hindered by the necessary change in the oxide structure [3, 9-13]. Consequently, a static negatively charged layer of adsorbed hydroxide ions at the surface is plausible to assume for inert atmosphere.

Based on the fact that oxygen reduction at oxide covered zinc electrodes is kinetically hindered compared to oxide covered iron electrodes [14-16], a strong decline of the O_2 partial pressure in inert atmosphere may effectively inhibit the oxygen reduction on zinc even without an applied polymer film. Moreover the ZnO wurtzite structure allows structural adaptation to the atmospheric oxygen partial pressure via free interstitials in the lattice [17] when conductively connected to metallic Zn. At very low oxygen partial pressure vacancies in the oxygen sub-lattice near the surface may be compensated by hydroxide inclusion. This results in a decreased charge density in the interface region at or within the adsorbed water layer. Consequently the accumulation of hydroxide ions at the zinc oxide surface will be distinctly reduced in inert atmosphere, so that no significant negative charge is established.

Also electrokinetic effects may be discussed as contributions to the observed different ion transport processes along iron oxide and zinc oxide surfaces in inert atmosphere. Neufeld et al. [18] found a deceleration of electrolyte spreading on zinc oxide surfaces in air with increasing amount of generated carbonate within the liquid layer. The stronger the surface alkalinisation caused by hydroxide ion formation, the more atmospheric CO_2 should dissolve to the liquid and react to carbonate ions. Therefore it was concluded that an electrolyte transport from a droplet is also strongly influenced by surface tension effects caused by changes of the ionic composition at the droplet edges. Chen et al. [19, 20] extended these studies to copper oxide surfaces and also specified the kinetic model for droplet spreading along zinc substrates in air. The pH reducing effect of carbonate formation closer to the point of zero surface charge within the spreading zone should be correlated with an increase of the oxide/electrolyte interface tension. This should result in higher activation energy for hydrated ion transport at the surface. Similar conditions should be discussed for ion transport along zinc and iron oxide in an atmosphere of purified nitrogen with strongly reduced O_2 and CO_2 partial pressures. Cation transport along iron substrates should occur at decreased hydroxide formation and pH; carbon dioxide dissolution within the electrolyte film should play an insignificant role in this case. The isoelectric points (IEP) of both substrates amount to pH 8.8-9 for ZnO [20, 21] and pH 7.8-8 for Fe(III) hydroxides and hydrous oxides [22]. In comparison to ZnO a higher negative hydroxide charge density at the electrolyte/iron oxide interface can be assumed as the oxygen reduction is less inhibited (see above). This consequently should also lead to a larger difference between surface pH and IEP, lower the electrolyte/iron oxide interface tension and promote an electrolyte layer spreading. For ZnO the difference between IEP and electrolyte/zinc oxide interface pH is expected to be distinctly smaller, also because the IEP was found to be more in the alkaline region. As a result, the respective interface tension should be increased and electrolyte spreading will be less probable.

Hydrated ion transport processes along polymer/oxide/metal-interfaces in inert atmosphere within an ultra-thin liquid layer may be similarly influenced by comparable differences in the respective electrolyte/zinc oxide and iron oxide interface tensions. Indeed it can be assumed that the polymer structure near the oxide surface will not be the same for iron and zinc oxide substrates. Therefore also the electrolyte/polymer interface tensions may differ. But as the ion transport mechanisms for polymer and non polymer covered iron and zinc substrates seem to be comparable, it is expected that this parameter may influence the process velocity, but does not seem to change the overall ion transport mechanism, anyhow.

Based on the presented results also the commonly accepted model for cathodic delamination at a polymer/substrate interface should be modified concerning the aspect how an electrolytic conductive connection is established between defect area (anode) and interface section beyond the electrolyte front position. Hydrated cations are attracted by an interface that contains negative surface excess charge. An electrolytic coupling element between the locally separated electrodes will be established leading to oxidative and hydrolytic degradation of the polymer/oxide/metal interface. Increased local interfacial hydroxide concentrations caused by oxygen reduction accelerate the ion transport due to the presence of electrostatic fields in humid air and the decrease of the electrolyte/substrate interface tension, whereas diffusion seems to play an insignificant role.

3.2.4. Conclusions

Results gained from studies of ion transport mechanisms on uncovered zinc/zinc oxide and iron/iron oxide substrates can be directly compared to those of the corresponding polymer/oxide/metal interfaces. The absence of any ion transport on oxide covered zinc in inert atmosphere does not seem to be dependent on the choice of the substrate material and thus the electrode potential in the defect. Selective cation movement along iron oxide requires an accumulation of negative charge near or at the oxide surface within the adsorbed water layer. Reduction of oxygen as residual gas in the nitrogen purged chamber of the Scanning Kelvin Probe leads to the formation of hydroxide ions at the surface. For oxide covered iron substrates it may be regarded as origin of the electric field affecting cations from the defect to move along the interface. A reduction of the negative oxide surface charge density by structural crystallographic lattice adaptation seems to be excluded for the various iron oxide structures. Electrokinetic effects may result in a decrease of the electrolyte/iron oxide interface tension and promote an electrolyte spreading as well.

For oxide covered zinc surfaces it is assumed that no negative surface charge is created when the chamber of the Scanning Kelvin Probe is purged with humid nitrogen. This assumption is based on the kinetically hindered oxygen reduction and the possible structural adaptation of the ZnO wurtzite structure. It can explain why no transport of ions is observed in atmospheres of extremely small oxygen partial pressures.

Under the conditions of cathodic delamination at high oxygen partial pressures interfacial hydroxide formation caused by oxygen reduction also determines the ion transport at polymer/oxide/metal interfaces.

3.2.5 References

[1] A. Leng, H. Streckel, M. Stratmann, Corr. Sci. 41 (1999) 547.
[2] A. Leng, H. Streckel, M. Stratmann, Corr. Sci. 41 (1999) 579.
[3] A. Leng, H. Streckel, K. Hofmann, M. Stratmann, Corr. Sci. 41 (1999) 599.
[4] W. Fürbeth, M. Stratmann, Corr. Sci. 43 (2001) 207.
[5] W. Fürbeth, M. Stratmann, Corr. Sci. 43 (2001) 229.
[6] W. Fürbeth, M. Stratmann, Corr. Sci. 43 (2001) 243.
[7] K. Wapner, M. Stratmann, G. Grundmeier, Electrochim. Acta 51 (2006) 3303.
[8] K.D. Childs et al., C.L. Hedberg (Ed.), Handbook of Auger Electron Spectroscopy, Third Edition, published by Physical Electronics Inc., Minnesota, 1995; p. 17 and p. 404.
[9] M. Stratmann, K. Bohnenkamp, H.-J. Engell, Corr. Sci. 23 (1983) 969.
[10] M. Stratmann, K. Bohnenkamp, H.-J. Engell, Werkstoffe und Korrosion 34 (1983) 604.
[11] M. Stratmann, K. Hoffmann, Corr. Sci. 29 (1989) 1329.
[12] M. Stratmann, Ber. Bunsenges. Phys. Chem. 94 (1990) 626.
[13] K. Hoffmann, M. Stratmann, Corr. Sci. 34 (1993) 1625.
[14] H. Dafydd, D.A. Worsley, H.N. McMurray, Corr. Sci. 47 (2005) 3006-3018.
[15] H.S. Wroblowa, S.B. Qaderi, J. Electroanal. Chem. 279 (1990) 231.
[16] V. Jovancicevic, J.O`M. Bockris, J. Electrochem. Soc. 133 (9) (1987) 1797.
[17] X.G. Zhang, Corrosion and Electrochemistry of Zinc, Plenum Press, New York, 1996.
[18] A.K. Neufeld, I.S. Cole, A.M. Bond, S.A. Furman, Corr. Sci. 44 (2002) 555.
[19] Z.Y. Chen, D. Persson, C. Leygraf, Corr. Sci. 50 (2008) 111.
[20] Z.Y. Chen, D. Persson, A. Nazarov, S. Zakipour, D. Thierry, C. Leygraf, J. Electrochem. Soc. 152 (9) (2005) B342.
[21] M. Valtiner, S. Borodin, G. Grundmeier, Langmuir 24 (2008), 5350.
[22] M. Kosmulski, Colloid and Surfaces A, 222 (2003) 113.

3.3 In-situ electrochemical Scanning Kelvin Probe Blister Test studies of the de-adhesion kinetics at polymer/zinc oxide/zinc-interfaces

3.3.1 Fundamentals

Within sections 3.1 and 3.2 it could be proven in detail that ion diffusion along a polymer/oxide/metal interface is not macroscopically effective, neither for ion transport processes in humid inert atmosphere, nor during corrosive delamination in humid air. The velocity of interfacial ion ingress in fact seems to be electrostatically driven and consequently has to be related to the electrochemical activity of the respective polymer/substrate interface structure. Its properties will strongly depend on the interfacial water amount, as H_2O is needed to stabilise transported ions by a hydrate shell [1-2]. Water also affects the electric double layer structure at the oxide surface and interacts with functionalities of adsorbed organic molecules [3-4]. The knowledge about the dependency of cathodic delamination on parameters such as the interfacial water activity therefore is of crucial importance for the prospective design of interfaces with improved stability towards corrosion.

Especially wet or chemical de-adhesion is mainly determined by the water amount at the interface since adsorbed interfacial H_2O leads to a substitution of polymeric binder which is adhering to the oxide surface via secondary forces [5-6]. Moreover, a significant water uptake of the polymer film leads to plastification and thereby to an increased energy consumption during mechanical de-adhesion. However, the loss of adhesion strength at the interface most often dominates the overall adhesion of the composite [7-11].

Starting from defects filled with aqueous electrolytes water can penetrate the organic film along the polymer/substrate interphase region. In humid atmospheres H_2O molecules will also diffuse through the organic bulk structure ingressing from the polymer/air interface. Both sources of water will affect the water activity at the front of the electrochemical de-adhesion processes.

Especially adhesives but also organic coatings are mechanically stressed either during usage (e.g. load bearing adhesive joints) or during the corrosion process it-self (e.g. blistering, filiform corrosion, etc.). Wapner et al. therefore developed a Scanning Kelvin Probe Blister-Test (SKP-BT) set-up to superimpose and study mechanical load on a polymer/oxide/metal interphase under corrosive conditions [4, 12-13].

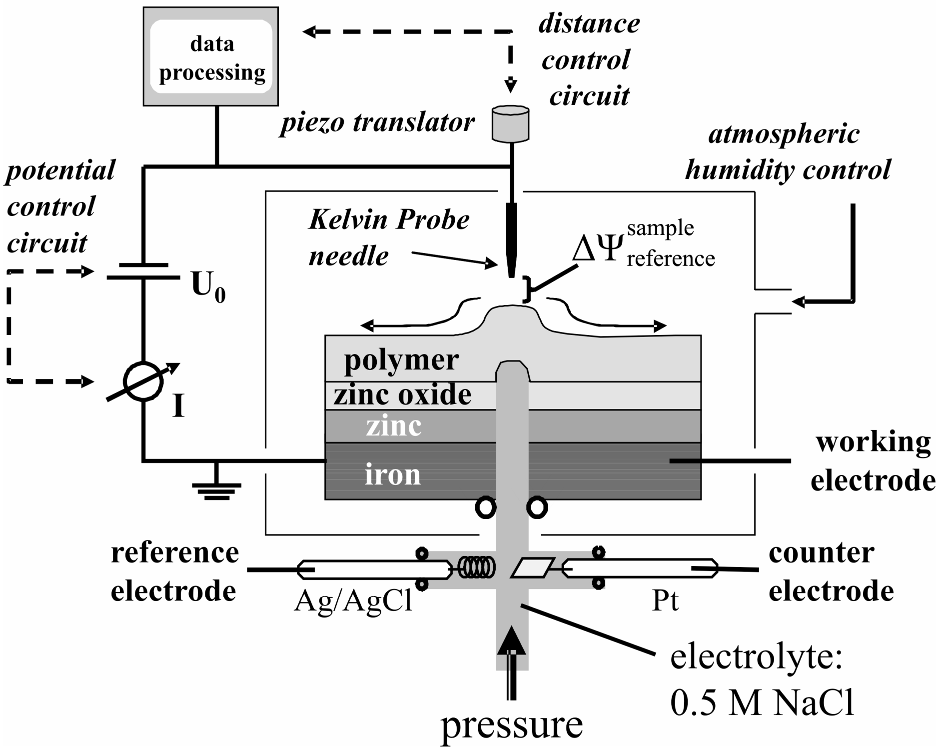

Fig. 3.25: Schematic overview of the pressurised and polarisable Scanning Kelvin Probe Blister-Test (SKP-BT) set-up. For details concerning height regulation and measurement principle see [12].

A partially freestanding adhesive film above a substrate hole was pressurised from the back side. With the chosen set-up bulging and blister growing should occur once the fracture energy of the adhesive is exceeded during interfacial corrosive attack. The process was compared to a peel test measurement at changing angles with respect to previous studies of the pressurised Blister Test [12, 14-23]. For the studies presented in this section the experimental approach was extended to a SKP-BT with polarisable metal working electrode to ensure constant and comparable electrochemical conditions for the corrosive processes within the defect area. Therefore a reference and counter electrode were immersed into the alkali halide solution and connected to a potentiostat. A schematic overview of the SKP-BT setup is shown in Fig. 3.25.

Attenuated Total Reflection Infrared Spectroscopy (ATR-IR) is especially sensitive to the relative water amount within the polymeric interphase on an ATR-crystal [24-28]. Within the here presented studies the technique was applied for an evaluation of the diffusion kinetics and saturation levels of water within the polymer matrix at different atmospheric moisture level. The results were compared to peel-off tests of the applied adhesive film at varying relative humidity to support the presented synergistic approach for fundamental investigations of corrosive and mechanic deformation and degradation processes at polymer/oxide/metal interfaces.

3.3.2 Experimental procedures

3.3.2.1 Application of polymeric films

A hot-curing two component epoxy-amine resin with a thickness of 150 μm was used (thickness control by a Surfix analyser, Phynix company, Cologne / Germany); see also section 3.1.2.1. It was applied on the substrate in dry nitrogen atmosphere after degassing and hardened for one hour at 120 °C with a pressure of 50 g/cm^2 [4,12,24]. Prior to the SKP-experiments, the sample was exposed to humid air (> 95 % r. h.) for 1 h at 40 °C to remove electrostatic charging from the polymer.

3.3.2.2 Substrates

Iron sheets, covered with an approx. 8 μm thick electrogalvanised zinc layer (received from voestalpine Stahl GmbH, Linz / Austria), were solvent and alkaline cleaned, then rinsed with water and dried as described in section 3.1.2.2. For SKP-BT experiments a circular hole of 1 mm diameter was prepared from the backside of the metal sample (4 x 4 cm) to the adhesive layer by a milling and chemical etching process. This procedure led to an undamaged adhesive film above the hole [12-13].

N-type silicon ATR crystals with base trapezoidal angles of 45° were cleaned with a 1:1 in volume hydrogen peroxide/ammonium hydroxide solution mixture. They were subsequently rinsed with ultra-pure water, dried in a nitrogen stream and coated with epoxy amine at the same layer thickness as applied for the SKP-BT experiments.

3.3.2.3 Analytical methods

SKP measurements were executed with a custom made Scanning Kelvin Probe [12]. The hole in the Blister Test samples was filled with 0.5 molar NaCl solution, then the sheets were fixed on the sample carrier. The defect area could be polarised in a three-electrode arrangement with a platinum counter electrode, Ag/AgCl reference electrode and grounded Blister-Test sample as working electrode applying an EG&G Potentiostat/Galvanostat, model 273 A (Princeton Applied Research, Oak Ridge/USA). For pressurisation a Low ΔP-Flow pressure meter/controller (Bronkhorst Mättig GmbH, Germany) via vessel was used. To adjust 97 % ± 1.0 % relative humidity (r.h.) and 82 % ± 1.5 % r.h. at 23.0 °C ± 0.5 °C within the SKP chamber a humidified air flow from water filled fritted gas wash bottles was mixed with dry air, if necessary. Delamination rates presented within section 3.3 are mean values calculated from several measurements. If not otherwise noted a basic cathodic polarisation of around 100 mV vs. open circuit potential (OCP) always to the same fixed value of $\approx -860\ \mathrm{mV_{SHE}}$ was applied to receive comparable electrochemical conditions for the corrosive processes within the defect area.

FTIR-ATR experiments were performed with a BioRad FTIR 3000 Spectrometer (Digilab, Germany), equipped with a MIR globar source, a DTGS detector and an internal reflection unit of Specac Ltd. (England). 148 interferograms were taken at room temperature with a spectral resolution of 4 $\mathrm{cm^{-1}}$. Reference spectra were recorded in dry nitrogen atmosphere before purging the gas volume above the adhesive with nitrogen at adjusted relative humidity, in-situ controlled by a Hygroflex/Hygroclip sensor (rotronic GmbH, Germany) at 22.9 ± 0.5°C. The change of the $\nu_{(H\text{-}O)}$ peak area was evaluated as a function of time [24].

Peel tests were performed at constant angle perpendicular to the sample surface and constant 3.4 mm/min velocity. Custom made equipment was applied [29-30]; stripes of 5 mm width were peeled off at different relative atmospheric humidity and at a temperature of 22.5 ± 0.5 °C.

3.3.3 Experimental results

3.3.3.1 Oxidative de-adhesion at 97 % and 82 % relative humidity

Leidheiser et al. [1] and later Leng et al. [2] proved that the progress velocity of the cathodic de-adhesion process rises with increasing hydrodynamic radii of the alkali cations. It was concluded that completely hydrated ions are transported along a polymer/oxide/metal interface. Wapner et al. [24] also reported this for ion transport studies in inert atmosphere with strongly reduced oxygen partial pressure. Therefore it should be expected that ion movement along a polymer/substrate interface requires a certain interphasial water activity. Under corrosive conditions this water amount can be transported together with the cations from an electrolyte filled defect forming a thin electrolyte layer between this area and the front of oxidative de-adhesion. However, in the case of wet de-adhesion the substitution of secondary forces between polymer and oxide by adsorbed water molecules already occurs after water diffusion through the polymer matrix to the interface without the requirement of lateral interfacial ion transport [5-6].

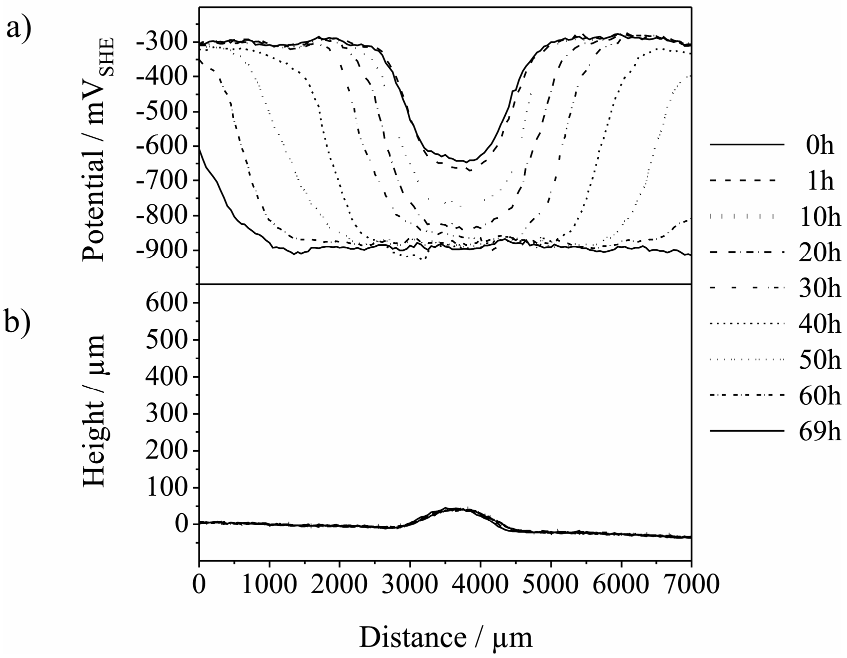

Fig. 3.26: SKP-BT corrosive de-adhesion study of an epoxy amine/zinc oxide/zinc interface at 100 mbar electrolyte pressurisation and 97 % r.h. a) SKP potential profiles. Mean delamination progress: 42 ± 1 µm/h. b) Topography of the adhesive film.

To distinguish the sources and effects of the interfacial water activity for corrosive delamination, the Scanning Kelvin Probe Blister-Test (SKP-BT) offers access to experiments at different relative humidity of the surrounding atmosphere for constant defect conditions. The partly freestanding adhesive film above the substrate hole (see Fig. 3.25) preserves the defect electrolyte composition during the change of the relative humidity above the polymer films.

Fig. 3.26 presents an SKP-BT de-adhesion study with an epoxy amine layer on zinc coated steel at a relative air humidity of 97 %. An excess electrolyte pressure of 100 mbar was applied. The topography of the adhesive film above the blister and the neighbouring region as well as the development of the two dimensional potential profiles are shown for comparison of the microscopic de-adhesion and interfacial reaction zones. The interface potential of the coated area of approximately -300 mV_{SHE} is typical for polymer coated zinc oxide/zinc interfaces [31]. The defect electrolyte is in contact to both zinc coating and the steel substrate due to the chosen sample design (see Fig. 3.25). The zinc corrosion potential determines the free corrosion potential within the defect area as measured by the SKP. With an additional cathodic polarisation of around -100 mV vs. OCP the stationary defect potential is around -900 mV_{SHE}. A broadening of the potential valley at a nearly constant linear rate was observed. This progress of the front of the potential gradient could be assigned to a cathodic de-adhesion process starting from the defect area; Fürbeth et al. also reported a combined cathodic/anodic delamination mechanism on zinc/zinc oxide [31]. Once an electrolytic connection to the defect is established, the kinetic barrier for oxygen reduction within this interface section diminishes and the interface potential is shifted towards the defect potential. The diffusion of oxygen through the polymer matrix ensures a sufficient concentration for a continuous interfacial oxygen reduction process. Calculating the lateral displacement of the turning points in the SKP potential profiles of Fig. 3.26 and reproduction measurements led to an averaged cathodic de-adhesion progress of 42 μm/h ± 1 μm/h (standard error). The topography scans of Fig. 3.26 reveal that an electrolyte overpressure of 100 mbar caused only a slight bulging of the adhesive film during the measurements. De-adhesion along the delaminated area is likely to be assumed, but premature damaging of the interface area beyond the expected electrolyte front position cannot be monitored with the SKP.

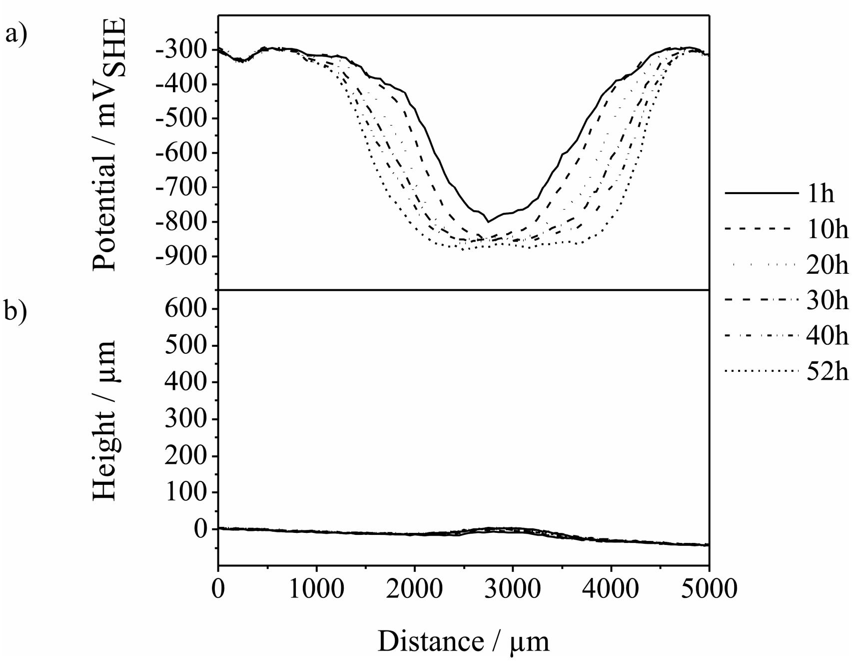

Fig. 3.27: SKP-BT corrosive de-adhesion study of an epoxy amine/zinc oxide/zinc interface at 100 mbar electrolyte pressurisation and 82 % r.h. a) SKP potential profiles. Mean rate of de-adhesion: 14 ± 2 µm/h. b) Topography of the adhesive film.

The experiment was repeated at 82 % relative humidity above the blister. Fig. 3.27 presents the received SKP potential profiles and development of the adhesive topography. The potential difference between defect and coated area was nearly identical to that one detected for 96% r.h. (compare Fig. 3.26). According to Leng et al. [29] this should point at comparable driving forces for cathodic delamination. Nevertheless, the broadening of the potential valley appears to be strongly decelerated. A detailed analysis of the potential profiles led to a progress rate of the cathodic delamination process of only 14 ± 2 µm/h. This can be explained by the reduced water partial pressure in the surrounding atmosphere. Several factors may contribute to the observed deceleration of the de-adhesion kinetics. A decreased water amount in the gas atmosphere should also lead to a decreased water saturation level within the adhesive film and within the interphase region. This should influence the viscoelastic properties of the polymer layer as well as the static water saturation level at the intact interface prior to a lateral ingress of hydrated ions. Moreover the value of the electrolytic resistance in the delaminated area should be increasing with a decreasing amount of interfacial water. Leng et al. and Grundmeier et al. [2, 32] discuss the formation of a thin water layer and/or a water enriched, gel-like polymer structure within the area of initial cathodic de-adhesion.

To equilibrate the reduced water partial pressure in a gas atmosphere of lower humidity, water will evaporate from the polymer matrix. For compensation, laterally transported water along the polymer/substrate interface will continuously diffuse from the delaminated area into the polymer matrix. The resulting reduced interfacial water activity will increase the interfacial concentrations of Na^+_{aq} and OH^-_{aq}. Consequently the ion mobility will be reduced due to larger retarding forces such as electrophoretic effects or Stokes friction. Necessary charge compensation between the local electrodes is impeded and less oxygen can be reduced at the delamination front position. This surely will end up with a decelerated delamination progress. Close to the defect these effects may play a minor role, as the increased electrolyte pressure should support a continuous supply with additional aqueous electrolyte.

If the interfacial water activity reaches a critical low value, it should converge more and more towards ice-like structures with a high degree of order. Mattmann et al. [33] investigated water adsorption isotherms on zinc oxide. He reported that for around 80 % r.h. two water monolayers will be strongly adsorbed on ZnO and that a change from 97 % r.h. to 82 % r.h. will lead to the evaporation of the additionally physisorbed liquid-like H_2O multilayers. Asay et al. [34] evaluated a surface coverage of three to four monolayer ice-like water on silicon oxide with a total layer thickness of around 16 Å at 82 % r.h. (at 21 °C). An atmospheric humidity decrease from 97 % r.h. to 82 % r.h. again resulted in a comparable liquid water layer thickness reduction by about 50 %. The diameter of hydrated sodium ions was evaluated to be around 3.5 Å [35], which is in the order of magnitude of two to three water layers [34]. A direct comparison to the respective conditions at the polymer/zinc oxide interface seems to be difficult; water adsorption sites should be at least partially saturated with polymer-to-substrate-interactions. Nevertheless, these values may illustrate that especially in the area where the polymer film starts to de-adhere the local water activity should have a strong influence on the local oxygen reduction kinetics.

3.3.3.2 Polymer water uptake at 97 % and 82 % relative humidity

To further evaluate the effect of atmospheric humidity on the interfacial polymer/substrate water amount, ATR-FTIR studies of the polymer water uptake were performed. Epoxy-amine layers were applied on a Si-ATR crystal and exposed to nitrogen atmosphere of 82 % r.h. and 97 % r.h. The peak intensity change of the asymmetric stretching vibration mode of water between 3620 cm^{-1} and 3060 cm^{-1} was detected as a function of time (see Fig. 3.28 - Fig. 3.30). It was assumed that the contribution of the underlying N-H stretching bond should be nearly constant. For further details of the set-up and the analysis of the spectra it is referred to the publications of Vlasak et al. and Wapner et al. [24, 36].

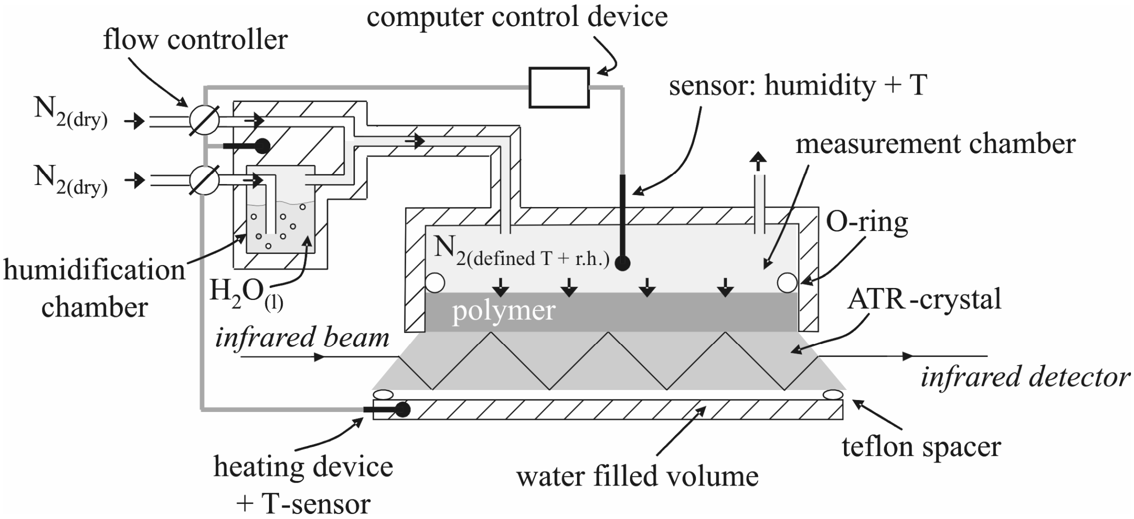

Fig. 3.28: Schematic illustration of the experimental ATR-infrared spectroscopy set up. The computer continuously compared temperature (T) and relative humidity (r.h.) within the measurement chamber to preset values and adjusted the mixture ratio of dry and water saturated N_2 via the flow controllers. The total gas flow was kept constant. Local temperature fluctuations were avoided by encasing measurement chamber, gas supply tubes, humidification chamber and gas mixture area by tempered water.

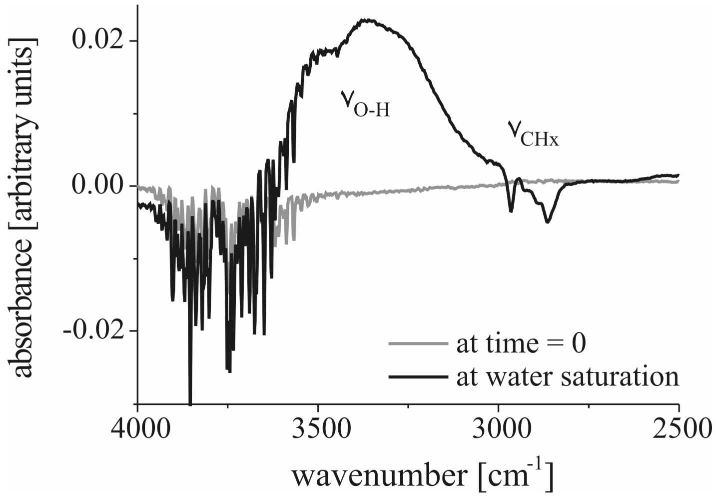

Fig. 3.29: ATR-IR spectrum of the ν_{O-H} stretching vibration, recorded before exposure to humid atmosphere and after the interfacial water activity reached a saturation level.

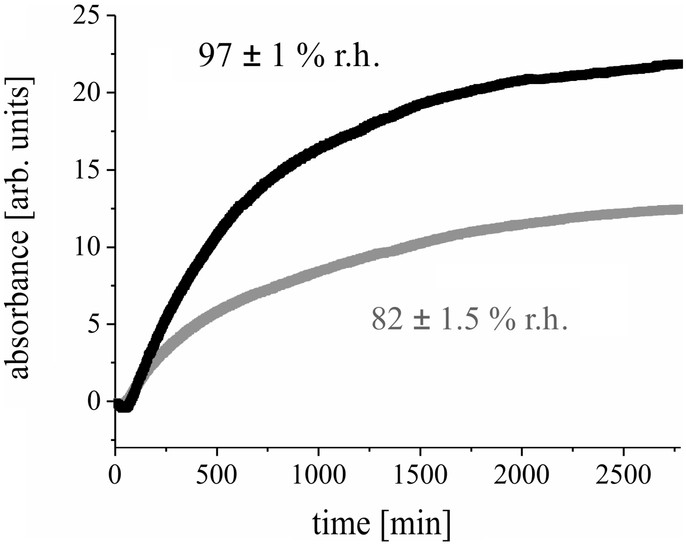

Fig. 3.30: Development of the $\nu_{(H\text{-}O)}$ peak intensity with time detected with ATR-FTIR (between 3620 cm^{-1} and 3060 cm^{-1}). An epoxy-amine layer was applied on a silicon ATR-crystal and exposed to humid nitrogen atmosphere. Mean saturation absorbance at 97 % r.h.: 20.7 ± 1.2 (standard error). Mean saturation absorbance at 82 % r.h.: 11.8 ± 1.3.

Because of the limited interfacial IR-penetration depth of around 246 nm at 3490 cm^{-1} [36] an increase of the $\nu_{(H\text{-}O)}$ intensity starts retarded. After adjustment of the respective atmospheric humidity it took around one hour until a first increase of the water activity could be detected due to H_2O diffusion through the polymer matrix. The higher the adjusted atmospheric humidity, the faster the resulting $\nu_{(H\text{-}O)}$ intensity increase and the higher the respective absorbance saturation level at longer time scales. With respect to the maximum peak areas the mean interfacial saturation water amount at 82 % r.h. was reduced by about 50 % in comparison to the amount at 97 % r.h, which is in the same order of magnitude as for the respective reduction of the water layer thickness on oxide covered Si [34]. For the polymer coated passive silicon substrate the sum of adsorbed interfacial water and the amount of H_2O within the polymer interphase contribute to the detected $\nu_{(H\text{-}O)}$ peak intensity. The observed de-adhesion rates presented with Fig. 3.26 and Fig. 3.27 reveal a reduction by a factor of three when changing from 97 % r.h. to 82 % r.h

3.3.3.3 Adhesion forces at different relative humidity

As not only the electrochemical processes but also the adhesion forces should be affected by a change in the interphasial amount of water, peel-off experiments at

82 % r.h. and 97 % r.h. were performed. After zinc/zinc oxide surfaces were coated with the adhesive film and exposed to the respective humid atmosphere the polymer was orthogonally peeled off with constant velocity. Fig. 3.31 shows a comparison between the detected forces.

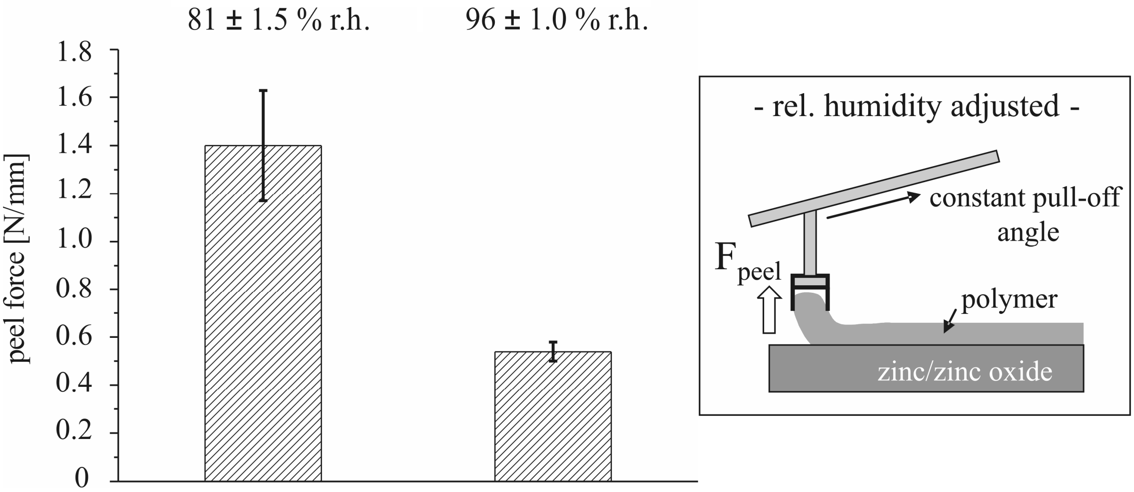

Fig. 3.31: Peel-off forces of epoxy amine layers adhered on zinc/zinc oxide substrates measured at ambient temperature for different relative humidity.

Compared to averaged peel forces of 1.4 ± 0.2 N/mm (standard error) at 81 % r. h. the force decreased to a value of 0.42 ± 0.04 N/mm at 96 % r. h. As the binding energy of oxide/water interactions generally should be higher, adsorbed H_2O molecules can replace the adhesive [5, 24]. H_2O is also known to act as softener for epoxy amine resins and therefore will affect the elastic properties and plastification [24]. Based on the lower adhesion forces at high relative humidity a continuous peeling of the polymer layer was observed, whereas for the lower moisture level of 82 % r.h. solely a stepwise peeling occurred in sections of typically 0.8 mm after around 1.5-fold elongation. The adhesive layer remained intact, but a sinusoidal alternation of the force/time graph resulted in rupture events at maximum force displayed in Fig. 3.31. No polymer residuals were found on the ZnO surface after peeling even at 82 % r.h.. However, submonolayer quantities of degradation products generated during humid exposure could not be excluded. The geometrical conditions of blister-test and peel-test certainly differ. A direct correlation between these methods therefore seems to be difficult, but indirect conclusions may be drawn. Relative differences in the delamination progress rates (see Fig. 3.26 and 3.27), peel-forces (Fig. 3.31) and interfacial water activities

(Fig. 3.30) for 96/97 % and 81/82 % r.h. surprisingly occur in the same order of magnitude, as they vary between a factor of two to three.

Wielant et al. ([37], see also section 3.4) investigated a set of four iron oxides coated with polyurethane and therefore applied other substrates, coatings and experimental conditions. Nevertheless it was found that relative peel-force differences are directly correlated to variations within cathodic delamination rates. The determination of surface energies clearly confirmed that these peel-force variations originate from the substrate structure and therefore can be attributed to the polymer/substrate interface ([37] and section 3.4). In this context the above mentioned analogy of interfacial water activity, SKP-BT- and peel-test results does not seem to occur fortuitous. It can be suggested that peel forces obviously visibly reflect varying interfacial water activities, which themselves determine the initial chemical conditions at the ZnO/epoxy amine interface. Adjustment of the interface structure to different atmospheric humidity consequently will be kept when electrochemical degradation is initiated. As a result the velocity of cathodic delamination obviously comparably responds to such relative changes of the adhesion forces, although a simple linear dependency cannot be postulated due to the complex interfacial corrosion processes.

It is the question whether the significance of peel-force variations is not underestimated for certain experimental conditions. Taking them into account a rough estimation of relative changes within the electrochemical de-adhesion progress does not seem to be inappropriate.

3.3.3.4 Effect of electrolyte pressure on the de-adhesion rate at different relative humidity

A more detailed investigation was intended to study the influence of mechanical stress applied to the polymer layer and the adhesive/substrate interface during cathodic delamination. SKP-BT experiments were carried out similarly to those presented in Fig. 3.26 and Fig. 3.27. But as an additional parameter now also an increased electrolyte pressure was adjusted. Fig. 3.32 and 3.33 present the resulting potential profiles and topography scans for 500 mbar overpressure at 97 % r. h. and 82 % r. h. . Fig. 3.32 confirms that at high atmospheric humidity the delamination progress indeed is accelerated. A velocity of $87 \pm 8\,\mu$m/h was observed which roughly corresponds to a doubled rate compared to an electrolyte overpressure of 100 mbar (see Fig. 3.26).

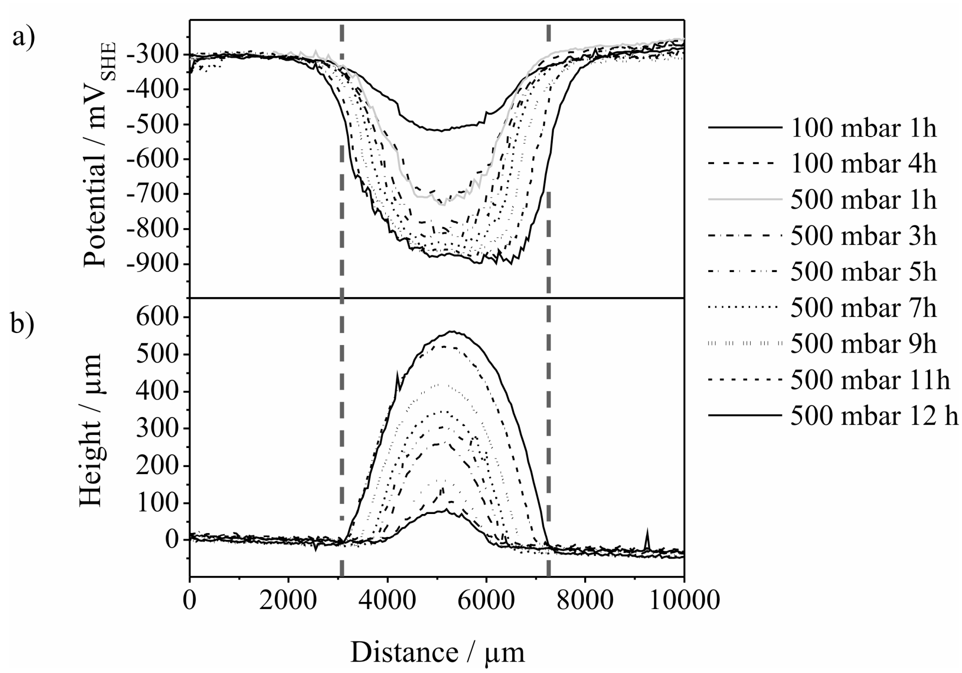

Fig. 3.32: SKP-BT corrosive de-adhesion study of an epoxy amine/zinc oxide/zinc interface at 500 mbar electrolyte pressure and 97 % r.h. a) SKP potential profiles. Mean delamination progress: 87 ± 8 µm/h. b) Topography of the adhesive film.

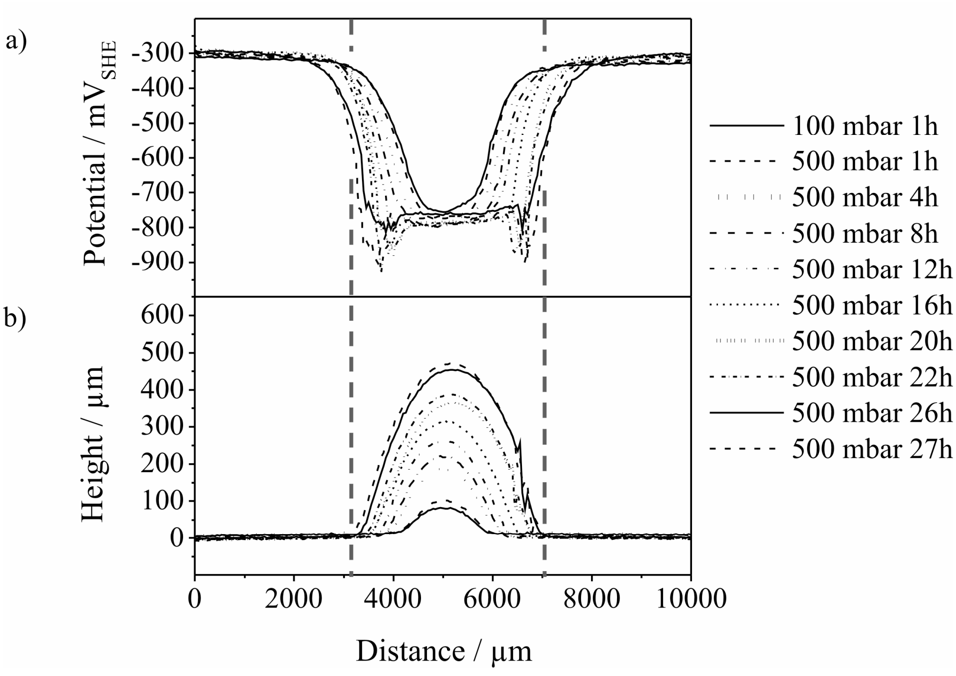

Fig. 3.33: SKP-BT corrosive de-adhesion study of an epoxy amine/zinc oxide/zinc interface at 500 mbar electrolyte pressure and 82 % r.h. a) SKP potential profiles. Mean delamination progress: 40 ± 6 µm/h. b) Topography of the adhesive film.

The blister formed by the adhesive film at 500 mbar and 97 % r.h. (see Fig. 3.32b) increased with the exposure to the mechanical and corrosive load. In contrast to Fig. 3.27b where almost no change in topography could be detected, now a tremendous bulging of the surface occurred up to 500 μm in height. Moreover, in parallel to the electrochemical interfacial degradation the blister grew in diameter, which means that the respective interface section was completely de-adhered from the oxide covered zinc substrate. During the whole measurement blister edge and electrolyte front position did not coincide. The vertical dashed lines in Fig. 3.32a and 3.32b support a comparison of delamination progress and blister growth exemplarily for the graphs recorded after 12 hours. Obviously, the adhesive/substrate interface potential decline preceded the mechanical lifting of the polymer film by about 1000 μm. It could be proven that interface potential detection and height regulation mode of the Scanning Kelvin Probe nearly exactly reach the same lateral resolution [12]. Consequently, electrochemical degradation of the interface seems to occur *before* increased electrolyte pressurisation results in macroscopic de-adhesion of the polymer film. Thus, electrochemical pre-damaging precedes the subsequent macroscopic mechanical degradation.

Several factors may contribute to the larger cathodic de-adhesion rate observed in this case. On the one hand the increased pressure leads to the formation of stress and strain in the polymer layer up to the zone where the delamination front is located. Stress release occurs by de-adhesion of the polymer film and the blister volume will be filled up with bulk electrolyte. The distance between blister edge and preceding front of electrochemical interface damaging is reduced and more or less constant because of a permanent blister broadening. Solely in this relatively small section interfacial oxygen reduction and therefore hydroxide formation has to be balanced by ion transport processes of Na^+_{aq} and OH^-_{aq} within a microscopic interfacial electrolyte layer. Charge compensation will be consequently supported and the electrochemical delamination is likely to be accelerated. On the other hand it can be assumed that a hydrostatic electrolyte overpressure of 500 mbar also leads to an increase of the pressure within the electrochemically pre-damaged zone. The thereby formed increased interfacial free volumes and nanoscopic interfacial cracks within the polymeric interphase and at the polymer/oxide interface could promote the ingress of ions and consequently accelerate the oxygen reduction kinetics in this region.

Comparison with Fig. 3.33 reveals similar potential profiles and topographic scans for the respective SKP-BT measurement at 82 % r. h. However, the measured de-adhesion rate of 40 ± 6 μm/h shows a deceleration by a factor of two in comparison to the atmosphere of high relative humidity. Again blister edge and electrolyte front position did not coincide during the whole measurement; electrochemical interface degradation was observed to run ahead of macroscopic de-adhesion. The lateral blister broadening again followed the corrosive de-adhesion progress constantly shifted. The vertical blister growth developed at same order of magnitude compared to that one illustrated in Fig. 3.32b, but the increase proceeded more slowly. At same electrolyte pressure the respectively reachable blister height consequently seems to be correlated to its lateral dimensions. This points at a similar polymer elasticity within the blister area for both experiments. Although additional water evaporates from the adhesive surface at lower atmospheric humidity, the comparably high electrolyte pressure continuously compensates the increased loss rate to ensure nearly static water content within the polymer film above the blister.

As already discussed for high relative humidity, the distance between bulk electrolyte in the defect area and the front of oxidative degradation is reduced and remains roughly constant due to continuous blister growth when working at high electrolyte pressures of 500 mbar. This supports the assumption that the applied mechanical load microscopically affects the area of initial electrochemical degradation. Consequently, the influence of reduced relative humidity seems to be mainly confined to this electrochemically pre-damaged zone rather than to the already bulk electrolyte filled blister area.

3.3.3.5 Influence of defect polarisation on the delamination rate

Fig. 3.34 presents potential profiles and topographic scans of a SKP-BT measurement with 100 mbar electrolyte pressure (at 97 % r.h.). It was started with a basic cathodic polarisation of -100 mV_{OCP} (which was also applied for the SKP-BT experiments already presented within this section 3.3; please consider section 3.3.2.3). After 21 hours, the potential of the working electrode was switched to -200 mV_{OCP}. The potential of the intact polymer/zinc oxide/zinc interface, detected by SKP, remained unaffected. Within the defect area the potential in fact cathodically shifted by only around additional 50 mV, resulting with an absolute value of at minimum -950 mV_{SHE} as illustrated by Fig. 3.34a. Nevertheless the delamination process occurred to be distinctly accelerated; an averaged progress rate of 174 ± 13 μm/h was reached. According to Leng et al. and Fürbeth et al. any additional cathodic polarisation of the electrolyte/substrate interface in defect and delaminated area should increase the cathodic current density of the galvanic element [2,29-31,38-39].

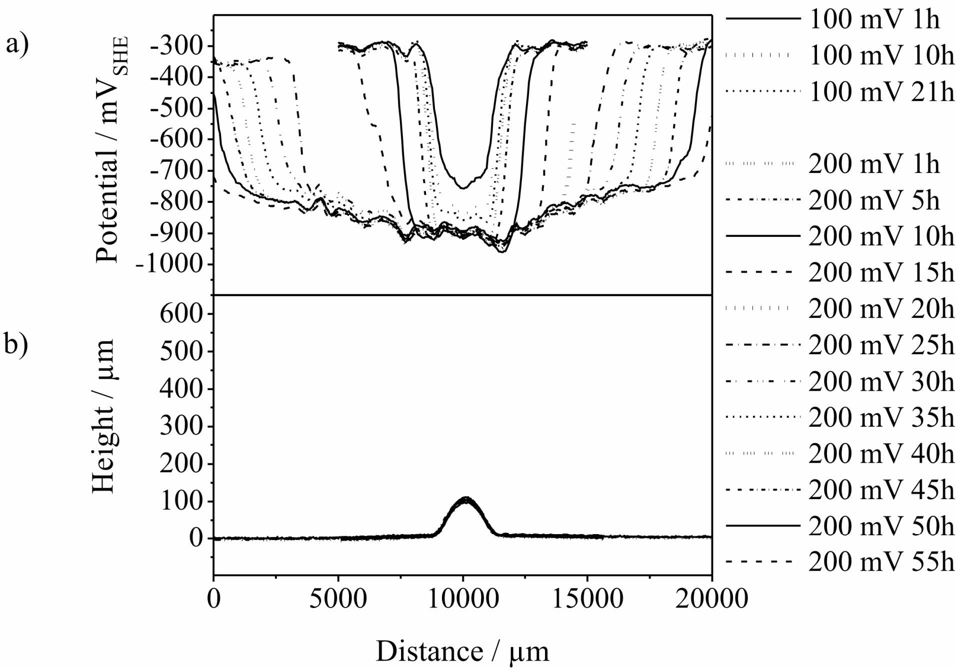

Fig. 3.34: SKP-BT corrosive de-adhesion study of an epoxy amine/zinc oxide/zinc interface at 100 mbar electrolyte pressure, 97 % r.h. and additional -100 mV cathodic polarisation of the defect. a) SKP potential profiles. Mean delamination progress: 174 ± 13 µm/h. b) Topography of the adhesive film.

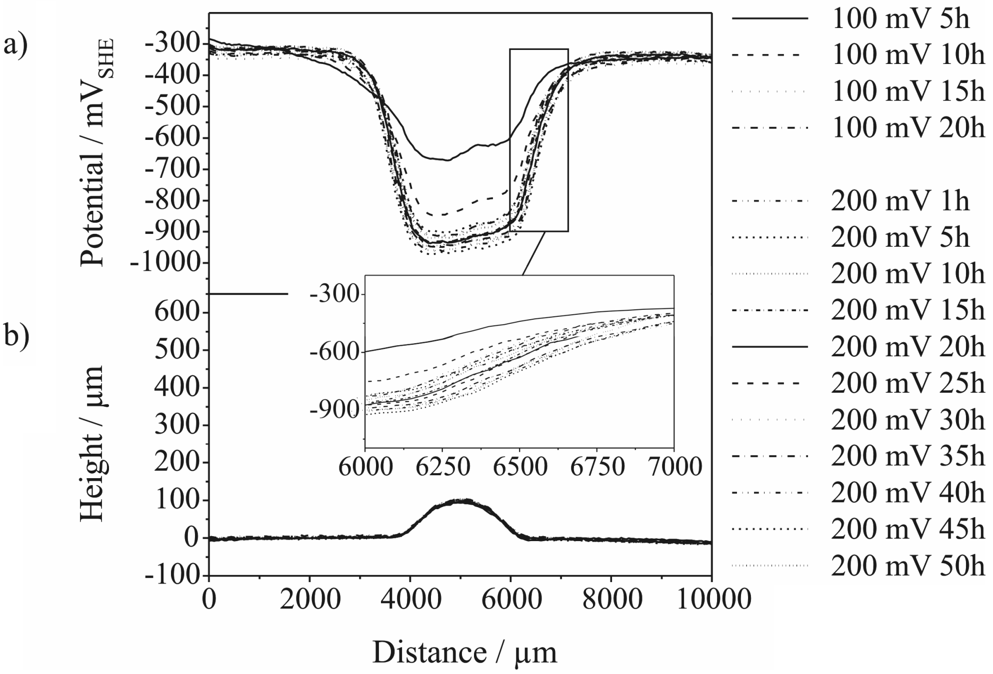

Fig. 3.35: SKP-BT corrosive de-adhesion study of an epoxy amine/zinc oxide/zinc interface at 100 mbar electrolyte pressure, 82 % r.h. and additional -100 mV cathodic polarisation of the defect. a) SKP potential profiles. Mean delamination progress: 6 ± 1 µm/h. b) Topography of the adhesive film.

As long as the O_2 diffusion limited maximum current density level is not reached, this is correlated to an accelerated oxygen reduction process which promotes the oxidative degradation of the interface due to increased hydroxide formation. Compared to the application of additional 400 mbar electrolyte pressure, cathodic interface polarisation obviously is an effective tool to affect cathodic delamination kinetics. This confirms the conclusions already drawn from analysis of Fig. 3.32 and Fig. 3.33. It was interpreted that electrochemical pre-damaging precedes a subsequent mechanical de-adhesion of the polymer. Consequently any direct promotion of the electrochemical interfacial processes should result in a distinctly accelerated delamination progress, but obviously does not lead to complete polymer de-adhesion as no blister growth can be detected (see Fig. 3.34b). Increased electrolyte pressure in contrast more indirectly supports interface degradation by reduction of the distance between the local electrodes (see section 3.3.3.4) for a better charge compensation or by expanding already existent free volumes at the epoxy amine/zinc oxide interface.

Fig. 3.35 illustrates an SKP-BT delamination experiment performed under the conditions of additional cathodic defect polarisation by -100 mV_{OCP} and reduced atmospheric humidity of 82 % relative humidity. Interestingly no acceleration of the interface degradation was observed. The progress rate instead decreased and with only 6 μm/h delamination nearly entirely stopped. In contrast to the respective processes at polymer/iron oxide/iron interfaces, oxidative de-adhesion at polymer/zinc oxide/zinc interfaces usually results in a precipitation of corrosion products within the delaminated area [2,29-31,38-39]. Iron is passive in alkaline environment; zinc hydroxide exhibits amphoteric properties and partly dissolves with increasing pH. According to Fürbeth et al. [30-31,39] a distinct zinc oxide layer growth occurs within the delaminated area via a dissolution/precipitation mechanism. It can be expected that accelerated electrode kinetics within the liquid/substrate interface section, caused by an increased cathodic polarisation, rapidly exceeds the solubility product of these zincate species at reduced interfacial water activity. They may preferably precipitate and promote a further oxide growth. This inhibits the electrode kinetics due to a decreased conductivity of the substrate bulk structure. Also effective charge compensation by cation/anion migration between the local electrodes should be impeded, because zinc oxides/hydroxides precipitated at the interface likely form physical barriers and reduce the interfacial mobility of cations of the defect electrolyte.

Fig. 3.35 indicates that the progress of corrosive interface degradation reached only about 250 μm during 20 hours of -100 mV$_{OCP}$ cathodic polarisation. Although this distance between defect area and electrolyte front position still is relatively small, a reduced atmospheric humidity of 82 % r.h. already strongly affects the delamination kinetics after an increase of the cathodic polarisation by additional -100 mV$_{OCP}$. The effect of a reduced H_2O activity at the polymer/substrate interface can be consequently confined to an interface section of about 250 μm. It was assumed before (see section 3.3.3.1) that a reduction of the interfacial water amount near the bulk electrolyte filled defect will be partly compensated when applying a hydrostatic pressure of 100 mbar. So consequently the selected set-up and experimental conditions obviously allow a specific affection of the electrolyte front position. In other words it can be confirmed that the relevant lateral dimensions of the \`electrolyte front´ can be quantified to cover less than 250 μm.

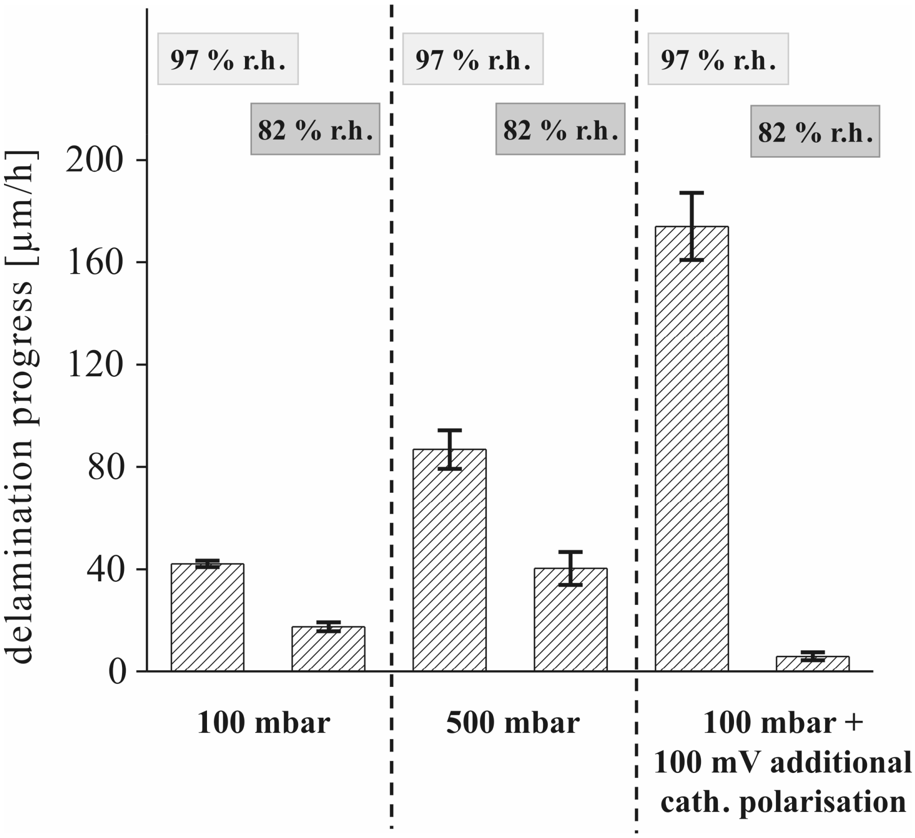

Fig. 3.36: Overview of the delamination rates recorded by SKP-BT experiments during variation of the electrolyte pressure, cathodic polarisation of the defect and relative humidity of the surrounding atmosphere.

Fig. 3.36 offers an overview of the gained SKP-BT results. The effectiveness of cathodic defect polarisation for the regulation of delamination kinetics can be visually confirmed. It is an interesting result that cathodic polarisation in combination with reduced atmospheric moisture leads to self-inhibition of corrosive de-adhesion processes. In fact, many polymer coated zinc surfaces in use for daily life are not continuously exposed to atmospheres of 97 % relative humidity. In such cases an additional cathodic protection of a coating defect would possibly lead to improved stability of adjacent polymer/substrate interface sections towards corrosive delamination of the cathodic type.

3.3.4 Conclusions

The Scanning Kelvin Probe Blister Test (SKP-BT) was introduced as tool for the synergistic investigation of the epoxy amine/zinc oxide/zinc interface stability during variation of atmospheric humidity, electrolyte pressure and cathodic polarisation of the defect. A blister solely grew applying a hydrostatic pressure of 500 mbar. It could be confirmed that the front of electrochemical interface degradation did not coincide with the blister edge. Cathodic delamination seemed to occur before the polymer layer macroscopically de-adhered. Obviously electrochemical pre-damaging precedes the subsequent mechanical degradation.

Moisture reduction resulted in a decrease of the cathodic de-adhesion kinetics by between a factor of two to three. Attenuated-Total-Reflection Infrared Spectroscopy (ATR-IR) studies confirmed a reduction of the interfacial water activity by the same order of magnitude. In contrast peel-off forces increased at comparable amount. Obviously these forces visibly reflect varying interfacial water activities. Initial adjustment of the polymer/substrate interface structure to different air humidity seems to be kept and determines the velocity of subsequent electrochemical degradation processes. Moreover the effect of reduced atmospheric moisture seems to be mainly influencing the electrochemically pre-damaged zone rather than the bulk electrolyte filled blister area.

Cathodic polarisation of the defect distinctly accelerated delamination, obviously by effective promotion of the local electrode kinetics. Atmospheric humidity reduction in combination with increased cathodic polarisation in contrast resulted in self-inhibition of corrosive de-adhesion, probably due to precipitation of amphoteric zinc oxide/ hydroxide species after exceedance of the solubility products and blockage of the galvanic cell. For a better understanding of cathodic polymer/substrate de-adhesion, future experiments consequently will have to focus on the interfacial water activity.

3.3.5 References

[1] H. Leidheiser, W. Wang, L. Igetoft., Prog. Org. Coat. 11 (1983) 19.
[2] A. Leng, H. Streckel, M. Stratmann, Corr. Sci. 41 (1999) 579.
[3] H. Leidheiser, Corrosion Control by Organic Coatings, H. Leidheiser (Ed.), Science Press, Princeton, NJ (USA), 1979.
[4] K. Wapner, Thesis, Ruhr-University Bochum/Germany, 2006.
[5] I. Linossier, M. Gaillard, M. Romand, J. Adhesion 70 (1999) 221.
[6] A.J. Kinloch, J. Mater. Sci. 17 (1982) 617.
[7] J. Yarwood, C. Sammon, C. Mura, M. Pereira, J. Mol. Liq. 80 (1999) 93.
[8] M.Y.M. Chiang, M. Fernandez-Garcia, J. Polym. Sci. 87 (2003) 1436.
[9] J. Feng, K.R. Berger, E.P. Douglas, J. Mater. Sci. 39 (2004) 3413.
[10] G.K .v.d. Wel, O.C.G. Adan, Prog. Org. Coat. 37 (1999) 1.
[11] C.L. Soles, A.F. Yee, J. Polym. Sci. Pt. B: Polym. Phys. 38 (2000) 792.
[12] K. Wapner, B. Schönberger, M. Stratmann, G. Grundmeier, J. Electrochem. Soc. 152 (2005) E 114.
[13] G. Klimow, K. Wapner, G. Grundmeier, Proceedings of the 3rd World Congress on Adhesion and Related Phenomena WCARP-III, (2006), p. 447.
[14] H. Dannenberg, J. Polym. Sci. V (1961) 125.
[15] M.G. Allen, S.D. Senturia, J. Adhes. 25 (1988) 303.
[16] D.A. Dillard, Y. Bao, J. Adhes. 33 (1991) 253.
[17] H.M. Jensen, B. Cochelin, J. Adhes. 47 (1994) 231.
[18] K.R. Jiang, L.S. Penn, J. Adhes. 32 (1990) 203.
[19] K.T. Wam, Y.W. Mai, Acta Metall. Mater. 43 (1995) 4109.
[20] J.G. Williams, Int. J. Fract. 87 (1997) 265.
[21] T.J. Chuang, T. Nguyen, S. Lee, J. Coat. Technol. 71 (1999) 75.
[22] N. Taheri, N. Mohammadi, N. Shahidi, Polym. Test. 19 (2000) 959.
[23] A. Shirani, K.M. Liechti, Int. J. Fract. 93 (1998) 281.
[24] K. Wapner, M. Stratmann, G. Grundmeier, Electrochim. Acta 51 (2006) 3303.
[25] L. Philippe, C. Sammon, S.B. Lyon, J. Yarwood, Prog. Org. Coat. 49 (2004) 302.
[26] L. Philippe, C. Sammon, S.B. Lyon, J. Yarwood, Prog. Org. Coat. 49 (2004) 315.
[27] T. Nguyen, E. Byrd, D. Bentz, C. Lin, Prog. Org. Coat. 27 (1996) 181.
[28] I. Linossier, F. Gaillard, M. Romand, J.F. Feller, J. Polym. Sci. 66 (1997) 2465.
[29] A. Leng, H. Streckel, M. Stratmann, Corr. Sci. 41 (1999) 547.
[30] W. Fürbeth, M. Stratmann, Corr. Sci. 43 (2001) 229.
[31] W. Fürbeth, M. Stratmann, Corr. Sci. 43 (2001) 207.
[32] G. Grundmeier, C. Reinartz, M. Rohwerder, M. Stratmann, Electrochim. Acta 43 (1998) 165.
[33] G. Mattmann, H.R. Oswald, F. Schweizer, Helvetica Chim. Acta 55 (1972) 1249

[34] D.B. Asay, S.H. Kim, J. Phys. Chem. B 109 (2005), 109, 16760.
[35] A. Kuba, E. Hawlicka, J. Mol. Liquids 112 (2004) 91.
[36] R. Vlasak, I. Klüppel, G. Grundmeier, Electrochim. Acta 52 (2007) 8075.
[37] J. Wielant, R. Posner, G. Grundmeier, H. Terryn, Corr. Sci. (2009), doi: 10.1016/j.corsci.2009.04.014
[38] A. Leng, H. Streckel, K. Hofmann, M. Stratmann, Corr. Sci. 41 (1999) 599.
[39] W. Fürbeth, M. Stratmann, Corr. Sci. 43 (2001) 243.

3.4 The dependency of cathodic delamination on different iron oxide/steel substrates – Combined adhesion and electrochemical interface studies

3.4.1 Fundamentals

As long as interfacial oxygen reduction is not rate determined by electron transfer kinetics, the progress of cathodic delamination along polymer/oxide/metal interfaces depends on the square root of time and is reflected by the interfacial cation mobility and transport rate [1]. Nevertheless parameters determinant for the cation mobility itself were not comprehensively investigated up to now. Therefore a detailed study of the dependency of interfacial ion mobility on the substrate properties will be a prerequisite for further predictions of polymer/metal oxide interface stabilities. Such investigations have to focus on the small interface section commonly described as electrolyte front position (see chapter 3.3). This region is especially sensitive to changes of the experimental conditions such as the interfacial water activity, which will affect the chemical and structural environment between polymer film and oxide substrate. A semi-quantitative connection could be drawn between interfacial water activity, relative polymer/substrate peel-force differences and velocity changes of a subsequently initiated cathodic delamination process within chapter 3.3.

Processes at the electrolyte front position can be correlated to the initial steps of corrosive delamination and preliminary interface degradation: (a) Interfacial enrichment of liquid water due to atmospheric H_2O diffusing through the polymer bulk [2], (b) replacement of secondary polymer-oxide interactions and partly saturation of oxide adsorption sites [3-4], (c) increase of interfacial free volumes by polymer swelling [5-7], (d) acceleration of the oxygen reduction kinetics, hydroxide formation, compaction of the electric double layer at the oxide/liquid interface, attraction of cations from the already delaminated area [1,8-12] and (e) adjustment of the oxide morphology due to passive layer formation at increasing interfacial pH [1]. Induced by the destruction of covalent bonds and by reactive radicals evolving during oxygen reduction [9], the polymer will be macroscopically lifted-off.

As for steel substrates no corrosion products precipitate in the delaminated area during cathodic delamination, the interfacial ion transport processes are only affected by the physicochemical condition of the interface. This enables the investigation of the influence of iron oxide surfaces with different structure and composition on the progress of cathodic delamination [13-14].

For the experimental approach presented in this chapter different steel/iron oxide substrates were covered by a pigment free polyurethane film. Scanning Kelvin Probe (SKP) studies of cathodic delamination processes are correlated to the results of polymer/oxide peel-off tests and oxide surface energies. Reactive wetting experiments along the uncoated substrates offer a further insight into the rate determining parameters for corrosive delamination at polymer/iron oxide interfaces [15-16][*].

3.4.2 Experimental procedures

3.4.2.1 Sample preparation

DC06 steel according to the EN10130(98) norm was applied as substrate. The steel surfaces were ground with SiC-paper (500-800-1200-4000 grid) and subsequently polished with 1 μm grade diamond paste to obtain mirror-like appearance. For specific formation of iron oxide layers, samples were treated by one of the four procedures described below [13-17]. (a) 'Thermal' oxide films were formed at 250 °C during

---

[*] *The approach presented within this chapter was developed in close cooperation with Dr. Jan Wielant and Prof. Herman Terryn from the Vrije Universiteit Brussel, who provided samples, coating and a detailed knowledge about the iron oxide properties. Measurements were performed at the Max-Planck-Institut für Eisenforschung GmbH, Düsseldorf by Jan Wielant and Ralf Posner. Text and composition of section 3.4 are adopted from publication [15], which was set up by Ralf Posner, assisted by Jan Wielant. The presented experiments and figures can also be found in Jan´s PhD thesis [16], embedded in a different, comprehensive textual context. Jan Wielant and Herman Terryn are thanked for the permission to present these cooperatively gained results as chapter within the present thesis.*

8 minutes in air. (b) To receive ‘Gardoclean’ oxides, polished steel substrates were immersed into a NaOH containing 80 g/L Gardoclean 390 solution (obtained from Chemetall / Germany) for 8 min at 70 °C. (c) Electrochemically passivated steel samples (`borate buffer´ oxide) were obtained in a 0.075 molar $Na_2B_4O_7 \cdot 10\ H_2O$ + 0.3 molar H_3BO_3 solution (pH = 8.2) after 1 h polarisation at 1.04 V_{SHE} applying a Pt-counter and calomel reference electrode. Prior to passivation, the steel sheets were cathodically polarised at -0.76 V_{SHE} for 30 minutes to remove the native oxide film. (d) Plasma oxides were formed first by a H_2/Ar plasma to remove residual organic contaminations, followed by a H_2O plasma treatment. For procedure details and parameters see [18]. Prior to coating application the four iron oxide sample types were ultrasonically cleaned for 5 minutes in acetone and chloroform.

As polymer film, a commercial two component Glasurit® lacquer from BASF Coatings AG, Germany, was used. A polyurethane lacquer was formed by mixing a polyacryl based resin (MS-Clear 923-155) with an isocyanate based hardener (HS-Topcoat Hardener 929-93) at 2:1 ratio. The coating thickness was around 60 μm and was set by a barcoater. Curing of the coating took place in ambient atmosphere for 4 days.

3.4.2.2 Analytical methods

Advancing contact angles on freshly prepared oxide films were obtained in inert atmosphere with 5 μl droplets at 0.2 μl/s advancing rate, applying a dataphysics Contact Angle System OCA 20. Surface energies were calculated applying the Owens-Wendt-Kaeble approach [19-21].

Peel tests were performed in humid atmosphere of > 95 % r. h. with custom made equipment [8,10] at constant angle perpendicular to the sample surface, constant rate of 3.4 mm/min and with strips of 5 mm in width. Coated samples were measured immediately after preparation or were exposed 24 h to humid atmosphere prior to the peel-off test.

SKP measurements were carried out with a custom made height regulated Scanning Kelvin Probe [22] in an atmosphere of high humidity (> 95 % r. h.).

Time-of-Flight Secondary Ion Mass Spectroscopy (ToF-SIMS) measurements have been executed by means of a PHI TRIFT CE, Physical Electronics, USA, applying a gallium ion gun at an acceleration voltage of 15 kV and a spot size of 100 x 100 μm.

3.4.3 Experimental results

3.4.3.1 Cathodic delamination along different iron oxide/polymer interfaces

Scanning Kelvin Probe (SKP) studies have been performed to reveal the influence of the iron oxide preparation procedure on the cathodic delamination kinetics at the polyurethane/substrate interfaces. The comparability of the observed delamination progress could be ensured by parallel investigation of sample sets exposed to the same environmental conditions. Thereby any interfering variations of oxygen partial pressure or relative atmospheric humidity could be avoided. Fig. 3.37 illustrates the detected potential profiles for the four studied oxide covered substrates. The progress of cathodic delamination is reflected by the lateral displacement of the turning points within the potential profiles of Fig. 3.37a-d [1]. Fig. 3.38 displays a linear dependency of the delamination front position versus the square root of time and confirms that the process was rate-determined by the interfacial ion mobility [1]. The averaged delamination rate varied between approximately 2120 μm/h$^{0.5}$ and 430 μm/h$^{0.5}$. It was carefully checked that it reproducibly decreased in the order ‘borate buffer’ oxide > ‘thermal’ oxide ≈ ‘plasma’ oxide > ‘Gardoclean’ oxide. The disproportionate deceleration of cathodic delamination on the plasma oxide at longer timescales (see Fig. 3.37b, Fig. 3.38) can be attributed to an ongoing passivation within the defect area. This phenomenon does not represent a typical property of the plasma substrate, as repeated experiments underlined. A higher linear potential slope between defect area and electrolyte front position can be correlated with a decelerated cathodic delamination process (see Fig. 3.39 and compare to Fig. 3.38). Such potential slope ($\Delta E_{\text{distance normalised}}$) is reflected by the IR drop between the local electrodes of the galvanic element, determined by Ohm´s law [9]:

$$\Delta E_{\text{distance normalised}} = I_c \cdot R_c \qquad (3\text{-}1)$$

I_c is the interfacial cation current density and R_c represents the distance normalised resistance towards interfacial cation transport. Quantification of R_c and I_c in fact is difficult. But it can be assumed that a large IR drop for the ‘Gardoclean’ oxide is attributed to a larger resistance R_c and a decreased interfacial Na^+ mobility compared to the ‘borate buffer’ oxide. Alternatively, an increased interfacial cation current I_c, is less plausible, as it is connected with accelerated oxygen reduction kinetics and consequently with an acceleration of the cathodic delamination process itself.

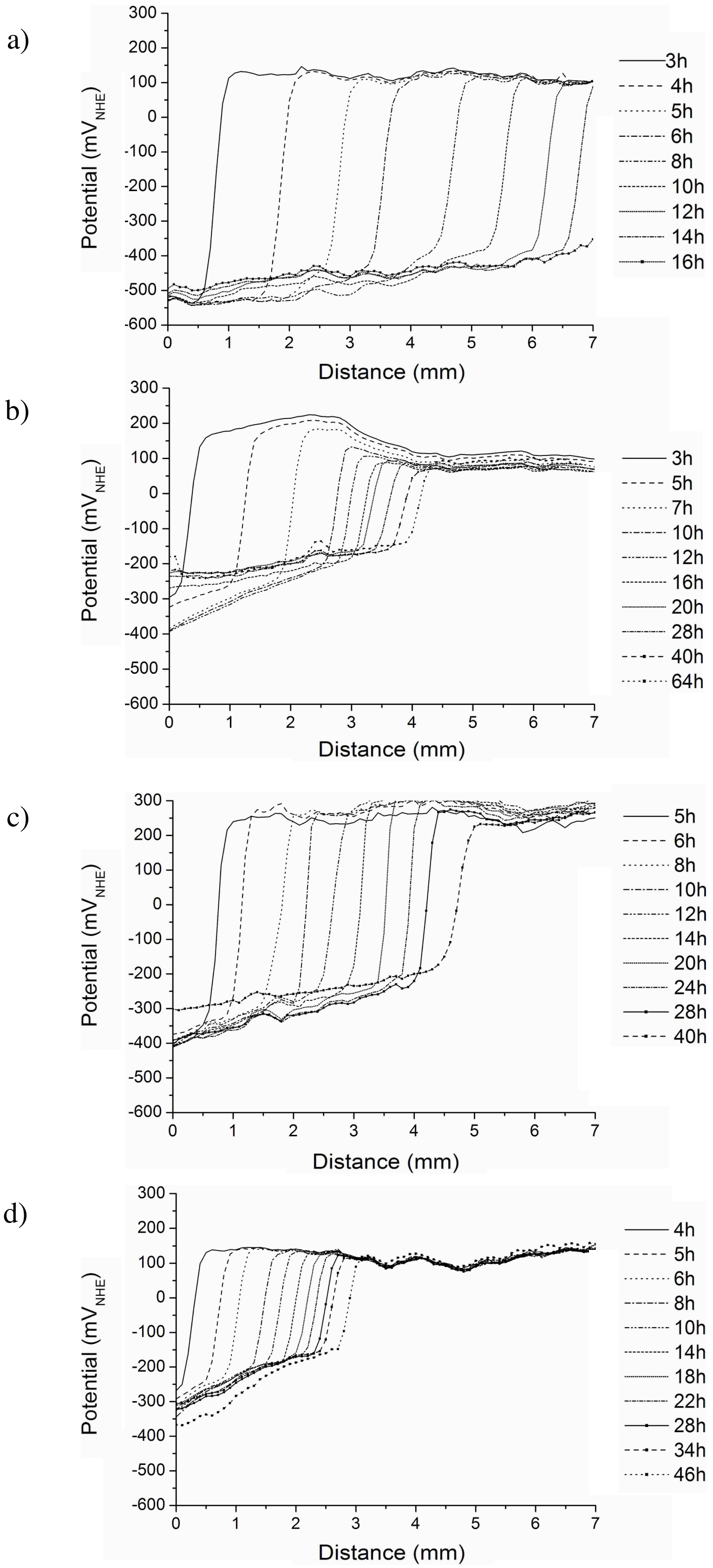

Fig. 3.37: SKP corrosive de-adhesion study for the four polyurethane/iron oxide interfaces in humid air, applying 0.5 molar NaCl solution as defect electrolyte. Illustrated are the potential profiles recorded on a) 'borate buffer' oxide, b) 'plasma' oxide, c) 'thermal' oxide, d) 'Gardoclean' oxide.

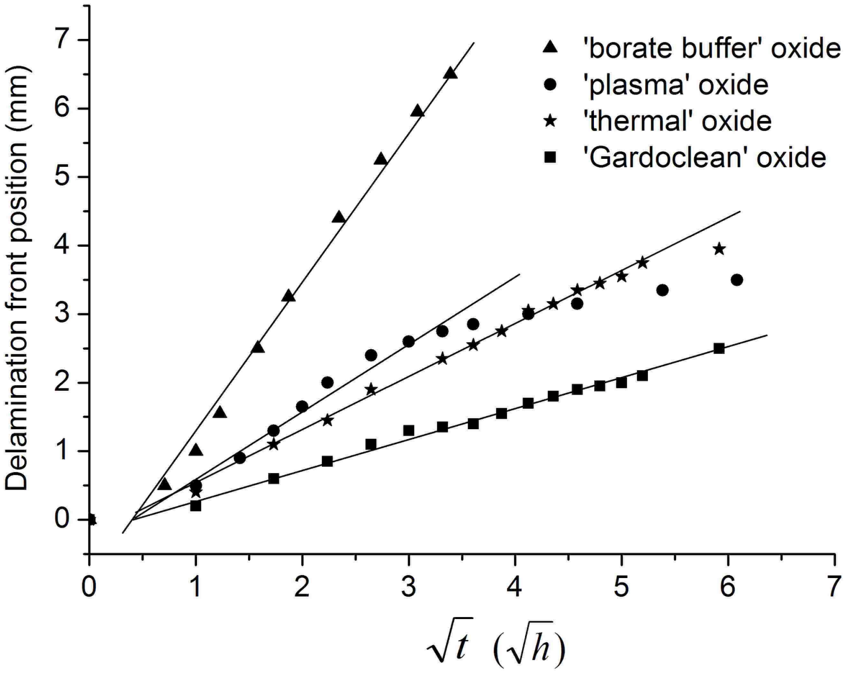

Fig. 3.38: Diagram of the delamination front position vs. square root of time, calculated from the potential profiles of Fig. 3.37.

sample	IR drop (mV/mm)
’borate buffer ’ oxide (fast)	7
’thermal ’ oxide	53
’plasma ’ oxide	60
’Gardoclean ’ oxide (slow)	73

Fig. 3.39: Typical values of the averaged distance normalised potential (IR) drop for the four iron oxides detected at the delaminated interface.

3.4.3.2 Polymer/substrate adhesion strength as function of the iron oxide type

The previous paragraph confirmed that the interfacial cation mobility determined the observed de-adhesion rate for the four iron oxides. To further evaluate if higher ion mobility is correlated to larger interfacial adhesion strength, polymer/iron oxide 90° peel-off tests were performed. A first approach concentrated on the remaining adhesion of the polyurethane based lacquer within the delaminated area. As expected the polymer could be easily lifted off, but the applied force was nearby the detection limit of the applied equipment (not shown here). A rough qualitative estimation nevertheless seemed to confirm that a large IR drop detected before by SKP was connected to a higher peel-off force in the delaminated area. But as a distinct tendency for the complete set of the four oxides could not be given following this approach, the polymer adhesion strength in the intact areas was investigated accordingly.

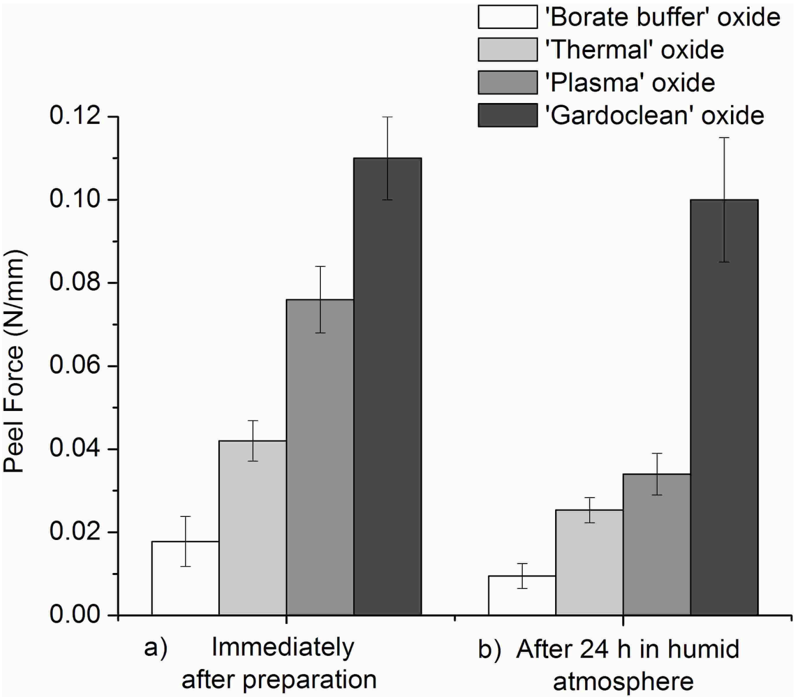

Fig. 3.40: Investigation of the polyurethane/iron oxide adhesion force by peel-off measurements, a) immediately after preparation in ambient atmosphere, b) after 24 h exposure to humid air.

Fig. 3.40a illustrates the resulting peel-off forces detected immediately after film application and curing. They varied between 0.02 N/mm and 0.11 N/mm and increased in the order ‘borate buffer’ oxide < ‘thermal’ oxide < ‘plasma’ oxide < ‘Gardoclean’ oxide. The tendency detected for corrosive delamination is remarkably well reflected. As the SKP experiments were performed in highly humid atmosphere, the peel-off experiments were repeated after 24 h of sample exposure to these conditions. An even better correlation was obtained, because the relative adhesion strength differences between ‘plasma’ and ‘thermal’ oxide are distinctly decreased and rather similar to the small delamination velocity differences for these two substrates (compare Fig. 3.40b with Fig. 3.38). In general all peel-off forces are reduced after exposure in humid air due to water replacing secondary polymer/iron oxide interactions [3]. It can be concluded that a gradual decrease of the polymer/iron oxide adhesion strength also directly results in gradually accelerated cathodic delamination kinetics. Initial adaptations of the interface structure after water uptake obviously will be maintained during the subsequent stages of electrochemical interface degradation caused by cathodic delamination. As always the same polymer was applied on the iron oxides, comparable bulk polymer swelling in humid air has to be supposed. But oxide morphology change during passivation and an expected increase of interfacial free volumes will occur differently, dependent on the substrate surface. Adhesion forces detected for the intact polymer/iron oxide interface at least qualitatively reflect such substrate properties.

3.4.3.3 Surface energy of the different iron oxides

Contact angle measurements have been performed on the four substrate types to gain a better understanding of the observed differences within the polyurethane/iron oxide adhesion forces. Fig. 3.41 illustrates the values detected for water.

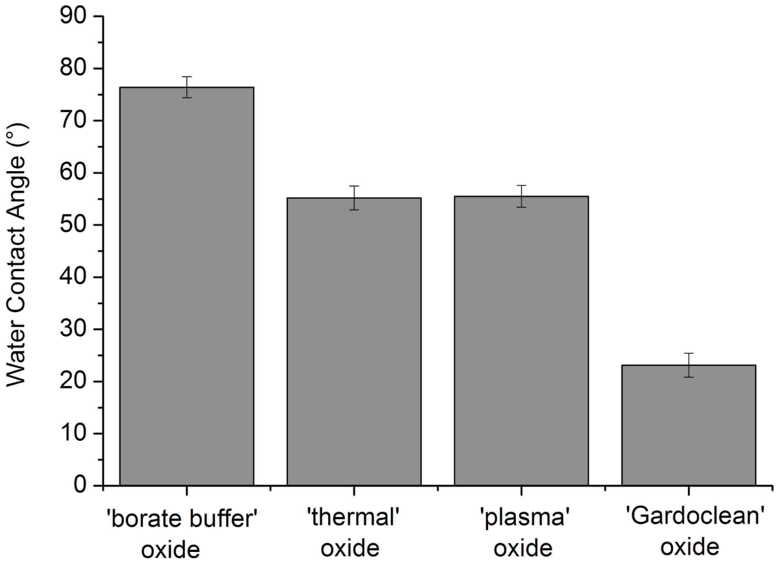

Fig. 3.41: Averaged water contact angles measured on the four iron oxide surfaces.

The surface wettability decreased within the order `borate buffer' oxide > 'plasma' oxide ≈ 'thermal' oxide > 'Gardoclean' oxide and generally reflects the observed tendency for the cathodic delamination progress as well as that one detected for the peel-off forces. The calculated oxide surface energies could be apportioned into polar and dispersive contributions (see Fig. 3.42). Obviously the polar component is an adequate parameter for the prediction of peel-off force variations and cathodic de-adhesion rates for the applied coating. The highest polar surface energy was determined for 'Gardoclean' oxide, the lowest for 'borate buffer' oxide. For 'plasma' oxide the polar component turned out to be slightly increased compared to that one of 'thermal' oxide. This remarkably exactly corresponds to the respective sequences illustrated in Fig. 3.38 and Fig. 3.40.

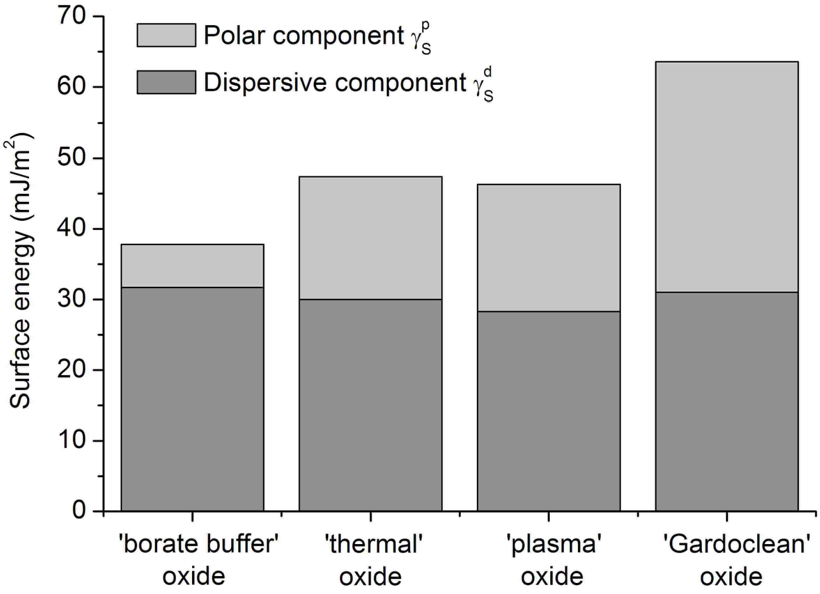

Fig. 3.42: Total surface energy of the four iron oxide substrates. Polar and dispersive components are indicated.

It can be confirmed that an increase of the polar surface energy component has a positive effect on the adhesion strength for polymer films with polar functional groups [23-24]. Some studies attributed these findings to an increased amount of interactions between surface hydroxyls and organic functionalities of the polymer [25-26]. In previous publications it was shown for the same set of oxides that the surface hydroxyl density alters the number of oxide/adsorbant interactions and the adsorption mechanism of organic molecules [13,16-17]. Less strong interactions take place when molecules are adsorbed on poorly hydroxylated surfaces ('thermal' and 'Gardoclean' oxide) compared to hydroxyl-rich surfaces ('borate buffer and 'plasma' oxide) [13,16-17]. For the polyurethane film, a higher hydroxyl density does not seem to result in a higher peel strength of the coating.

Anyhow the peel forces of the polyurethane films indicate that the oxide surface energy is a determining parameter towards adhesion (compare Fig. 3.40 and Fig. 3.42) and that the differences in adhesion strength can be attributed to the oxide surface chemistry and/or to the very first nanometers of the polymer/substrate interphase. The hydrophilic properties of the oxide surfaces determine structural interface adjustments due to water ingress, which are directly reflected by different polymer/substrate adhesion forces.

3.4.3.4 Electrolyte spreading along the uncoated iron oxide surfaces

It could be proven that the interfacial cathodic delamination progress indirectly depends on the hydrophilic surface properties via the polymer/substrate adhesion strength. Nevertheless a direct correlation of cation mobility and surface energy may be effective as well. To further analyse how a polyurethane layer determines the interfacial ion transport, reactive electrolyte wetting experiments on the uncoated oxide surfaces were performed. Fig. 3.43 presents SKP potential profiles recorded for 0.5 molar KBr liquid spreading on the four bare substrates in humid air. By addition of ≈ 3 % agar, the defect electrolyte viscosity was increased to prevent it from immediate leaking (see section 3.2). Nevertheless a thin liquid film began to spread along the oxides starting from the solid droplets at the defect area. The wetted surface areas remained shiny, whereas the defect area was red coloured by precipitation of corrosion products. The SKP potential profiles recorded during this process varied concerning absolute potential levels of wetted and dry surface (see Fig. 3.43), but in shape were similar to those obtained for cathodic delamination at the polyurethane/iron oxide interfaces (see Fig. 3.37). The spreading velocity lay between approximately 2150 μm/h$^{0.5}$ and 550 μm/h$^{0.5}$ and reproducibly decreased within the order ‘plasma’ oxide > ‘Gardoclean’ oxide ≈ ‘thermal’ oxide > ‘borate buffer’ oxide (see Fig. 3.44). It does not seem to be correlated with the tendency observed before for cathodic delamination at the coated iron oxides (compare Fig. 3.38 with Fig. 3.44). Furthermore surface energies and water contact angles, which were also determined on the bare oxides, do not allow the prediction of any electrolyte wetting tendency.

Therefore it had to be ensured that liquid spreading along this set of uncoated iron oxide surfaces is dominated by electrostatically determined migration of defect electrolyte cations, as it was already generally concluded for iron surfaces within section 3.2. Fig. 3.45 presents ToF-SIMS profiles recorded on the ‘Gardoclean’ and ‘borate buffer’ oxide surfaces after termination of the electrolyte wetting experiments. The latter showed slowest electrolyte spreading (see Fig. 3.44). The process therefore should be most susceptible for any contribution of diffusive ion transport.

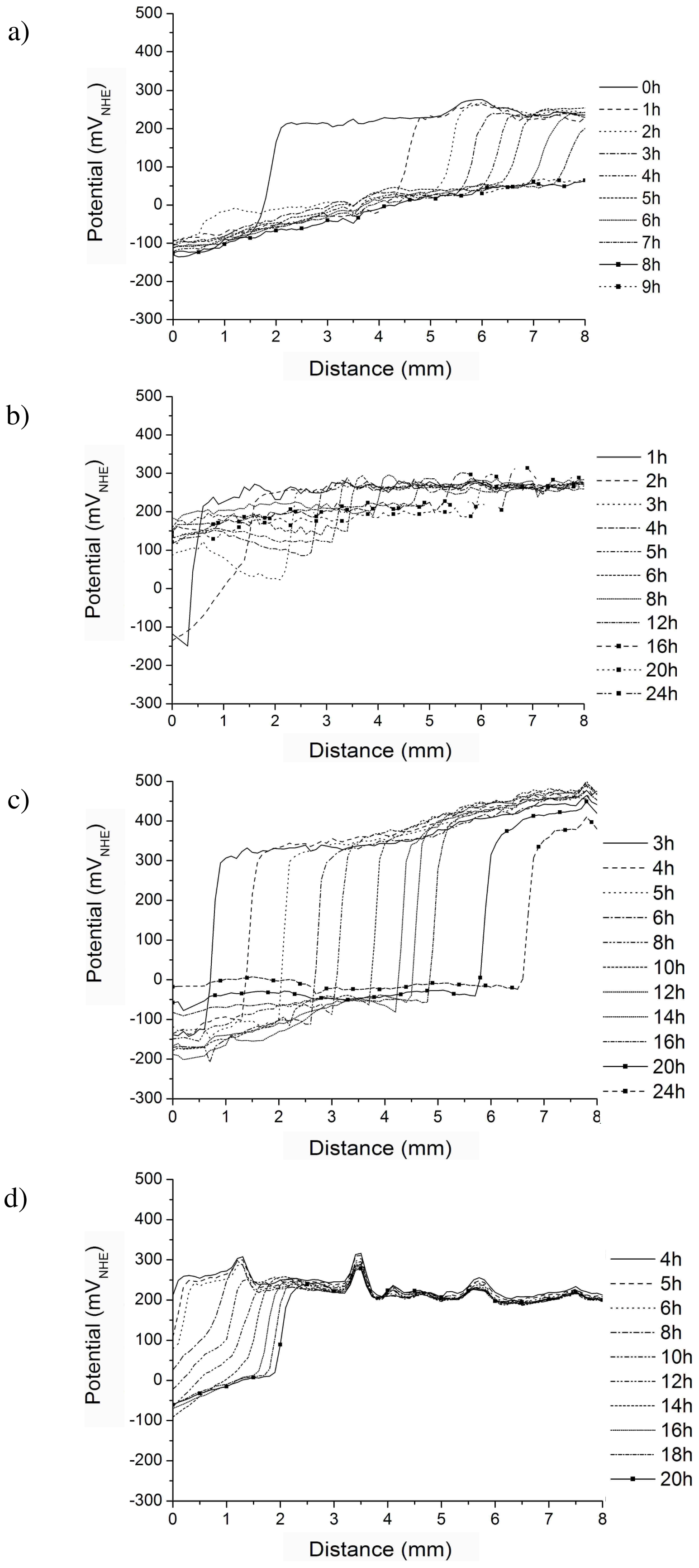

Fig. 3.43: Reactive electrolyte wetting of uncoated iron oxide surfaces in humid air applying 0.5 molar KBr solution of high viscosity after addition of agar. Illustrated are the potential profiles for a SKP study on a) 'plasma' oxide, b) 'Gardoclean' oxide, c) 'thermal' oxide, d) 'borate buffer' oxide.

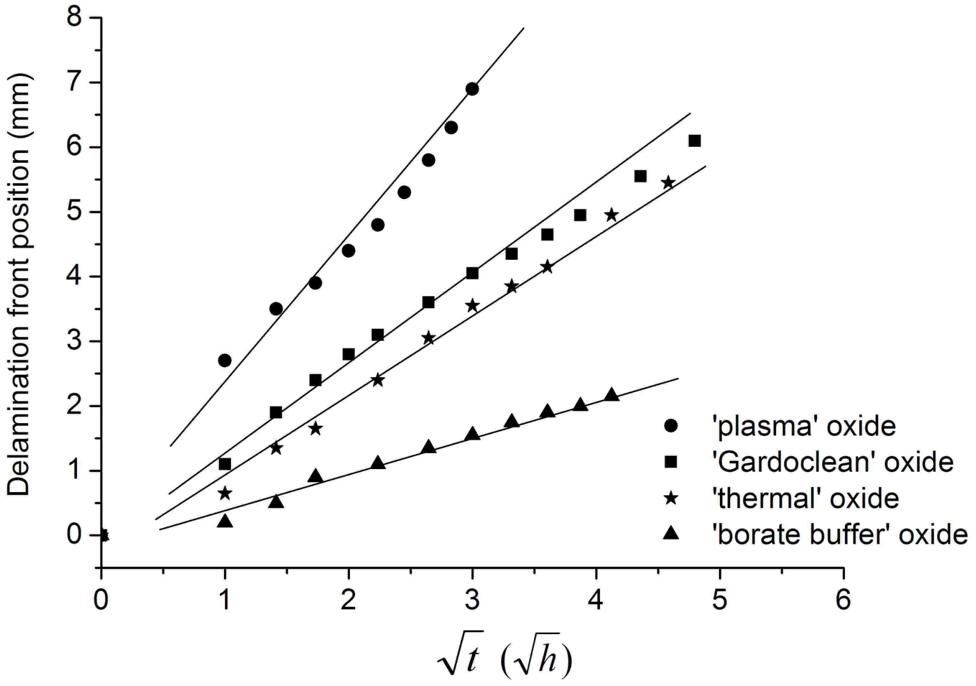

Fig. 3.44: Diagram of the spreading front position vs. square root of time, calculated from the potential profiles of Fig. 3.43.

For the 'Gardoclean' oxide, unusual potential profiles have been recorded (see Fig. 3.43b) which may point at a changed process mechanism. Although a quantitative comparison of K^+ and Br^- amount is not possible, the distribution of bromide and potassium ions at the surfaces reflects the different sample areas. A varying amount of KBr could be detected within the defect section. At the transition to the spreaded area, the Br^- signal diminishes, but K^+ still is definitively detectable. In agreement to the conclusions drawn in section 3.1 and section 3.2, a basic contamination level for both ions is reached on the unaffected surface beyond the electrolyte front position. Obviously solely cations are transported into the electrolyte wetted sections. This is consistent with the assumption of an oxygen reduction induced K^+ transport process necessary for charge compensation after OH^- formation at the substrate surface (see section 3.2). In this context, both ion transport mechanisms at uncoated 'Gardoclean' and 'borate buffer' oxide are comparable. Deviations due to application of NaCl solution for cathodic delamination studies at the polymer coated substrates and KBr solution for the spreading experiments along the uncoated iron oxides are not to be expected according to the results presented in section 3.1. As also a square root of time dependency is observed (see Fig. 3.44), the basic mechanisms of electrolyte spreading and cathodic delamination are comparable.

So obviously ion mobility at the uncoated iron oxides is not dependent on the substrate surface energy, whereas it plays a crucial role for the progress of cathodic delamination at the polyurethane/iron oxide interfaces. For the latter case, surface energies even seem to allow semi-quantitative predictions of the interface stability for sets of similar samples. Based on the detected correlation of delamination progress tendencies to the respective coating/oxide adhesion forces, the presented results may help to introduce conventional polymer/substrate peel-off tests as cost-efficient method for such an evaluation.

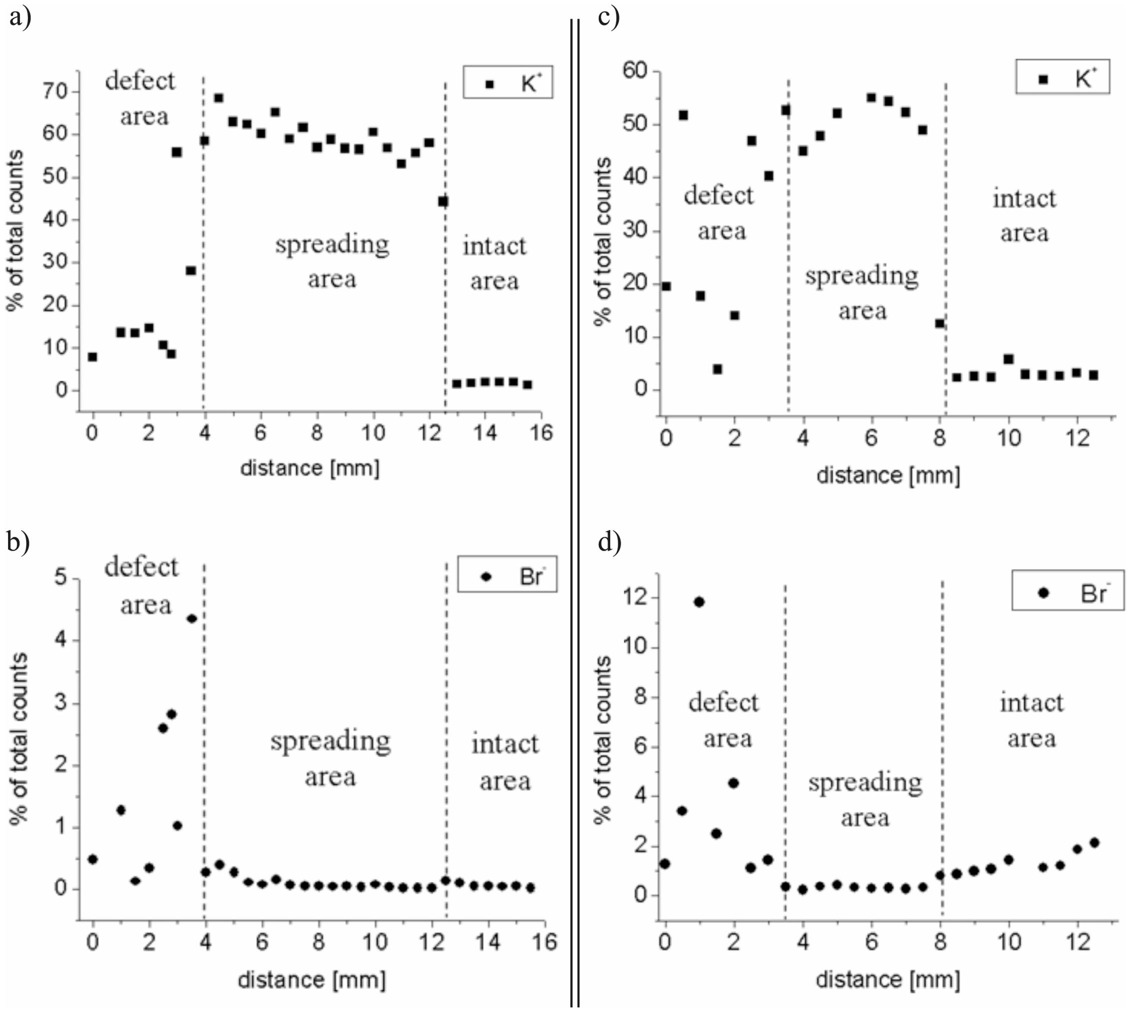

Fig. 3.45: ToF-SIMS ion profiles recorded on iron oxide surfaces after reactive electrolyte spreading in humid air. Highly viscous 0.5 molar KBr solution, stabilised with agar, was applied as electrolyte. a) K^+ distribution on 'Gardoclean' oxide, b) correlated Br^- distribution on 'Gardoclean' oxide, c) K^+ distribution on 'borate buffer' oxide, d) correlated Br^- distribution on 'borate buffer' oxide.

3.4.4. Conclusions

The present results offer a further insight into the dependency of interfacial ion mobility on the rate determining parameters for transport controlled cathodic delamination processes at polymer/iron oxide interfaces. Moreover, parameters influencing the cation mobility itself were investigated in detail. A direct connection could be detected between oxide surface energies, adhesion of the polymer film after sample exposure in humid atmosphere and the delamination rate of the polyurethane coating on the steel substrates with different interfacial iron oxide structure and morphology. An increasing polar oxide surface energy component was correlated with increasing polymer/iron oxide peel-off forces and deceleration of delamination within the order 'borate buffer' oxide > 'thermal' oxide ≈ 'plasma' oxide > 'Gardoclean' oxide. In contrast, reactive electrolyte spreading along the uncoated oxide substrates was not dependent on the oxide surface energies, although both spreading and delamination are dominated by migration of cations from the defect electrolyte to the cathodic delamination front. It can be concluded that hydrophilic oxide surface properties determine structural changes of the polyurethane/substrate interface after ingress of atmospheric water. They are directly reflected by differences of the polymer/substrate adhesion forces and will be maintained during the subsequent stages of cathodic delamination.

3.4.5 References

[1] A. Leng, H. Streckel, M. Stratmann, Corr. Sci. 41 (1999) 579.
[2] D.B. Asay, S.H. Kim, J. Phys. Chem. B 109 (2005), 109, 16760.
[3] I. Linossier, M. Gaillard, M. Romand, J. Adhesion 70 (1999) 221.
[4] A.J. Kinloch, J. Mater. Sci. 17 (1982) 617.
[5] W. Possart, B. Valeske, J. Adhesion 75 (2001) 129.
[6] C. Wehlack, W. Possart, Macromol. Symp. 205 (2004) 251.
[7] J.K. Kruger, W. Possart, R. Bactavachalou, U. Muller, T. Britz, R. Sanctuary, P. Alnot, J. Adhesion 80 (2004) 585.
[8] A. Leng, H. Streckel, M. Stratmann, Corr. Sci. 41 (1999) 547.
[9] A. Leng, H. Streckel, K. Hofmann, M. Stratmann, Corr. Sci. 41 (1999) 599.
[10] W. Fürbeth, M. Stratmann, Corr. Sci. 43 (2001) 207.
[11] W. Fürbeth, M. Stratmann, Corr. Sci. 43 (2001) 229.
[12] W. Fürbeth, M. Stratmann, Corr. Sci. 43 (2001) 243.
[13] J. Wielant, T. Hauffman, O. Blajiev, R. Hausbrand, H. Terryn, J. Phys. Chem. C 111(35) (2007), 13177.

[14] J. Wielant, V. Goossens, R. Hausbrand, H. Terryn, Electrochimica Acta 52 (2007), 7617.
[15] J. Wielant, R. Posner, G. Grundmeier, H. Terryn, Corr. Sci. (2009), doi: 10.1016/j.corsci.2009.04.014
[16] J. Wielant, Thesis, Vrije Universiteit Brussel, April 2009, ISBN 978-90-5487-563-5.
[17] J. Wielant, R. Posner, G. Grundmeier, H. Terryn, J. Phys. Chem. C 112(33) (2008), 12951.
[18] J. Raacke, M. Giza, G. Grundmeier, Surf. Coat. Techn. 200 (2005), 280.
[19] D. Owens, R. Wendt, J. Appl. Pol. Sci. 13 (1969) 1741.
[20] N. Correia, J. Moura Ramos, B. Saramago, J. Calado, J. Coll. Int. Sci. 189 (1997), 361.
[21] S.-J. Park, J.-S. Kim, J. Coll. Int. Sci. 244 (2001) 336.
[22] K. Wapner, B. Schönberger, M. Stratmann, G. Grundmeier, J. Electrochem. Soc. 152 (2005) E 114.
[23] T. Okamatsu, Y. Yasuda, M. Ochi, J. Appl. Polym. Sci. 80 (2001), 1920.
[24] A. Neumann, R. Good, J. Coll. Int. Sci. 38 (1972), 341.
[25] B. Uner, M. Ramasubramanian, S. Zauscher, J. Kadla, J. Appl. Polym. Sci. 99 (2006), 3528.
[26] J. van den Brand, O. Blajiev, P. Beentjes, H. Terryn, J. de Wit, Langmuir 20 (15) (2004), 6308.

3.5 Investigation of the interface stability of styrene/acrylate copolymer films applied on iron and zinc substrates

3.5.1 Fundamentals

Within the previous chapters it was focussed on the principles of interfacial ion transport and the importance of the interfacial water activity for the prediction of cathodic delamination kinetics. Also the analysis of the influence of different iron oxide substrates on adhesion and the velocity of corrosive delamination was investigated. The present section now completes the selected academic approach and tries to further clarify the influence of polymer structures on the coating/substrate interface stability.

As water borne organic coatings are of increasing importance for the corrosion protection of metals, numerous studies focussed on the mechanical, physical and chemical properties of polymer latex films [1-3]. When casted onto wettable substrates, the dispersions form water insoluble organic coatings. Film formation is supported by annealing above a minimum film formation temperature, usually correlated with the glass transition temperature (T_g) of the polymer [1-2,4-5]. Although a universal film formation mechanism is still under discussion [1], a three phase model is commonly accepted (see also Fig. 3.46). By evaporation of water, the latex solid content is concentrated to 60-70 % volume fraction (stage I) [1]. During stage II, the particles first come into irreversible contact, the overall rate of water evaporation distinctly decreases and particle deformation occurs, especially for soft latices [1]. Subsequently, initial formation of a continuous film starts (stage III). Via interparticle channels and subsequently by diffusion through the polymer surface layer remaining water leaves the film. Hydrophilic dispersion additives, e.g. surfactants, can reduce the rate of water removal due to polar interactions with water molecules. Especially soft latices further coalesce based on capillary forces and due to polymer chain interdiffusion, and particle interfaces become less distinct or smear [1]. It is reported that the interdiffusion capability is strongly dependent on the molecular weight of the polymer [4], the annealing temperature [2,4] and time of annealing [1,2], the spatial distribution of chain ends near the interface [6] as well as the steric and electrostatic stabilisation of the latex [7].

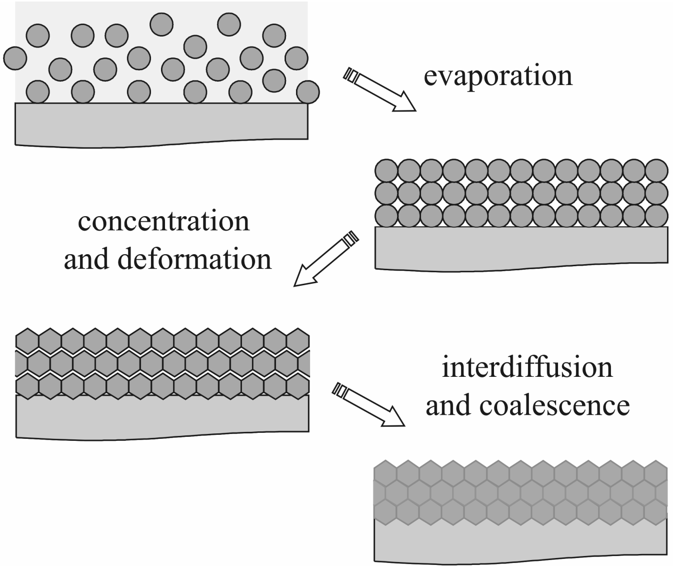

Fig. 3.46: Schematic illustration of the film formation mechanism in latex coatings [10].

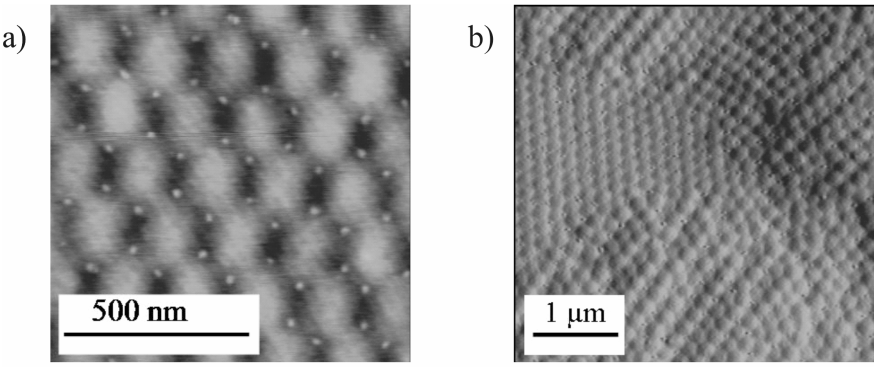

Fig. 3.47: Typical surface structures of latices investigated in section 3.5. a) AFM-potential amplitude image of a monomolecular nBA/Sty(T_g= -40 °C) layer after dip coating with 24 µm/s at 80 % r.h., diluted 1:5. Z-axis: 200 nm, substrate: Si-wafer. b) AFM-topography of a nBA/Sty(T_g= -40 °C) film applied on a cleaned Si-wafer by dip coating (14 µm/s at 50 % r.h.). Z-axis: 200 nm. For classification of the latex films see Fig. 3.49.

The formation of spherical, octahedral and also honeycomb like particle structures were reported after investigation of the layer topography [1,8,9]. Fig. 3.47 offers a visual impression of the surface topography for films applied in the present study.

Depending on polymer film composition and layer structure, a varying corrosion resistance of the films is observed. A previous study investigated adhesion forces of different latex layers applied on metallic substrates by peel-off tests [3] and reported preferential de-adhesion at the polymer/substrate interface. But beside corrosion exposure tests [3], available reports hardly allow a systematic evaluation of the polymer/metal oxide interface stability as function of non-pigmented latex formulations under the conditions of electrochemically driven interface deterioration. Rossenbeck et al. [10] and Grundmeier et al. [9] investigated the corrosion protective effect of Zn-phosphate additives in water borne dispersion coatings and reported a deceleration of delamination kinetics after the interfacial release of phosphate or molybdate ions.

The present study in contrast focuses on the latex film/oxide/iron interface stability as function of the monomer composition of different pigment free copolymer dispersions. The influence of the polymer T_g on film formation was evaluated by Electrochemical Impedance Spectroscopy (EIS). Its effect on the velocity of interfacial cathodic delamination along different metallic substrates was analysed by means of SKP. The results are compared to the influence of cross linking reagents and polymer chain length control applied during emulsion polymerisation of the latex particles.

3.5.2 Experimental procedures

3.5.2.1 Substrates

Iron samples of 99.99 % purity were ground and polished, residues ultrasonically removed with ethanol, then dried in a nitrogen stream. Smooth stainless steel substrates were cleaned in the same way. All used chemicals and solvents were of p.a. quality. Iron sheets, covered with an approx. 8 μm thick electrogalvanised zinc layer (received from voestalpine Stahl GmbH, Linz / Austria), were solvent and alkaline cleaned, then rinsed with water and dried as described in section 3.1.2.2. Preparation of an artificial iron/zinc transition was performed also according to section 3.1.2.2. Si-wafer were cleaned in an aqueous solution of 30 % NH_3/H_2O_2 at 80 °C, subsequently rinsed with water and dried. For polymer plasma deposition of a 10 nm SiO_2 layer on iron substrates, samples were first oxygen microwave plasma cleaned (400 W, 0.2 mbar, v = 2 mm/s; microwave source by Roth and Rau, Wüstenbrand/Germany), then exposed to a gas mixture of O_2 and hexamethyldisiloxane (volume ratio 20:1 at 0.2 mbar with 300 W and 15 mm/s). SiO_2 thickness control was performed by ellipsometry (SE 800, Sentech, Berlin/ Germany). For details see [11].

3.5.2.2 Application of polymer films

Latex films were received from water-borne acrylic model copolymer dispersions based on n-butyl acrylate (nBA)/styrene (Sty), 2-ethyl hexylacrylate (EHA)/Sty or nBA/EHA/Sty with a T_g between ≈ -40 °C and 40 °C; for details see Fig. 3.49. The averaged particle size was 203 ± 4 nm (determined by dynamic light scattering and hydrodynamic chromatography), the dispersion viscosity always ≈ 10 mPas·s, its pH 7.7 ± 0.6 and the solid content 40 %. Except a variation of the nBA-EHA-Sty monomer ratio, the emulsion polymerisation recipe for all latices was kept constant, including the surfactant amount, unless otherwise noted. The dispersions were provided by BASF SE, Ludwigshafen/Germany and applied on the respective substrates by spin coating at 1500 rpm during 30 s using a P 6700 (Specialty Coating Systems Inc., Indianapolis/ USA). The layers were subsequently annealed in a furnace at temperatures between 40 °C and 120 °C without addition of solvent as film forming agent. Layers with a thickness of 3-6 μm were received, analysed by cross section images in a scanning electron microscope, model LEO 1550 VP (Carl Zeiss/Germany). Measurements with a Leica DMLM microscope and an ICM 1000 confocal laser (λ = 633 nm) scan unit (Leica Microsystems, Wetzlar/Germany) as well confirmed that the resulting layer thickness was not correlated with the latex T_g.

3.5.2.3 Analytical methods

SKP measurements were carried out with a custom made Scanning Kelvin Probe [12] in an atmosphere of high humidity (> 95 % r.h.) at room temperature (≈ 22 °C). Cathodic delamination was initiated by filling an artificial coating defect always with 0.5 molar NaCl solution.

Static contact angles on the latex coated Si surfaces were obtained with 5 μl droplets, applying a dataphysics Contact Angle System OCA 20. Surface energies were calculated applying the Owens-Wendt-Kaeble approach [13-15].

The latex T_g could be evaluated by differential scanning calorimetry, applying a Mettler Toledo DSC 822 (Gießen/Germany).

All EIS measurements were performed at room temperature (≈ 22 °C) on latex covered stainless steel substrates with a chloride free borate buffer solution (with pH 8.4). A potential amplitude of 10 mV was applied at the open circuit potential of the investigated sample system covering a frequency range of 1 Hz to 10^5 Hz. A FAS2 Femtostat (Gamry Instruments, Warminster/USA) was used, connected to a micro capillary cell with a glass capillary of 1 mm in diameter and a silicon ring gasket on top. A force sensor controlled the contact pressure on the substrate and ensured a constant working electrode area. Macroscopic experiments were carried out on a working electrode area of 1 cm in diameter with a Compactstat (Ivium Technologies B.V., Eindhoven/The Netherlands). The capacity of the adhesive film was determined at phase maximum, usually at 10 kHz. The water uptake of the polymeric films could be calculated following the approach of Brasher and Kingsbury [16-17]. Coefficients for water diffusion through the polymer layers were evaluated according to the studies of Vlasak et al. and Zhang et al. [16,18].

3.5.3 Experimental results

3.5.3.1 Evaluation of the latex film barrier properties towards water ingress

Previous sections emphasised the importance of the interfacial water activity for the polymer/substrate adhesion forces and the velocity of a subsequently occurring, electrochemically driven interface delamination. The main initial water ingress pathway is H_2O diffusion through the polymer bulk or via layer fissures. Diffusion along a polymer/substrate interface from a coating defect will be hardly effective on a macroscopic scale, in particular under the conditions of cathodic delamination or when ions are transported (chapters 3.1 and 3.2). Consequently, interfacial water ingress is primarily connected to the barrier properties of the polymer. Therefore EIS measurements were performed to evaluate achieved latex coating qualities after layer application on stainless steel and film formation.

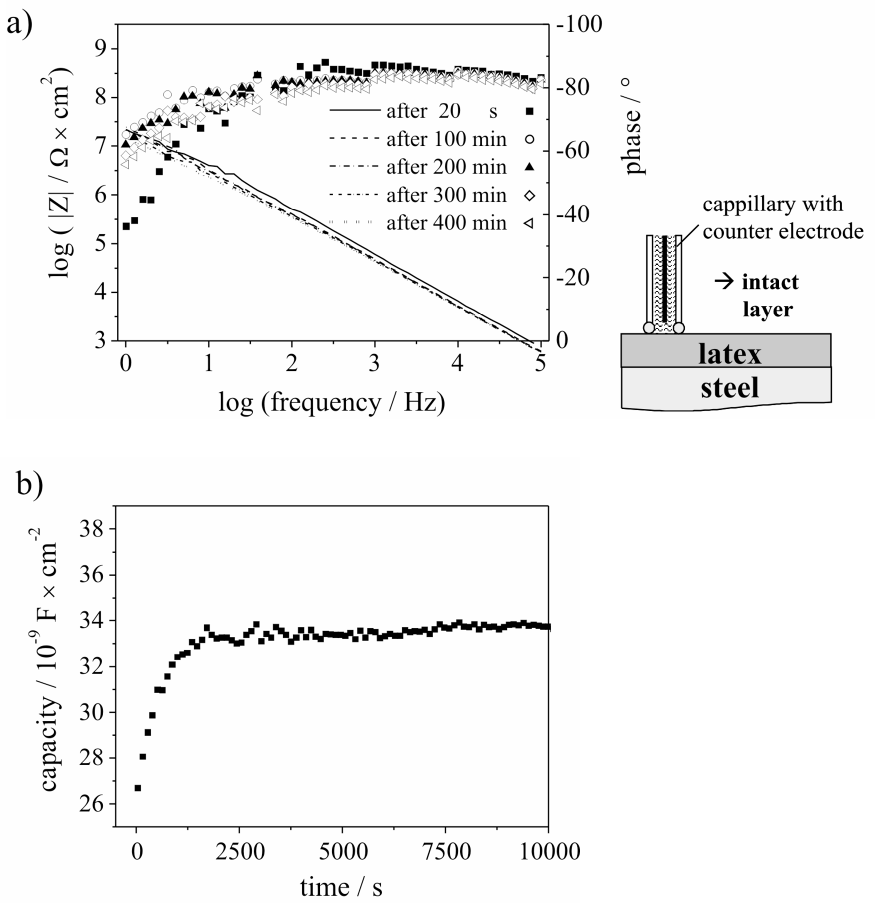

Fig. 3.48: Water uptake of latex system nBA/Sty(T_g = -20 °C) after film formation for 1 h at 60 °C. a) Bode-plots, b) coating capacity development with time, displayed for 10 kHz.

Fig. 3.48a presents the time dependent development of Bode-plots recorded on coating nBA/Sty(T_g = -20 °C). For the classification of the latex films see Fig. 3.49. A phase value of > 80° dominates a wide frequency range and is nearly constant during the whole measurement time. Consequently, the detected impedance appears to be mainly determined by the coating capacitance C_p and points at a completely formed, nearly defect free latex layer [16]. Calculation of C_p at phase maximum and illustration vs. time (see Fig. 3.48b) allows estimation of the saturation capacitance and initial C_p development in order to determine the coefficient for water diffusion through the polymer bulk. With $1.7 \pm 1.0 \cdot 10^{-10}$ cm^2/s (see Fig. 3.49) it ranges in the order of magnitude also determined by Galliano et al. [3]. With constant time of one hour and an annealing temperature of 60 °C, a decreasing film quality with increasing T_g could be detected. Already for the systems with a T_g of $\approx$ 0 °C surface areas with local defects and/or micro fissures more and more affect the impedance spectra.

coating category	exact T_g [°C]	D [10^{-10} cm^2/s]	ϕ [%]
nBA/Sty(T_g= -40 °C)	-42.5	1.7	7.2
nBA/Sty(T_g= -20 °C)	-22.0	1.7	4.8
nBA/Sty(T_g= 0 °C)	-2.3	2.2	7.9
nBA/Sty(T_g= 20 °C)	19.0	1.7	8.5
nBA/Sty(T_g= 40 °C)	39.0	---	---

coating category	exact T_g [°C]	D [10^{-10} cm^2/s]	ϕ [%]
EHA/Sty(T_g= -40 °C)	-42.0	1.1	4.2
EHA/Sty(T_g= -20 °C)	-17.7	2.6	4.2
EHA/Sty(T_g= 0 °C)	1.4	2.6	4.8
EHA/Sty(T_g= 20 °C)	19.6	2.9	3.2
EHA/Sty(T_g= 40 °C)	42.5	---	---

coating category	exact T_g [°C]	D [10^{-10} cm^2/s]	ϕ [%]
nBA/EHA/Sty(T_g= -20 °C)	-19.2	2.4	4.8
nBA/EHA/Sty(T_g= 40 °C)	38.1	---	---

Fig. 3.49: Overview of the latex systems, classified with respect to the applied monomer composition of nBA/Sty, EHA/Sty and nBA/EHA/Sty. The T_g *category is mentioned in brackets. Exact polymer* T_g*, relative water uptake* ϕ *and coefficient D for water diffusion through the polymer bulk after annealing for 1 h at 60 °C are displayed. For calculation of D an averaged film thickness of 5 µm was estimated; statistical thickness variations led to an averaged uncertainty of* $D \approx \pm 1.0 \cdot 10^{-10}$ cm^2/s.

Fig. 3.50a illustrates Bode-plots recorded on an intact area of a nBA/Sty(T_g = 0 °C) layer. Fig. 3.50b in contrast represents the Bode-plots for a defect-rich surface section of nBA/Sty(T_g = 0 °C). Phase value and absolute impedance distinctly decreased at lower frequencies during the first minutes of the experiment. Obviously coating pores and micro cracks accelerated the electrolyte ingress [19].

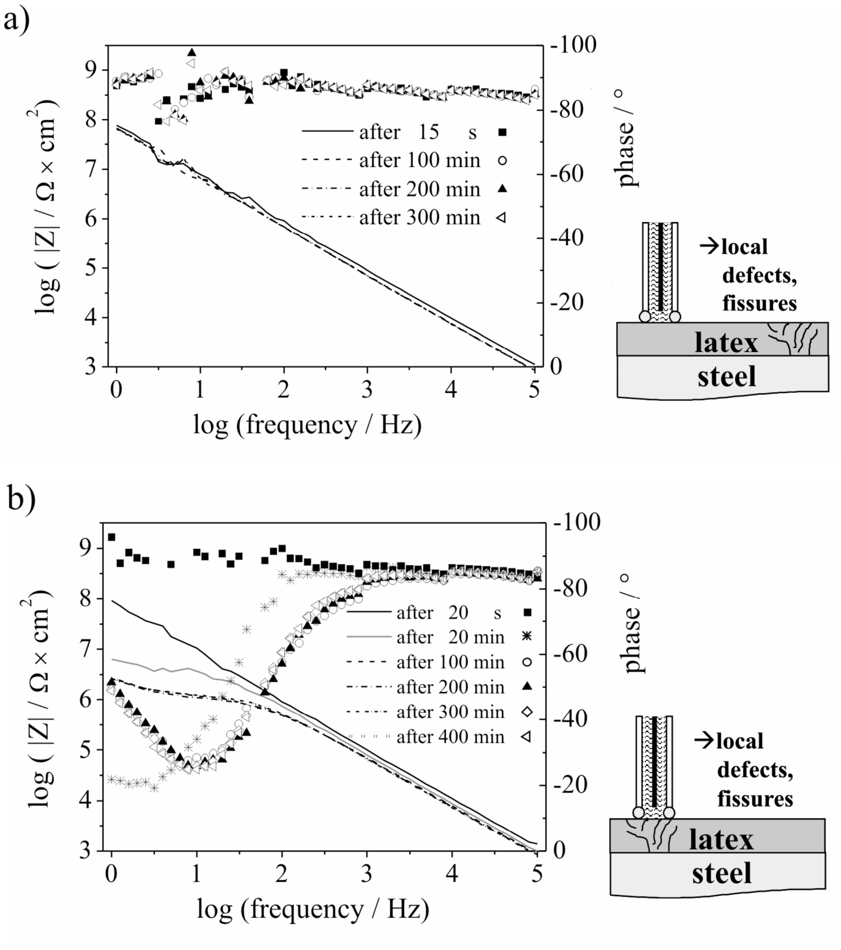

Fig. 3.50: Barrier properties of latex system nBA/Sty(T_g = 0 °C) after film formation for 1 h at 60 °C. a) Bode-plots recorded on a nearly defect-free film surface area, b) Bode-plots recorded on a coating area with local defects and/or fissures.

A nearly entire loss of coating corrosion protection was received for the latex systems of $T_g \approx 40$ °C, annealed 1 h at 60 °C. Fig. 3.51b exemplarily displays the Bode-plots recorded on a layer of EHA/Sty(T_g = 40°C). The maximum impedance value (measured at 1 Hz) with $\approx 1 \cdot 10^6\ \Omega\cdot\text{cm}^2$ is about three orders of magnitude smaller in comparison to those of Fig. 3.48a and 3.50a with $\approx 1 \cdot 10^{-2}\ \Omega\cdot\text{cm}^2$. For the 20 s initial measurement two time constants of C_p and a parallel double layer capacitance C_{DL} seem to contribute to the observed phase graph maxima. Such circuit is expected as typical for coatings with large pores [16,19]. For a schematic illustration see also Fig. 3.52.

Anyhow, the shape of the impedance spectra in Fig. 3.51b quickly converges towards that one received for the uncoated steel surface displayed in Fig. 3.51a. Obviously, no complete film formation was achieved. This result can be attributed to the small temperature difference between polymer T_g and applied film formation temperature [1-2,4].

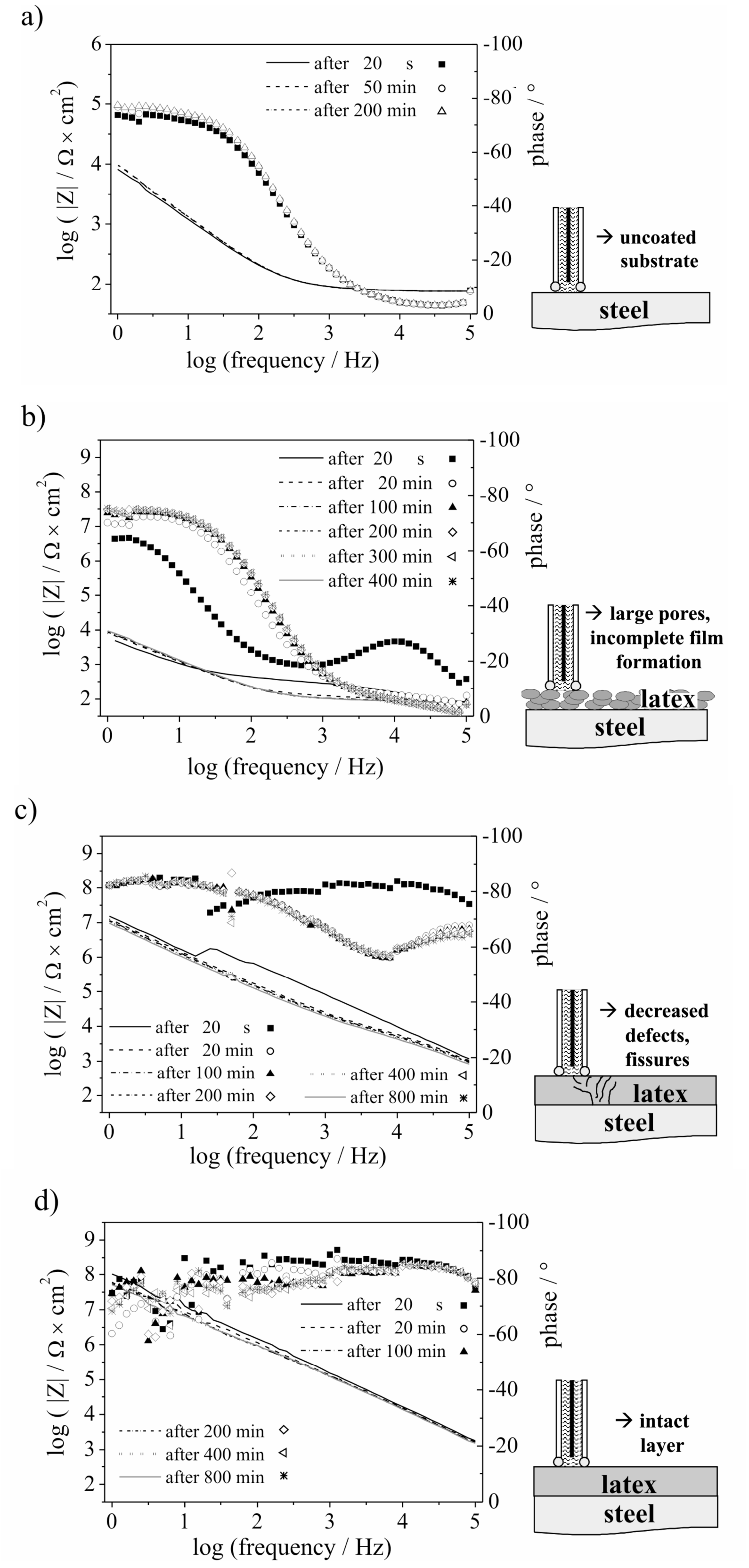

Fig. 3.51: Barrier properties of latex system EHA/Sty(T_g = 40 °C). a) Bode-plots recorded on the uncoated steel substrate (see also section 3.1), b) Bode-plots recorded after annealing of EHA/Sty(T_g = 40 °C) for 1 h at 60 °C, c) Bode-plots recorded after annealing of EHA/Sty(T_g = 40 °C) for 1 h at 80 °C, d) Bode-plots recorded after annealing of EHA/Sty(T_g = 40 °C) for 1 h at 100 °C.

As expected, improved barrier properties were received after annealing for 1 h at 80 °C (see Bode-plots of Fig. 3.51c), but nevertheless an entirely capacitively dominated impedance spectrum could be solely recorded after film formation for 1 h at 100 °C, as can be seen from Fig. 3.51d. The maximum impedance value of $\approx 1 \cdot 10^{-2}\ \Omega \cdot cm^2$ at 1 Hz in this case is comparable to those received for nBA/Sty(T_g = -20 °C) and nBA/StyT_g = 0 °C), annealed 1 h at 60 °C.

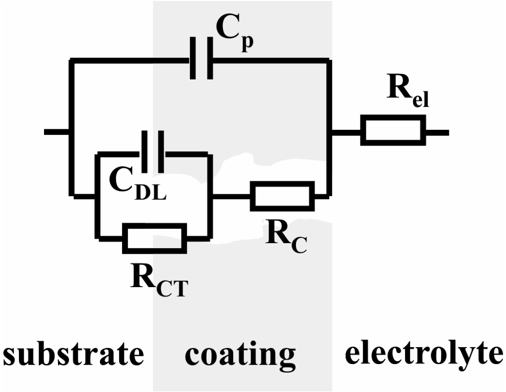

Fig. 3.52: Common equivalent circuit for a defect containing polymer film with C_p: coating capacitance, R_{el}: electrolyte resistance, R_C: coating resistance, R_{CT}: charge transfer resistance, C_{DL}: double layer capacitance [16].

Coefficients for water diffusion through the polymer bulk were solely calculated for impedance spectra with a dominant coating capacitance C_p. The resulting values for all 1 h at 60 °C annealed coatings of the series nBA/Sty, EHA/Sty and nBA/EHA/Sty with a T_g between -40 °C and 20 °C are displayed in Fig. 3.49. Additionally, Fig. 3.53 lists the respective coefficients for the latices of the T_g 40 °C-category, cured 1 h at 100 °C. Obviously, water uptake and coefficients for water diffusion through the polymer films cannot be correlated to the glass transition temperatures. A slight tendency within the diffusion coefficients for EHA/Sty latices displayed in Fig. 3.49 remains below the limit of statistical significance. It is the question whether the diffusion kinetics for EHA/Sty coatings are generally accelerated compared to nBA/Sty latices, but nevertheless their averaged water uptake with 4.1 ± 0.7 % remains constantly smaller in comparison to nBA/Sty layers, which exhibit a value of 7.1 ± 1.6 % (see Fig. 3.49). The presented results confirm that the amount of water at the polymer/oxide/iron interface rises with increasing pore density and microscopic fissures within the coating. Layer defects are a result of an incomplete film formation, which is directly correlated to the T_g of the applied polymer. Latices of the T_g 40 °C-category require an annealing temperature of at least 100 °C for adequate film formation if the curing time of 1 hour is kept constant. However, the comparison of Fig. 3.49 and Fig. 3.53 confirms a slightly reduced water uptake and smaller water diffusion coefficients compared to the coatings of lower T_g, cured 1 h at 60 °C.

coating	D [10^{-10} cm²/s]	ϕ [%]
nBA/Sty(T_g= 40 °C)	0.9	3.7
EHA/Sty(T_g= 40 °C)	1.7	1.6
nBA/EHA/Sty(T_g= 40 °C)	0.7	1.9

Fig. 3.53: Calculated relative water uptake ϕ and water diffusion coefficients D for the latices with a $T_g \approx 40$ °C, after film formation for 1 h at 100 °C (uncertainty of $D \approx \pm 1.0 \cdot 10^{-10}$ cm²/s).

Up to a latex T_g of 20 °C, water diffusion through defect free layer sections occurs with comparable velocity within the nBA/Sty and EHA/Sty coating series, indicating that particle interfaces are comparably compacted. The availability and efficiency of nanoscopic interparticle channels for water diffusion does not vary significantly. Nevertheless it cannot be excluded that polymer chain interdiffusion for the coalescing latex particles occurs to different extents during annealing. The monomer composition between the single coating T_g-categories continuously differs as well as the temperature difference between respective T_g and applied curing temperature. This should also affect the polymer chain mobility. However, such effects seem to be superposed by other parameters. As a constant amount of surfactant agent was applied during emulsion polymerisation of the latex dispersions, it can be expected that the density of hydrophilic surfactant groups exposed to particle interfaces and into free volumes between the particles will not vary too much after polymer film formation. Repulsion of hydrophobic organic macromolecules will additionally counteract an accelerated polymer chain interparticle diffusion. This could explain why the EIS data seem to indicate comparable water diffusion kinetics within the nBA/Sty and EHA/Sty coating series. In this context the monomer composition of the applied dispersions are better reflected by the increased relative water uptake of nBA/Sty-latex layers. The H_2O ingress velocity for these coatings may be decreased or similar to EHA/Sty films, but obviously the water amount simultaneously entering the polymer indeed is higher applying nBA/Sty dispersions.

3.5.3.2 Corrosion stability of latex/iron oxide interfaces applying nBA/Sty dispersions

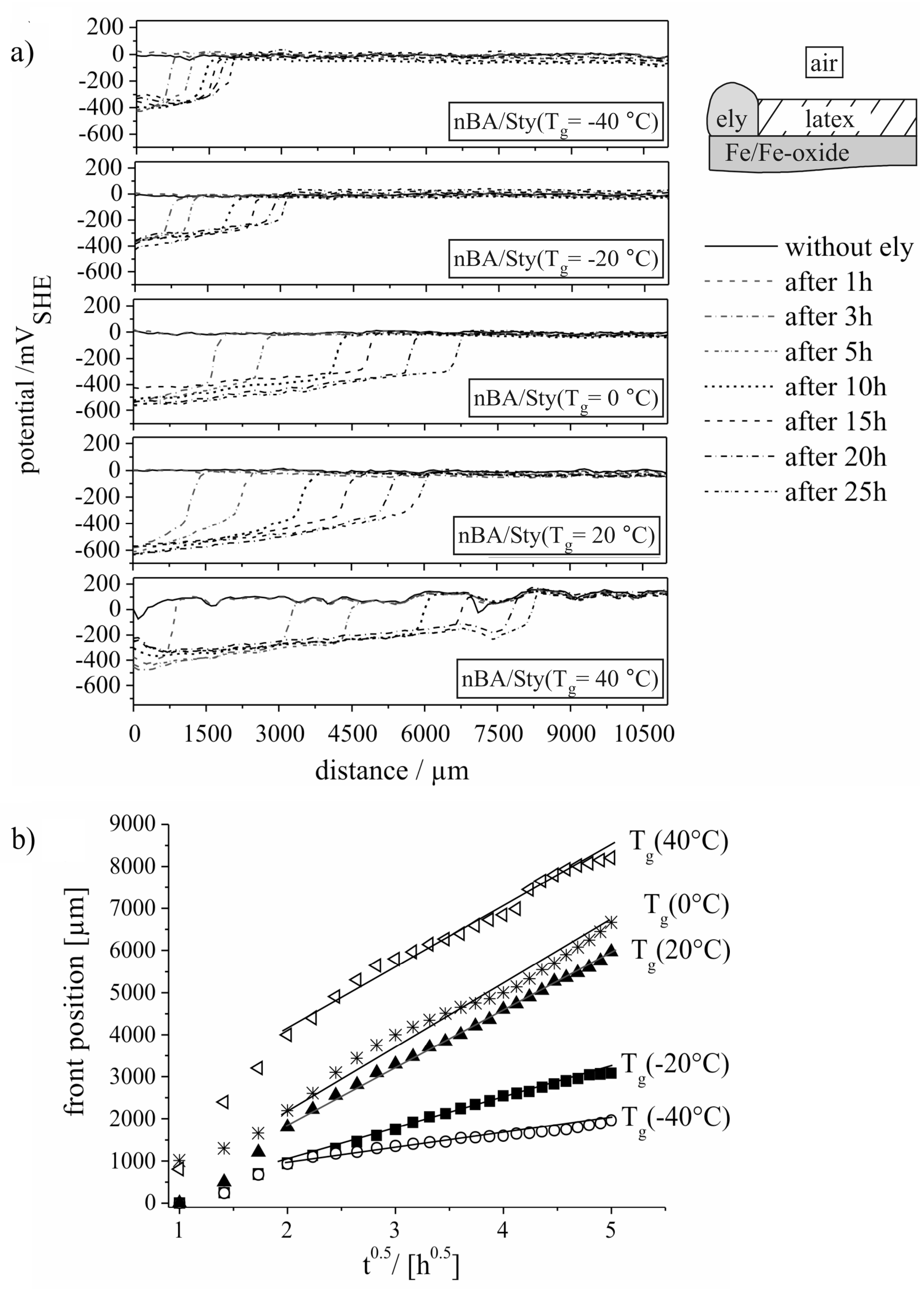

Fig. 3.54: SKP cathodic delamination study of nBA/Sty-iron oxide/iron interfaces in humid air. Film formation was performed by annealing for 1 h at 60 °C, except system nBA/Sty(T_g = 40 °C), which was cured 1 h at 100 °C. a) SKP potential profiles, b) diagram of the delamination front position vs. square root of time, calculated from the potential profiles of Fig. 3.54a.

Cathodic delamination was initiated at latex/iron oxide/iron interfaces and monitored by SKP potential mapping to further reveal the influence of different coating formulations on the interface stability in particular with respect to the polymer T_g.

As variations within the latex compositions between sequent nBA/Sty T_g-categories were relatively small, the comparability of the observed corrosive de-adhesion progress again had to be ensured by parallel investigation of sample sets exposed to the same environmental conditions. Thereby any interfering fluctuations of oxygen partial pressure, temperature and relative atmospheric humidity could be avoided. Fig. 3.54 illustrates the detected potential profiles for the five nBA/Sty coatings. As it was the intention to focus on defect free polymer layers, the latices were cured for 1 h at 60 °C, except the layer of system nBA/Sty(T_g = 40 °C), which was annealed for 1 h at 100 °C.

Obviously the cathodic delamination process for the nBA/Sty coating series proceeds accelerated with increasing T_g of the latex layers (see Fig. 3.54a). The progress of corrosive de-adhesion again is reflected by the lateral displacement of the turning points within the potential profiles of Fig. 3.54a [20]. The respective graphs of Fig. 3.54b indicate that the corrosive de-adhesion kinetics follow a square root of time dependency after an initiation period. This points at a transport controlled process as rate-determining step typically reported for cathodic delamination and was associated with the interfacial Na^+_{aq} cation mobility between defect area and electrolyte front position [20]; see also section 3.4. It was observed that the interface degradation rate of sample nBA/Sty(T_g = 20 °C) was slightly smaller compared to nBA/Sty(T_g = 0 °C). This does not represent a typical property of the respective coating. In fact it was recognised that one sample of a set of five latex/iron oxide interfaces investigated in parallel often did not follow the general tendency. But repeated measurements confirmed that such variation occurred statistically.

Fig. 3.55 illustrates SKP potential profiles recorded during an interfacial ion transport study of the nBA/Sty coatings, started in humid nitrogen atmosphere and continued in humid air. Proceeding interface deterioration in N_2 atmosphere was detected for latices with a T_g at or above 20 °C (see Fig. 3.55a). For latices with a T_g smaller than 20 °C, an unspecific reduction of the interface potential near the defect is solely observable for longer exposure times. Consequently it can be confirmed that application of the nBA/Sty(T_g = 20 °C) film usually does not result with an exceptionally stable interface, as it seemed to be indicated by Fig. 3.54a.

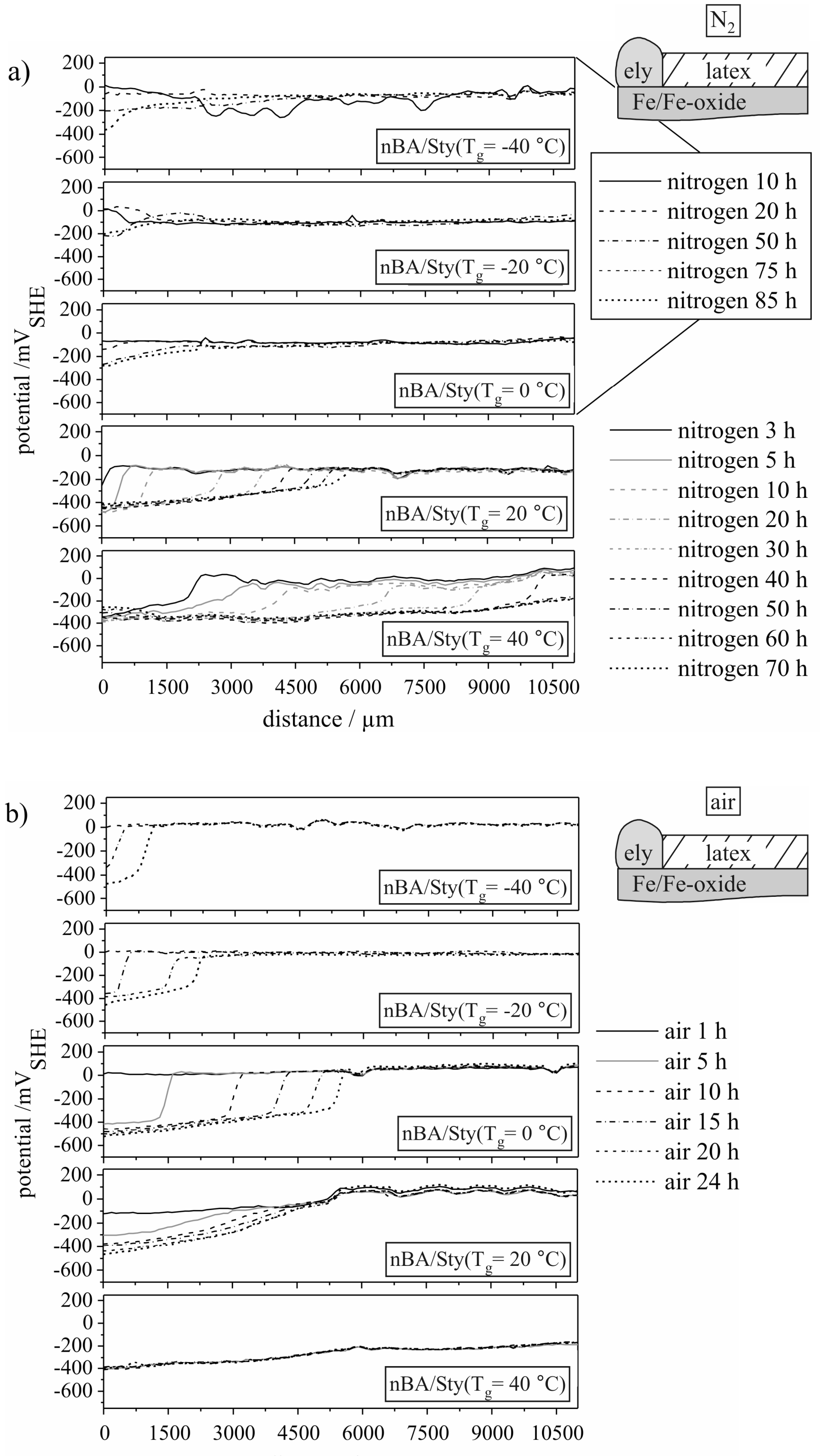

Fig. 3.55: SKP interfacial ion transport and cathodic delamination study of nBA/Sty-iron oxide/iron interfaces. Film formation was performed by annealing for 1 h at 60 °C, except system nBA/Sty(T_g = 40 °C), which was cured for 1 h at 100 °C. a) SKP potential profiles recorded in humid nitrogen atmosphere, b) SKP potential profiles recorded after switching to humid air.

Cathodic delamination in air and interfacial electrolyte ingress in nitrogen atmosphere are determined by comparable mechanisms of preferential cation transport (see sections 3.1 and 3.2). But the process velocity in oxygen deficient atmosphere should be reduced. Potentials of the intact polymer/substrate interface are similar for latices with a $T_g < 20$ °C and $T_g = 20$ °C. Consequently, interfacial ion transport is to be expected, but obviously does not occur due to kinetic inhibition. This can be attributed to a more compact latex/iron oxide interface with smaller interfacial free volumes at lower polymer T_g. Although water uptake is similar for the latices with a glass transition temperature ≤ 20 °C (see Fig. 3.49), impedance measurements confirmed that the amount of coating defects is reduced at low polymer T_g. After the experiment displayed in Fig. 3.55a was continued in air, cathodic delamination started for the nBA/Sty coatings with a $T_g < 20$ °C. Fig. 3.55b illustrates that its progress again rose with increasing glass transition temperature and confirms the tendency already reported after analysis of Fig. 3.55a. No ongoing delamination was detected for the nBA/Sty($T_g = 40$ °C) sample, because the interface was already extensively pre-damaged in nitrogen atmosphere before. Less pre-damaging is visible for the potential profiles of sample nBA/Sty($T_g = 20$ °C). Sustained interface potential decrease occurred within the area of preceding ion transport in inert atmosphere. Nevertheless cathodic delamination stopped after around 5000 μm, probably due to kinetic inhibition.

3.5.3.3 Corrosion stability of latex/iron oxide interfaces applying EHA/Sty dispersions

SKP cathodic delamination and interfacial ion transport studies were also performed for the EHA/Sty coating series. Fig. 3.56a illustrates SKP potential profiles recorded during sample exposure in humid nitrogen atmosphere. It can be confirmed that interface stability decreases with increasing latex T_g without any exception. Probably due to reduced polymer adhesion compared to the investigated samples of Fig. 3.55a, ion transport is also detected along interfaces with a latex T_g of less than 20 °C. It could not be entirely clarified whether this finding concerns intrinsic latex properties of nBA/Sty and EHA/Sty or just statistically occurs. Anyhow, the mentioned interface stability order is maintained after subsequent initiation of cathodic delamination in air (see Fig. 3.56b).

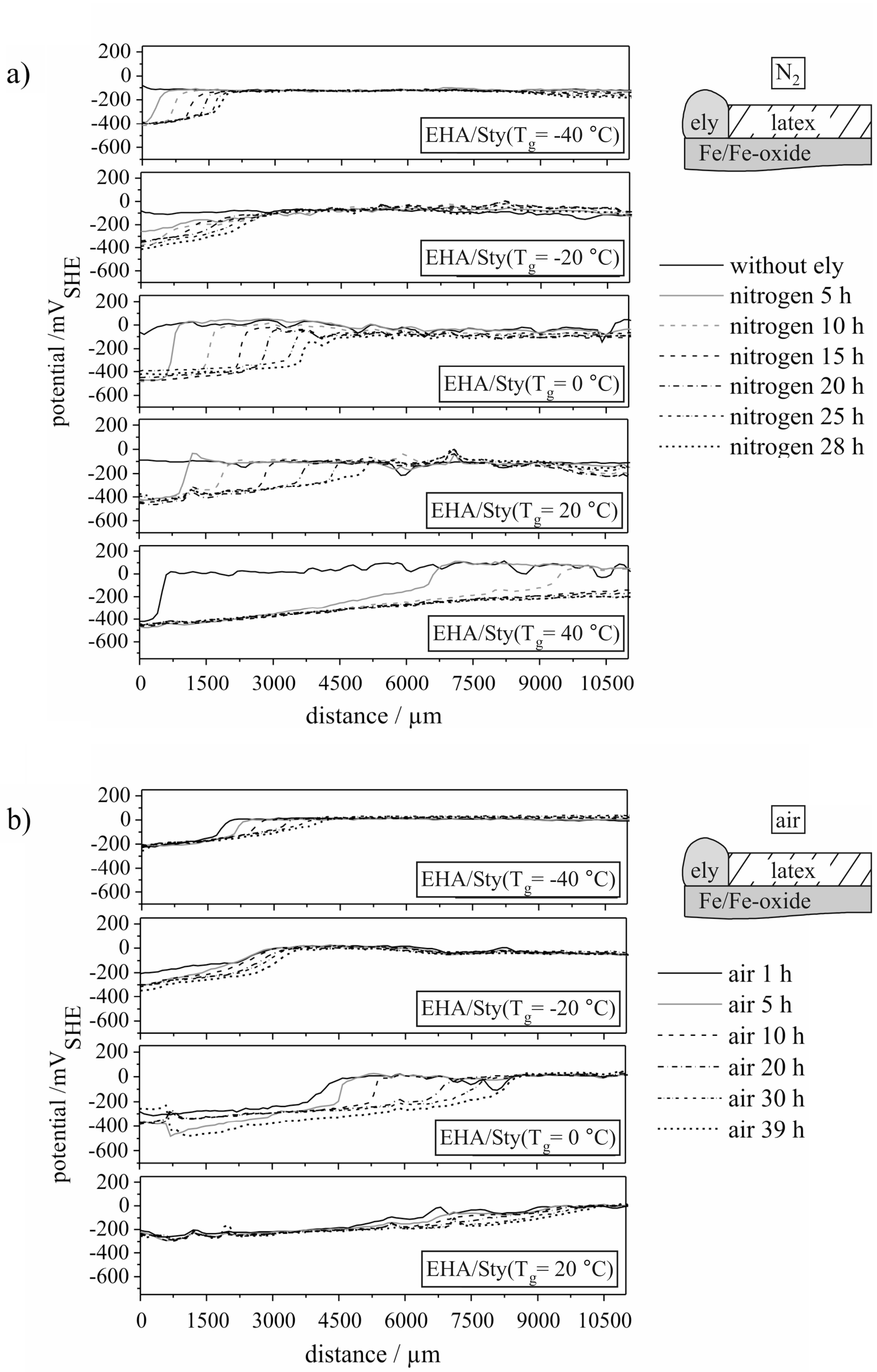

Fig. 3.56: SKP interfacial ion transport and cathodic delamination study of EHA/Sty-iron oxide/iron interfaces. Film formation was performed by annealing for 1 h at 60 °C, except system EHA/Sty(T_g = 40 °C), which was cured for 1 h at 100 °C. a) SKP potential profiles recorded in humid nitrogen atmosphere, b) SKP potential profiles recorded after switching to humid air.

A quantitative comparison of turning points versus √t is omitted, because the lateral potential step width within the potential profiles strongly varied or developed unspecifically. Furthermore monitoring of the interface degradation of sample EHA/Sty(T_g = 40 °C) had to be aborted, as corrosion occurred extremely fast. Fig. 3.57 offers a visual impression of EHA/Sty coatings, applied on iron/iron oxide substrates and after the samples were exposed to humid air for four days.

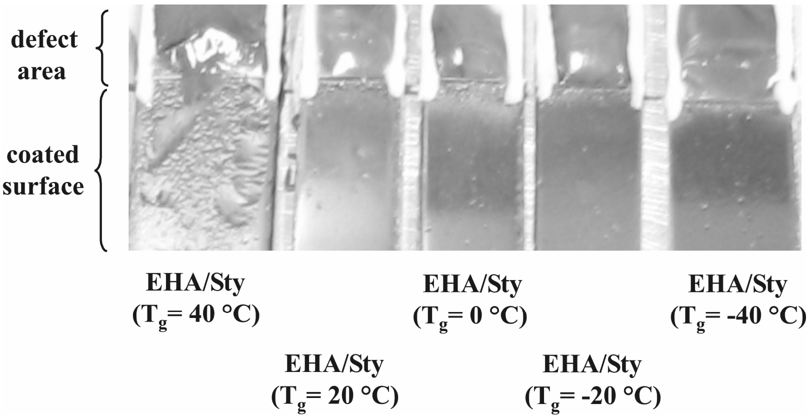

Fig. 3.57: Corrosive de-adhesion study of EHA/Sty coated iron substrates. Latex film formation was performed by annealing for 1 h at 60 °C, except system EHA/Sty (T_g = 40 °C), which was cured for 1 h at 100 °C. The picture was taken after four days of sample exposure to humid air.

Although cathodic delamination was detectable on all substrates, solely for sample EHA/Sty(T_g = 40 °C) an extensive film deterioration was observed. The coating layer was partially de-adhered and the defect electrolyte widely spread along the surface. Obviously latex EHA/Sty(T_g = 40 °C) did not provide an acceptable corrosion resistance, although cured for 1 h at 100 °C. Lower interface stability of nBA/Sty (T_g = 40 °C) coated substrates, annealed for 1 h at 100 °C, compared to nBA/Sty (T_g = 20 °C) samples, heated for 1 h to 60 °C, was detected as well (see Fig. 3.54 and Fig. 3.55). Obviously curing at 100 °C for 1 h indeed improves the latex barrier properties, as it was monitored by impedance spectroscopy, but the disadvantageous effect of a T_g higher than 22 °C ambient temperature nevertheless could not be compensated. Latices of the T_g(40 °C) category are in glassy, brittle state at room temperature. The interfacial contact between the nano-rough surface and the formed polymer layer is likely to be smaller for films with high T_g compared to latices with lower T_g. Such improved interfacial contact and mobility of polymer chains promotes a reduction of free volumes at the polymer/substrate interface and a stronger inhibition of the interfacial cathodic reduction process. T_g(40 °C)-polymers take up less water than latices in rubber-like state (compare Fig. 3.49 and Fig. 3.53). But an expected decrease of the interfacial water activity again does not seem to compensate disadvantageous effects arising from mechanic polymer properties at an ambient temperature below T_g.

3.5.3.4 Comparison of the latex coating series

Surface energies of latex films were calculated based on contact angle measurements to further evaluate the effect of the applied monomer composition on the resulting resistance towards coating/substrate interface degradation and on the achieved polymer barrier properties. They were separated into polar and dispersive contributions and are displayed in Fig. 3.58.

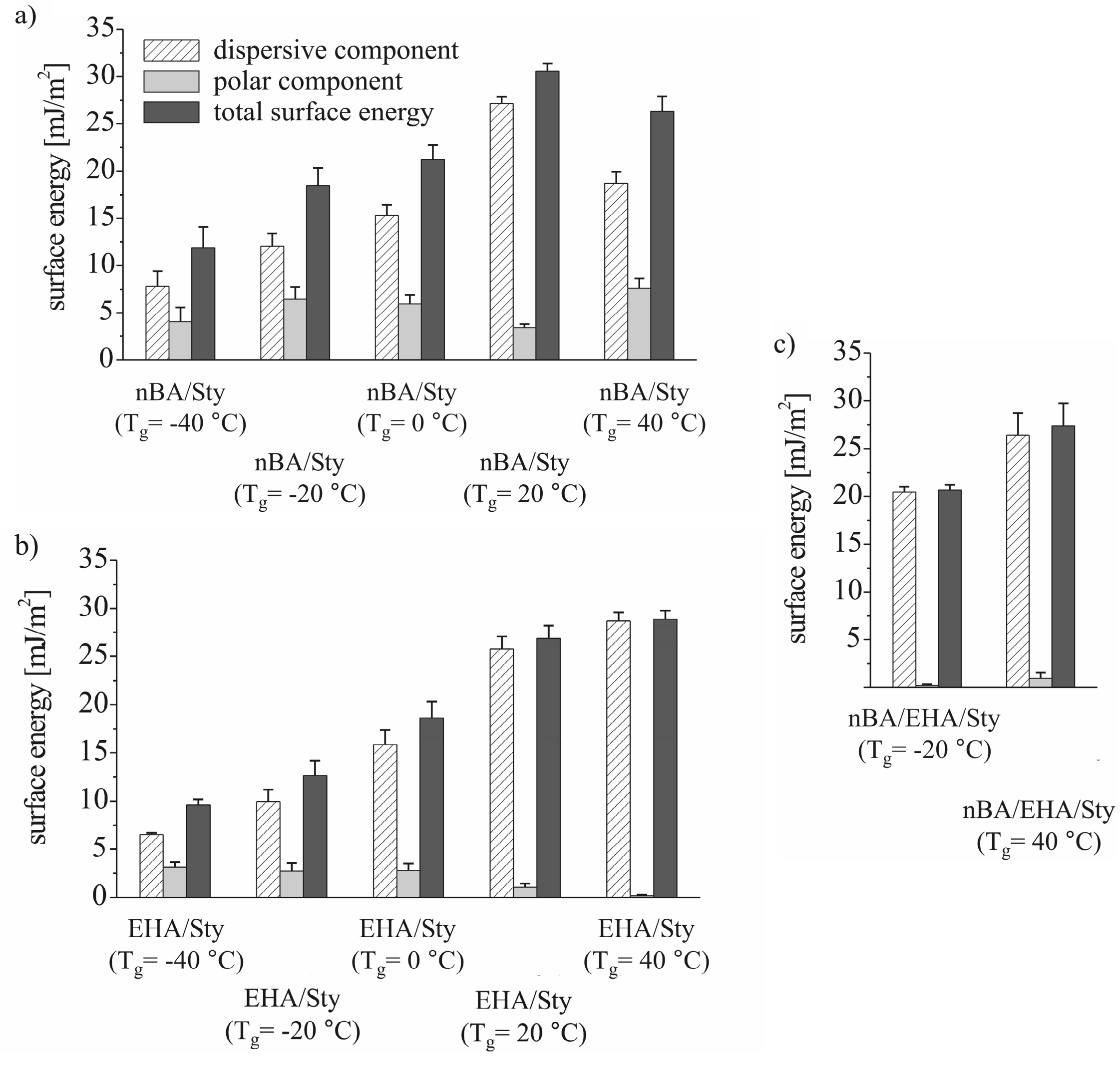

Fig. 3.58: Total surface energy of the latex coatings (cured for 1 h at 60 °C) with indication of polar and dispersive component. a) polymer series nBA/sty, b) polymer series EHA/Sty, c) polymer series nBA/EHA/Sty.

A general increase of the total surface energy corresponds to higher latex glass transition temperatures. This tendency is determined by a correlated increase of dispersive interactions. A continuous reduction of the polar component with higher T_g was solely observed for the EHA/Sty coatings. The total surface energy levels were similar for the nBA/Sty, EHA/Sty and nBA/EHA/Sty series, varying between ≈ 10 mJ/m^2 for the T_g(-40 °C)-category and ≈ 30 mJ/m^2 for the T_g(40 °C)-category. They point at comparable macromolecular chain lengths for latices of different monomer composition, but same glass transition temperature. Surfactants applied during emulsion polymerisation tend to enrich at the latex surfaces during film formation [1]. To check the reliability of the achieved data, contact angle measurements were repeated after rinsing the coatings with water and ethanol. It was proven that such a rinsing procedure did not change the above reported results.

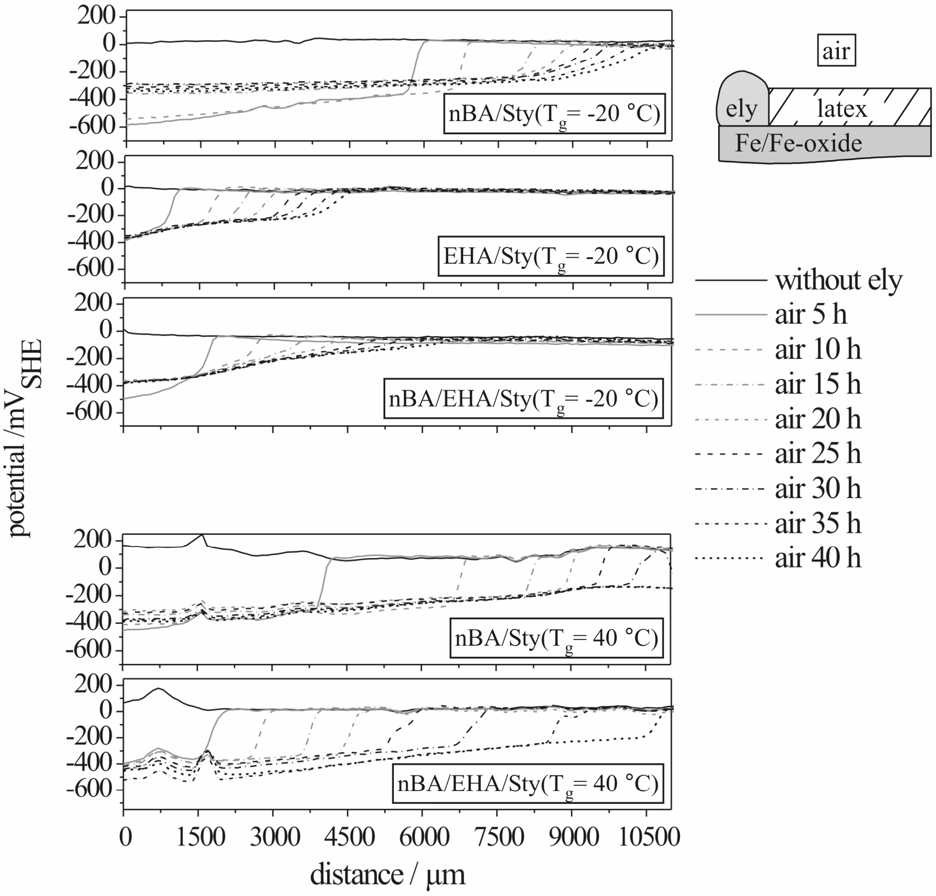

Fig. 3.59: Comparison of the interface stability of nBA/Sty, EHA/Sty and nBA/EHA/Sty layers applied on iron substrates. Latices of the T_g(-20 °C)-category were annealed for 1 h at 60 °C, latices of the T_g(40 °C)-category were annealed for 1 h at 100 °C. Displayed are the SKP potential profiles of a cathodic delamination study performed in humid air.

To further evaluate the influence of the applied monomers, the polymer/substrate interface stability of the three coating series were compared. Fig. 3.59 illustrates a cathodic delamination study performed with the T_g(-20 °C) latices, nBA/Sty ($T_g = 40$ °C) and nBA/EHA/Sty($T_g = 40$ °C) applied on iron oxide covered iron. The delamination velocity increased in the order EHA/Sty < nBA/EHA/Sty < nBA/Sty for the samples with a T_g of -20 °C, and interface degradation for nBA/Sty($T_g = 40$ °C) was accelerated compared to nBA/EHA/Sty($T_g = 40$ °C) as well. Obviously a copolymer mixture of n-butyl acrylate, styrene and 2-ethylhexyl acrylate indeed led to averaged interface stability compared to pure nBA/Sty and EHA/Sty compositions. A distinct description of the macromolecular structure as function of the applied monomers, the resulting molecular conformation and its influence on the final latex particle composition cannot be given based on the presented data. However, it can be confirmed that application of the monomer n-butyl acrylate obviously leads to polymer layers with larger water uptake (see Fig. 3.49 and Fig.3.53).

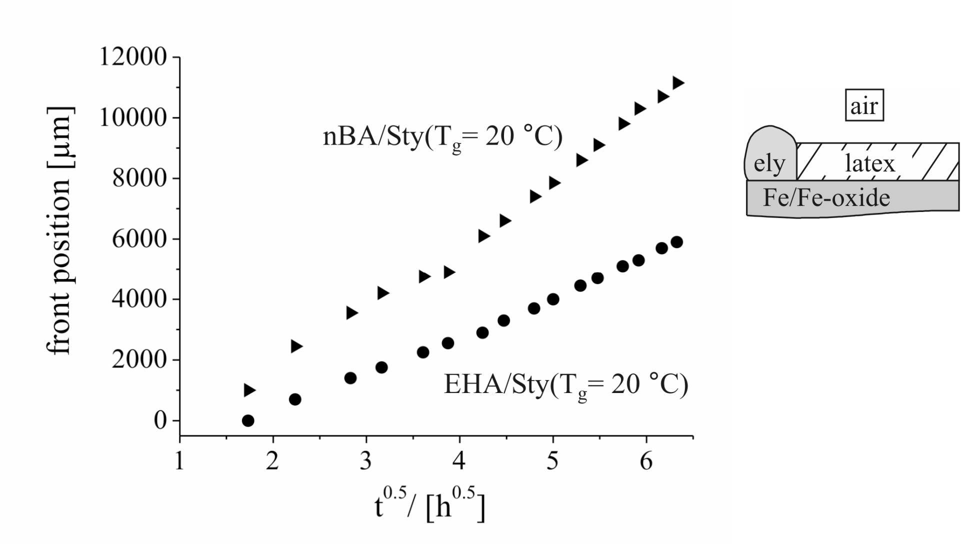

Fig. 3.60: Comparison of the interface stability of nBA/Sty($T_g = 20$ °C) with EHA/Sty($T_g = 20$ °C), annealed for 1 h at 60 °C after application on iron substrates. Displayed is the respective cathodic delamination front position versus square root of time, calculated from SKP potential profiles gained during a corrosive de-adhesion study performed in humid air.

Fig. 3.60 displays the front position versus √t plots calculated from a simultaneously performed cathodic delamination study of nBA/Sty($T_g = 20$ °C) and EHA/Sty ($T_g = 20$ °C) coatings. It can be confirmed that latex layers based on 2-ethylhexyl acrylate/styrene copolymer compositions led to improved interfacial stability during cathodic delamination. A schematic overview of the tendencies gained towards cathodic delamination resistance of latex coated iron oxide/iron substrates is additionally illustrated in Fig. 3.61.

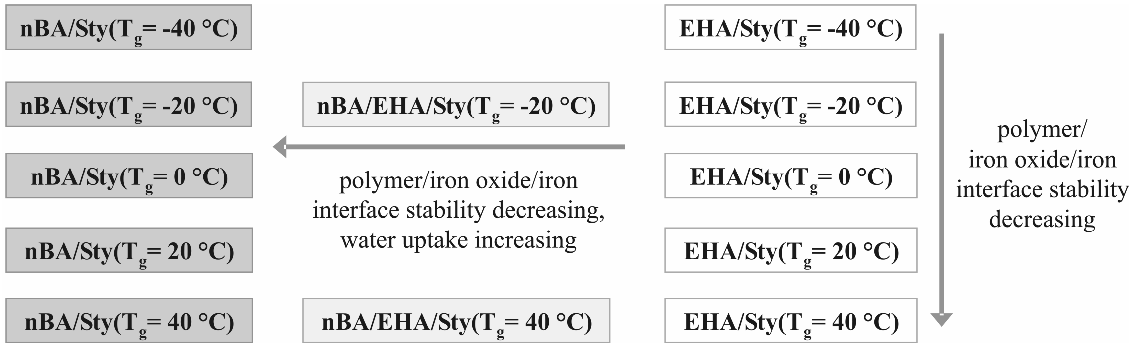

Fig. 3.61: Overview of the tendencies gained towards cathodic delamination resistance of latex coated iron oxide/iron substrates.

3.5.3.5 Evaluation of the latex/oxide/metal interface stability as function of the substrate material

After evaluation of the interface stability of latex polymers applied on iron substrates studies were extended to coated zinc samples. It was intended to check whether tendencies observed during interfacial corrosive de-adhesion can be also detected for different substrate material.

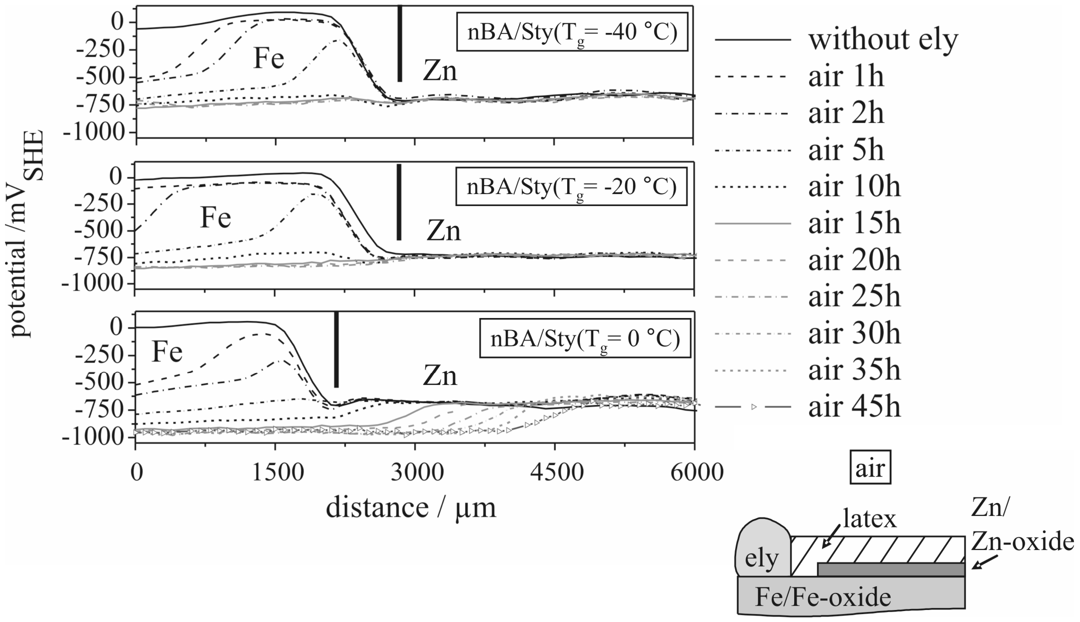

Fig. 3.62: Corrosive delamination along nBA/Sty coated iron-zinc transitions. Film formation was performed by annealing for 1 h at 60 °C. Displayed are SKP potential profiles recorded in humid air.

Fig. 3.62 illustrates SKP potential profiles recorded for such processes along iron/zinc transitions after coating with nBA/Sty latices of a T_g between -40 °C and 0 °C. The change of the metal surface can be easily identified by a distinct potential decrease from around 0 mV_{SHE} to between approximately -750 mV_{SHE} and -950 mV_{SHE}. The kinetics of corrosive delamination were decelerated when the electrolyte front position reached the zinc area; for nBA/Sty(T_g= -40 °C) and nBA/Sty(T_g= -20 °C) the process even completely stopped. It has to be pointed out that Zn as the less noble metal obviously cathodically polarised the whole interfacial area in contact with electrolyte, including the defect section. Its potential was shifted to around -950 mV_{SHE}, as well and resembled that one detected for zinc. Very stable interfaces on zinc substrates were received with a nBA/Sty layer of a T_g below 0 °C. This generally confirms the conclusion that the velocity of corrosive de-adhesion rises with increasing glass transition temperature of the polymer. A detailed study of the potential profiles of Fig. 3.62 additionally underlines that the SKP obviously does not detect a potential difference on the nBA/Sty(T_g= -40 °C) and nBA/Sty(T_g= -20 °C) samples between delaminated iron area and the intact latex/zinc interface. This points at the absence of any relevant driving force for corrosive delamination according to [20-25]. Within section 3.2 it could be proven that such criterion does not necessarily apply to reactive electrolyte spreading processes along uncoated substrates with an artificial iron/zinc transition. Fig. 3.62 now shows that driving forces for cathodic de-adhesion indeed seem to be existent for the selected composition and geometry of polymer coated samples, but occur to be masked towards detection by SKP unless the interface structure allows the ingress of hydrated ions from the defect. Once the defect area is cathodically polarised by zinc, the progress of ion transport can be monitored with the Scanning Kelvin Probe again. Obviously the polymer/substrate interface is less compact for nBA/Sty(T_g= 0 °C) coated zinc oxide/zinc surfaces compared to latices with lower T_g.

The experiment presented with Fig. 3.62 was also repeated for cathodic delamination studies of nBA/Sty covered iron/silicon oxide interfaces. Fig. 3.63 presents the respective SKP potential profiles recorded along an artificial Fe/SiO_2 transition. A 10 nm silicon oxide layer was generated by plasma polymer deposition. It was proven to result in an effective corrosion protection of the interface [11,26]. Such procedure is also commercially applied as SiO_2 is non-conductive. It therefore reduces the electrochemical activity and especially inhibits interfacial oxygen reduction processes at the substrate surface, dependent on the silicon oxide surface coverage [11,26].

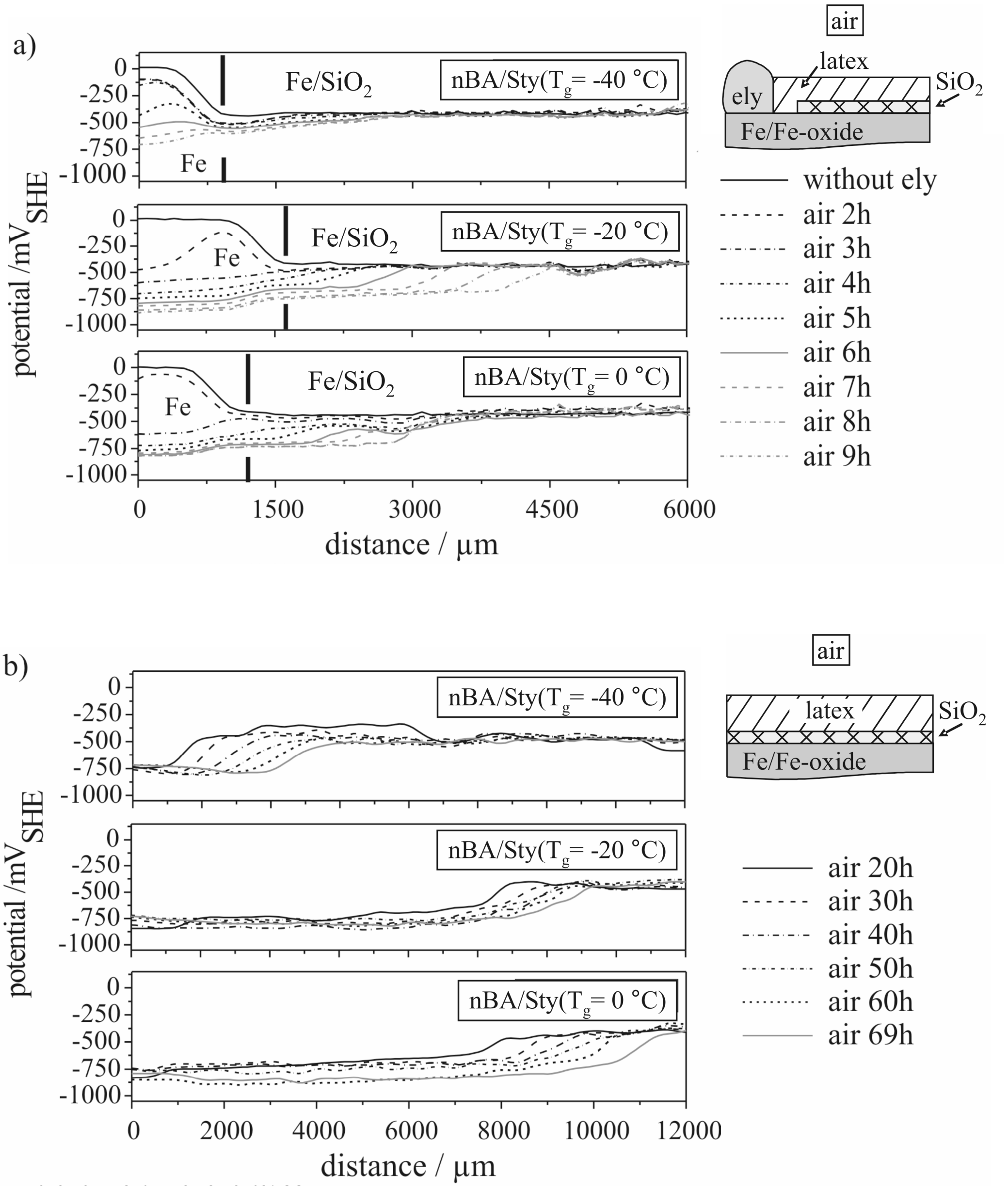

Fig. 3.63: Cathodic delamination along nBA/Sty coated iron-SiO_2 transitions. 10 nm SiO_2 films were generated on iron substrates by plasma polymerisation (see section 3.5.2.1). Polymer film formation was performed by annealing for 1 h at 60 °C. Displayed are SKP potential profiles recorded in humid air, a) directly along the Fe/SiO_2 transitions, b) within the SiO_2 modified area at later time.

Due to the additional thin isolating layer, the potential of the latex/SiO_2/iron oxide/iron interface is cathodically shifted to around -500 mV_{SHE}. This can be explained by a reduced initial oxygen reduction current density. With iron oxide oxidation as counter reaction the isolated electrochemical cell at the intact interface consequently leads to a steady state at reduced anodic overpotential [20-22]; see also chapter 1. But as the silicon oxide film is porous and the polymer/SiO_2/Fe-oxide adhesion may be reduced, interfacial ion transport proceeds along all three samples. It occurs with relatively high velocity compared to the progress observed for latex coated zinc substrates (see Fig. 3.62). Therefore it can be assumed that capillary forces distinctly contribute to the overall ion transport rate. Fig. 3.63a indicates slowest progress for the nBA/Sty(T_g= -40 °C) coated sample and highest rate for ion transport along the nBA/Sty(T_g= -20 °C)-iron oxide/iron interface. It can be nevertheless concluded that fast transport is correlated to an increasing latex glass transition temperature when continuously recording SKP potential profiles also at longer times (see Fig. 3.63b). After 69 hours the progress of de-adhesion results in the sequence 0 °C > -20 °C > -40 °C, which is obviously determined by the polymer T_g. It seems to adequately reflect the thermodynamic process driving forces. Potential profiles monitored during the initial state of ion transport along latex coated SiO_2/Fe-transitions in contrast appear to be more influenced by kinetic effects distorting the expected T_g tendency. This can be attributed to local inhibition or acceleration of electrode kinetics, probably due to a defect rich polymer structure near the SiO_2/Fe border.

It is interesting to note that the interface potential of the delaminated iron area between defect and silicon oxide/iron transition is also cathodically shifted after the ion front reached the SiO_2 modified interface section (compare Fig. 3.63a with Fig. 3.62). This unexpected result may be explained by assuming that the silicon oxide structure partly degrades after ingress of hydrated ions from the defect. A subsequent acceleration of oxygen reduction kinetics is not unlikely. Low-molecular dissolved or hydrated oxidic silicon species are usually negatively charged [27]. If they take part within a charge compensation process between the local electrodes of a galvanic cell, necessary e.g. to enforce cathodic delamination, these anions are potentially transported in direction to the defect. But as they are comparatively poorly soluble, partial precipitation may take place after local exceedance of the solubility products due to fluctuations of the interfacial water amount or inhomogeneity of the interface structure. This can further block the electrochemical activity of the iron hydroxide surface. The oxygen reduction current density decreases, resulting in a more cathodic interface potential detected by the SKP. Also changes within the surface dipole moments could contribute to the observed effects after adsorption of oxidic silicon species within the iron area between defect and SiO_2 modified interface section [28-30]. Nevertheless it has to be generally concluded that solely poor corrosion protection was achieved with the selected sample systems presented within Fig. 3.63.

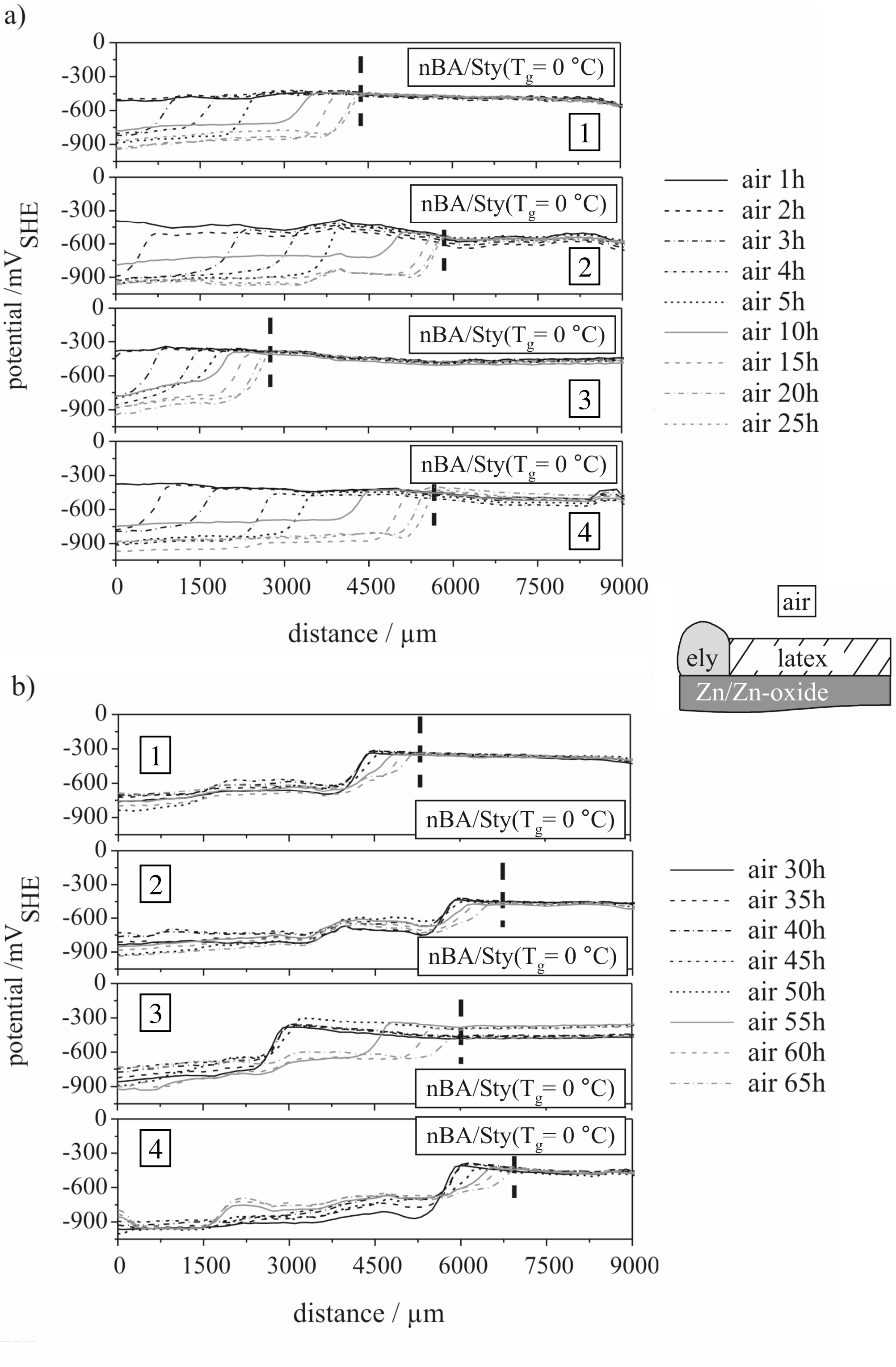

Fig. 3.64: Corrosive delamination study of nBA/Sty(T_g = 0 °C)- zinc oxide/zinc interfaces. Film formation was performed by annealing for 1 h at 60 °C. Displayed are SKP potential profiles, a) after reduction of the atmospheric humidity from > 95 % r.h. to 70 ± 5 % r.h. at t = 4 hours, b) after re-increasing the humidity to > 95 % r.h. at t = 47 hours. Bold dashed lines visualise the delamination progress after 25 and 65 hours.

To further reveal the influence of iron defects for corrosive de-adhesion along polymer coated zinc surfaces, experiments were continued applying also zinc as substrate material within the defect region. Fig. 3.64 offers a visual impression of the delamination progress along a set of four identically prepared and simultaneously investigated nBA/Sty(T_g= 0 °C)-zinc oxide/zinc interfaces. The SKP potential profiles indicate large fluctuations within the electrolyte front position. They confirm a general experience made during the investigation of additional sets of latex coated zinc samples when applying zinc also in the defect: No significant correlation could be detected between latex T_g and velocity of interface delamination due to tremendous, obviously statistical fluctuations of the progress rate (not shown here, but e.g. see also Fig. 3.67). For latex coated iron substrates, such tendencies were always detectable with remarkable reproducibility (compare with sections 3.5.5.2 to 3.5.5.4).

Even if poor adherence of latex films to zinc oxide surfaces is supposed compared to iron substrates, the influence of the defect substrate material nevertheless seems to be of great importance. This means that a Zn defect provides additional driving force for corrosive de-adhesion processes along adjacent latex/zinc oxide/zinc interface sections. But a zinc defect can solely indirectly affect the already degraded interface. Accelerated delamination progress has to be related to an increased oxygen reduction current density at the electrolyte front position, which is enabled by an improved ion exchange between the local electrodes of the galvanic cell for reasons of charge compensation. Compared to iron local chemical processes occurring within an electrolyte covered Zn defect obviously amplify the electrostatic attraction of anions from the delaminated area and/or support the repulsion of cations to the delamination front position. This finding is to be prospectively investigated in detail.

Fig. 3.64 additionally confirms that corrosive de-adhesion processes accelerated by electrochemical stimulation of the interfacial electrode kinetics become susceptible for kinetic inhibitions. This could be also concluded after analysis of Scanning Kelvin Probe Blister Test studies performed at varying atmospheric humidity and increased cathodic polarisation of the defect (see section 3.3.3.5). During the measurement displayed in Fig 3.64a the effect of the interfacial water activity was evaluated by reduction of the relative atmospheric humidity from > 95 % r.h. to around 70 % r.h. after the first 4 hours of the experiment. The ion transport velocity thereby was reduced on all four samples, but especially inhibited on sample 3. In section 3.3.3.5 it was assumed that this can be attributed to the precipitation of corrosion products within the delaminated area after exceedance of solubility products at reduced interfacial water activity. This should consequently block the galvanic cell. After 25 hours the delamination front positions result in relatively large variations. Re-increase of the humidity to > 95 % r.h. at t = 45 hours did not distinctly affect delamination on samples 1, 2 and 4, but sample 3 underwent a strong acceleration (see Fig. 3.64b). Obviously the kinetic blockage was overcome and species precipitated before were resolved again. In the end the electrolyte front positions at all four interfaces equalised to a certain extent, but still varied more than it would have been expected from the investigation of four identically prepared samples of the same batch (compare to the relative differences detected for cathodic de-adhesion along iron substrates, coated with latices of different T_g; see sections 3.5.5.2 to 3.5.5.4).

3.5.3.6 Influence of the polymer network density on the stability of latex/oxide/metal interfaces

In sections 3.5.5.1 to 3.5.5.4 the effect of the polymer T_g on the latex/iron oxide/iron interface stability was investigated. Also contributing effects of film quality and latex interparticle diffusion during film formation were discussed.

coating	D [10^{-10} cm^2/s]
nBA/Sty(T_g= 0 °C)	2.4
nBA/Sty(T_g= 0 °C + 0.5 pphm tDMC)	0.1
nBA/Sty(T_g= 0 °C + 1.0 pphm tDMC)	0.2
nBA/Sty(T_g= 0 °C + 0.5 pphm BDDA)	1.1
nBA/Sty(T_g= 0 °C + 2.0 pphm BDDA)	1.0

Fig. 3.65: Overview of coefficients D for water diffusion through nBA/Sty(T_g= 0 °C)-films. The polymer network density was modified during emulsion polymerisation applying different amounts (pphm = parts per hundred million) of 1,4-butandiole diacrylate (BDDA) as cross-linking reagent and tertiary dodecylmercaptane (tDMC) to reduce the average polymer chain length. After spin coating, the layers were annealed for 1 h at 60 °C. For calculation of D an averaged film thickness of 5 µm was estimated; statistical thickness variations led to an averaged uncertainty of $D \approx \pm 1.0 \cdot 10^{-10}$ *cm²/s.*

This chapter extends the approach to layers received from copolymer dispersions with increased network density and reduced averaged polymer chain length within the single latex particles. Modifications were performed during emulsion polymerisation focussing on system nBA/Sty(T_g= 0 °C). The process recipes were identical to those of the dispersions applied before, except the addition of either 0.5 pphm (parts per hundred million) or 1.0 pphm tertiary dodecylmercaptane (tDMC) as reagent for macromolecular chain length control. Alternatively, 0.5 pphm or 2 pphm of 1,4-butandiole diacrylate (BDDA) were used for increased macromolecular density. It is known that cross-linking generally inhibits particle interdiffusion [31]. The effect of cross linking agents on the resulting coating films and their mechanic and chemical properties are intensively investigated [32-36]. Nevertheless detailed information of its effect on the resulting latex/substrate interface stability are hardly available.

With Differential Scanning Calorimetry (DSC) it could be confirmed that application of tDMC and BDDA did not result with nBA/Sty polymers of characteristic different glass transition temperature compared to the basic system nBA/Sty(T_g = 0 °C). The layer thicknesses were comparable to those of the unmodified nBA/Sty, EHA/Sty and nBA/EHA/Sty series after an identical spin coating process (30 s at 1500 rpm) as well. Film barrier properties could be evaluated by EIS. The velocity of water diffusion through the bulk polymer was calculated for an estimated film thickness of 5 μm; Fig. 3.65 presents the received data. Measurements in this case were not carried out with a microcapillary cell, but on a circular area of 1 cm in diameter (see section 3.5.2.3). The Bode plots (not shown here) therefore rather resembled Fig. 3.50b, but nevertheless allowed the determination of the coating capacitance usually at 10 kHz (phase > 80°) [16]. The water uptake was in the same order of magnitude compared to the unmodified films applied in previous sections 3.5.3.1 to 3.5.3.4; see also Fig. 3.49. However, it strongly fluctuated and therefore was not a suitable parameter for the analysis of characteristic changes within the polymer network of tDMC and BDDA modified latices. Nevertheless a slight decrease of the H_2O diffusion coefficient was detected for films with reduced averaged polymer chain length compared to those composed of particles with highly cross-linked macromolecules. Because of their dense polymer structure it can be expected that water diffusion through BDDA modified latices occurs decelerated compared to identical processes at system nBA/Sty(T_g = 0 °C), as it is indicated by Fig. 3.65.

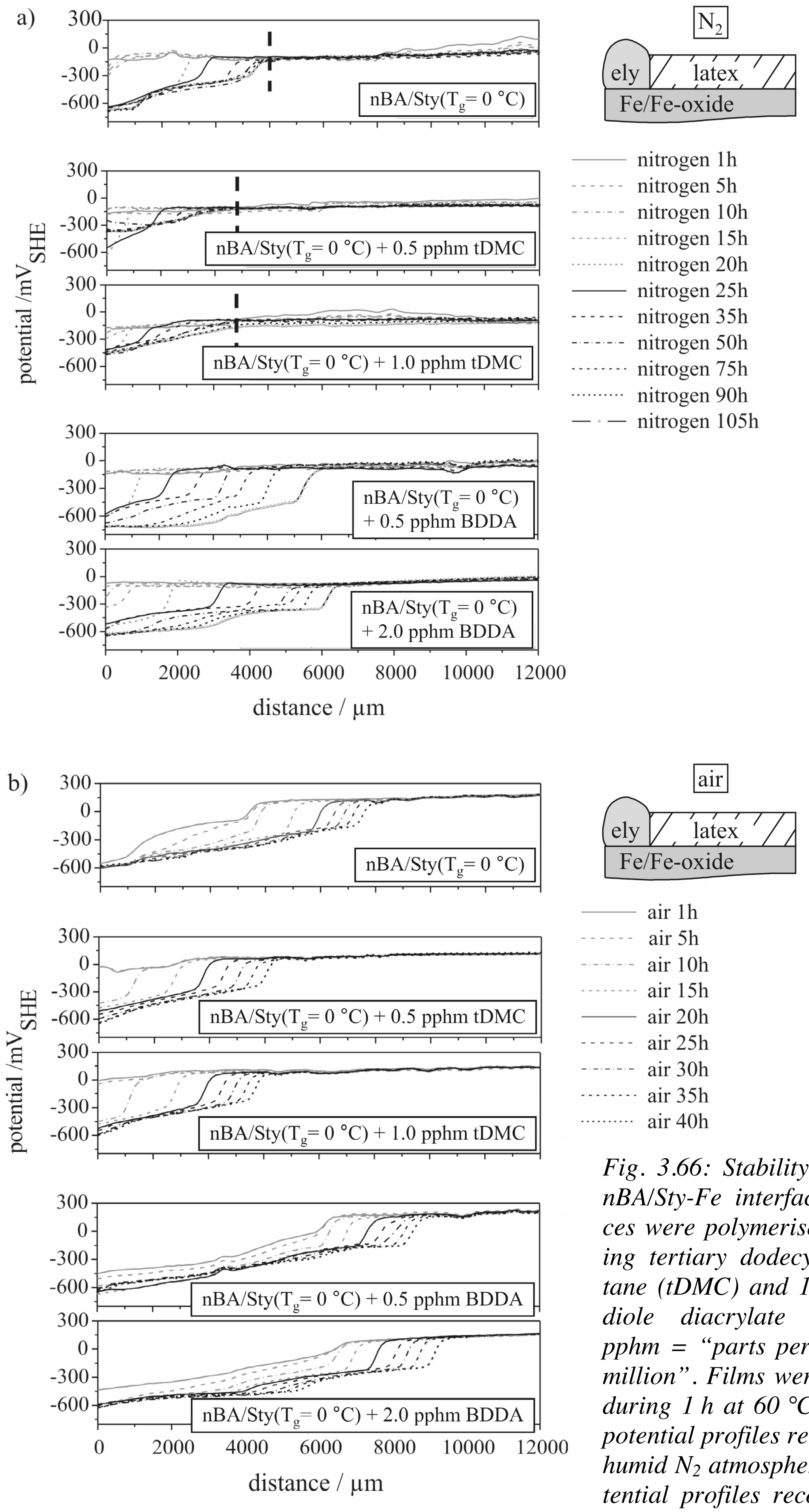

Fig. 3.66: Stability study of nBA/Sty-Fe interfaces. Latices were polymerised applying tertiary dodecylmercaptane (tDMC) and 1,4-butandiole diacrylate (BDDA); pphm = "parts per hundred million". Films were formed during 1 h at 60 °C. a) SKP potential profiles recorded in humid N_2 atmosphere, b) potential profiles recorded after switching to humid air.

The advantageous effect of tDMC in this context may be explained with an improved coalescence of latex particles during film formation, supported by shorter and mobile polymer chains bridging interparticle free volumes. This obviously overcompensates the expected easy water ingress through the particle bulk with its less dense macromolecular structure compared to the BDDA modified latices.

To further investigate whether the influence of tDMC is not limited to inhibited water diffusion through the polymer bulk, but also affects the latex/iron oxide/iron interface stability, cathodic delamination processes were initiated at these systems, monitored by SKP. Fig. 3.66 illustrates the received potential profiles. The experiment was started in humid nitrogen atmosphere (Fig. 3.66a).

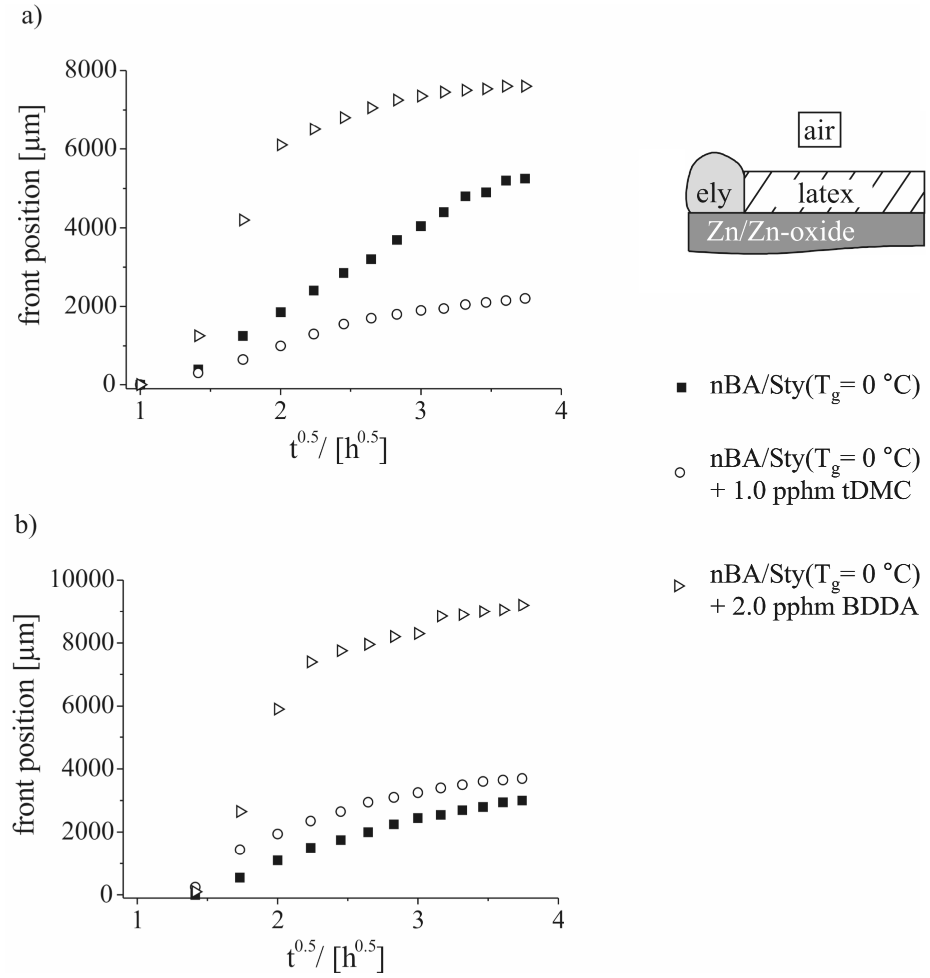

Fig. 3.67: Comparison of the stability of nBA/Sty(T_g = 0 °C)-zinc oxide/zinc interfaces, annealed for 1 h at 60 °C. Modification of the latex dispersions was performed during emulsion polymerisation by applying different amounts (pphm = parts per hundred million) of 1,4-butandiole diacrylate (BDDA) as cross-linking reagent and tertiary dodecylmercaptane (tDMC) to reduce the average polymer chain length. Displayed is the respective cathodic delamination front position versus square root of time, calculated from SKP potential profiles gained during two corrosive de-adhesion studies (a,b) performed in humid air.

Bold dashed lines allow an easy visual identification of the maximum interfacial ion transport progress after 105 hours measurement time for samples with uncharacteristic potential step width of the profiles.

Application of both 0.5 pphm and 1.0 pphm led to decelerated ion transport kinetics compared to basic system nBA/Sty(T_g= 0 °C). Doubling of the tDMC amount during emulsion polymerisation additionally seemed to have a slightly advantageous effect, as it was detected by means of SKP. In contrast the quadruplication of the BDDA quantity to 2 pphm indeed destabilised the interface compared to system nBA/Sty(T_g= 0 °C + 0.5 pphm BDDA). Both BDDA modified latices exhibited accelerated ion transport processes after application on iron oxide/iron surfaces, anyhow. The described tendency was also maintained after switching to humid air and initialisation of cathodic interface delamination (see Fig. 3.66b). It has to be pointed out that the interface stabilisation/de-stabilisation was well reproducible on iron substrates.

Although already indicated by the EIS results within Fig. 3.65, such effects nevertheless should be mainly attributed to the structural condition of the polymer/substrate interface. In analogy to the conclusions drawn in section 3.5.3.3 it is additionally assumed that higher cross-linked polymer chains are less mobile, diffusion of macromolecules is decelerated and consequently an adequate interfacial contact between nano-rough oxide surface and formed polymer layer is not achieved. Relatively large interfacial free volumes are still existent. They allow an accelerated interfacial transport of ions in humid nitrogen atmosphere and increased oxygen reduction current densities during sample exposure in humid air. This should promote cathodic delamination processes. On the other hand macromolecules with reduced averaged chain length are more mobile, should be able to easily diffuse into interfacial free volumes and thereby may effectively inhibit an oxidative degradation of the interface. This should especially apply to films in their flexible, elastic state for a T_g lower than ambient temperature during the experiment.

The interface stability of tDMC and BDDA modified latex films were also investigated applying zinc substrates. In agreement to the observations reported in section 3.5.3.5 the progress of corrosive delamination strongly fluctuated. Fig. 3.67 therefore exemplarily displays delamination front position versus $\sqrt{t}$ graphs for the basic system nBA/Sty(T_g= 0 °C) and layers modified with 1.0 pphm tDMC and 2 pphm BDDA. The turning points of the SKP potential profiles were calculated from corrosive de-adhesion measurements of two sets of samples (Fig. 3.67a and Fig. 3.67b). In fact application of the cross-linking agent again resulted with faster delamination kinetics, but the effect of tDMC remained unspecific on zinc substrates. Stabilised latex/substrate interfaces (Fig. 3.67a) were received as well as accelerated corrosive de-adhesion processes (Fig. 3.67b). The interfacial contact between oxide surface and latex layer obviously was that poor that the advantageous influence of tDMC could not be effective at all. Larger free volumes at the interface probably could not be bridged by polymer chain diffusion.

3.5.3.7 Influence of curing time and temperature on the stability of latex/oxide/metal interfaces

The impedance measurements of section 3.5.3.1 proved adequate barrier properties and complete film formation after latices with a $T_g \leq 20$ °C were cured for 1 h at 60 °C.

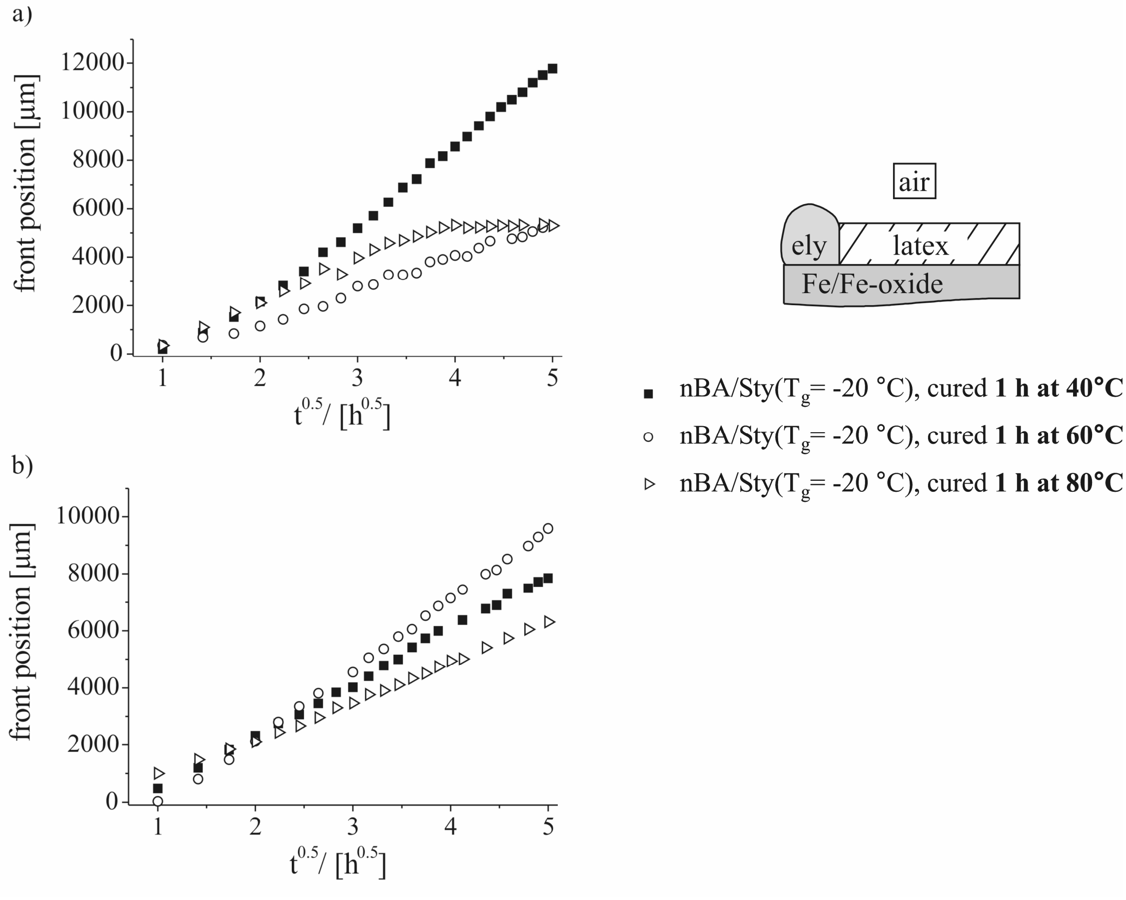

Fig. 3.68: Comparison of the stability of nBA/Sty(T_g = -20 °C)-iron oxide/iron interfaces, annealed for 1 h at different temperatures. Displayed is the respective cathodic delamination front position versus square root of time, calculated from SKP potential profiles gained during two corrosive de-adhesion studies (a,b) performed in humid air.

It was also shown that the number of pores increased with rising glass transition temperature under these conditions. The SKP results of chapters 3.5.3.2 to 3.5.3.4 and 3.5.3.6 on the other hand confirmed that the coating/substrate interface stability was determined by the latex T_g and polymer network density, but could not be generally correlated to water uptake and H_2O diffusion through the latex films. Polymer barrier properties and the latex/substrate interface stability do not seem to automatically depend on each other. It is the question whether a further improvement of the latex/substrate interface stability can be achieved by adjustment of the film formation parameters even though EIS measurements already indicated sufficient resistance towards water ingress. It is known that interparticle diffusion and layer coalescence can be promoted by long-term annealing at elevated temperatures after a first film formation step [1]. For industrial application, such procedure can be uneconomic.

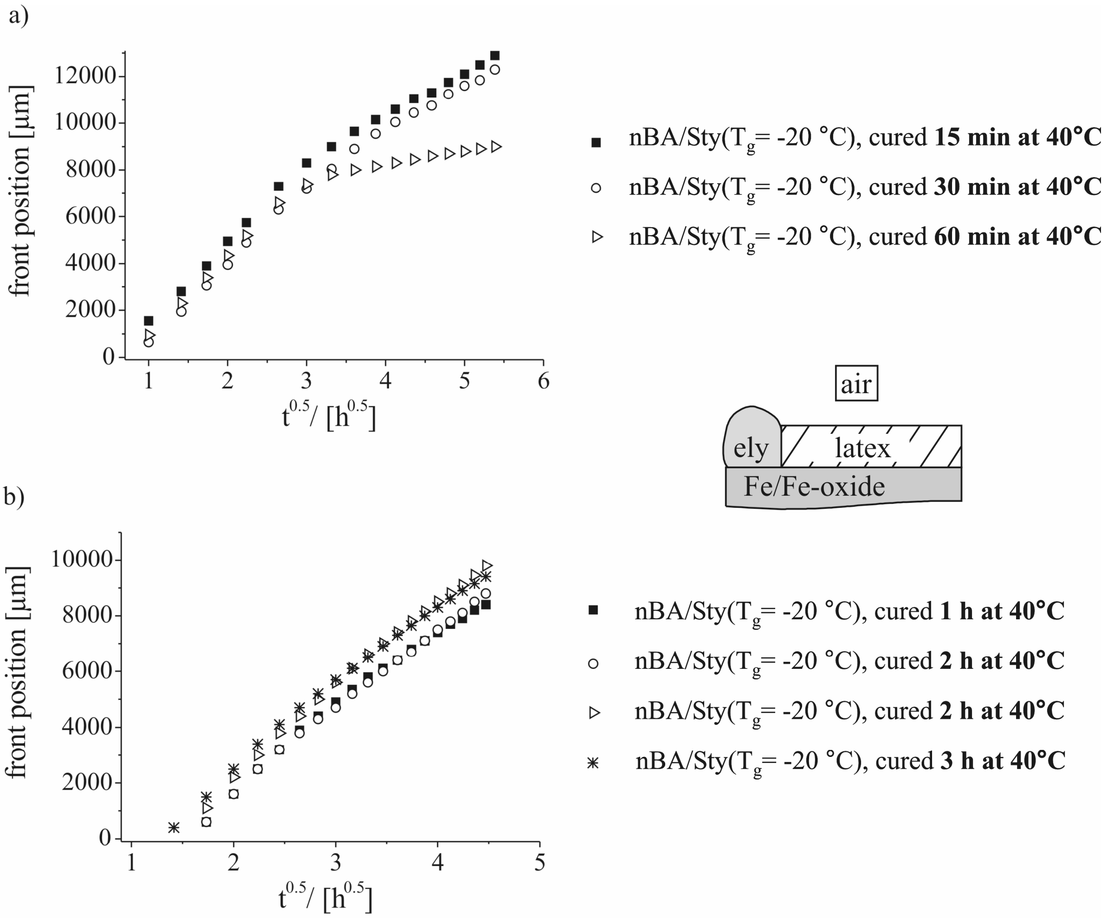

Fig. 3.69: Comparison of the stability of nBA/Sty(T_g = -20 °C)-iron oxide/iron interfaces, annealed for different times at 40 °C. Displayed is the respective cathodic delamination front position versus square root of time, calculated from SKP potential profiles gained during two corrosive de-adhesion studies (a,b) performed in humid air.

Within the here presented study it was consequently focussed on curing times between 15 minutes and 3 hours; the annealing temperature was varied between 40 °C and 120 °C. Fig. 3.68 illustrates two sets of cathodic delamination front position versus √t graphs for latex nBA/Sty(T_g= -20 °C) applied on iron substrates. It exhibited sufficient capacitive properties when probing by EIS (see Fig. 3.48). Film formation was performed for 1 h at a temperature of 40 °C, 60 °C and 80 °C. No general improvement of the interface stability with increasing annealing temperature could be detected. It can be stated that curing at 80 °C in fact did not always result in decelerated cathodic delamination kinetics, but a disadvantageously influence on the interface stability was not effective, anyhow. As the samples cured at 40 °C never showed best performance towards corrosive de-adhesion resistance, it was tried to evaluate whether a variation of the annealing time could lead to improved interface stabilities.

Fig. 3.69 presents delamination front position versus √t graphs again for polymer nBA/Sty(T_g= -20 °C) applied on iron substrates, this time cured at 40 °C for 15-60 minutes (Fig. 3.69a) and 1-3 hours (Fig. 3.69b). In comparison to Fig. 3.68, only slight variations of the cathodic delamination tendency along the respective latex/iron oxide/iron interfaces could be detected. In fact it did not make a relevant difference whether the basic curing time of 1 h usually applied within this chapter 3.5 was extended or shortened. Fig. 3.69a indicates a deceleration of the corrosive de-adhesion kinetics at longer exposure times to humid air. This may be attributed to a statistic effect. Nevertheless it can be concluded that already 1 h curing in fact supported more or less complete film formation.

The analysis was also extended to tertiary dodecylmercaptane (tDMC) modified nBA/Sty(T_g= 0 °C) latices. Fig. 3.70 displays the respective SKP potential profiles recorded after initialisation of cathodic interface delamination. Curing was performed at 60 °C and 120 °C. Samples exposed to elevated temperature exhibited a poor resistance towards corrosive de-adhesion. The investigated interface section of sample nBA/Sty(T_g= 0 °C 1.0 pphm tDMC) already entirely degraded due to fast cathodic delamination kinetics within the first 41 hours of the experiment. Annealing at 120 °C resulted in destabilised polymer/oxide/metal interface stability in this case. It was reported that curing even above the water boiling point further supports latex film formation [1]. The same obviously does not necessarily apply to the latex/substrate interface area. Although final conclusions cannot be easily drawn based on the available data, it might be supposed that interfacial water as applied solvent abruptly evaporated once heated up to the boiling point. This may have led to irreversible structural adjustments weakening the polymer/oxide adhesion. Ammonia was applied as neutralising reagent for the latex dispersions. Its accelerated expel at higher film formation temperature may have lowered the interfacial pH and thereby increased the number of protonated carboxylate functionalities. They may have easily formed dimer structures and thereby were not accessible to ionic interactions with metal centres of the oxide layer any more. This could explain less stable interface stabilities towards subsequently initiated cathodic delamination processes.

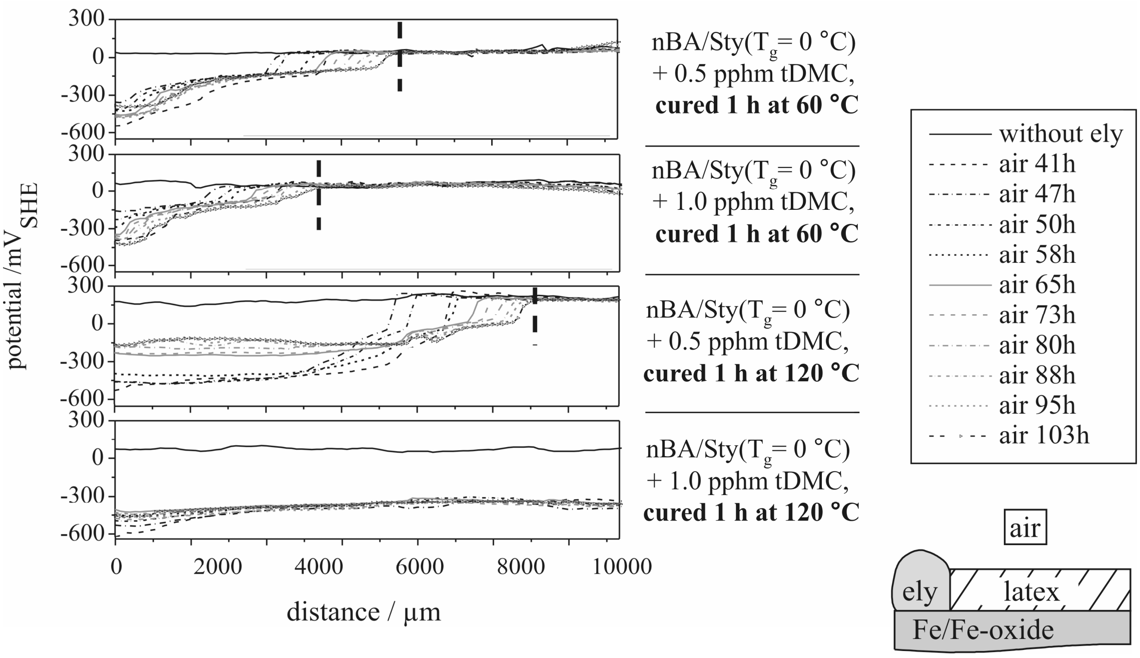

Fig. 3.70: Corrosive delamination study of nBA/Sty(T_g = 0 °C)- iron oxide/iron interfaces. Modification of the latex dispersions was performed during emulsion polymerisation by applying different amounts (pphm = parts per hundred million) of tertiary dodecylmercaptane (tDMC) to reduce the average polymer chain length. Film formation was performed after spin coating by annealing for 1 h at 60 °C or 120 °C. Displayed are SKP potential profiles recorded in humid air. Bold dashed lines visualise the delamination progress after 103 hours.

In this context it is concluded that a variation of the curing temperature seemed to be more effective for the adjustment of resulting latex/substrate interface stabilities than the application of different annealing times. The latter parameter probably rather allows a release of stress and strain within the films which casually results in improved interfacial contact between nano-rough oxide surface and formed polymer layer. Thereby an unspecific reduction of cathodic delamination kinetics may be achieved. The curing temperature in contrast affects the activation energy for interparticle and polymer chain diffusion. As long as the boiling point of the applied solvent is not reached, this can directly promote the film coalescence. Such process nevertheless does not seem to result in improved latex/iron oxide/iron interface stabilities in every case as it is indicated by Fig. 3.68.

3.5.4 Conclusions

Water uptake measurements as well as cathodic delamination and interfacial ion transport studies were performed with n-butyl acrylate (nBA)/styrene (Sty), 2-ethylhexyl acrylate (EHA)/Sty and nBA/EHA/Sty latex copolymer layer applied on oxide covered iron substrates. It could be proven that the velocity of corrosive de-adhesion continuously rises in the order EHA/Sty < nBA/EHA/Sty < nBA/Sty and with increasing glass transition temperature (T_g) of the coatings. Latices with a $T_g \leq 20$ °C exhibited adequate barrier properties towards water uptake after one hour curing at 60 °C. Layers of the same coating series also resulted in comparable water uptake and H_2O diffusion rates through the bulk polymer. For EHA/Sty layer a generally lower water uptake was detected compared to the nBA/Sty series. This confirms that a higher interfacial water activity will support a subsequent cathodic delamination process. Determination of the coating surface energies reflected increasing polymer crosslinking with rising T_g values whereas electrochemical impedance measurements pointed at an increase of layer pores and defects. A T_g value significantly smaller than the ambient temperature of around 22 °C should increase the mobility of polymer chains, lead to optimised interface contact formation and improve the inhibition of corrosive polymer/iron oxide interface degradation. Latices of the T_g(40 °C)-category required annealing for 1 h at 100 °C for adequate film formation. Impedance spectra comparable to those of coatings with lower T_g could be achieved, but cathodic delamination and interfacial ion transport nevertheless occurred distinctly accelerated. The disadvantageous effect of a T_g above ambient temperature and the resulting glassy-like, brittle state of the coating layers obviously could not be compensated with a decreased water uptake and although H_2O diffusion was calculated to be decelerated.

No correlation of T_g and delamination kinetics could be detected for latex/zinc oxide/ zinc interfaces when zinc was also applied as substrate material within the defect area.

The delamination processes resulted in an increased susceptibility towards kinetic inhibitions. Insufficient corrosion resistance was also achieved by deposition of a thin SiO_2 plasma polymer between latex film and iron oxide/iron surface. The silicon oxide layer probably provided additional capillary forces and thereby promoted the interfacial transport of hydrated ions.

Latex films with dense polymer network and highly cross-linked macromolecules destabilised the coating/iron interface. Decrease of the average polymer chain length in contrast had an advantageous effect on the interfacial resistance towards cathodic delamination. Obviously low cross-linked, short macromolecules exhibit a higher mobility, promote interparticle diffusion and improve the contact between polymer and substrate surface. Such effects could not be observed for respectively investigated coated zinc samples. Coefficients for water diffusion through the latex films could be roughly correlated to the macromolecular network condition, but polymer barrier properties and the latex/substrate interface stability nevertheless do not seem to automatically depend on each other.

An increase of the curing temperature resulted in unspecific improvement of the latex/iron oxide/iron interface stability, as long as the boiling point of the applied solvent was not reached. An extension of the annealing time was less effective to achieve decelerated cathodic delamination kinetics.

3.5.5 References

[1] P.A. Steward, J. Hearn, M.C. Wilkinson, Adv. Coll. Interf. Sci. 86 (2000), 195.
[2] Turshatov, J. Adams, D. Johannsmann, Macromolecules 41 (14), (2008), 5365.
[3] Galliano, D. Landolt, Prog. Org. Coat. 44 (2002), 217.
[4] H.J. Butt, R. Kuropka, B. Christensen, Colloid Polym. Sci. 272 (1994), 1218.
[5] J. Zhang, S. Hu, J. Rieger, S. V. Roth, R. Gehrke, Y. Men, Macromolecules 41 (12), (2008), 4353.
[6] J.N. Yoo, L.H. Sperling, C.J. Glinka, A. Klein, Macromolecules 24 (1991), 2868.
[7] B.J. Roulstone, M.C. Wilkinson, J. Hearn, Polym. Int. 27 (1992), 43.
[8] A.C.I.A. Peters, G.C. Overbeek, A.J.P. Buckmann, J.C. Padget, T. Annable, Prog. Organ. Coat. 29 (1996), 183.
[9] G. Grundmeier, B. Rossenbeck, K.J. Roschmann, P. Ebbinghaus, M. Stratmann, Corr. Sci. 48 (2006), 3716.
[10] B. Rossenbeck, P. Ebbinghaus, M. Stratmann, G. Grundmeier, Corr. Sci. 48 (2006), 3703.
[11] T. Titz, F. Hörzenberger, K. Van den Bergh, G. Grundmeier, *(part I),* submitted to Corrosion Science.

[12] K. Wapner, B. Schönberger, M. Stratmann, G. Grundmeier, J. Electrochem. Soc. 152 (2005) E 114.
[13] D. Owens, R. Wendt, J. Appl. Pol. Sci. 13 (1969) 1741.
[14] N. Correia, J. Moura Ramos, B. Saramago, J. Calado, J. Coll. Int. Sci. 189 (1997), 361.
[15] S.-J. Park, J.-S. Kim, J. Coll. Int. Sci. 244 (2001) 336.
[16] R. Vlasak, I. Klüppel, G. Grundmeier, Electrochim. Acta 52 (2007) 8075.
[17] D.M. Brasher, A.H. Kingsbury, J. Appl. Chem. 4 (1954) 62.
[18] J.T. Zhang, J.M. Hu, J.Q. Zhang, C.N. Cao, Prog. Org. Coat. 49 (2004), 293.
[19] A. Amirudin, D. Thierry, Prog. Org. Coat. 26 (1995), 1.
[20] A. Leng, H. Streckel, M. Stratmann, Corr. Sci. 41 (1999) 579.
[21] A. Leng, H. Streckel, M. Stratmann, Corr. Sci. 41 (1999) 547.
[22] A. Leng, H. Streckel, K. Hofmann, M. Stratmann, Corr. Sci. 41 (1999) 599.
[23] W. Fürbeth, M. Stratmann, Corr. Sci. 43 (2001) 207.
[24] W. Fürbeth, M. Stratmann, Corr. Sci. 43 (2001) 229.
[25] W. Fürbeth, M. Stratmann, Corr. Sci. 43 (2001) 243.
[26] T. Titz, F. Hörzenberger, K. Van den Bergh, G. Grundmeier, *(part II)*, submitted to Corrosion Science.
[27] E. Riedel, Anorganische Chemie, 4. Aufl., Berlin-New York, de Gruyter 1999.
[28] J. Wielant, T. Hauffman, O. Blajiev, R. Hausbrand, H. Terryn, J. Phys. Chem. C 111(35) (2007), 13177.
[29] J. Wielant, R. Posner, G. Grundmeier, H. Terryn, J. Phys. Chem. C 112(33) (2008), 12951.
[30] J. Wielant, Thesis, Vrije Universiteit Brussel, April 2009, ISBN 978-90-5487-563-5.
[31] N. Kessel, D.R. Illsley, J.L. Keddie, J. Coat. Technol. Res., 5 (2008), 285.
[32] R.G. Joshi, T.P. Ziemer, W. Mao, W. Shen, F.N. Jones, J. Coat. Technol. Res. 6 (2009), 47.
[33] B.G. Bufkin, J.R. Grawe, J. Coat. Technol. 50,
Part I: 641 (1978), 41;
Part II: 643 (1978), 67;
Part III: 644 (1978), 83;
Part IV: 645, (1978) 70;
Part V: 647, (1978) 65.
[34] M.A. Winnik, J. Coat. Technol. 74, 925 (2002), 49.
[35] M.A. Winnik, Polym. Prep. 44 (2003), 100.
[36] A. Zosel, G. Ley, Macromolecules 26 (1993), 2222.

Chapter 4 –

Overall Conclusions and Outlook

The present study followed a comprehensive experimental approach to reveal the mechanisms of ion transport processes at polymer/oxide/metal interfaces, to evaluate determinant parameters for the progress of corrosive de-adhesion and to address them to the so called `electrolyte front position´. This could be achieved after probing of the interface stability by initiation of cathodic or combined cathodic/anodic delamination and monitoring its progress in particular with the height-regulated Scanning Kelvin Probe. The polymer/substrate interface design could be specifically adjusted by variation of the substrate material, in particular zinc and iron samples or steel substrates with distinct iron oxide structure. It was also focussed on the influence of the interfacial contact between adhesive layer and nano-rough oxide surface as well as the barrier properties of latex copolymer films of different monomer composition, glass transition temperature and polymer network density. Important results were received towards a distinctly increased knowledge of corrosion processes at polymer/oxide/metal interfaces and promising strategies for interface protection.

The transport of hydrated ions along polymer/oxide/metal interfaces does not depend on diffusion, as it was postulated up to now. In fact, ion migration in an electrostatic field is dominant even in extremely oxygen deficient humid atmosphere. Such processes can be detected at polymer/iron interfaces, but not for polymer coated zinc samples. It can be supposed that an initial reduction of residual oxygen will occur on iron substrates. This may lead to an accumulation of a surplus of negative charge at the oxide surface due to hydroxide formation, which electrostatically attracts cations from an electrolyte filled coating defect. A reduction of the negative oxide surface charge density in nitrogen atmosphere by structural crystallographic lattice adaptation seems to be excluded for the various iron oxide structures. On zinc oxide either no comparable excess charge is existent in inert atmosphere, or a continuous reduction of residual O_2 is impeded at low oxygen partial pressures. This assumption is based on a kinetic barrier for oxygen reduction and a possible structural adaptation of the ZnO wurtzite structure. The mentioned results are of distinct importance for prospective approaches aiming at a specific design of polymer/oxide interfaces with improved stability towards corrosive de-adhesion. It was shown that interfacial ion diffusion is *not* the initial step of cathodic delamination. In fact water cannot be entirely prevented from diffusing through a polymer layer and accessing the adhesive/substrate interface. Wet de-adhesion consequently may result. But as long as the electrochemical activity of the substrate surface can be blocked, e.g. by application of a conversion chemistry layer, no ingress of ions from an electrolyte filled coating defect will be of relevance. This is important as the presence of additional ions at the interface usually leads to a compaction of the respective electrolytic double layer. It lowers the activation energy barrier for thermodynamically allowed corrosion processes and thereby potentially supports the degradation of a polymer/oxide/metal interface.

It could be shown that the basic mechanisms of interfacial ion transport at buried interfaces of polymer coated substrates and reactive electrolyte spreading processes along uncoated oxide surfaces are equivalent. A selective cation transport occurs on zinc and iron substrates in humid air, whereas no such process could be detected on zinc oxide in nitrogen atmosphere of extremely reduced oxygen partial pressure. Again the formation of a surplus of negative charge at the surface and a correlated electrostatic attraction of cations from the defect electrolyte seem to be determinant. It could be also estimated that electrokinetic effects should be contributing. A larger difference between surface pH and isoelectric point will result in a decrease of the electrolyte/iron oxide interface tension and additionally promote an electrolyte spreading. These findings are extremely helpful for the future analysis of organic/oxide interface structures. Reactive electrolyte spreading can be applied to simulate corrosive delamination processes after specific adsorption of model molecules, e.g. self-assembling monolayer, on metal oxides. Easy access is gained to monitor the resulting adjustment of the molecular structure during alkalisation of and oxygen reduction processes at the oxide surface, because the organic/oxide interface is not really `buried´ any more. Also a systematic step by step design of polymer/oxide/metal interfaces is accessible to better estimate the single effects of oxide surface structure, corrosion protective coating (e.g. plasma polymer film, conversion chemistry layer or thin phosphate film), adhesion promoting organic primer and topcoat. Last but not least distinctly simplified interface structures open the gate for any theoretical approach. It will be possible to experimentally check theoretically predicted delamination progress rates at computer designed, simplified organic/oxide interfaces. The applied theoretical tools thereby can be prospectively improved to more and more replace complex, extensive and expensive experiments.

Measurements in Scanning Kelvin Probe Blister-Test geometry allowed a variation of mechanical and corrosive load applied to an electrolyte filled coating defect. In combination with a selective adjustment of the atmospheric humidity a specific affection of the corrosive delamination front could be achieved. It was thereby proven that electrochemical interface degradation precedes a macroscopic polymer de-adhesion. The progress of delamination strongly responded to the available interfacial water activity. It was shown that initial adjustment of the polymer/substrate interface structure to different air humidity seems to be kept and determines the velocity of subsequent electrochemical degradation processes. Relative differences in polymer/substrate peel-off forces at varying atmospheric moisture occurred to be generally suited for the prediction of relative velocity differences of a following corrosive delamination. Increase of the hydrostatic electrolyte pressure in the defect accelerated these processes. This was attributed to an expansion of interfacial free volumes and to a compensation of the increased interfacial water loss rate near the electrolyte front position at reduced air humidity. Cathodic defect polarisation was an effective tool to address corrosive de-adhesion kinetics. Nevertheless it was also found to end up with self-inhibition at reduced atmospheric moisture; the relevant lateral dimensions of the electrolyte front thereby could be confined to cover less than 250 μm. The followed approach allowed a further insight into the complexity of oxidative interface degradation and can be regarded as basis for the extension of the experiments to advanced interface designs. This in particular applies to additional corrosion protective layers between adhesive and oxide/metal substrate.

By variation of different iron oxide structures it could be proven that the polar component of the surface energy is a suitable parameter to predict the resulting adhesion strength after coating with a polyurethane layer. Subsequently initiated cathodic delamination processes at the polymer/substrate interface strongly responded to the detected tendencies within the adhesion forces. This result will help to further introduce relatively cost-efficient peel-off tests for the estimation of interface stabilities even towards corrosive delamination in future. It was furthermore shown that the velocity of reactive electrolyte spreading along uncoated iron oxide surfaces is *not* connected to their water contact angles and surface energies. Electrode kinetics obviously play a dominant role.

A detailed study of the dependency of the polymer network condition and composition was performed applying styrene/acrylic copolymer films with different glass transition temperature on iron and zinc substrates. A comparison of film barrier properties with the resulting latex/substrate interface stabilities towards corrosive de-adhesion revealed that water uptake and the rate of H_2O diffusion through the polymer bulk do not automatically determine the delamination kinetics. In contrast, the interfacial contact between nano-rough oxide surface and filmed polymer seems to be extremely important for the progress of interfacial ion transport. Flexible and elastic polymers with a glass transition temperature below ambient temperature did not only result in reduced pore density within the films, but obviously were also able to seal interfacial free volumes to inhibit corrosive delamination. An advantageous effect of reduced averaged polymer chain lengths was explained with an increased macromolecular mobility to support latex particle interdiffusion and coalescence. In contrast a higher network density resulted in destabilised polymer/substrate interfaces. A stepwise inhibition of ion transport beyond simulated iron-zinc and iron-SiO_2 cut-edges, coated with latices of decreasing glass transition temperature, underlined the benefit of these measurements for industrial application purposes.

The results presented in this study were already used to re-adjust the scientific focus and approaches followed within the Max-Planck-Institut für Eisenforschung and associated groups. This in particular applies to the fact that strong efforts are currently made to evaluate the importance of the water activity at polymer/substrate interfaces instead of an investigation of interfacial ion diffusion processes. Furthermore this work in particular underlines the huge importance of the Scanning Kelvin Probe as tool for the analysis of corrosion processes at polymer/oxide/metal interfaces.

Appendix

Abbreviations

Acronyms

AES	Auger Electron Spectroscopy
AFM	Atomic Force Microscopy
anod	anodic
ATR-IR	Attenuated Total Reflection-Infrared Spectroscopy
BDDA	1,4-butandiole diacrylate
cath	cathodic
Diff	(as index:) diffusion
DSC	Differential Scanning Calorimetry
EHA	ethyl hexylacrylate
EIS	Electrochemical Impedance Spectroscopy
ely	electrolyte
HOMO	Highest Occupied Molecular Orbital
HSAB	Hard Soft Acid Base concept
IEP	IsoElectric Point
IR	Infrared Spectroscopy
IR drop	potential drop
LUMO	Lowest Unoccupied Molecular Orbital
nBA	n-butyl acrylate
NHE	Normal Hydrogen Electrode (= SHE)
OCP	Open Circuit Potential
ox	oxide
pH	potentia Hydrogenii
pol	polymer
pphm	parts per hundred million
PZC	Point of Zero Charge
ref	reference
r.h.	relative humidity
SEM	Scanning Electron Microscopy
SHE	Standard Hydrogen Electrode (= NHE)
SKP	Scanning Kelvin Probe
SKP-BT	Scanning Kelvin Probe Blister-Test
Sty	styrene
tDMC	tertiary dodecylmercaptane
ToF-SIMS	Time-of-Flight Secondary Ion Mass Spectrometry
XPS	X-ray Photoelectron Spectroscopy

Latin symbols

a	activity
A	area
Å	angstrom
c	concentration
C	capacitance
°C	degree Celsius
C_C	coating capacitance
C_{DL}	double layer capacitance
cm	centimetre
cm^{-1}	wavenumber
C_{p0}	coating capacitance extrapolated to time = 0
C_{psat}	coating capacitance at saturation level
d	difference/or: distance/or: penetration depth
d_0	mean plate distance
D	diffusion coefficient
$_D$	(as index:) Donnan
e	elementary charge
E	energy/or: electric field strength
$\vec{E}$	electric field
eV	electron volt
$E_{binding}$	binding energy
E_{corr}	corrosion potential
E_{kin}	kinetic energy
f	frequency
F	Faraday constant/or: force
$\vec{F}_E$	electric force
$\vec{F}_R$	friction force
g	gram
G	free enthalpy
h	Planck constant/or: hour
Hz	hertz
i	current density
$_i$	(as index): species
I	intensity/or: current
I_0	current amplitude
I_c	interfacial cation current density
J	particle flow
k	absorption factor
kHz	kilohertz
kJ	kilojoule
l	electrode distance
L	litre
ln	natural logarithm
log	logarithm (decadal)
$_m$	(as index:) modulation
mbar	millibar
mJ	millijoule
mm	millimetre
mV	millivolt

n_1,n_2	refractive indices
N	Newton
nm	nanometre
p	pressure
Pas	pascal
Q	charge
r	ion radius
R	universal gas constant/or: resistance
R_{el}	electrolyte resistance
R_c	distance normalised resistance towards cation transport
R_C	coating resistance
R_{CT}	charge transfer resistance
s	second
t	time/or: transference number
T	temperature
T_g	glass transition temperature
u	ion mobility
U	voltage/or: potential drop within an electrolyte
U_0	voltage amplitude
U_{ext}	external voltage
v	velocity
W	watt
W_{ad}	work of adhesion
$W_{cohesion}$	work of cohesion
x	first dimension
z	charge number
Z	impedance
z_e	electron charge number

Greek symbols

γ	angle of incidence
Δ	difference
ε_0	dielectric constant in vacuum
ε_r	material dependent dielectric constant
ε_w	dielectric constant of water
η	viscosity
θ	contact angle
λ	wavelength
μ	chemical potential
μ_0	chemical potential for standard conditions
$\tilde{\mu}$	electrochemical potential
$\tilde{\mu}_e$	electrochemical potential of an electron
μl	microlitre
μm	micrometre
υ	frequency
ζ	specific resistance
π	circle constant (Ludolph´s constant, Archimedes´ constant)
σ^D	dispersive component of the interface tension

σ_{lg}	.	.	interface tension liquid-gas
σ^{P}	.	.	polar component of the interface tension
σ_{sg}	.	.	interface tension solid-gas
σ_{sl}	.	.	interface tension solid-liquid
Φ	.	.	electron work function
ϕ	.	.	water uptake
φ	.	.	Galvani potential
χ	.	.	surface potential
ψ	.	.	Volta potential
ω	.	.	angular frequency
Ω	.	.	ohm

Publications (Date: July 2009)

The following peer-reviewed publications were achieved during the last three years:

J. Wielant, R. Posner, G. Grundmeier, H. Terryn, *“Cathodic delamination of polyurethane films on oxide covered steel - Combined adhesion and interface electrochemical studies”,* Corr. Sci. 51 (2009), p. 1664.

R. Posner, G. Giza, R. Vlasak, G. Grundmeier, *”In-situ electrochemical Scanning Kelvin Probe Blister Test studies of the de-adhesion kinetics at polymer/zinc oxide/zinc-interfaces”,* Electrochim. Acta 54 (2009), p. 4837.

B. Lange, R. Posner, K. Pohl, C. Thierfelder, G.Grundmeier, S. Blankenburg, W.G. Schmidt,*”Water adsorption on hydrogenated Si(111) surfaces”,* Surface Science 603 (2009), p. 60.

R. Posner, T. Titz, K. Wapner, M. Stratmann, G. Grundmeier *“Transport processes of hydrated ions at polymer/oxide/metal interfaces. Part 2. Transport on oxide covered iron and zinc surfaces”,* Electrochim. Acta 54 (2009), p. 900.

R. Posner, K. Wapner, M. Stratmann, G. Grundmeier, *“Transport processes of hydrated ions at polymer/oxide/metal interfaces. Part 1. Transport at interfaces of polymer coated oxide covered iron and zinc substrates”,* Electrochim. Acta 54 (2009), p. 891.

J. Wielant, R. Posner, G. Grundmeier, H. Terryn, *“Interface dipoles observed after adsorption of model compounds on iron oxide films: Effect of organic functionality and oxide surface chemistry”*, Journal of Physical Chemistry C 112 (2008), p.12951.

Manuscripts submitted to peer-reviewed journals:

R. Posner, K. Wapner, S. Amthor, K.J. Roschmann, G. Grundmeier,*“Electrochemical investigations of the coating/substrate interface stability for styrene/acrylate copolymer films applied on iron”*, submitted to Corrosion Science.

R. Posner, M. Marazita, S. Amthor, K.J. Roschmann, G. Grundmeier, “*Influence of interface chemistry and network density for styrene/acrylate copolymer coated zinc and iron substrates on the kinetics of corrosive de-adhesion”*, submitted to Corrosion Science.

Manuscripts in preparation for submittance:

R. Posner, G. Giza, M. Marazita, G. Grundmeier, *“Corrosive de-adhesion and ion transport kinetics at polymer coated zinc interfaces,* SiO_2 *modified iron substrates and simulated iron/zinc cut-edges”.*

M. Santa, R. Posner, G. Grundmeier, *“Study of the 2-mercaptobenzothiazole/gold and silver interface degradation during reactive electrolyte wetting processes”.*